Doctoral theses at NTNU, 2023:86

Spyridon Chapaloglou

Data-driven sizing and control of energy storage

for wind-powered offshore platforms

Energy Management and Control of Offshore Platforms Integrating Renewable Energy

Doctoral thesis

NTNU
Norwegian University of Science and Technology
Thesis for the Degree of Philosophiae Doctor
Faculty of Information Technology and Electrical Engineering
Department of Electric Power Engineering

NTNU
Norwegian University of Science and Technology

Spyridon Chapaloglou

Data-driven sizing and control of energy storage

for wind-powered offshore platforms

Energy Management and Control of Offshore Platforms Integrating Renewable Energy

Thesis for the Degree of Philosophiae Doctor

Trondheim, March 2023

Norwegian University of Science and Technology
Faculty of Information Technology and Electrical Engineering
Department of Electric Power Engineering

NTNU
Norwegian University of
Science and Technology

NTNU
Norwegian University of Science and Technology

Thesis for the Degree of Philosophiae Doctor

Faculty of Information Technology and Electrical Engineering
Department of Electric Power Engineering

ISBN 978-82-326-5995-1 (printed ver.)
ISBN 978-82-326-5544-1 (electronic ver.)
ISSN 1503-8181 (printed ver.)
ISSN 2703-8084 (online ver.)

Doctoral theses at NTNU, 2023:86

Printed by NTNU Grafisk senter

Dedicated to my parents,
Nikolaos and Angeliki

Abstract

One of the key aspects of facing the global environmental crisis and achieving sustainable development for future societies is re-thinking the way energy is produced and managed to serve the demand. This perspective calls for new technologies and methods for shaping how future power systems will operate for all residential, commercial, and industrial sectors. However, such efforts would not be complete without considering the particular case of isolated power systems, where additional challenges emerge. Those become even more critical for isolated industrial power systems where the restrictive environmental policies and regulations to be adopted may not be favorable to strict case-specific technical requirements. A characteristic example of this comes from the Oil & Gas (O&G) industry, where the next-generation isolated offshore platforms will integrate renewable energy, profoundly affecting the way those should be operated.

This thesis considers the significant environmental impact of offshore O&G operations, and explores various concepts toward decarbonizing this sector and dealing with the open technical challenges associated with the integration of renewable sources in a cost-effective way. The ideas presented throughout the thesis target this goal and are framed into a hierarchical structure where the use of energy storage is investigated as a potential solution from various perspectives and considering different time scales.

The first idea being presented is an optimal techno-economical analysis of energy storage that considers the uncertainty arising from both loading conditions and renewable (wind) power generation. This analysis enables decision makers to identify proper storage sizing and system configurations that maximize wind penetration and minimize fuel consumption. Nevertheless, modeling the uncertainty when considering the operation of such systems is not trivial and this can heavily impact the sizing results. Then, a new method is developed to capture the effects of combined uncertainties more accurately by generalizing the underlying patterns from the available datasets using statistical learning. This allows more accurate estimation of the potential techno-economical benefits created by the energy storage integration.

We then note that the above analyses refer to the daily operation of an O&G platform using historical information for longer reference periods (i.e., years) and even though this is useful for the investment decision process, this does not capture the effects of real-time operation. To address that, in the following chapters, this thesis revisits the problem of optimal operation under uncertainty from the real-time dispatch time scale (sub-hourly). One of the major challenges related to this time scale is the presence of sudden variations and non-smooth transitions in both load and wind power

generation. Those further complicate the problem of deciding the optimal commitment and dispatch of the conventional power generating units, in the presence of additional degrees of freedom that come from the energy storage, which acts as a connecting rod across time. This thesis thus presents a method devised for that purpose that exploits available historical data and machine learning to better quantify such non-anticipated events, and that leads to better energy management decisions while considering several objectives (environmental, economical, and technical) simultaneously. The potential of this energy management algorithm is demonstrated through case studies where fuel consumption, operational costs, and switching of the conventional units are reduced compared to the corresponding deterministic state-of-the-art-method.

The challenges of renewable integration for isolated systems are, however, distributed in various time scales, where the optimal decisions taken on one time scale may affect the system in another (shorter) one. One of the most notorious problems in isolated power systems is that of real-time active power balancing and frequency regulation. This becomes even more important for the case of isolated offshore O&G platforms that integrate renewable energy, and this not only because of the reduced system inertia but also because of the sudden yet large scale active power variations resulting from various operations. Narrowing to such time scales and further deeper in this thesis, new methods are developed that leverage historical data with probabilistic machine learning and risk to optimally coordinate the use of conventional units and energy storage to regulate the grid frequency while simultaneously tracking a techno-economical optimal operation under uncertain conditions. Such methods are focused on finding optimal control laws and allocating optimal storage capacity and primary reserves, providing frequency support with bounded and pre-defined deviation from the system's optimal operating point, while ensuring frequency stability. In this way, decisions satisfying objectives at higher time scales do not heavily interfere with technical requirements from lower ones, alleviating the impact of optimal energy management decisions, under user-defined risk acceptance and corresponding theoretical guarantees, paving the way toward fully autonomous and sustainable O&G platforms.

Acknowledgements

Before diving into the technical content of the present thesis, I would like to express my gratitude to some people, without whom this result would have never been possible.

First and foremost I would like to thank my supervisors, Prof. Elisabetta Tedeschi and Prof. Damiano Varagnolo, for their guidance in both technical and non-technical matters, any time of the day and day of the year, throughout the whole PhD project period. I owe a further thank you to my main supervisor Prof. Elisabetta Tedeschi, who trusted me and supported me even before the beginning of this project. The project itself would have never existed without her. In my case, I feel extremely lucky because my co-supervisor stood more like a second main supervisor, adding an extra technical dimension on the multi-disciplinary character of this project. For that I owe an additional thank you to Prof. Damiano Varagnolo.

I also want to express my gratitude to both the Norwegian Academy of Science and Letters (Det Norske Videnskaps-Akademi - DNVA) and the Onassis Foundation that honored me with their scholarships, that made this project come true.

The results and the scientific contributions achieved in this thesis, would not be possible without the combined efforts and teamwork of my collaborators. Therefore, I would like to thank particularly Dr. Francesco Marra (Equinor ASA), Andreas Faanes (writing his Master thesis under my supervision), Prof. Danilo Iglesias Brandao (Federal University of Minas Gerais), and Prof. Vincenzo Trovato (University of Trento and Imperial College London) and my colleagues Erick Fernando Alves, Babak Abdolmaleki, and Joseph Kiran Banda (NTNU). I would also like to thank Prof. Fernando Pinhabel Marafao (Sao Paulo State University - UNESP) and Prof. Magnus Korpås (NTNU) who were my mid-term evaluators and provided me with useful feedback on the continuation and completion of the project.

Besides technical skills, guidance, and collaboration, realizing such a large project requires stable psychological conditions, emotional management, and constant personal development not only in technical but also in human-related features. For that, I owe to acknowledge my friends that stood by my side, supported me ethically and psychologically, and helped me develop during these years. Even though the list of people I would like to thank in this part is really long and probably a whole new chapter in the thesis would be required, I will mention indicatively some of them for whom I will always be grateful for sharing together this PhD experience, including bad and good moments. Thus I thank Michalis Varkas, Andreas Giannakis, Michalis Spitieris, Artemis Baika, Babak Abdolmaleki, Augusto Matheus Dos Santos Alonso, and Erick Fernando Alves. In addition, I would like to thank my friends Fedon Pateromichelakis

and Kostas Tziotis for their support even before the beginning of the PhD but also throughout it, despite being geographically away.

A special thanks goes to Vasiliki Gkavidou who has been by my side, especially during the last months of this project, showing me affection, and care, helping me practically with several everyday living-related tasks, and giving me unceasing ethical/psychological support to complete this project in the best possible way.

I want to express my profound gratitude to my brother Charalampos Chapaloglou and sister Georgia Chapaloglou, for their incessant and selfless support, in person and remotely. They have always been there when I needed them, providing me with thoughtful, honest advice but also embracing my happiness at moments of joy as if it was theirs. I am grateful to my sister who has always been taking care of me since I have memories, not only as her very young brother but almost like a second mother. I am proud of her and the family she has made. Also, I will always remember that, the first day this PhD journey started, one of the most important days in my life, my brother was physically there, helping me with my first steps in a new country, the same way he has always been helping me, advising me, and motivating me in the most significant moments, no matter the time and place. I am proud of him and this thesis would not be the same without his support.

Last but definitely not least, I want to express my deepest gratitude to my parents Angeliki and Nikolaos Chapaloglou. There are not enough words to be brought together that could accurately encapsulate how proud I feel of my parents, both as a couple and individually for each of them and for separate reasons. I owe them the person I have become because it is their combined love, efforts, and commitment that granted me everything I consider good in myself and the opportunity to develop into the person I envisioned. Every personal achievement will always reflect a part and an aspect of them. This thesis is dedicated to them.

Contents

List of Figures

Chapter 4

Appendix C

List of Tables

Chapter 6

Chapter 7

Chapter 8

Appendix A

Appendix B

Dissemination of research

List of publications

Here follows the dissemination of the research outcomes, during the PhD project period:

C1 **Spyridon Chapaloglou**, Damiano Varagnolo and Elisabetta Tedeschi, Techno-Economic Evaluation of the Sizing and Operation of Battery Storage for Isolated Oil and Gas Platforms with High Wind Power Penetration, *IECON 2019 - 45th Annual Conference of the IEEE Industrial Electronics Society*.

J1 **Spyridon Chapaloglou**, Damiano Varagnolo, Francesco Marra and Elisabetta Tedeschi, Data-informed scenario generation for statistically stable energy storage sizing in isolated power systems, *Journal of Energy Storage* **51**, 104311 (2022).

J2 **Spyridon Chapaloglou**, Damiano Varagnolo, Francesco Marra and Elisabetta Tedeschi, Data-driven energy management of isolated power systems under rapidly varying operating conditions, *Applied Energy* **314**, 118906 (2022).

C2 **Spyridon Chapaloglou**, Damiano Varagnolo, Francesco Marra and Elisabetta Tedeschi, Data dependent concurrent storage sizing and control design for frequency support in isolated power systems. *2021 European Control Conference (ECC)*.

J3 **Spyridon Chapaloglou**, Andreas Faanes, Damiano Varagnolo and Elisabetta Tedeschi, Multi-objective control of isolated power systems under different uncertainty approaches. *Sustainable Energy, Grids and Networks (SEGAN)* **32**, 100853 (2022).

C3 **Spyridon Chapaloglou**, Danilo I. Brandao and Elisabetta Tedeschi, Dynamic Converter Capacity Allocation for Multifunctional Energy Storage Systems in Oil and Gas Applications. *2021 Sixteenth International Conference on Ecological Vehicles and Renewable Energies (EVER)*.

C4 Joseph Banda, **Spyridon Chapaloglou** and Elisabetta Tedeschi, MV Multi-functional Retrofit Converter for Enhanced Power Quality on O&G Platforms. *2022 IEEE 13th International Symposium on Power Electronics for Distributed Generation Systems (PEDG 2022)*.

C5 **Spyridon Chapaloglou**, Babak Abdolmaleki and Elisabetta Tedeschi, Optimal Sizing and Placement of Droop-based Converters in DC Microgrids With ZIP Loads. *2022 2^{nd} International Conference on Sustainable Mobility Applications, Renewables and Technology (SMART)*.

J4 **Spyridon Chapaloglou**, Erick Alves, Vincenzo Trovato and Elisabetta Tedeschi, Optimal Energy Management in Autonomous Power Systems with Probabilistic Security Constraints and Adaptive Frequency Control. *IEEE Transactions on Power Systems* pp. 1–12, (2023).

From the above list, only C1, J1, J2, C2, J3, J4 are directly related to this PhD thesis in accordance with Figure 1.2 and as presented in Chapters 3 to 8 .

Below, scientific contributions besides the scope of the PhD project but associated with the broader research topics (Renewable Energy Source (RES) integration in island systems and Energy Management Systems (EMSs)) are listed:

J5 **Spyridon Chapaloglou**, Athanasios Nesiadis, Petros Iliadis, Konstantinos Atsonios, Nikos Nikolopoulos, Panagiotis Grammelis, Christos Yiakopoulos, Ioannis Antoniadis and Emmanuel Kakaras, Smart energy management algorithm for load smoothing and peak shaving based on load forecasting of an island's power system, *Applied Energy* **238**, Pages 627-642 (2019).

J6 **Spyridon Chapaloglou**, Athanasios Nesiadis, Konstantinos Atsonios, Nikos Nikolopoulos, Panagiotis Grammelis, Angel Carrera and Oscar Camara, Microgrid energy management strategies assessment through coupled thermal-electric considerations. *Energy Conversion and Management* **228**, 113711 (2021).

Nomenclature

Acronyms

$\mathcal{MVN}$	multivariate normal (Gaussian)
FP	*Full Parametrization*
$i.i.d.$	Independent and Identically Distributed
NP	*No Parametrization*
oob	Out-Of-Bag
pdf	probability density function
PWL	Piece-Wise Linear
ro	Robust Optimization
$RoCoF$	Rate of Change of Frequency
RV	Random Variable
RV	*Random Variable*
sa	Scenario Approach
SF	*State Feedback* parametrization
sg	*scenario generation*
so	Stochastic Optimization
SoC	State of Charge
SoE	State of Energy
sr	*scenario reduction*
FFS	Fast Forward Selection
MC	*Monte Carlo*
VSS	*Value of Stochastic Solution*
APD	Active Power Disturbance
APS	Autonomous Power System
BESS	Battery Energy Storage System
BPS	Bulk Power System
CAPEX	capital expenditure
CDF	Cumulative Distribution Function
COI	Center of Inertia
CRF	Capital Recovery Factor
CRPS	Continuously Ranked Probability Score
DMPC	Deterministic Model Predictive Control
ECDF	Empirical Cumulative Distribution Function
ED	Economic Dispatch
EMS	Energy Management System
ESS	Energy Storage System
FCUC	Frequency-Constrained Unit Commitment
FFR	Fast Frequency Regulation
FRR	Frequency Restoration Reserves
GHG	GreenHouse Gas
GT	Gas Turbine
IMC	Internal Model Control
ISE	Integral Square Error
KDE	Kernel Density Estimation
LB	Lower Bound
LFC	Load Frequency Control
LP	Linear Program
LQR	Linear Quadratic Regulator
LTI	Linear Time Invariant

MILP	Mixed-Integer Linear Program
MIMO	Multi-Input Multi-Output
MINLP	Mixed Integer Nonlinear Problem
MLE	Maximum Likelihood Estimation
MPC	Model Predictive Control
MSE	Mean Squared Error
NRMSE	Normalized Root Mean Squared Error
NWM	Numerical Weather Models
NWP	Numerical Weather Prediction
O&G	Oil & Gas
OPEX	operational expenditure
PFC	Primary Frequency Control
QP	Quadratic Programming
QRF	Quantile Random Forest
RES	Renewable Energy Source
RF	Random Forest
SAA	Sample Average Approximation
SCMPC	Scenario Model Predictive Control
SMPC	Stochastic Model Predictive Control
SOS	Special Ordered Set
SP	Stochastic Program
UB	Upper Bound
UC	Unit Commitment
UN	United Nations
UNESCO	United Nations, Educational and Cultural Organization
VRC	Variable Robustness Control

Part I

BACKGROUND

Chapter 1

Introduction

1.1 Background information

It only takes one quick web search with the keywords "humanity global challenges" to realize that the energy problem is one of them. The United Nations (UN) has listed climate change and the human fingerprint on GreenHouse Gas (GHG) emissions among its list of high priority global issues [1]. UNESCO has put the topic of "*Emissions Free Technology: Changing the Fossil Fuel Paradigm*" among the top and most compelling challenges for the future of humanity and the planet [2] and toward the implementation of the *Sustainable Development Goals (SDGs)* as defined by UN (*no. 7 - affordable and clean energy*). Clean and renewable electricity is also listed among the global challenges by the *World Resources Institute* [3] while the *Global Challenges Foundation* has put sustainable development for addressing global climate change and meeting the growing energy demand efficiently among the challenges needing global cooperation [4].

It is now clear why approaching the solution of such a great-scale problem requires global efforts and cooperation, established by international agreements (i.e., *Paris Agreement*, *Kyoto Protocol*) and radical policies such as the target set by the *European Green Deal* for Europe to be the world's first carbon-neutral continent by 2050 [5]. Achieving this requires strict regulations and energy policies across all different energy-related sectors such as the built environment, transportation, and power generation as well as across all types of energy consuming industries.

In that aspect, the O&G industry is deemed amongst the most emissions intensive, with the production and use of O&G accounting for over half of GHG emissions associated with energy consumption [6]. As an example, we may consider the O&G production in UK during 2018, which generated around 13.2 million tonnes of CO_2 emissions, with around 74% of them being the result of "in-situ" electric power generation from own gas production [7]. Such emissions become even more critical for offshore operations where those can be easily spread across larger areas due to the high wind conditions that favor pollutants dispersion, maximizing their detrimental impact [8, 9]. This is the case for the offshore O&G production in the *Norwegian Continental Shelf (NCS)* where the generated emissions (13.3 Mt CO_2 equivalent) were responsible for around 26.6% of the total Norwegian GHGs in 2020 [10, 11]. Considering that Norway was Europe's largest O&G producer in 2020 and that it covers about 2.3% of the global oil demand and 2.9% of the global natural gas demand [12], this highlights

the potential and significance of decarbonizing O&G operations, especially offshore, in achieving Europe's tight climate change targets. Such targets are then reflected in adopting proper national policies and regulations, as is the case for Norway, which aims for a 50-55% emissions reduction by 2030 compared to 1990 [13]. Similar targets have now been adopted by all EU countries through the "Fit for 55" package [5]. In addition, as has been expressed by the O&G UK (OGUK) and Offshore Energies UK (OEUK) organizations, the UK aims for a world-leading low-carbon offshore industry accounting for only 0.5 million tonnes of GHG emissions by 2050 [7]. Most of those policies share a common ground when it comes to the replacement of "in-situ" power generation with green power sources [7] and taking advantage of the North Sea region, which has a capacity target of 300 GW for offshore wind power by 2050 [14].

The implementation of the aforementioned regulations and policies also affects the strategy for development of world-leading O&G industries, such as the Norwegian Equinor ASA. In particular, the integration of RES (focusing on wind power) in offshore O&G platforms has been proposed by the construction of offshore wind farms at nearby locations. This idea is currently being implemented through the *Hywind-Tampen* project [15], which is expected to be completed by 2022. For that project, 11 wind turbines with a combined capacity of 88 MW will provide renewable power locally to the remote platforms (about 140 km off the Norwegian coast), aiming for significant emissions reductions, estimated to 200,000 tonnes of CO_2 and 1,000 tonnes of NO_x per year. Similar intentions have been also expressed by the *Crown Estate Scotland* where recent studies [16] promote the integration of offshore O&G platforms with wind energy under the Innovation and Targeted Oil and Gas (INTOG) initiative [17], using combined wind and Gas Turbine (GT) generators in parallel.

However, introducing intermittent RES to a power system with highly variable operating conditions, such as the offshore O&G platforms, is directly dependent on the capability to store energy. As it has been remarkably stated in [17]:

"The variability of power is considered the biggest technical challenge to the integration of offshore wind and oil and gas infrastructure"

From that, it is then straightforward to understand the significance and potential contribution of integrating an Energy Storage System (ESS) to such systems.

It is a fact that battery technologies have been greatly improved in recent years as a result of the continuous breakthroughs and improvements related to the energy density and specific energy characteristics [18]. This has allowed for the widespread adoption of batteries in several industries (i.e., road and maritime transport sectors), positioning it as an adequately reliable and mature technological solution for other sectors to adopt. In addition, following global trends in battery system costs [19] and, in particular, cost projections of lithium-ion technology [20], it is straightforward to observe a consensus that prices are expected to keep falling in upcoming years. For example, as has been projected by the International Renewable Energy Agency (IRENA), the installed costs

of battery storage systems could fall by two-thirds (66%) by 2030 [21]. Such forecasts have also promoted the use of batteries in power system applications, paving the way for utility-scale batteries [22, 23]. This fact is also supported by the recent and expected improvements to the round-trip efficiencies [18], which have a particularly important role in the scalability of Battery Energy Storage Systems (BESSs). An important aspect that is also facilitating the reduction of batteries' prices comes from diminishing the marginal production cost by using large-scale mass production facilities, the so-called *megafactories*. Several such facilities are currently under construction in countries all over the globe, with Norway being one of them [24, 25], further supporting its role in the renewable transition.

It is then not surprising that BESSs are becoming a popular choice for the portfolio of renewable power providers. Not only can BESSs help toward smoothing of the power provision by RESs, but given a considerable size, they can also provide operational flexibility and support the grid. Such features, though beneficial to any kind of power system, are particularly important for remote isolated grids. One relevant and interesting application comes from the integration of offshore wind with batteries, as is the case for the *Batwind* project from *Equinor*. This shows the potential for BESSs to contribute toward making renewable energy more cost competitive for several applications. Such solutions have also been investigated for the case of offshore O&G installations, where hybrid power plants enable increased efficiency and lower emissions, as is the case for the deep-water *West Mira* oil rig in the North Sea [26].

1.2 Objectives and Scope

1.2.1 Motivation

Following the facts from the previous section, it now becomes clear that the integration of RESs and BESSs in the offshore O&G industry is linked with several benefits and is deemed necessary to achieve the strict environmental goals as described. However, achieving this technological transition for the case of remote isolated offshore power systems is accompanied by various challenges entangling and complicating its implementation.

Such remote power systems, which are governed by stochastic power injections and time varying inertia due to intermittent dispatch of the conventional units, are prone to various technical problems in different time scales, ranging from sub-optimal operation to power quality issues. The time-varying loads and the intermittent renewable power injections result in uncertain dynamics that not only affect the safe operation of these grids but also complicate the ESS sizing problem, which, in practice, involves not only technical but also economical decision criteria.

The basic components that are typically parts of a modern isolated industrial power system, include conventional power generation units that are used as base units, different types of loads depending on the type of relevant equipment, some kind of RES (i.e., wind power), and an ESS acting as the multi-time scale energy buffer between

generation and consumption. That is also the case for the power systems within the offshore O&G industry. Then, three main questions (*Q1-Q3*) naturally arise:

Q1: How can we size an ESS (i.e., BESS) to provide operational flexibility and increased efficiency in isolated (industrial) power systems that integrate RESs in an economically effective way and under the presence of multiple uncertainties?

Q2: Given an available ESS in such isolated power systems, how should we operate the various power-related assets, to achieve economical and environmental efficient and sustainable operation, when the system is affected by the same sources of uncertainty as for the sizing problem, acting in multiple time scales?

Q3: Even under properly sized and managed ESSs, how can we further exploit them to provide ancillary grid services with minimum interaction between goals set on a higher time scale compared to the one of the power system dynamics?

As has been stated by Sebastian Bringsværd, head of floating wind development at Equinor [27]:

"The value in storage is not necessarily in the amount of energy you can store, but how you optimize, control and offer smarter energy solutions."

It is therefore clear that benefits emerging from the integration of ESS spanning multiple time scales depend on the way this is controlled. It is also true that different storage-related problems, depending on the decision-makers' perspective, share common sources of uncertainty. From the cost-benefit point of view, we have the sizing and EMS design problems and from the grid services, the control design problem. However, decisions concerning the future must be made *here and now*, in the absence of future information. Therefore, although both decisions (sizing and control) refer to future system operation, uncertainty needs to be inferred from available observations of the past.

Typical alternatives involve the use of deterministic reference time periods leading to *certainty-equivalent* problems, which fail to generalize on possible future outcomes. Others consider the extreme (and likely non-representative) cases, even if those are very unlikely to happen, leading to over-conservatism sacrificing potential benefits. Others rely on point forecasts for decision making, but the extrapolation quality is highly dependent on the method, the available data, and the time horizon considered. Most importantly, high-quality extrapolation is still an open mathematical (statistical) challenge.

1.2.2 *Aim of the thesis*

Therefore, aiming for sustainable isolated offshore O&G platforms, the idea proposed through this PhD thesis is the integration of appropriately sized battery energy storage (BESS) to the platform's power system and the development of smart EMSs and control algorithms to operate it. The goal of the proposed solutions is to compensate the stochasticity of the intermittent renewable power generation, considering at the same time the different possible operational patterns and lack of system information (i.e., plant model, disturbance model). The methods developed and described in the following chapters are related to the sizing and control of the storage system from the longer term techno-economic optimization and grid services provision perspectives, presenting potential benefits in multiple time scales, which are naturally linked on the energy level through the ESS and under the same sources of uncertainty.

As explained before, different uncertainty modelling approaches can be followed depending the selected degree of conservatism and the availability of historical information. To that aim, data-driven methods are explored throughout this PhD thesis, to leverage uncertainty modelling assumptions due to lack of future information, by combining statistical analysis and probabilistic machine learning, justifying the "Data-driven" part of the thesis title.

1.3 THESIS OUTLINE

The holistic research approach followed in this thesis is illustrated in Figure 1.1. To highlight the inter-dependencies among the publications produced as part of the research outcomes of this thesis and the research questions, following the conceptual framework graphically summarized in Figure 1.1, we provide the flowchart in Figure 1.2 and then a short description of each chapter of this thesis. Each chapter is associated

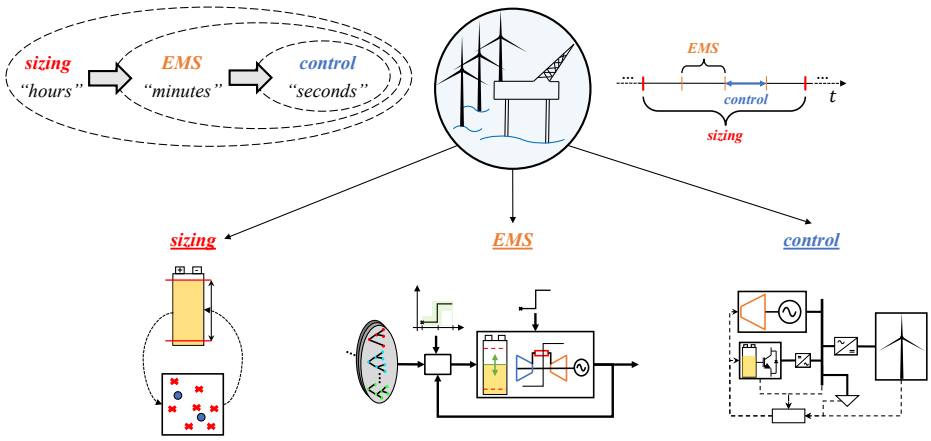

FIGURE 1.1. Thesis graphical abstract and hierarchical approach representation

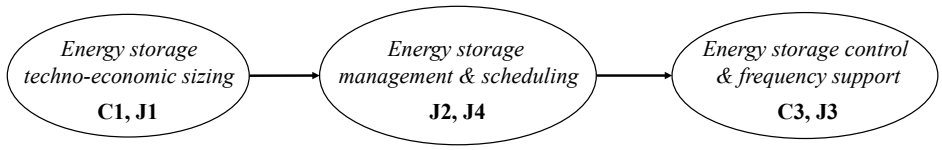

Figure 1.2. Conceptual flowchart and publications allocation

with one of the publications as presented in Dissemination of research.

Chapter 2: In the second chapter of this thesis, the research context and the methodological approach are presented, along with an extended summary of the whole thesis itself. The intention of this chapter is to give the reader all the relevant theoretical/-scientific background associated with the work presented in detail in the rest of the chapters, as well as a standalone limited version of those, presenting the main developed methods and results.

Chapter 3: In the third chapter, a preliminary approach is presented for the techno-economic sizing of a BESS under uncertainty. The effect of various system parameters is demonstrated through a sensitivity analysis, leading to some first insights regarding the optimal configuration of offshore O&G platforms that integrate wind power and ESS.

Chapter 4: In the fourth chapter, a data-driven methodology for the techno-economic sizing of a BESS under multiple and coupled uncertainties is presented. The developed methodology is suitable for 2-stage Stochastic Optimization (*so*) problems with multi-dimensional uncertainties and mixed integer recourse and is demonstrated for the case of a wind-powered O&G platform in which the GTs units can be shut down or turned on during the expected operation.

Chapter 5: In the fifth chapter, the focus is transferred to the operational problem and how to optimally design the EMS for the case of wind-powered O&G platforms that integrate a BESS. A data-driven methodology is derived, shedding light on the potential benefits when considering the uncertainty from the rapidly varying operational conditions and wind intermittency. The method is formulated as a control problem, making its applicability straightforward and suitable to cases where non-smooth disturbances affect a power system.

Chapter 6: In the sixth chapter, a data-driven control design method is presented for providing frequency support with an ESS. Again, the target application is isolated O&G platforms that integrate wind power. The proposed method offers user-defined risk-dependent concurrent control and sizing designs for the ESS.

Chapter 7: In the seventh chapter, a data-driven multi-objective control framework is presented for isolated power systems that integrate stochastic wind power injections and a BESS. Different uncertainty approaches and control parametrizations are compared, leading to various stochastic controllers with different probabilistic performance. The proposed framework is capable of providing simultaneous frequency regulation and State of Charge (SoC) tracking for the ESS.

Chapter 8: In the eighth chapter, an advanced data-driven EMS version is derived, building upon the EMS algorithm presented in Chapter 5, for the case of isolated industrial power systems. The developed EMS integrates safety guarantees for the continuous system operation along with its optimization goals, including techno-economic objectives. The primary control layer is designed to optimally integrate the ESS contribution while respecting optimal schedules defined in a higher time-scale. An adaptive uncertainty quantification framework is proposed that can capture rapid variations of the net load, leading to a time-varying control framework that can guarantee a user-defined probabilistic demand satisfaction.

Chapter 9: In the ninth and final chapter of this thesis, the main conclusions are presented along with comments, discussions, and future work perspectives.

1.4 Research contributions

In this section, the main scientific contributions are summarized. The following contributions are derived from the scientific publications related to this thesis and presented in detail in Chapters 3 to 8:

- propose an optimal ESS sizing methodology for isolated power systems with significant RES penetration. Such methodology considers the relationship between the optimization problem and uncertainty modelling, accounting for the effects of coupled load and RES uncertainties.
- propose a predictive EMS for isolated power systems, which integrates multiple objectives and is capable of quantifying very short-term uncertainties to optimally manage the system under irregular events, relying just on past information.
- provide guidelines for concurrent sizing and control design of ESSs, for robust frequency regulation of isolated ac power systems, under user-defined conservatism.
- propose a control framework for achieving simultaneous frequency regulation and SoC tracking for isolated ac power systems with a BESS, under stochastic RES power injections, model uncertainty, and different control policies.

- propose an EMS for isolated ac power systems, capable of simultaneously achieving optimal scheduling and secure system operation under dynamic uncertainty considerations and bounded impact on the ESS schedule.

Besides those, we also summarize contributions not directly related to the PhD thesis but derived during the PhD project period:

- propose the use of a multi-functional converter for integration of a BESS in O&G platforms, responsible for providing local compensation to increase local power quality. An algorithm is proposed that optimally adjusts the multiple services given power capacity restrictions from the BESS converter.

- propose a method for simultaneous sizing and siting of droop-controlled distributed generators to guarantee optimal current sharing and safe grid operation, for DC microgrids with constant power loads.

1.5 References

[1] U. Nations, "Global Issues," publisher: United Nations. [Online]. Available: https://www.un.org/en/global-issues Cited on page/s 3.

[2] https://plus.google.com/+UNESCO, "Top challenges for the future of humanity and the planet include sustaining ocean health, reversing biodiversity loss and addressing infectious agents," May 2015. [Online]. Available: https://en.unesco.org/news/top-challenges-future-humanity-and-planet-include-sustaining-ocean-health-reversing Cited on page/s 3.

[3] . G. S. N. Suite 800, Washington, D. 20002, and U. . P. .-. . Fax +1729-7610, "Tackling Global Challenges," May 2018. [Online]. Available: https://www.wri.org/strategic-plan/tackling-global-challenges Cited on page/s 3.

[4] "15 Global Challenges – The Millennium Project." [Online]. Available: https://www.millennium-project.org/15-global-challenges/ Cited on page/s 3.

[5] "A European Green Deal." [Online]. Available: https://ec.europa.eu/info/strategy/priorities-2019-2024/european-green-deal_en Cited on page/s 3, 4.

[6] L. Fletcher, T. Crocker, J. Smyth, and K. Marcell, "Which oil and gas companies are ready for the low-carbon transition?" CDP, Tech. Rep., Nov. 2018. Cited on page/s 3.

[7] M. Elgenedy, K. Ahmed, G. Burt, G. Rogerson, and G. Jones, "Unlocking the UK Continental Shelf Electrification Potential for Offshore Oil and Gas Installations: A Power Grid Architecture Perspective," *Energies*, vol. 14, no. 21, p. 7096, Oct. 2021. [Online]. Available: https://www.mdpi.com/1996-1073/14/21/7096 Cited on page/s 3, 4.

[8] R. Cichowicz, G. Wielgosiński, and W. Fetter, "Effect of wind speed on the level of particulate matter PM10 concentration in atmospheric air during winter season in vicinity of large combustion plant," *J Atmos Chem*, vol. 77, no. 1-2, pp. 35–48, Jun. 2020. [Online]. Available: https://link.springer.com/10.1007/s10874-020-09401-w Cited on page/s 3.

[9] "Air Quality Measurements Series: Wind Speed and Direction." [Online]. Available: https://www.clarity.io/blog/air-quality-measurements-series-wind-speed-and-direction Cited on page/s 3.

[10] "Emissions to air." [Online]. Available: https://www.ssb.no/en/natur-og-miljo/forurensning-og-klima/statistikk/utslipp-til-luft Cited on page/s 3.

[11] E. SF, "Towards a low-emission Norwegian industry.pdf," ENOVA SF, Tech. Rep., Nov. 2017. Cited on page/s 3.

[12] BP, "bp Statistical Review of World Energy 2021," BP, Tech. Rep. 70th edition, Jul. 2021. Cited on page/s 3.

[13] M. o. C. a. Environment, "Norway steps up 2030 climate goal to at least 50 % towards 55 %," Feb. 2020, publisher: regjeringen.no. [Online]. Available: https://www.regjeringen.no/en/historical-archive/solbergs-government/Ministries/kld/news/2020-nyheter/norge-forsterker-klimamalet-for-2030-til-minst-50-prosent-og-opp-mot-55-prosent/id2689679/ Cited on page/s 4.

[14] "Boosting Offshore Renewable Energy." [Online]. Available: https://ec.europa.eu/commission/presscorner/detail/en/IP_20_2096 Cited on page/s 4.

[15] "Hywind Tampen." [Online]. Available: https://www.equinor.com/energy/hywind-tampen Cited on page/s 4.

[16] "New report: electrification of North Sea oil and gas would boost innovation and help meet decarbonisation targets - News - Crown Estate Scotland." [Online]. Available: https://www.crownestatescotland.com/news/new-report-electrification-of-north-sea-oil-and-gas-would-boost-innovation-and-help-meet-\decarbonisation-targets Cited on page/s 4.

[17] I. Corrigan, "Innovation and Targeted Oil and Gas Decarbonisation: Offshore Market Review," Crown Estate Scotland, Tech. Rep., Apr. 2022. Cited on page/s 4.

[18] I. R. E. Agency, "Electricity storage and renewables: Costs and markets to 2030," IRENA, Abu Dhabi, Tech. Rep., Oct. 2017. Cited on page/s 4, 5.

[19] I. I. R. E. Agency, "Behind The Meter Batteries – Innovation Landscape Brief," International Renewable Energy Agency, Abu Dhabi, Tech. Rep., 2019. Cited on page/s 4.

[20] M. Wilshire, "Future trends in energy," Portland, OR, USA, Aug. 2018. Cited on page/s 4.

[21] I. I. R. E. Agency, "Electricity storage and renewables: Costs and markets to 2030," International Renewable Energy Agency, Abu Dhabi, Tech. Rep., Oct. 2017. Cited on page/s 5.

[22] "BATSTORM: Battery-based energy storage roadmap," Tech. Rep. Cited on page/s 5.

[23] K. Mongird, V. V. Viswanathan, P. J. Balducci, M. J. E. Alam, V. Fotedar, V. S. Koritarov, and B. Hadjerioua, "Energy Storage Technology and Cost Characterization Report," Tech. Rep. PNNL-28866, 1573487, Jul. 2019. [Online]. Available: http://www.osti.gov/servlets/purl/1573487/ Cited on page/s 5.

[24] "FREYR could use half of 100GWh target capacity for storage; eyes system integrator play," Mar. 2022. [Online]. Available: https://www.energy-storage.news/freyr-could-use-half-of-100gwh-target-capacity-for-storage-eyes-system-integrator-play/ Cited on page/s 5.

[25] "Freyr Battery secures clean power for planned gigafactory in Norway." [Online]. Available: https://renewablesnow.com/news/freyr-battery-secures-clean-power-for-planned-gigafactory-in-norway-785851/ Cited on page/s 5.

[26] S. Settemsdal, L. Barstad, and W. Voss, "Hybrid power plants can help decarbonize offshore drilling rigs and vessels," *Endeavor Business Media*, no. Offshore, p. 4, May 2020. Cited on page/s 5.

[27] "Equinor has installed Batwind - the world's first battery for offshore wind - equinor.com." [Online]. Available: https://www.equinor.com/news/archive/26june2018-equinor-has-installed-batwind Cited on page/s 6.

Chapter 2

Research Context and Methodology

This chapter aims to overview the thesis while focusing on: *a)* the methodological parts leveraged during the PhD, *b)* the discussions regarding the main outcomes and contributions of the papers included in the following chapters, and *c)* the conceptual connections among these papers. The chapter starts by giving some basic background information about the most relevant mathematical concepts and most useful tools for our purposes. This part emphasizes the relevance of the concepts and tools to the proposed methods, however, such concepts and tools will be presented in even greater detail in each corresponding chapter. The information below acts thus as the minimum required basis for better understanding the developments presented in the thesis, their assumptions, and the associated potential directions for improvement. This will be followed by an extended unified summary of the papers, where the main ideas and results are presented under a single integrated framework that encompasses the core contributions of this thesis.

2.1 Background Mathematical Concepts

2.1.1 Approaches to Uncertain Optimization

Uncertainty can be integrated into an optimization problem in several ways, depending on the perspective of the decision maker and the context of the problem itself. Thus, different degrees of conservatism can be represented by different formulations. To illustrate that, and without loss of generality, we consider the *minimization* problem of a cost function $J(\theta, \delta)$ that depends on both decisions variables $\theta \in \Theta \subseteq \mathbb{R}^d$ and the uncertainty realization (random sample) $\delta \in \Delta$. As such, the general problem can be expressed in the most general way as

$$\min_{\theta \in \Theta} \{J(\theta, \delta))\}. \tag{2.1}$$

If the worst-case paradigm is to be followed, meaning that the decision will be guaranteed against all possible uncertainty realizations, no matter their probability distribution, then the following Robust Optimization (ro) problem is to be solved

$$\min_{\theta \in \Theta} \left[\max_{\delta \in \Delta} J(\theta, \delta) \right] \tag{2.2}$$

where δ is allowed to take any possible value in Δ. However, such a paradigm can be over-conservative and rather pessimistic with respect to reality. An additional difficulty stems from the way Δ is considered, which in most of the cases is simply a hyper-rectangle of the form $\left[\underline{\delta}, \overline{\delta}\right]$, the limits of which may be hard to define based on real-life experience.

Another approach stems from the use of a probability measure $\mathbb{P}$ over Δ and the expected cost. In this case, the decision maker is interested in making a good decision on average, expressed by the problem

$$\min_{\theta \in \Theta} \mathbb{E}_{\Delta}\left[J(\theta, \delta)\right] = \min_{\theta \in \Theta} \left[\int_{\Delta} J(\theta, \delta)\, d\mathbb{P}\right] \tag{2.3}$$

where the above Lebesgue integral expresses the average cost of the objective function over the probability space of the events included in Δ. In practice, formulation eq. (2.3) can be very challenging to solve (numerically or analytically) since *i)* a closed form for $\mathbb{P}$ is required and *ii)* even for a numerical approximation, for high dimensional spaces, Δ (which represents almost the standard case in real-life applications) can be computationally intractable to solve the multidimensional integral. This can be circumvented with specialized techniques for sampling $\mathbb{P}$ and using the Sample Average Approximation (SAA), but such approaches come with their own challenges. Nevertheless, even if we are able to solve/approximate eq. (2.3), leading to less conservatism compared to eq. (2.2) (i.e., $J(\theta^*|eq.\ (2.3)) \leq J(\theta^*|eq.\ (2.2))$, where θ^* is the optimal value argument), the solution is highly dependent on the way $\mathbb{P}$ is considered/estimated/defined and thus the optimization result can have high variance.

An alternative approach to leverage conservatism of ro eq. (2.2) is to allow for a probabilistic satisfaction of the uncertainty induced constraints. In other words, we aim to optimize over a reduced set of the uncertainty space/domain $\Delta_\epsilon \subset \Delta$, meaning that we leave out of the problem the set/domain $\Delta - \Delta_\epsilon$, the probability of which is $\mathbb{P}\{\Delta - \Delta_\epsilon\} = \epsilon$. Equivalently since $\mathbb{P}\{\Delta\} = \mathbb{P}\{\Delta_\epsilon \cup (\Delta - \Delta_\epsilon)\} = 1 \Rightarrow \mathbb{P}\{\Delta_\epsilon\} = 1 - \epsilon$, meaning that the probability of the uncertainty domain over which we eventually optimize is $1 - \epsilon$. This way of modulating robustness leads to the *chance-constrained* version of eq. (2.1) problem, expressed as

$$\min_{\theta \in \Theta, \Delta_\epsilon \in \mathbb{R}} \left[\max_{\delta \in \Delta_\epsilon} J(\theta, \delta)\right]. \tag{2.4}$$

The reason for placing Δ_ϵ among the optimization variables is that we are searching for reduced sets Δ_ϵ that will give us the best improvement of the cost function with respect to the worst-case performance or, in other words, we seek to leave out the set $\Delta - \Delta_\epsilon$, which will give the best improvement of the optimal value performance. So if $\theta \in \Theta_\delta$ is the feasibility set of eq. (2.4) (or equivalently of eq. (2.2) when considering Δ_ϵ instead of Δ), then by the *chance-constrained* formulation, it holds that

$$\theta^* = \arg\min_{\theta \in \Theta_\delta} \left[\max_{\delta \in \Delta_\epsilon} J(\theta, \delta)\right] \Rightarrow \mathbb{P}\{\delta \in \Delta : \theta^* \in \Theta_\delta\} \geq 1 - \epsilon, \tag{2.5}$$

meaning that the solution of the robust problem with the reduced uncertainty set is guaranteed against any constraint from the original set (including the unseen uncertainty set) by a probability of at least $1 - \epsilon$. Nevertheless, numerically computing the solution of eq. (2.4) is extremely demanding in the general case. Indeed, easing such a computation would require not only knowing a closed form of the probability function—something that happens in extremely rare cases—but also avoiding curses of dimensionality associated with the fact that the space of the uncertain parameters typically increases in time. Finally, the *Random Variable*s (RVs) typically interact (i.e., are not independent), implying that $\mathbb{P}$ is a multivariate distribution for which the analytical (or at least numerically fast) solution of eq. (2.4) still remains an open mathematical problem.

Scenario Approach

Despite the difficulties presented above, in recent years, a new theory has been constructed to address the problem of solving eq. (2.4) by means of randomly sampling instances of the uncertainty and without requiring the explicit knowledge of the distribution $\mathbb{P}$. The only requirements are related to the structure of the optimization problem and the feasibility domain, which need to be convex. The following paragraphs summarize, then, the main reasoning behind such a *scenario approach* (sa).

Consider then that for a given point $\left(\bar{\theta}, \bar{J}\right)$ the risk function is defined as

$$\mathcal{R}\left(\bar{\theta}, \bar{J}\right) = \mathbb{P}\left\{\delta : J\left(\bar{\theta}, \delta\right) > \bar{J}\right\} \ . \tag{2.6}$$

One may then express the same concept through the violation set of a given Θ_δ set, i.e., that quantity definable as the set $\{\delta \in \Delta : \theta \notin \Theta_\delta\}$. Then, the violation probability of $\theta \in \Theta_\delta$ (or simply the probability of the violation set) is defined as

$$\mathcal{V}(\theta) = \mathbb{P}\{\delta \in \Delta : \theta \notin \Theta_\delta\} \tag{2.7}$$

Conceptually, bounding the violation function by ϵ is interpreted as keeping the risk that the optimal solution is violating a constraint emerging from a $\delta \in \Delta$ less than ϵ, which is mathematically expressed as

$$\mathcal{R}(\theta^*, J^*) \leq \epsilon \Rightarrow \mathbb{P}\{\delta \in \Delta : \theta^* \notin \Theta_\delta\} \leq \epsilon \Rightarrow \mathcal{V}(\theta^*) \leq \epsilon \tag{2.8}$$

where θ^*, J^* is the optimal solution and the optimal objective value associated to eq. (2.4). As a remark, we note that the sa differs from other uncertain optimization approaches mentioned in section 2.1.1 in the sense that sa relies only on a finite number of random occurrences of the uncertain parameters to leverage robustness and risk. In other words, sa solves the chance constrained problem eq. (2.4) without explicitly considering any specific probability measure over Δ.

Then, generating N Independent and Identically Distributed ($i.i.d.$) random samples δ_i distributed each as $\mathbb{P}$ means generating a multi-dimensional sample $\boldsymbol{\delta} =$

$(\delta_1, \ldots, \delta_N) \in \Delta^N$ distributed as $\mathbb{P}^N$. Each of the components in this multi-dimensional sample induces a deterministic constraint, resulting in a different feasible solution space denoted by the set Θ_{δ_i}. Therefore, the combined feasible space for eq. (2.4) when including the multi-sample $\boldsymbol{\delta}$ is

$$\theta \in \bigcap_{i=1,\ldots,N} \Theta_{\delta_i}. \tag{2.9}$$

This approach corresponds to approximating the difficult-to-solve chance constrained problem given by eq. (2.4) by means of a robust optimization program with a finite number of constraints. The latter can then be solved efficiently by numerical solvers. Note that this approximation may be especially precise (and thus the solution one obtains with the latter be close "enough" to the original one) especially when the number of scenarios is thoughtfully selected.

We also note that the combined feasible space defined in eq. (2.9) is such that when solving the robust program for the multi-sample, giving us the optimal decisions and cost $(\theta^*(\delta_1, \ldots, \delta_N), J^*(\delta_1, \ldots, \delta_N))$ correspondingly, we get guarantees regarding the amount of the probability space that is excluded when solving the chance constrained problem eq. (2.4). Alternatively, this robust program is a finite representation of eq. (2.4) for the same risk level. However, since $\boldsymbol{\delta}$ is random, then $\mathcal{R}(\theta^*(\boldsymbol{\delta}), J^*(\boldsymbol{\delta}))$ is also a RV. Finding how this RV is distributed is explained by the main theorems from [1], which can be summarized as

$$\begin{aligned} &\mathbb{P}^N\{\mathcal{V}(\theta^*) > \epsilon\} \leq \sum_{i}^{d} \binom{N}{i} \epsilon^i (1-\epsilon)^i \Rightarrow \\ &\mathbb{P}^N\{\mathcal{R}(\theta^*(\boldsymbol{\delta}), J^*(\boldsymbol{\delta})) \leq \epsilon\} \geq 1 - \sum_{i}^{d} \binom{N}{i} \epsilon^i (1-\epsilon)^i \end{aligned} \tag{2.10}$$

This means that the probability that we violate an unseen constraint with a probability higher than ϵ is no bigger than a value that depends on the sample size N and the problem's complexity d. Equivalently, the probability that risk is small (bounded by ϵ) is greater than the cumulative distribution of a Beta $RV \sim \mathcal{B}(d, N-d+1)$. The risk is dominated by a Beta distribution and therefore, the same guarantees required for the solution in eq. (2.5) hold for a finite random sample without explicitly specifying $\mathbb{P}$. The theorem expressed in eq. (2.10) can also be simplified through a mathematical manipulation to the following version, which is easier to implement in practice [1]:

> for any $\epsilon \in (0, 1)$ (risk parameter) and $\beta \in (0, 1)$ (confidence parameter), if the number of scenarios N satisfies
>
> $$N \geq \frac{2}{\epsilon}\left(\ln\frac{1}{\beta} + d - 1\right), \tag{2.11}$$
>
> then with probability $\geq 1-\beta$, it holds that $J^*(\boldsymbol{\delta})$ is $\epsilon-$risk guaranteed, that is, $\mathbb{P}\{\delta \in \Delta : J(\theta^*, \delta) > J^*\} \leq \epsilon$.

The theorem above states that if we select N random scenarios, then we can be "very" confident (more formally, in the sense of letting $1 - \beta \to 1$) that the solution we get θ^* from the problem

$$\min_{\boldsymbol{\theta} \in \Theta} \left[\max_{i=1,\dots,N} J(\boldsymbol{\theta}, \delta_i) \right] \tag{2.12}$$

will satisfy constraints with a probability higher than ϵ for other random samples that were not included in the N scenarios used to solve eq. (2.12). This theorem provides a user-friendly way to compute N, and this enhances the applicability of the overall approach when this needs to be calculated several times, such as in cases of rolling horizon numerical optimal control. In practice, the user-defined confidence parameter can be set very low (i.e., $\beta = 10^{-7}$) meaning that we can be very confident that the violation probability will be limited by ϵ. However, a major implementation difficulty arises when, even for relatively large ϵ, the optimization problems complexity is large, meaning that d is a large number. For this case, the *sa* has been extended to include guarantees for arbitrary scenario removal, meaning that the decision maker has a degree of freedom in increasing the risk they are willing to take, so that some constraints can be removed, leading to less computationally-demanding optimization problems. In addition, very lately extensions of the theory have been proposed for the case of unstructured optimization problems (i.e., non-convex case), lifting some of the limitation of the initial *sa* and providing powerful guarantees for the case of integer optimization programs.

2.1.2 Stochastic Optimization and Mixed-Integer Linear Programming

As seen previously, the approach of uncertainty modelling within an optimization problem highly depends on the information available, on the type (structure) of the problem itself, and on the choice of the decision maker (which may be application-specific and affected by other human-related factors). However, a very interesting case emerges when the optimization problem can be expressed as a Linear Program (LP) or a Mixed-Integer Linear Program (MILP). This particular structure has been deeply investigated in the field of *Operational Research* due to the simplicity of the solution procedures in LPs (i.e., the so-called simplex algorithm), the possibility to integrate multiple stages and sequential decisions in the same problem, and the vast applicability in several scientific domains and engineering principles. Among the various approaches, the *so* framework has proven to be significantly useful for integrating uncertainty into multi-stage problems under some sort of risk [2].

Two-stage stochastic optimization

Many engineering problems such as the sizing of components can be cast as two-stage *so* programs. In this subcategory, the optimization variables are divided into two sets: the first-stage decision variables $\mathbf{x}$ and the second-stage variables $\mathbf{y}$. The first-stage

variables represent the *here-and-now* decisions that the decision maker needs to make (i.e., the size of equipment) and the second-stage variables represent the *wait-and-see* decisions (the so-called *recourse action*) that basically depend on the realization of uncertainty. Therefore, if $\boldsymbol{\xi} \in \Omega$ is the vector of random (uncertain) parameters, which take values from an event space Ω indexed by ω, the second-stage variables can be expressed as function of the unveiled uncertainty and the first-stage decision, i.e., as $\mathbf{y}(\mathbf{x}, \omega)$. To clarify the notation and improve readability, we note that a random outcome from the event space Ω is denoted as $\boldsymbol{\xi}(\omega)$. Moreover, the sequential decision problem can be expressed as

$$\mathbf{x} \xrightarrow{yields} \boldsymbol{\xi}(\omega) \xrightarrow{yields} \mathbf{y}(\mathbf{x}, \omega). \tag{2.13}$$

Again we consider a minimization problem (without loss of generality) for which the objective function $F(\mathbf{x}, \boldsymbol{\xi})$ is also a *RV* since it is a function of the first-stage decisions and the random parameters. The stochastic problem can then be written in its standard form as

$$\begin{aligned} SP &= \min_{\mathbf{x}} \{F(\mathbf{x}, \boldsymbol{\xi}) \mid A\mathbf{x} \geq b \ \cap \ \mathbf{x} \geq 0\} \\ &= \min_{\mathbf{x}} \{\mathbf{c}^T\mathbf{x} + \mathbb{E}_{\xi}\left[Q(\mathbf{x}, \boldsymbol{\xi})\right] \mid A\mathbf{x} \geq b \ \cap \ \mathbf{x} \geq 0\} \end{aligned} \tag{2.14}$$

where for a particular realization $\boldsymbol{\xi}(\omega)$, the mixed integer recourse function $Q(\mathbf{x}, \boldsymbol{\xi})$ is defined as

$$\begin{aligned} Q(\mathbf{x}, \boldsymbol{\xi}(\omega)) = \min_{\mathbf{y}} \{\boldsymbol{q}(\omega)^T\mathbf{y}(\omega) \mid W(\omega)\mathbf{y}(\omega) \geq h(\omega) - T(\omega)\mathbf{x} \ \cap \ \mathbf{y}(\omega) \geq 0 \\ \cap \, \mathbf{y}_b \subset \mathbf{y} : \mathbf{y}_b \in \{0, 1\}\}. \end{aligned} \tag{2.15}$$

The objective function $F(\mathbf{x}, \boldsymbol{\xi})$ is thus composed by two parts, one related to the first-stage decisions and the recourse function, which depends on the uncertainty realization. As it is easy to observe, the feasible space for the first-stage is fixed and denoted as

$$\mathcal{X} = \{\mathbf{x} \mid A\mathbf{x} \geq b \ \cap \ \ \mathbf{x} \geq 0\} \tag{2.16}$$

while the feasible space for the second stage depends on the first-stage decision and the particular uncertainty realization and is denoted as

$$\begin{aligned} \mathcal{Y}(\mathbf{x}, \boldsymbol{\xi}(\omega)) = \{\mathbf{y}(\omega) \mid W(\omega)\mathbf{y}(\omega) \geq h(\omega) - T(\omega)\mathbf{x} \ \cap \ \mathbf{y}(\omega) \geq 0 \\ \cap \, \mathbf{y}_b \subset \mathbf{y} : \mathbf{y}_b \in \{0, 1\}\} \end{aligned} \tag{2.17}$$

where $\mathbf{y}_b \subset \mathbf{y}$ is the subset of second-stage variables, which are binaries, representing the integrality constraints of the problem. The recourse value problem is then given as

$$RV = \min_{\mathbf{x}} \{\mathbb{E}_{\xi}\left[F(\mathbf{x}, \boldsymbol{\xi})\right] \mid \mathbf{x} \in \mathcal{X}\} = \min_{\mathbf{x}} \{\mathbb{E}_{\xi}\left[Q(\mathbf{x}, \boldsymbol{\xi})\right] \mid \mathbf{x} \in \mathcal{X}\} \tag{2.18}$$

By taking a finite number of samples (i.e., $\omega = 1, \ldots, |\Omega|$) and using the SAA technique [2], we can write the deterministic equivalent formulation of the recourse value problem as

$$\begin{aligned}
\min_{\mathbf{x},\mathbf{y}} \{ \mathbf{c}^T \mathbf{x} \quad & + \sum_{\omega=1}^{|\Omega|} \pi(\omega) \boldsymbol{q}(\omega)^T \mathbf{y}(\omega) \} \\
A\mathbf{x} & \geq b \\
T(1)\mathbf{x} + W(1)\mathbf{y}(1) & \geq h(1) \\
\vdots \qquad\qquad \ddots & \quad \vdots \\
T(|\Omega|)\mathbf{x} + W(|\Omega|)\mathbf{y}(|\Omega|) & \geq h(|\Omega|) \\
\mathbf{x} \geq 0,\ \mathbf{y} \geq 0,\ \mathbf{y}_b \in \{0,1\} &
\end{aligned} \tag{2.19}$$

where $\mathbf{y}(\omega)$ represents the scenario-specific second-stage variables, $\pi(\omega)$ and the corresponding probability of scenario ω. Those problems can become very large and computationally intractable even for a relatively small number of scenarios $|\Omega|$ since MILPs are combinatorial *NP-complete* problems and scale poorly with the number of binary variables. On the other hand, increasing the dimensionality of the uncertain parameters $\boldsymbol{\xi} \in \Omega$ means that to accurately capture/describe Ω, we should use several scenarios. Higher computational efficiency (lower computational times) can be achieved in some cases by using decomposition techniques (i.e., Benders). However, the presence of binaries in the second stage makes the recourse non-convex and thus approximating $\mathbb{E}_\xi [Q(\mathbf{x}, \boldsymbol{\xi})]$ becomes challenging. Specialized branch-and-bound methods incorporating cuts can then be used, as mentioned later, but still the numerical complexity of such problems remains an open challenge. On that perspective, this thesis proposes a heuristic (as explained later in section 2.2.1) that facilitates the solution of two-stage stochastic programs with integer recourse. This technique is then demonstrated for the particular application of energy storage sizing in an isolated power system that integrates renewable sources and dispatchable units.

The benefits for solving a stochastic optimization problem compared to its simpler model variations can be expressed through commonly used metrics such as the *Value of Stochastic Solution*. For this calculation, the *Expected Value* problem is considered as

$$EV = \min_{\mathbf{x}} \{ F(\mathbf{x}, \mathbb{E}_\xi [\boldsymbol{\xi}]) \mid \mathbf{x} \in \mathcal{X} \} \tag{2.20}$$

where the uncertain vector $\boldsymbol{\xi}$ is replaced by its expected value, the latter numerically approximated by the sample average of the considered scenarios. The solution of eq. (2.20) gives the optimal decision $\mathbf{x}_d^* (\mathbb{E}_\xi [\boldsymbol{\xi}])$. Taking the expectation of the *EV*, we then get the problem

$$EEV = \mathbb{E}_\xi \left[F(x_d^* (\mathbb{E}_\xi [\boldsymbol{\xi}]), \boldsymbol{\xi}) \right] \tag{2.21}$$

which represents the part of the recourse problem from eq. (2.14) for a given first-stage

decision. Finally, the *Value of Stochastic Solution* can be computed as

$$\begin{gathered} VSS = RV - EEV \Rightarrow \\ VSS = \min_{\mathbf{x}}\{\mathbb{E}_{\xi}\left[F(\mathbf{x}, \boldsymbol{\xi})\right] \mid \mathbf{x} \in \mathcal{X}\} - \mathbb{E}_{\xi}\left[F(x_d^*\left(\mathbb{E}_{\xi}\left[\boldsymbol{\xi}\right]\right), \boldsymbol{\xi})\right]. \end{gathered} \tag{2.22}$$

Solution procedure

As mentioned before, stochastic optimization problems with binary variables can be very hard to solve due to the combinatorial nature of the binary decisions and the multiple scenarios required to represent the probability measure. Thus, when the feasible set is large, a *divide-and-conquer* strategy can be applied to solve the problem by partitioning it into smaller subsets, solving each of them independently and then selecting the best solution of all. Most importantly, it may be not necessary to solve all of these problems, since to prove the optimally of the original problem, it can be sufficient just to find Lower Bounds (LBs) on the individuals. This is also the reasoning behind one of the most useful and typically implemented in commercial solvers algorithm, the *Branch-and-Bound*.

The algorithm starts by solving a relaxed version of the original problem in which constraints $\mathbf{y}_b \in \{0, 1\}$ are relaxed into $\mathbf{y}_b \in [0, 1]$. The solution to this problem provides the best possible LB, since no integrality constraints are considered at all. Then, a binary variable $y_b^{(k)}$ is selected for branching leading to two different problem variants, that is $y_b^{(k)} = 0 \ \vee \ y_b^{(k)} = 1$. The two problems now include one additional constraint depending on the branch and they are solved independently. At this point there are four alternative outcomes: *i)* the problem is infeasible, *ii)* the best objective is worst (bigger) than the current best solution (*incumbent*)), *iii)* a feasible solution to the original problem is found (all integrality constraints are satisfied) providing an Upper Bound (UB) on the objective of the original problem, and *iv)* none of the previous is true and the search continuous deeper in the same branch by selecting a new (different) variable $y_b^{(k+1)}$ for further branching, adding one more layer to the tree search. In any of the cases *i-iii*, the corresponding branch is pruned (fathoming of the candidate solution) since it cannot give any better solution by keep searching this particular branch, which means, in practice, adding more constraints. In case *iii)*, the candidate solution is kept to the memory and then compared to other possible solutions from other branches being explored. The best LB up to that moment becomes the new (updated) LB. In this way, the whole combinatorial tree representing the feasible solutions to the problems is efficiently explored until a preset relative difference between UB and LB (duality gap) is reached.

Modern MILPs solvers enhance the efficiency of Branch-and-Bound by including presolve and problem conditioning steps where the size of the problem is reduced and the formulation is tightened, adding cutting planes that cut off relaxation solutions, implementing rules for branching variable selection to limit the search tree size, and using primal heuristics for finding integer feasible solutions. Nevertheless, problems

described as in eq. (2.19) still remain challenging to solve especially when considering the dependency of the result on the scenario set used, as a discrete representation of a potentially continuous and multivariate distribution function.

Scenario Reduction

A common practice in solving such problems is reducing their size by considering smaller subsets of the original scenario set by implementing *scenario reduction* (sr) techniques. Such algorithms are trying to find subsets from the original scenario set that accurately describe the original problem by losing the minimum amount of information. Again this task is not trivial since it involves probability distances and relates to the so-called *Monge-Kantorovitch transportation problem*, which for the case of discrete probability distributions can be cast as the following optimization problem

$$\min_{\mathcal{J}} \left\{ \sum_{i \in \mathcal{J}} \pi_i \min_{j \notin \mathcal{J}} c_T(\boldsymbol{\xi}^i, \boldsymbol{\xi}^j) \ : \ \mathcal{J} \subset \{1, \dots, |\Omega|\} \mid |\mathcal{J}| = |\Omega| - |\Omega_s| \right\} \tag{2.23}$$

where $\mathcal{J}$ is the index set of the scenarios to be removed from the initial scenario set Ω, which has $|\Omega|$ scenarios. The set Ω_s is the set of preserved scenarios with a predefined scenarios number $|\Omega_s|$, π_i is the discrete probability of scenario $\boldsymbol{\xi}^i$, and $c_T(\cdot)$ is a multidimensional distance metric. Equation (2.23) is known as the *optimal reduction problem* and is a *0-1 NP-hard* problem and the functional to be minimized inside eq. (2.23) is the *Kantorovich* distance ($D_K(\mathbb{P}, \mathbb{Q})$), which measures the distance between (multivariate) distributions $\mathbb{P}, \mathbb{Q}$, and its value is given as the optimal value of a *linear transportation problem*. To solve eq. (2.23) efficiently, many heuristic algorithms have been proposed with one of the most popular (and the one used throughout this thesis) being the Fast Forward Selection (*FFS*). A visual demonstration of the algorithm is provided in Figure 2.3

2.1.3 Statistical learning and Scenario generation

To implement any sr technique or to even solve eq. (2.19), the decision maker needs first to populate the initial scenario set Ω or, in other words, find a discrete representation of the probability measure $\mathbb{P}$ over which the stochastic optimization problem will be solved. This process is call *scenario generation* (sg). Despite the amount of different methods that exist, most of them share the same challenge, which is the inference of a potentially multivariate distribution function. Given the lack of a single universal technique, several conceptually different approaches may be applied, depending on the simplifications/assumptions used. The situation becomes more complicated when simultaneously considering different multivariate stochastic processes that have a combined effect on the optimization problem, as will be discussed in sections 2.2.1 and 2.2.2. The common ground for all these methods is the use of available historical datasets to estimate $\mathbb{P}$. Therefore, it becomes obvious that such methods can greatly

benefit from the implementation of *statistical learning* for building inference models that will generate appropriate inputs for the optimization model. This also highlights the direct connection and complementarity of *so* with *data-based methods* (i.e., machine learning) pointing out a great potential for the future of decision making.

In many engineering applications, the stochastic part of eq. (2.14) comes in the form of a stochastic process. One particularly powerful method for modelling the stochastic time-dependence of the *RV* is the use of copula functions. Those are functions that "couple" or join together one-dimensional marginal distributions in multivariate distribution functions. That is, if $X_1, \ldots, X_N$ are *RV*s with Cumulative Distribution Functions (CDFs) $F_{X_1}(x_1), \ldots, F_{X_N}(x_N)$, correspondingly then the joint distribution can be written as the N-dimensional function [3]

$$\boldsymbol{F}(x_1, \ldots, x_N) = \boldsymbol{C}(F_{X_1}(x_1), \ldots, F_{X_N}(x_N)) \tag{2.24}$$

with density

$$\boldsymbol{f}(x_1, \ldots, x_N) = \boldsymbol{c}(F_{X_1}(x_1), \ldots, F_{X_N}(x_N)) \prod_{i=1}^{N} f_{X_i}(x_i) \tag{2.25}$$

with $f_{X_i}(x_i)$ the probability densities of the marginals. If $F_{X_1}(x_1), \ldots, F_{X_N}(x_N)$ are invertible, it holds that

$$X_i \sim F_{X_i}(x_i) \Rightarrow F_{X_i}^{-1}(X_i) = U_i \sim \textit{unif}\,[0,1] \;\; \forall\, i = 1, \ldots, N \tag{2.26}$$

and eq. (2.24) can be rewritten as

$$\boldsymbol{C}(u_1, \ldots, u_N) = \boldsymbol{F}(F_{X_1}^{-1}(u_1), \ldots, F_{X_N}^{-1}(u_N)) \tag{2.27}$$

meaning that the Copula function can be defined in the uniform domain through the *Probability Inverse Transform (PIT)*. To apply such a transformation, one should use the marginal CDFs $F_{X_i}(x_i)$, which in most cases are unknown or do not belong to a particular parametric family. In such cases, one may use the empirical CDF (Empirical Cumulative Distribution Function (ECDF)) defined at any given point x from the available historical data as

$$\hat{F}_{X_i}^{e}(x) = \frac{1}{T} \sum_{t=1}^{T} \mathbb{1}\{X_t \leq x\} \tag{2.28}$$

where T is the amount of observations and x_t the corresponding data points. However, for sampling the copula, the non-smooth ECDF will not give very accurate estimations and one would have to perform some interpolation (i.e., linear) beforehand. An alternative to directly produce smooth CDFs is to use the *Kernel Density Estimation (KDE)*

method in which a non-parametric density of the true (unknown) marginal $f_{X_i}(x)$ is estimated as

$$\hat{f}^h_{X_i}(x) = \frac{1}{hT}\sum_{t=1}^{T}\mathcal{K}\left(\frac{x - x_t}{h}\right) \Rightarrow \hat{F}^h_{X_i}(x) = \int_{-\infty}^{x}\hat{f}^h_{X_i}(z)\,dz \tag{2.29}$$

where h is the bandwidth of the smoothing kernel $\mathcal{K}(\cdot)$ and $\hat{F}^h_{X_i}$ the corresponding estimated CDF. The significance of estimating the CDFs and using the inverse transform is that this transformation does not affect the dependence structure in the RVs. In particular, since this is an increasing transformation, it does not affect the ranks of the values (before and after) and therefore, the rank correlation information is preserved. This fact is the basis for how the copula method preserves the dependence structure of the training dataset by simply keeping the same ranking among the uniform and probability transformed variables.

One particular useful and common selection for the structural dependence is the multivariate normal (Gaussian) ($\mathcal{MVN}$) *Copula*, which consists of coupling together many normal RVs. Let $\boldsymbol{\rho}$ be a symmetric, positive definite matrix with $diag\{\boldsymbol{\rho}\} = \mathbf{1}$ and $\boldsymbol{\Phi}_\rho$ the standardized multivariate normal distribution with correlation matrix $\boldsymbol{\rho}$, then $\mathcal{MVN}$ is defined as

$$\boldsymbol{C}(u_1, \ldots, u_N|\boldsymbol{\rho}) = \boldsymbol{\Phi}_\rho(\Phi^{-1}(u_1), \ldots, \Phi^{-1}(u_N)) \tag{2.30}$$

where Φ^{-1} is the inverse of the standard Normal distribution and $\Phi^{-1}(u_i) = z_i$ and $Z_i \sim \mathcal{N}(0, 1)\ \forall\ i = 1, \ldots, N$. The corresponding density can be expressed as

$$\boldsymbol{c}(u_1, \ldots, u_N|\boldsymbol{\rho}) = \frac{1}{\sqrt{|\boldsymbol{\rho}|}}\exp\left(-\frac{1}{2}\boldsymbol{z}^T(\boldsymbol{\rho}^{-1} - \mathbb{1})\boldsymbol{z}\right) \tag{2.31}$$

where $|\boldsymbol{\rho}|$ is the determinant of $\boldsymbol{\rho}$, $\boldsymbol{z}^T = [z_1, \ldots, z_N]$ and $\mathbb{1}$ the identity matrix. To calculate and eventually use the conditional Gaussian copula eq. (2.31), the correlation matrix parameter needs to be estimated first. This can be done by using the Maximum Likelihood Estimation (MLE) method.

Given T observations and a set of parameters $\theta \in \Theta$ to be estimated, the likelihood for observation t is denoted as $\mathcal{L}_t(\theta|T)$ and the corresponding log-likelihood as $\ell_t(\theta|T) = \ln \mathcal{L}_t(\theta|T)$. The log-likelihood function for the $i.i.d.$ observations can be computed as

$$\mathcal{L}(\theta|T) = \prod_{t=1}^{T}\mathcal{L}_t(\theta|T) \xrightarrow{\ln} \ell(\theta|T) = \sum_{t=1}^{T}\ell_t(\theta|T) \tag{2.32}$$

Considering that the likelihood is $\mathcal{L}_t(\theta|T) = \boldsymbol{f}(x_1^t, \ldots, x_N^t)$ (the defined probability density function applied at a given observation) and using eq. (2.31) considering uniform marginals, then applying eq. (2.32) to eq. (2.25) gives the following log-likelihood

function

$$\ell(\theta|T) = -\frac{T}{2}\ln|\boldsymbol{\rho}| - \frac{1}{2}\sum_{t=1}^{T}\boldsymbol{z}_t^T(\boldsymbol{\rho}^{-1} - \mathbb{1})\boldsymbol{z}_t \tag{2.33}$$

since $\ln f_{X_i} = 0$ when $X_i \sim \mathcal{U}[0,1]$ and where $\boldsymbol{z}_t^T = [z_1^t, \ldots, z_n^t] = [\Phi^{-1}(u_1^t), \ldots, \Phi^{-1}(u_N^t)]$. In this case, parameter $\theta = \boldsymbol{\rho}$ and the MLE can be computed in closed form as

$$\hat{\boldsymbol{\rho}}_{ML} = \arg\min_{\boldsymbol{\rho}} \ell(\theta|T) = \frac{1}{T}\sum_{t=1}^{T}\boldsymbol{z}_t\boldsymbol{z}_t^T \tag{2.34}$$

Notably, such a calculation is based on the available data and since the MLE estimator of the covariance matrix is biased, when the dataset to estimate the sample covariance is small, the Bessel's correction should be used with $T-1$ in the denominator. In this way, we get the unbiased estimator, which for big T is the same as the MLE one.

Having such an estimate we, can use Cholesky decomposition to generate correlated random values that can be seen as realizations of the stochastic process that affect the optimization problem, eq. (2.14). We consider a random vector Y with covariance matrix $\mathbb{E}[YY^T]$ and a random vector X with uncorrelated *RV*s (i.e., $\mathbb{E}[X_iX_j] = 0$) for which $\mathbb{E}[X_i] = 0$ (zero mean) and $\mathbb{E}[(X_i - \mathbb{E}[X_i])^2] = 1$ (unit variance) $\forall\ i$. It holds that $\mathbb{E}[XX^T] = \mathbb{1}$ since variables in X are uncorrelated and because of unit variance. Then, given a covariance matrix $\hat{\boldsymbol{\rho}}_{ML}$ (symmetric and positive semi definite by definition), we take the Cholesky decomposition as $\hat{\boldsymbol{\rho}}_{ML} = LL^T$. Nexr, if we take the random vector $Z = LX$, we have

$$\mathbb{E}[ZZ^T] = \mathbb{E}[LXX^TL^T] = L\,\mathbb{E}[XX^T]L^T = L\mathbb{1}L^T = \hat{\boldsymbol{\rho}}_{ML} \tag{2.35}$$

Therefore, the *RV*s of Z are now transformed to be correlated as $\hat{\boldsymbol{\rho}}_{ML}$. This fact can be used for solving eq. (2.14) when the dimensionality of the uncertain parameters is high or when there are more *RV*s involved with different distributions. In such cases, the integration of the corresponding copulas required for the expectation term $q(\mathbf{x}) = \mathbb{E}[Q(\mathbf{x}, \boldsymbol{\xi})]$ in eq. (2.14) is practically impossible (intractable). Instead, we can use a sampling approach (i.e., *Monte Carlo* (*MC*)) to approximate $q(\mathbf{x})$ by sampling from the derived copula distribution using a $\mathcal{MVN}$ random generator as a proxy and inverse transforms as explained above. In that sense, we can then use the sample average to build an unbiased estimator for $q(\mathbf{x})$ as

$$\hat{q}_N(\mathbf{x}) = \sum_{\omega=1}^{N}\pi(\omega)Q(\mathbf{x}, \boldsymbol{\xi}(\omega)) \tag{2.36}$$

which by the *law of large numbers* converges to the true value ($\hat{q}_N(\mathbf{x}) \to q(\mathbf{x})$), leading to the equivalent SAA presented in eq. (2.19). The samples are called "scenarios" in the context of *so*, and they represent outcomes of the *RV*s, following particular distributions.

Probabilistic forecasting

However, there are cases where an optimization problem of the form eq. (2.14) needs to be solved iteratively as time evolves using input scenarios that are case specific to the time. This means that the marginals $F_{Y_1}(y_1), \ldots, F_{Y_N}(y_N)$ are no longer static distributions but conditional to time or possibly to some other explanatory variables, which are in turn a function of time, i.e., $F_{Y_1}(y_1|X_r = x_r(t)), \ldots, F_{Y_N}(y_N|X_r = x_r(t))$, where t stands for time and X_r are the explanatory variables taking the particular time-dependent value $x_r(t)$. In practice, those unknown distributions need to be estimated based on prior information from the most recent historical data in a recursive way, pointing to the use of regression. Using a regression technique, one can provide point estimates for a statistic of interest associated with the marginals. That is, given a dataset $\mathcal{D} = \{X, Y\}_{i=1}^{N}$ where X are the input features (*regressors*) and Y the response variable (*observations*) where $Y \sim F(y|X = x)$, a function $f(X)$ can be found such that $\hat{y} = f(X)$ is an estimator of $\mathbb{E}[Y|X = x]$ or, in other words, the predicted value of the actual value y. However, such point estimates do not provide information about the whole distribution of interest. Therefore, either strong assumptions need to be made for residuals of the predictions to construct approximate prediction intervals (i.e., least squares linear regression - normal errors) or different approaches should be used. An alternative is to perform quantile regression, which makes the assumption that the conditional quantiles are given as a linear function of the explanatory variables and calculate the parameters of those functions by solving an optimization problem.

Another option for performing quantile regression without unnecessary strict assumptions and computational effort is to use machine learning methods. One of the most natural extensions of methods that rely on ensembles for predictions is to use the information from all ensemble members to estimate the required distribution. Random Forest (RF) is one of the most established interpretable machine learning algorithms for solving both regression and classification problems/tasks relying on ensembles of decision trees and can be therefore considered as a reasonable choice for quantile estimation [4, 5]. RFs training relies mainly on two basic concepts, which are *bagging* and *feature randomization*. The first component is again derived from two main ideas in machine learning, which are *bootstraping* and *aggregating*.

Bootstrapping

Since this is a fundamental concept in machine learning and all statistical methods, some useful details are given here to better clarify its use in later chapters. Bootstraping is basically a resampling technique, which means we generate several samples with replacement from an initial sample. This is particularly useful when we do not have a large sample to support asymptotic behaviors of an estimator, meaning that we cannot assume that the sampling distribution is normal (*central limit theorem*). In addition, such a technique is quite valuable when we do not know any precise formula for the standard error of the estimate of the statistic under analysis (which exists only

for specific statistics such as the mean). It is remarkable that any statistic, which by definition means any quantity (composite measure) computed from values in a sample that is considered for a statistical purpose, could be considered for bootstrap estimation.

In the context of RFs, this is used in the following way. Assuming that we want to populate the forest with $|\mathcal{T}|$ trees, then the original dataset $\mathcal{D} = \{X, Y\}_{i=1}^{N}$ is resampled with replacement creating $|\mathcal{T}|$ datasets of the same size. In other words, randomly selected values are drawn from $\mathcal{D}$ to create $\mathcal{D}_t,\ \forall\ t \in \mathcal{T}$ datasets and each tree t will be trained only on its corresponding dataset $\mathcal{D}_t$. Then, the datasets $\mathcal{D}_t^{oob} = \mathcal{D} \setminus \mathcal{D}_t$ are called the *out-of-bag (oob)* samples and can be used as an accurate estimate of the prediction error of the RF model without needing to set aside a separate testing set [4]. This method provides a good trade-off when the dataset is not large enough. It requires less computation as it allows one to test the data as it is being trained. Further, since the model is validated on the *oob* samples, which means data has not been used while training the model in any way, there is not any leakage of data and henceforth this ensures a better predictive model. This, in turn, results in less variance of the predicted output since the model does not over-fit to the training set, which is one of the fundamental problems in regression trees.

Variance estimation by simulation

One additional useful application of the random sampling with replacement principle is described as follows. Given a random sample $\xi_1, \ldots, \xi_N \in \Omega_s$ from a population Ω with CDF F, we denote as $M = g(\xi_1, \ldots, \xi_N)$ the statistic of interest. That means that our statistic is a function of the sample data and different draws would give different values for the statistic. In that sense, recalling that a stochastic program can be written as

$$J^* = \min_{\mathbf{x}} J(\mathbf{x}, \xi \in \Omega_s) \tag{2.37}$$

where Ω_s is a sampled realizations set, a statistic could be the objective value J^* since this depends on the sample of the uncertain parameter ξ with the mapping $g : \Omega_s \to \mathbb{R}_{\geq 0}$ being the optimization problem itself. Then, we can estimate/approximate the variance of $Var(J^*)$ by simulation as *1)* Draw a random bootstrap sample Ω_s with size $|\Omega_s|$ from Ω, *2)* Compute statistic J_m^* for the sample (i.e., solve eq. (2.19)), *3)* Replicate steps *1* and *2* M times and gather $\{J_1^*, \ldots, J_M^*\}$ statistics, and *4)* Get the variance of $Var(J^*)$ from these M statistics. However, since the distribution of the population F can be unknown or hard to estimate (i.e., when several RVs in a *so* program have different distributions and it is hard to approximate the combined one), we can then compute an estimate of the true statistic instead based on the ECDF from the drawn sample Ω_s (sampling distribution). Eventually, following the procedure described

above, we can approximate the unbiased sample variance as

$$s^2 = Var(\hat{J}^*) = \frac{1}{M-1}\sum_{m=1}^{M}\left(\hat{J}^*{}_m - \frac{1}{M}\sum_{m=1}^{M}\hat{J}^*{}_m\right)^2 \tag{2.38}$$

Random Forests training and response

An additional feature on the training of RFs is the input feature randomization. That means that if L features are stacked in the input vector X to predict the output Y, then for each tree $f_t(x),\ t \in \mathcal{T}$ only a random subset of those is selected to be available for individual training. This so-called *random subspace* method accounts for increased variability of the predicted response, meaning that some trees learn to predict specific patterns of the dataset whereas others learn different patterns, which is particularly useful when one wants to estimate the whole distribution $\hat{F}(y|X=x)$ of potential responses. Finally, the combined averaged response from the trees participating in the response, indexed by the set S, is taken as the mean prediction of the RF (*aggregation*)

$$\hat{y} = \frac{1}{\sum_{t\in\mathcal{T}}\mathbb{1}\{t\in S\}}\sum_{t\in\mathcal{T}} f_t(x)\mathbb{1}\{t\in S\} \approx \mathbb{E}[Y|X=x] \tag{2.39}$$

The developed RF is validated based on the samples that were not used for its training by monitoring the *oob* error. For tree $f_t(x),\ t \in \mathcal{T}$, the sample of $\mathcal{D}_t$ observations are available for training and at one given tree node, n, only a subset of those has passed down the previous branch, the indices of which are gathered in set $\mathcal{J}$. Then, a subset of available predictors $\{x_1, \ldots, x_p\}$ where $p \leq L$ is considered for the particular tree and one of them is selected for splitting. The set of the indices of missing predictors is denoted as $\mathcal{X}_U$. If each observation is assigned equal importance, then $w_j = \frac{1}{|\mathcal{D}_t|}$, and the probability that an observation is in node n is estimated as

$$P(\mathcal{J}) = \sum_{j\in\mathcal{J}} w_j \tag{2.40}$$

by basically counting how many observations out of the original set have fallen in node n. Then, all predictor variables with indices $\notin \mathcal{X}_U$ are selected one by one and the best way to split node n using x_i is determined by maximizing the reduction in Mean Squared Error (MSE) ΔI over all splitting candidates. For a candidate split variable, two new sub-nodes are created, denoted by n_L and n_R, each of them containing the set of indices of observations that they fall in, denoted as $\mathcal{J}_L$ and $\mathcal{J}_R$, respectively. The reduction in the MSE is calculated as

$$\Delta I = P(\mathcal{J})\varepsilon - P(\mathcal{J}_L)\varepsilon_{n_L} - P(\mathcal{J}_R)\varepsilon_{n_R} \tag{2.41}$$

where ε_n is the corresponding *MSE* of node n, calculated as

$$\varepsilon_n = \sum_{j \in \mathcal{J}} w_j \left(y_j - \frac{1}{|\mathcal{J}|} \sum_{j \in \mathcal{J}} y_j \right)^2 \tag{2.42}$$

Finally, the best cut point for the candidate splitting variable x_i is calculated at the point where MSE is minimized. Then, the performance of the trees and eventually the whole forest is validated using the corresponding $\mathcal{D}_t^{oob}$ and monitoring the calculated MSE.

2.1.4 Numerical Optimal Control

The concepts described in the previous sections can all be integrated under the framework of numerical optimal control for dynamical systems. This involves the class of controllers that relate to the solution of an optimization problem either for finding an optimal set of parameters for a specified control law structure $f(\boldsymbol{\theta})$, that is

$$\boldsymbol{\theta}^* = \arg\min_{\boldsymbol{\theta}} \{ J(\boldsymbol{x}, f(\boldsymbol{\theta})) \mid \boldsymbol{\theta} \in \Theta \cap \boldsymbol{u} = f(\boldsymbol{\theta}) \in \mathcal{U} \cap \boldsymbol{x} \in \mathcal{X} \} \tag{2.43}$$

or for calculating a feasible numerical sequence of values that directly minimizes a cost function, as

$$\boldsymbol{u}^* = \arg\min_{\boldsymbol{u}} \{ J(\boldsymbol{x}, \boldsymbol{u}) \mid \boldsymbol{u} \in \mathcal{U} \cap \boldsymbol{x} \in \mathcal{X} \} \tag{2.44}$$

where $J(\cdot)$ represents a cost function including some control objectives. In both cases, constraints can be included so that both the states and the control inputs are kept in their feasible sets $\mathcal{X}, \mathcal{U}$, respectively. Then, following the different approaches to uncertain optimization described in section 2.1.1, we can develop robust or stochastic optimal controllers depending on whether the worst-case or the expected case is considered. Again, we can also use the *sa* to modulate robustness and include risk into the worst-case problem formulation.

For the case of robust control for Linear Time Invariant (LTI) systems, one well-established and applied methodology is the H_∞ *Mixed-Sensitivity Loop Shaping*. Under this approach, the plant $G(s)$ to be controlled with controller $K(s)$ is augmented including penalizing weights $W_p(s)$, $W_u(s)$, and $W_i(s)$ on the tracking error, the control input, and the system output, respectively. Then the peak gain from the augmented input signals $w(t)$ to the augmented output $w(t)$ ($z(t) = F(G, K)w(t)$),

$$\|F(G,K)\|_\infty = \max_{w(t) \neq 0} \frac{\|z(t)\|_2}{\|w(t)\|_2} \tag{2.45}$$

is minimized. This is most commonly expressed in the frequency domain in terms of a MIMO system transfer function $M(s)$ and its maximum singular value as

$$\|M(s)\|_\infty = \sup_{\omega \in R} \bar{\sigma}[M(j\omega)] \tag{2.46}$$

where $M(s)$ is the transfer function from w to z and is expressed as the weighted system

$$\|M(s)\|_\infty = \left\| \begin{bmatrix} W_p S \\ W u K S \\ W_i T \end{bmatrix} \right\|_\infty \leq \gamma \leq 1 \tag{2.47}$$

where $S = (I+GK)^{-1}$ is the sensitivity function, KS the control effort, and $T = I - S = GK(I+GK)^{-1}$ the complementary sensitivity function. The task is to choose weights $W_p(s)$, $W_u(s)$, and $W_i(s)$ such that disturbance rejection, low control effort, and robustness are simultaneously achieved. For that we require high loop gain $L = GK$ at low frequencies, to achieve good reference tracking and disturbance rejection and quick roll off of L at high frequencies for robust stability and measurement noise attenuation. This loop shape is equivalent to small S at low frequency and small T at high frequency. This problem translates into an *LMI* constrained optimization problem where the target controller K is returned with the least possible achieved γ value. For the robustness part, it is common to consider a multiplicative representation of input uncertainty based on a random perturbation $\Delta_I(s) : \|\Delta_I\|_\infty \leq 1$. Then, if G is the nominal system, the uncertain system $\tilde{G}(s)$ can be described as $\tilde{G}(s) = G(I + W_i \Delta_I)$ where

$$|W_i| \geq \max_\omega \bar{\sigma} \left(G^{-1}(\tilde{G} - G)(j\omega) \right) \tag{2.48}$$

and $W_i(s)$ is a scalar weight bounding the uncertainty of plant $\tilde{G}$.

A different approach to robust control design, particularly suitable for discrete LTI systems, is to work directly with the associated control signals and use mathematical programming to formulate the design problem as a robust optimization of the form eq. (2.2) as

$$\min_{\boldsymbol{\theta}} \{\eta \mid \boldsymbol{x} \in \mathcal{X} \cap \boldsymbol{u} = f(\boldsymbol{\theta}) \in \mathcal{U} \cap \eta \geq g(\boldsymbol{x}, \boldsymbol{u}, \boldsymbol{\xi}) \cap \boldsymbol{\xi} \in \Omega\} \tag{2.49}$$

where $\boldsymbol{\xi}$ represents a random realization of the disturbance confined in the uncertainty space Ω, η is an UB for the performance metric $g(\boldsymbol{x}, \boldsymbol{u}, \boldsymbol{\xi})$, expressing a control objective (i.e., disturbance rejection) and $f(\cdot)$ is the particular control law structure (i.e., linear with respect to state signals/affine with respect to disturbance signal). Additional constraints on the states and control inputs are represented through the feasible sets $\mathcal{X}$ and $\mathcal{U}$, respectively.

Following a different uncertainty approach to leverage conservatism, it is possible to build stochastic controllers in the sense that our optimization objective is achieved on average. In such a case, if we consider an additive uncertainty affecting the states, and express the LTI dynamical system as

$$\boldsymbol{x}_+ = A\boldsymbol{x} + B\boldsymbol{u} + D\boldsymbol{\xi}, \ \boldsymbol{\xi} \in \Omega \tag{2.50}$$

and the control objective is expressed as

$$\min_{\boldsymbol{u}} \{\mathbb{E}_\Omega [J(\boldsymbol{x}, \boldsymbol{u})]\} \tag{2.51}$$

with a finite time quadratic cost function expressed as

$$\mathbb{E}_{\Omega}\left[J(\boldsymbol{x},\boldsymbol{u})\right] = \mathbb{E}_{\Omega}\left[\sum_{t=0}^{T} \boldsymbol{x}_t^T Q\boldsymbol{x} + \boldsymbol{u}_t^T R\boldsymbol{u}_t\right] \tag{2.52}$$

and the probability $\mathbb{P}$ over Ω is Gaussian, then we get the famous *Linear Quadratic Gaussian (LQG)* formulation. Different variations of the control design problem eq. (2.51) can be implemented by using various functions for J (i.e., economic objective), relaxing the assumption for $\mathbb{P}$ (i.e., *sa*) and including constraints into the problem formulation (i.e., feasible sets $\boldsymbol{x} \in \mathcal{X}, \boldsymbol{u} \in \mathcal{U}$). A natural extension to eq. (2.51) includes a model for the dynamics of the system to be controlled as a constraint leading to a Stochastic Model Predictive Control (SMPC) controller. Since the SMPC scheme implements a receding horizon strategy by iteratively solving the constrained stochastic optimization problem calculating an optimal sequence of values (i.e., eq. (2.44)), it is, therefore, straightforward to associate it with the stochastic programming framework mentioned in section 2.1.2, allowing for constraints to be also included in the problem.

Such an approach is particularly useful for the class of discrete-time linear hybrid systems [6], where the logical parts of processes (on/off switches, binary states) and heuristics knowledge about plant operation can be modeled through the *Mixed-Logic Dynamical Systems* framework as integer linear inequalities. In that sense, any arbitrary non-linear cost function can be approximated by linear approximations (*PWA*), non-convex parts can be reformulated using disjunctive logic and binary variables, and then the optimization problem can be formulated as a standard MILP where uncertainty is integrated using scenarios. Those can encapsulate both the parameters' uncertainty in the data matrices of eq. (2.50) (i.e., $A(\boldsymbol{\delta}),\ B(\boldsymbol{\delta}),\ \boldsymbol{\delta} \in \Delta$) and the exogenous random disturbances (i.e., discretization of the stochastic process $\boldsymbol{\xi}$). Thus, given the generic discrete hybrid dynamical system

$$\begin{aligned} \boldsymbol{x}_+ &= f(\boldsymbol{x},\boldsymbol{u},\boldsymbol{\delta},\boldsymbol{\xi}) \\ \boldsymbol{x} \in \mathcal{X} &= \{(\boldsymbol{x}_c,\boldsymbol{x}_b) \in \mathcal{X}_c \times \{0,1\}\} \\ \boldsymbol{u} \in \mathcal{U} &= \{(\boldsymbol{u}_c,\boldsymbol{u}_b) \in \mathcal{U}_c \times \{0,1\}\} \\ F(\boldsymbol{\delta})\boldsymbol{x} + G(\boldsymbol{\delta})\boldsymbol{u} + D\boldsymbol{\xi} &\preceq \mathbf{0} \end{aligned} \tag{2.53}$$

where $\boldsymbol{\delta}$ represents model uncertainty in the parameters, $\boldsymbol{\xi}$ is the exogenous random disturbance, $\boldsymbol{x}_+$ the state variables in the next discrete time instant, $\boldsymbol{x}_c$, $\boldsymbol{u}_c$, and $\boldsymbol{x}_b$, $\boldsymbol{u}_b$ the subsets of continuous and binary control variables, respectively, and $\mathcal{X}_c, \mathcal{U}_c$ the feasible sets for the continuous states and control inputs, respectively. Then optimal control $\boldsymbol{u}^*$ and decision $\boldsymbol{v}^*$ variables sequences can be calculated for the whole prediction horizon T as the solution of the deterministic equivalent MILP (eq. (2.19)) and a finite scenario set with N equiprobable *i.i.d.* samples $\{(\boldsymbol{\xi}(\omega),\boldsymbol{\delta}(\omega)) \in \Omega \times \Delta\}$

indexed by ω as

$$[\boldsymbol{u}^*, \boldsymbol{v}^*]^T = \underset{\boldsymbol{u},\boldsymbol{v}}{\arg\min} \left\{ \sum_{\omega=1}^{N} \sum_{t=0}^{T} J_\omega \left(\boldsymbol{x}_t(\omega), \boldsymbol{u}_t(\omega), \boldsymbol{v}_t(\omega) \mid \boldsymbol{\xi}_0 \right) \right\}$$
$$\boldsymbol{x}_t(\omega) \in \mathcal{X},\ \boldsymbol{u}_t(\omega) \in \mathcal{U},\ \ \boldsymbol{v}_t(\omega) \in \mathcal{V},\ \boldsymbol{x}_{t+1}(\omega) = f(\boldsymbol{x}_t(\omega), \boldsymbol{u}_t(\omega), \boldsymbol{\delta}_t(\omega), \boldsymbol{\xi}_t(\omega)),$$
$$\boldsymbol{u}_0(\omega = i) = \boldsymbol{u}_0(\omega = j),\ \boldsymbol{v}_0(\omega = i) = \boldsymbol{v}_0(\omega = j),\ \forall\, i, j \tag{2.54}$$

where $\boldsymbol{\xi}_0$ is the measurement of the uncertain disturbance at the root node, J_ω represents the economic cost function per stage and scenario, and $\boldsymbol{v}$ represents additional decision variables that do not appear in the system's dynamics but affect the economic cost. Then, only the first time step optimal variables $\boldsymbol{u}_\mathbf{0}^*$ and $\boldsymbol{v}_\mathbf{0}^*$ are applied to the system and the planning horizon is shifted one step ahead. The first three constraints define the feasible set for the states, control inputs, and other decision variables per stage and scenario, the fourth constraint expresses the dynamics of the system, and the last constraint is the causality constraint, meaning that the control input that will be finally applied to the system $\boldsymbol{u}_\mathbf{0}^*$ should be unique, independent of the scenario realization, since all of them share a common initial node at $t = 0$. This approach is referred to as *scenario-based* Model Predictive Control (MPC).

2.2 Overview of the thesis

After having established the necessary theoretical background and the main mathematical tools to be used in the quest to answer the research questions presented in Chapter 1, it is now possible to dive into some technical details leading to the main research outputs and results. An extended summary of the developed methods and achieved outcomes regarding our target application is presented below, unifying the content of the various research papers that were the foundation for the scientific contributions of this thesis.

2.2.1 Techno-economic energy storage system sizing under uncertainty

Sizing under different system configurations, technical limits, and initial conditions

The first task to investigate the potential benefits of integrating ESS in offshore wind-powered O&G platforms relates to finding the optimal size for it, in terms of energy capacity and power capability. Such a decision is naturally connected with an investment decision, and it is therefore meaningful to consider a techno-economic optimization perspective. To address uncertainties stemming from the intermittent wind power production and from the assumption of no knowledge/information of the future load demand, the *so* framework was used.

The optimization problem was formulated as a two-stage Stochastic Program (SP) capturing the discounted investment costs during the investment's lifetime at the first stage (variables $\mathbf{x}$) and operational costs from the power generating units of the platform in the second-stage (variables $\mathbf{y}$). The operational horizon was considered to be a whole day with an hourly second-stage decisions resolution. Then, the uncertainty was integrated into the problem by using a whole-year dataset (365 daily profiles) for the aggregated platform load and wind power production. The wind power produced was assumed to be originating from a wind farm operating at the same (nearby) offshore location. This assumption aligns with the actual intended implementation of the Hywind-Tampen project [7], which during the time period of writing this thesis, has already begun construction. The power producing units in the platform are GTs, which, due to their flexibility, can operate in load following mode in conjunction with the ESS. Nevertheless, for this first analysis, continuous operation of the GTs was assumed, meaning that the operator would not shut down any of them, making it possible to derive a linear formulation of the deterministic equivalent *so* problem and therefore, introduce 365 scenarios denoted as $\widetilde{\boldsymbol{\xi}}$, accounting for the whole year of operation (based on the historical dataset). The problem's objective was then expressed as

$$f(\mathbf{x}; \widetilde{\boldsymbol{\xi}}) = \boldsymbol{c}^T\mathbf{x} + \min_{\mathbf{y}}\{\mathbb{E}_{\widetilde{\boldsymbol{\xi}}}[\boldsymbol{q}^T\mathbf{y}]\} \tag{2.55}$$

The goal of this first sizing analysis was to reveal the dependencies among the various parameters involved in the problem and examine the optimal ESS size with

respect to different system configurations. Those parameters were the number of operating GTs $N_{gt} = \{1, 2\}$, their technical minimum limits $\gamma = \{20\%, 30\%\}$, the wind power penetration $w_p = \{50\%, 100\%\}$ (with respect to the peak load demand), and the initial SoC of the energy storage system $SoC_0 = \{0\%, 25\%, 50\%, 75\%, 100\%\}$ in the beginning of the scheduling horizon (beginning of each day - scenario). Thus, the optimization problem was run over all possible parameter combinations and the results were compared with respect to the corresponding sizing decision and its effect on the expected system operation compared to an identical system that does not include ESS. Such a comparison was assessed in terms of the expected benefits from economic, environmental, and efficient operation perspectives, based on the expected daily cost reductions (daily benefit), CO_2 emissions reduction, and energy dumping reduction. In particular, the daily benefit was defined as

$$DB(N_{gt}, \gamma, w_p, SoC_0) = \mathbb{E}_{\widetilde{\boldsymbol{\xi}}}[\boldsymbol{q}^T \mathbf{y} \mid \mathbf{x} = 0] - \mathbb{E}_{\widetilde{\boldsymbol{\xi}}}[\boldsymbol{q}^T \mathbf{y} \mid \mathbf{x}^* = \arg\min_{\mathbf{x}} f(\mathbf{x}; \widetilde{\boldsymbol{\xi}})] \tag{2.56}$$

Similarly, the daily expected CO_2 emissions reduction was calculated based on the expected fuel consumption associated with the GT power production second-stage variables and the fuel to CO_2 combustion proportionality. The daily expected energy dumping reduction was calculated again directly by the second-stage dump power variables. This power dumping capability represented a dump load for dissipating energy to ensure power balance and, from the optimization problem perspective, ensure its feasibility. Following the current sizing approach, this term was not penalized, allowing it to dump energy at no cost.

The main results of these analyses are summarized in the following. It was found that, in general, the larger the ESS in terms of capacity, the higher the expected DB, while the latter was much less correlated with a higher power rating. This is justified by the fact that the power demand is fixed and generation constrained from the available resources whereas the amount of stored energy can be used to substitute energy provided by GTs. In addition and as a natural consequence, the larger the ESS capacity, the higher the expected reduction in CO_2 and energy dumped (since all of these variables were proportional in this setup). Interestingly, it was noticed that depending on how many GTs are in operation (N_{gt}), increasing the wind power penetration w_p does not necessarily mean that a larger ESS would lead to higher DB. A larger ESS would be promoted only for the case where $N_{gt} = 1$, whereas for the case of $N_{gt} = 2$, since there is already enough base load capacity, the energy would be preferably dumped at no cost. An interesting effect was also observed from the technical minimum γ, which from the ESS sizing perspective was equivalent to operating with more GTs or having higher w_p, since the GTs are enforced to provide larger amounts of base load. Then, for specific combinations ($N_{gt} = 2$ and $\gamma = 30\%$) where more than enough base power is guaranteed, no techno-economical optimal ESS size was found. Also, in accordance with our intuition, having a balanced initial SoC ($SoC_0 = 50\%$) would typically lead to higher DB, since the ESS is prepared to be used in all cases where either charging

or discouraging is required early in the day. Eventually, and summarizing the above observations, the following relation was found for the DB

$$\begin{gathered} w_p = 50\% : \\ DB(N_{gt} = 2, \gamma = 20\%) \geq DB(N_{gt} = 1, \gamma = 30\%) \geq DB(N_{gt} = 1, \gamma = 20\%) \\ w_p = 100\% : \\ DB(N_{gt} = 1, \gamma = 20\%) \geq DB(N_{gt} = 1, \gamma = 30\%) \geq DB(N_{gt} = 2, \gamma = 20\%) \end{gathered} \tag{2.57}$$

in which notably, $DB(N_{gt} = 2, \gamma = 20\%, |w_p = 50\%)$ is the best for the case of $w_p = 50\%$ and the worst for $w_p = 100\%$. This leads, in turn, to the following concluding statement:

Increasing the wind power penetration ($w_p = 50\% \rightarrow w_p = 100\%$) means that we can afford a larger capacity ($+156\%$) ESS with only one GT ($N_{gt} = 1$) and achieve significant reductions (-154%) in terms of operational costs, emissions, and dumped energy. In other words, the method to achieve such reductions is to increase w_p and replace one GT with a properly sized ESS.

Sizing under optimal commitment decisions and coupled uncertainties

From the previous analyses, it becomes evident that significant benefits are anticipated from the integration of an ESS to a wind-powered O&G platform when there is the possibility to operate with one fewer GT. This can be important for platforms that have more than a couple of GTs operating in parallel (such as the case of Hywind-Tampen fields [7]) and where the decision of shutting down or turning on different GT units may be a part of the optimization procedure. For this reason, the ESS sizing approach that was presented above was enhanced with the integration of the Unit Commitment (UC) problem in the second stage where operational decisions need to be made. Therefore, the second-stage problem was formulated as

$$Q(\mathbf{x}, \widetilde{\boldsymbol{\xi}}) = \min_{\mathbf{y}} \{ \boldsymbol{q}^T \mathbf{y} \mid W\mathbf{y} \geq \widetilde{\boldsymbol{\xi}} - T\mathbf{x} \cap \mathbf{y} \geq 0 \cap \mathbf{y}_b \subset \mathbf{y} : \mathbf{y}_b \in \{0, 1\} \} \tag{2.58}$$

where net load is defined as $\widetilde{\boldsymbol{\xi}} = \widetilde{\boldsymbol{\xi}}^{\ell} - f_w(\widetilde{\boldsymbol{\xi}}^{w}), \widetilde{\boldsymbol{\xi}}^{\ell} \in \Omega^{\ell}, \widetilde{\boldsymbol{\xi}}^{w} \in \Omega^{w}$. From eq. (2.58), we notice that a subset of the second-stage decisions are binaries ($\mathbf{y}_b$) denoting the on/off decisions for different GT units and all uncertainty is gathered just on the right hand side of the inequalities constraints. Nevertheless, we highlight that the random vector $\widetilde{\boldsymbol{\xi}}$ depends on two different *RV*s emerging from two completely unrelated stochastic processes; that is, the aggregated platform load demand $\widetilde{\boldsymbol{\xi}}^{\ell} \in \Omega^{\ell}$, which is assumed to be unknown in advance and the stochastic in nature wind speed $\widetilde{\boldsymbol{\xi}}^{w} \in \Omega^{w}$, which leads to random wind power injections. Therefore, the net load is just a marginal representation of the combined uncertainties and not an accurate representation of

the coupled uncertainties, since it does not capture the combinatorial effects of the RVs.

The challenge when integrating probabilistic uncertainty and binary decisions into an optimization problem is that it becomes very easily intractable to solve, even by using decomposition techniques since the resulting MILP problems are *NP-hard*. The standardized way to facilitate the solution of such problems is to implement a selection of particular random occurrences of $\widetilde{\boldsymbol{\xi}}$. Such selection techniques are commonly referred to as sr techniques because they take an initial set $\Omega : \widetilde{\boldsymbol{\xi}} \in \Omega$, and after applying an algorithmic procedure, they end up with a reduced subset $\Omega_s \subset \Omega : \widehat{\boldsymbol{\xi}} \in \Omega_s$, where subscript s stands for the *selected* or preserved scenarios. If the initial random process is continuous in nature (such as the power consumption of a continuously operating system or the power production from a source) then the particular selection decided by the sr is a discretization of the true process. The subsets derived by such discretizations need to be small enough so that the problem is tractable but should also capture the variability of the true process so that we minimize the bias on our decisions. In particular, for sizing analyses based on two-stage formulations such as the one presented above, all available past-observed information should be considered to replicate potential second-stage outcomes. This means uncertainty quantification is much more complex compared to a planning problem where forecasts are typically used to limit the search space, especially for high dimensional uncertainties as in our case. Then, the question arises of how representative those subsets are for the true underlying stochastic process. Therefore, we seek to find just as many scenarios as are needed but without compromising generalization or the solution quality of the sizing problem. For the two-stage setup presented above where the second stage represents a whole day of operation (dimensionality of the random process is 24), it is appropriate to question *which "typical/representative" days to consider without loosing generality but respecting the properties from the observed data and keeping the computational time as short as possible*.

Then, following the sg methodology described in section 2.1.3, we can efficiently generalize from the observed datasets by non-parametric distributions estimation and replicate the statistical properties that define each RV to generate new ones that were not observed before but could have been generated by the underlying mechanism $(\widetilde{\xi}_t^{\ell}, \widetilde{\xi}_t^{w})$. In this case, each random vector $\widetilde{\boldsymbol{\xi}}^{\ell}$ or $\widetilde{\boldsymbol{\xi}}^{w}$ is composed of a sequence of $t = 1, \ldots, 24$ RVs each. However, it is not only the sequence of the RVs but also their combinations that determine each uncertainty realization of $\widetilde{\boldsymbol{\xi}}$. To illustrate this important fact that is typically not addressed, we refer to Figure 2.1. The green profiles represent a realization of $\widetilde{\boldsymbol{\xi}}^{\ell}$ and the red ones a realization of $\widetilde{\boldsymbol{\xi}}^{w}$. However, two realizations of each do not only define two profile combinations (namely two scenarios), but two additional scenarios could be derived from the same profiles by just swapping them. This fact significantly increases the problem complexity because of the combinatorial search space of $\widetilde{\xi}_t^{\ell}$ and $\widetilde{\xi}_t^{w}$ on top of the combinatorial non-convex MILP formulation. To demonstrate the numerical difficulty arising from this fact, we

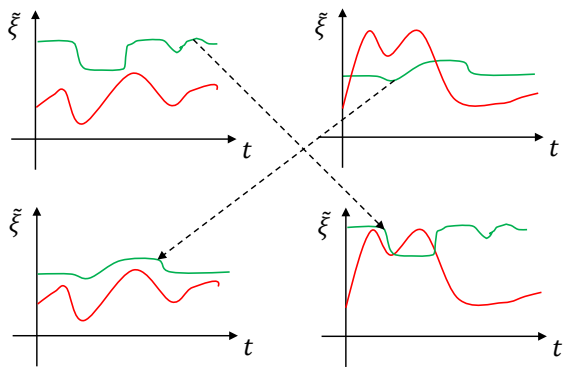

Figure 2.1. Combinatorial dependency of the net load to random load and Renewable Energy Source generation profiles

consider a very coarse discretization for both variables, $\widehat{\xi}_t^{\ell} \in \Omega_s^{\ell}$, $\widehat{\xi}_t^{w} \in \Omega_s^{w}$ where there are only three possible levels ($|\Omega_s^{\ell}| = |\Omega_s^{w}| = 3$) for each variable per time period. This would then lead to a total of $3^{24} \times 3^{24}$ theoretical permutations. Therefore, it is necessary not only to confine those permutations in sequences that could have been generated by the underlying multivariate distribution but also to consider the way $\widetilde{\boldsymbol{\xi}}^{\ell}$ and $\widetilde{\boldsymbol{\xi}}^{w}$ are combined. Such astronomical search spaces cannot be directly embedded into the optimization problem, but they can be sampled to produce an estimator of the true objective value.

To deal with the dependency of the sample and the solution of the sizing problem, the methodology summarized in Figure 2.2 was proposed, leading to optimally reduced subsets with respect to the statistical stability of SPs [8]. Since any reduced sampled dataset, which is necessary for a tractable problem, is missing/ignoring information, this will, in turn, affect the SP solution, leading to objective values that vary significantly with respect to the sampled discretization used to solve it. This means that the solutions we get are not consistent and if we randomly draw a new sample, the solution will change significantly, reducing our confidence in the sizing result. In the proposed setup, we infer the multivariate distributions of the *RV*s and then we do not enforce any particular combination rule but instead perform a *MC* sampling of the individual multivariate distributions to populate the combinatorial space. Then, for the reduced subset to adequately capture the combinatorial variability, we need to ensure that this will contain cases where "typical" profiles from one variable are not only combined with "typical" profiles from the other but also with the ones that are not so "typical". For that, we make use of the following observation: by implementing the commonly adopted heuristic for *sr FFS*, we can identify which patterns (profiles) are most "typical" for each dataset (see figs. 2.3a and 2.3b). Additionally, we can use exactly the same algorithmic procedure in a complementary way to discover the least "typical" patterns (see figs. 2.3c and 2.3d), which could have indeed been generated by the underling stochastic process with equal probability since the random draws of the *MC* approach

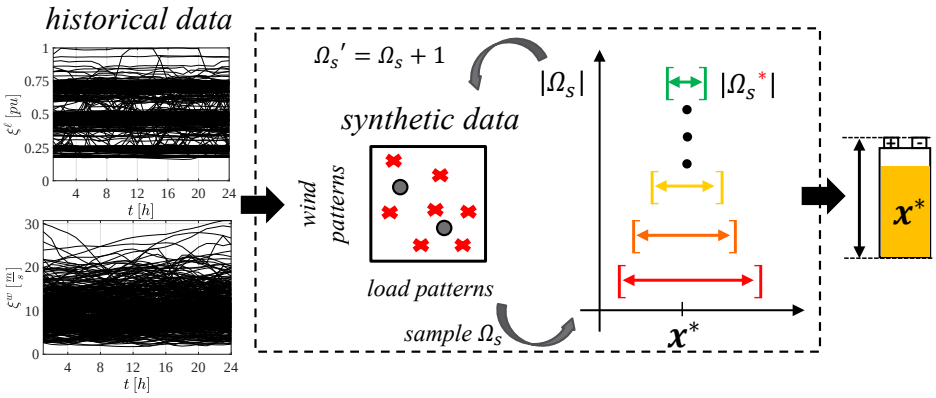

FIGURE 2.2. Proposed algorithm for statistically stable Energy Storage System sizing

are unbiased and equiprobable (*i.i.d.*). A visualization of how the *FFS* can be used to identify the first 10 most and least "typical" patterns in the datasets is presented in Figure 2.3. Further observing Figure 2.3, we see that *FFS* keep patterns that are representative of their dataset. Those tend to be very similar among them for load profiles ξ^{ℓ} fig. 2.3a (blue profiles) concentrated around the "average" value ($0.5\ pu$). Similar trends can be noticed for wind power profiles ξ^{w}. However, such a selection is biased because it does not consider the cases where one "typical" pattern of one variable could be combined with a non "typical" (red profiles) from the other. In our proposed method, we use the concept of "typical" profiles produced by such a procedure to rank the patterns and use the rank statistics of the *MC* generated sample directly. This basically allows us to map the samples in a low dimensional space where the combinations are represented by a single point. Then, this two-dimensional map can be easily further reduced using a clustering technique, but we now guarantee that the clusters will span the whole combinatorial space, allowing for all possibilities (i.e., $\{(typical\ \xi^{\ell}, typical\ \xi^{w}), (non-typical\ \xi^{\ell}, typical\ \xi^{w}), \ldots\}$). In other words, our method guarantees that in every random draw (*MC* sample), all possible combinations will exist in the reduced scenario set, without specifically biasing one particular combination just because of that combination's occurrence based on the individual probabilities of load and wind profiles.

An alternative approach that has been widely used in relevant studies is to define a specific preset correlation value for load and the renewable power generation. Such values may come from location and case specific statistical analyses based on long term historical observations. Besides the specificity of requiring such correlation values that do not justify general applicability/validity, such a concept would be more meaningful for renewable sources that follow basic repetitive patterns (i.e., PV power - day/night hours). However, for highly intermittent resources like wind power, such a selection is vague. Other alternatives for generating reduced subsets are discussed in detail in

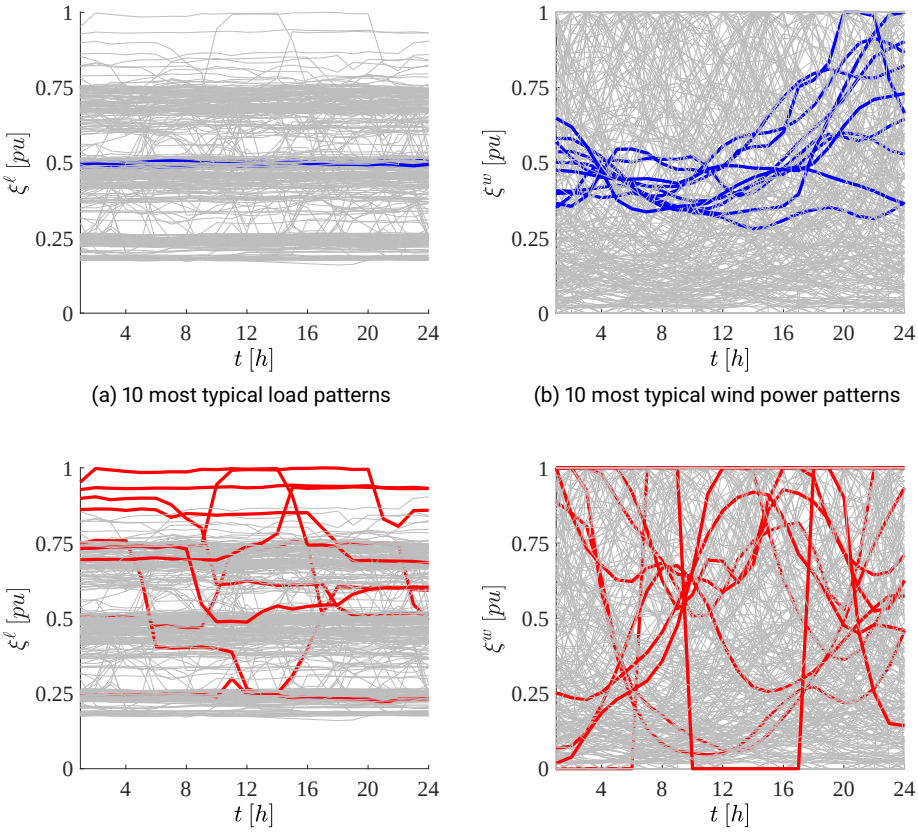

(a) 10 most typical load patterns

(b) 10 most typical wind power patterns

(c) 10 least typical load patterns

(d) 10 least typical wind power patterns

FIGURE 2.3. Implementation of Fast Forward Selection to identify typical and non typical patterns in datasets

Appendix A Supplementary information for Chapter 4.

By implementing the proposed strategy, we were able to reduce the variance of the objective value estimator and achieve better performance in terms of statistical stability compared to other methods. In addition, since no specific requirement was set in the form of the cost function (as long as the whole formulation remains a MILP), it was possible to include a risk measure in the cost to explore the risk management capability of the ESS sizing decision: that is, to minimize the worst-cases expected cost. The *Conditional Value at Risk* measure was used for this, and the whole resulting optimization problem was solved for the optimally reduced scenarios subset Ω_s^* decided from the developed methodology explained above. Interestingly, it was found that the optimal solution for the expected scenario implies no ESS while integrating uncertainty into the problem would lead to a non-zero sizing solution. Then the expected daily benefits

were quantified through the *VSS* and it was found that $\sim 1,000$ € could be saved per day on average with a properly sized ESS and the possibility to shut down GTs. Similar expected environmental savings were calculated for the CO_2 emissions and the dumped energy. Moreover, it was found that we could not efficiently/significantly limit the risk with the ESS sizing decision, since the cost distribution for the worst-cases was found to be quite similar for both the risk-neutral ad risk-averse problems, meaning that there is no decision that can reduce the average cost of the high-cost scenarios. This limitation was justified by the use of the scenarios subset Ω_s^* that captured samples from all possible combinations of load and wind power patterns. Thus, the high-cost scenarios corresponded to combinations of high load and low wind profiles. In such situations, there is no economical way of storing any energy, since the intensive GTs operation cannot be avoided and therefore, managing the risk is not a meaningful option for this specific setup. Nevertheless, reduced costs are expected on average compared to the no storage case, even when increasing the investment costs (referring to conservative future battery price estimations). Summarizing the above, it can be stated that:

The objective value of the optimal sizing decision is not only a function of the decision variables but is also conditional on the uncertainty set used in the optimization problem. The proposed method considers the effect of this coupling and identifies minimum cardinality scenario subsets that optimally explore the combined uncertainty space, leading to statistically stable two-stage MILP formulations.

2.2.2 Optimal energy management under multiple objectives and uncertainty

Stochastic predictive control with uncertainty quantification for irregular events

The sizing results presented in the previous section (section 2.2.1) give an indication of how large an ESS should be regarding the target application of wind-powered offshore O&G platforms, to provide not only economic and environmental benefits during operation but also be an economically feasible investment. For this reason, the operational stage was estimated through the second-stage cost function eq. (2.58). Despite this simplification being particularly useful since it leads to tractable numerical optimization problems, it is still missing the particularities that occur during the smaller time scales of the system operation. In that case, the various assets including the decided ESS are already available in the system and depending on their coordination different operational regimes can be achieved, each one accompanied by different benefits and drawbacks. This eventually frames the problem to be solved by an EMS, which is to promote operational regimes that are more advantageous in terms of cost and environmental impact.

The case of the considered isolated power system that integrates renewable energy is particularly interesting because of its unique features related to the time evolution of both loading conditions and RES generation. Since it is an industrial system, the load patterns are very different compared to a smoothed aggregated load over large residential areas. In addition, the fact that this is in an offshore location, where strong winds involving wind gusts of high energy and short duration, complicates the situation further. As an example, we refer to fig. 2.4a where one year long load profiles for two different offshore platforms (A, B), along with the wind speed for the same location, are provided. As is evident, both types of time series are quite intermittent with the load especially characterized by sudden variations. Zooming in on the red box region of fig. 2.4a, we can observe the same signals for different zoom levels (Figure 2.4). In fig. 2.4b, we can more clearly observe the sudden changes in loading conditions for both platforms for the period of a couple of months. Zooming in further on the red box of fig. 2.4b and focusing on what happens in a single day, the step-wise (step-like) load transitions are now evident from fig. 2.4c (marked in red in fig. 2.4c). Such rapidly varying operating conditions make the problem of designing an optimal EMS particularly challenging. From a prediction point of view, such events are irregular because they follow no pattern and, under the assumption of no prior future information, are hard to anticipate. Not only that but, most importantly, such events may also threaten the safe and continuous operation of such isolated systems. Similar effects but with smoother transitions can be also observed from the wind speed time-series, where trend reversals may be the cause for a continuously fluctuating power generation (i.e., in contrast with a smooth PV power production where power ramps are mainly aligned with the global day vs. night pattern). Such features enhance the EMS overall complexity especially when multiple potentially conflicting objectives need to be satisfied. Exploiting the

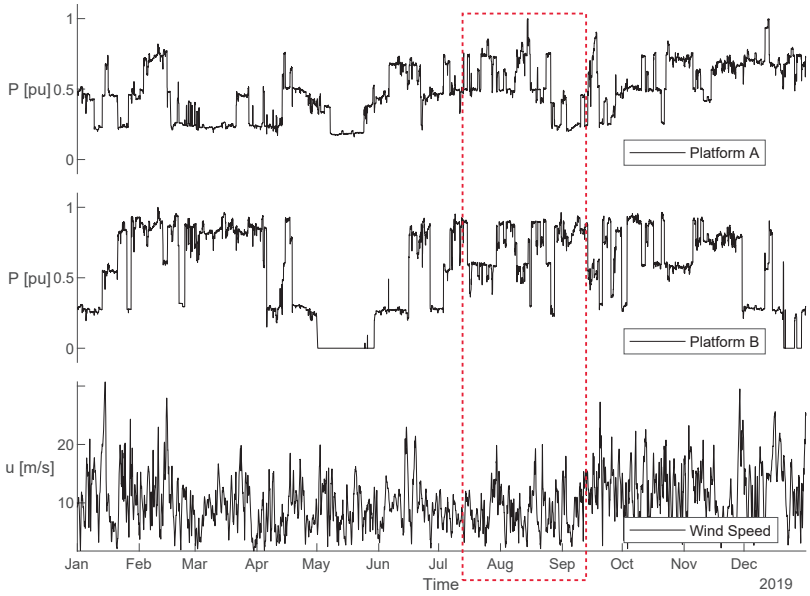

(a) One year long aggregated load and wind speed time series for two nearby offshore O&G platforms

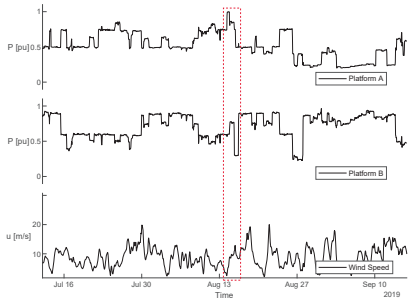

(b) Detail from fig. 2.4a

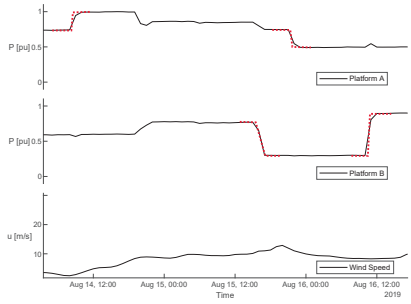

(c) Detail from fig. 2.4b

FIGURE 2.4. Detailed views of fig. 2.4a

uncertainty quantification principles adopted for the ESS sizing problem, a data-driven EMS was developed using the SMPC framework as described in section 2.1.4. For that, the multiple objectives were aggregated in a single stochastic cost function and an adaptive *sg* methodology was employed to solve the optimal SP in a recursive way. Such objectives included the marginal cost of energy supplied by the conventional

GTs (i.e., GT operating in maximum efficiency point), the GT startup costs and state transition costs, the cost of having GT turned on, the degradation due to cycling of the ESS, and the penalization of curtailed energy to the dumping load. Similarly to the sizing analysis (section 2.2.1), batteries were considered for the ESS. The power system was modelled as a control system using the *power node* modelling framework for the ESS where an optimal control sequence is to be found that minimizes the cost and leads to a feasible state trajectory, defined by the system dynamics and state and input constraints (as described from eq. (2.54)). There are two major facts making the control design problem challenging: *i)* the uncertain disturbance and *ii)* that it is a hybrid control system, meaning that both continuous and binary variables are included. This is because of the binary representation of the "ON" / "OFF" state of a GT, x_{gt}, and the binary decision related to the shutting down or turning on the GT units (b^{off}, b^{on} respectively), as illustrated in Figure 2.5.

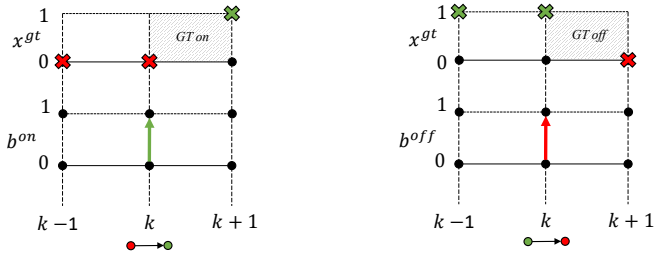

FIGURE 2.5. Induced binary logic in the control problem stemming from the plant operation

Those variables describe the logical implications behind the system operation, such as the fact that if a GT is "OFF", it cannot produce power or it cannot be further shut down. In other words, Figure 2.5 can be translated to the following implications

$$\begin{aligned} x_k^{gt} = 0 \wedge b_k^{on} = 1 \rightarrow x_{k+1}^{gt} = 1 \\ x_k^{gt} = 1 \wedge b_k^{off} = 1 \rightarrow x_{k+1}^{gt} = 0 \end{aligned} \tag{2.59}$$

It is then apparent that the complexity of the problems increases for several GT units. In addition, binary variables can be used in the linearization process of non-linear functions such as the GT-specific fuel consumption or the degradation curve of the BESS. All of these logical implications can then be translated to a MILP formulation where methods such as *Branch-and-Cut* can be used to solve them in real time.

Regarding the first aforementioned challenge, a method was developed integrating adaptive probabilistic forecasting within the optimal control problem. This was based on estimating conditional probabilities for the uncertain variables (load and wind) and using the latest information to construct scenarios that could then be used for the deterministic reformulation of the *so* problem, and therefore, be embedded in the MILP formulation. The goal of such a forecasting module is to have an adaptive uncertainty quantification that could eventually capture the sudden variations and irregular events

of the involved time series but without using any prior future information. This means that no look-ahead forecasts are available (i.e., wind speed forecasts coming from Numerical Weather Prediction (NWP) models or the operations schedule of the platform). Such a requirement allows the applicability of the proposed EMS in various time scales possibly below the granularity of weather forecasts and aiming for an autonomously operating platform (i.e., with minimum human intervention). This was achieved by selecting auto-regressive models that rely only on past information.

A data-driven method based on Quantile Random Forests (QRFs) was proposed for the adaptive probabilistic forecasting feature of the EMS and a recursive correlation estimation for the adaptive sg. The QRF method relies on the well proven machine learning algorithm of RFs described in section 2.1.3. For each lead time k in the look-ahead horizon, a dedicated RF was trained so that it only predicts the uncertain variable for the specified lead time. Then an ensemble of RF (ensemble of ensembles) was used to perform the multi-step ahead prediction as illustrated in Figure 2.6. A dedicated model was then built for each RV.

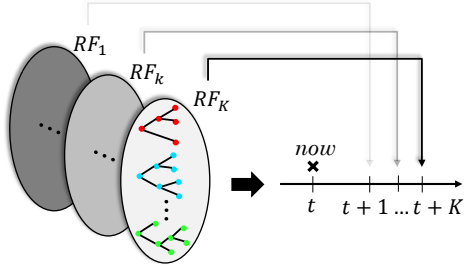

FIGURE 2.6. Ensemble of RFs for multi-step ahead predictions

The important element in the selection of the QRF method is that the whole distribution of the uncertain variable can be estimated based on input features X, which in this case are the lagged values of the RV Y (measurements). If we want to estimate the conditional distribution of value y given a specific input value $X = x$, we can then use the ECDF of the response weights of the trees in the forests based on their own training datasets (bootstrapped samples). This procedure is described through the quantile function as

$$Q_\tau(x) = \inf \left\{ y : \sum_{j=1}^{N} \sum_{t \in \mathcal{T}} \frac{1}{|\mathcal{T}|} \frac{\mathbb{1}\{X_j \in \mathcal{S}_t(x)\}}{\sum_{n=1}^{N} \mathbb{1}\{X_n \in \mathcal{S}_t(x)\}} \mathbb{1}\{Y_j \leq y\} \geq \tau \right\} \tag{2.60}$$

where τ is the specified quantile level we seek to estimate, $\mathcal{S}_t(x)$ is the leaf set containing the value x, and $\mathbb{1}\{X_j \in \mathcal{S}_t(x)\}$ checks whether the j^{th} observation with

input value X_j fall in the leaf set $\mathcal{S}_t(x)$ of tree $t \in \mathcal{T}$, where $j = 1, \ldots, J$ are the indices of the observations used as a training bootstrap sample to the particular tree t. This feature can be then used along with the estimation of the time dependent multivariate distributions of the RV for the specified look-ahead horizon (through a statistic Σ denoting a correlation matrix) and generate potential future trajectories. This time-dependent estimation is illustrated in Figure 2.7 where on the vertical axis, the discrete real-time is represented with t and on the horizontal axes, the lead times are represented with k, for a look-ahead horizon equal to the length of lagged predictor values equal to 2. Then, the issue time (green) is the moment when the forecast is issued, the predictors (blue) are the points in the past that are used by the auto-regressive forecasting engine, and the forecasts (red) are just the future forecasted values. At $t-3$, the red dots represent the forecast points for $t-2$ and $t-1$ using the statistic Σ_{t-3}. This is also the most recent update of the statistic Σ, which can be transferred to time t, for which the values at $t-1, t-2$ are then known and can be used as predictors. Then, the whole sequence is shifted right in $t+1$ where the most recent available estimation is Σ_{t-2} and the whole process is repeated.

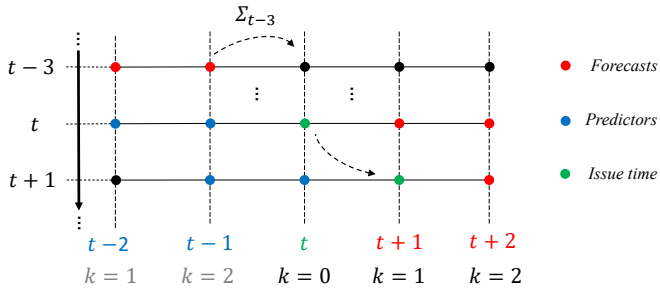

FIGURE 2.7. Rolling horizon basis for recursive correlation estimation

Following the methodology described above, it was possible to achieve adaptive uncertainty quantification and detect possible sudden step-wise variations in the load. In other words, the combination of the time-dependent probabilities and the constantly updating correlation information could then be used to distinguish future values with potentially high and low expected variations, as illustrated in Figure 2.8.

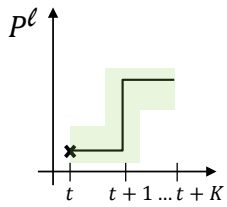

FIGURE 2.8. Future step-wise load variation (black) and target uncertainty pattern estimation (green)

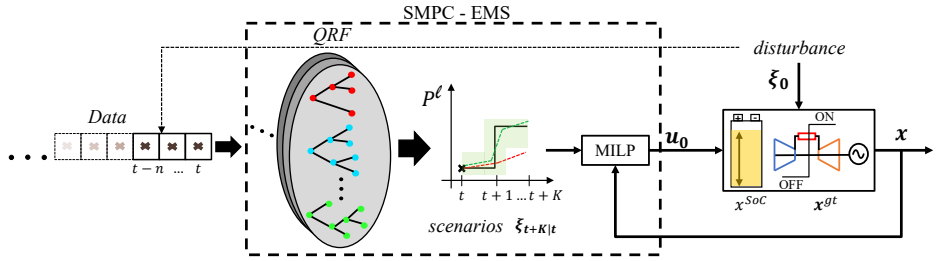

FIGURE 2.9. Overall proposed Stochastic Model Predictive Control-Energy Management System scheme

This feature was integrated into the proposed *scenario-based* SMPC-EMS, the performance of which was tested/validated against several case studies characterized by different daily operational regimes and wind power trends within a whole year period. Such case studies reflected situations of various combinations of low or high loading conditions including load stepping up or stepping down and wind power ramping up or down. The overall proposed methodology is summarized in Figure 2.9. With the proposed methodology, it was possible to significantly improve the very short-term uncertainty quantification capabilities compared to a standard benchmark model (CH-Pen) that used all the historical data available. This was quantified through the *skill score* improvement calculated on the *Continuously Ranked Probability Score (CRPS)* basis. The very high skill scores achieved for both load and wind power time series (around 90%) were justified since the variation implied through the whole historical datasets with the benchmark method was extremely large, leading to very pessimistic probabilistic forecasts. Just as an example, we recall that for the load time series (Platform A) from fig. 2.4a, the minimum to peak variations range is $0.17 - 1\ pu$, clearly indicating the benefits from an adaptive uncertainty estimation such the one proposed. In addition, the proposed method was compared against the deterministic version of the MPC denoted as Deterministic Model Predictive Control (DMPC)-EMS, where only point forecasts are available for the controller and against a simple benchmark rule-based strategy. Using the SMPC-EMS, various benefits were quantified over DMPC-EMS in terms of fuel savings (translated into emissions reduction up to 2.56%), operation cost savings up to 12.86%, and reduction in status transitions (on/off switching) for the GTs up to 35.29%. Such benefits were also accompanied by improvements in the cycling behavior of the BESS, which can be translated into further operational cost reduction, while for most cases, the dumped energy was kept to a minimum value and was not deteriorated compared to the DMPC-EMS case. Summarizing the above, we can conclude that:

Combining so and MILP within an optimal predictive control framework can efficiently

solve the energy management of isolated power systems with dispatchable units, under the presence of very short-term demand and generation uncertainty and non-smooth variations of operating conditions. This was validated under the proposed SMPC-EMS for the case of offshore wind-powered O&G platforms, leading to potential operational benefits.

2.2.3 Frequency support from the ESS under different uncertainty and control representations

Risk-dependent and power limited disturbance rejection

In the previous section, evidence was provided that under the proposed framework, optimal energy management can be achieved, leading to reduction of operational costs, emissions, and the wear and tear of the GTs while avoiding over-straining the ESS. Nevertheless, despite such advantages, it is very important to consider the effect of these decisions on the lower time scale and on the continuous operation of the system, where potentially critical issues could lead to unstable and non-safe conditions.

Moving in this direction and considering the commonly adopted coupling between active power variations and ac systems' frequency, the frequency regulation problem was studied for the target application. This involves isolated power systems with flexible GT units (synchronous generation), wind power and ESS integration, and rapidly varying operating conditions. In particular, the control design for frequency support provision by the ESS was explored under the natural limitation of its power rating and risk considerations for the uncertain disturbance. For the proposed design procedure, it was assumed that at least one GT will be "ON", providing system reliability and operating in its maximum efficiency point, providing damping to the ac power system by a defined droop setting. Then the coupling between the control effort and the power limits (saturation) of the ESS was explicitly considered in the design problem, leading to proper concurrent sizing and control law solutions, when disturbance uncertainty is considered. This was embedded in the design problem using a data-based approach free of unnecessarily tight assumptions (i.e., regarding the probability distributions) or the over-conservatism from norm bounded perturbations that ignore the actual observed disturbance signals. For this, sequences of high resolution net load variations were induced by sampling the available historical datasets for load and wind speed. For the latter, low time-scale variations (i.e., $\sim$ seconds) were constructed from lower resolution data values (i.e., $\sim$ minutes) using validated spectral methods for interpolation and data generation (Chapter B.1).

Since the target was to derive a power control law for the ESS following a data-based approach, the control law was constructed directly on the discrete domain, where the use of numerical optimization is straightforward. To emulate the *virtual inertia* functionality of the ESS when providing power to the system as a function of the frequency deviations, the commonly used output feedback configuration was selected, which was eventually converted into a disturbance feed-forward compensator by using the *Internal Model Principle (IMC)*. Then, the control action was parameterized

as an affine function of the disturbance signal (input disturbance with respect to the power system plant). Therefore, given perfect information of the plant model and the uncertain disturbance, perfect regulation could be achieved and the optimal compensator gain versus power rating could be designed as

$$\frac{q_0}{\bar{u}} = \sup_{\delta \in \Delta} \left\| \frac{1}{\Delta \boldsymbol{P}_d(\delta)} \right\|_\infty = \sup_{\delta \in \Delta,\, t \in T} |\Delta P_d(t, \delta)^{-1}| \tag{2.61}$$

where q_0 is the feed-forward gain, $\bar{u}$ the power rating, $\Delta P_d(t, \delta)$ the active power deviation acting as disturbance and which is a function of the uncertainty and time, Δ the uncertainty set for each RV (i.e., load and wind power), and T the control horizon for the minimization of the Integral Square Error (ISE) of the frequency deviations. Nevertheless, even if perfect system information is available, the uncertainty set Δ (for each RV) is unknown and needs to be modelled. For this, the sa was used, formulating the optimization problem as in eq. (2.49) and allowing for a user-defined risk selection as a hedging mechanism against the unknown disturbances.

With the proposed method, it was possible to find risk-dependent pairs $(q_0, \bar{u})$ that could compensate all sampled disturbances but a small predefined fraction, for which the controller would saturate. Then, taking advantage of the *variable robustness* framework of the sa and considering that worst-cases may be induced by the least "typical" patterns (as discussed in section 2.2.1), a sr algorithm was employed (*FFS*) to characterize the performance improvement versus risk dependency. Then it was found that removing 29 scenarios from the initial sample would give the best trade-off of performance improvement (66% smaller objective value) and risk deterioration (risk level increased from 1% to 3.23%). Even though it was demonstrated for a static case, it is simple to implement such methodology in a recursive way together with the SMPC-EMS described in section 2.2.2, so that uncertainty sets are refreshed based on the latest information, updating the control law for frequency support but also finding time-varying and risk-dependent bounds of the maximum power injections ($\bar{u}$), guaranteeing that the provided ancillary service will have a bounded impact on the SoC schedule of the ESS. Summarizing the above, we conclude:

The provision of frequency support by the ESS is not only linked to its maximum power capabilities but also to the very short-term potential disturbances. With the proposed methodology, we could find optimal combinations of control law and maximum power requirements for the ESS, so that proper frequency regulation is achieved by accepting a user-defined risk of not achieving it.

Optimal isochronous frequency regulation and state of charge tracking

So far, it has been demonstrated that a properly sized ESS can be used in various time scales to mitigate issues emerging from the uncertainty characterizing both supply and demand. In particular, for the lower time scale, it was shown that risk-averse

frequency support can be provided with bounded effects on the power requirements from the ESS that could be translated into energy bounds, for the compensation horizon. Nevertheless, such multi-scale functionality of the ESS could affect its optimal SoC schedule coming from the EMS. To deal with this issue, a supervisory control scheme was proposed for coordinating both the GT and the ESS to achieve simultaneous frequency regulation and SoC tracking, while also respecting operational constraints. In addition, the combined effects of disturbance and parameters uncertainty were integrated into the control design problem, lifting the assumption of perfect plant knowledge. Moreover, a higher fidelity model was implemented for the ESS (which again, and in accordance with the previous analyses, was based on batteries), capturing the rate capacity and charge relaxation effects.

To achieve the multiple control objectives for the Multi-Input Multi-Output (MIMO) system, the MPC framework was employed along with the sa, resulting in SMPC controller proposals. The overall system including the considered power and control systems is illustrated in Figure 2.10. For this configuration, the GT was assumed to be operating in its maximum efficiency point (for a given load) while in isochronous operation. This means that it constantly tracks the frequency providing continuous regulation to its nominal value, and therefore, a load disturbance would cause it to deviate from its current efficient operating point. However, since the ESS is also part of this configuration, it could contribute by supporting the grid, ensuring that the frequency is tightly regulated with minimum deviation of the GT from its efficient operating point during the transient. Nevertheless, the contribution from the ESS should only occur during the transient period and in a way that does not

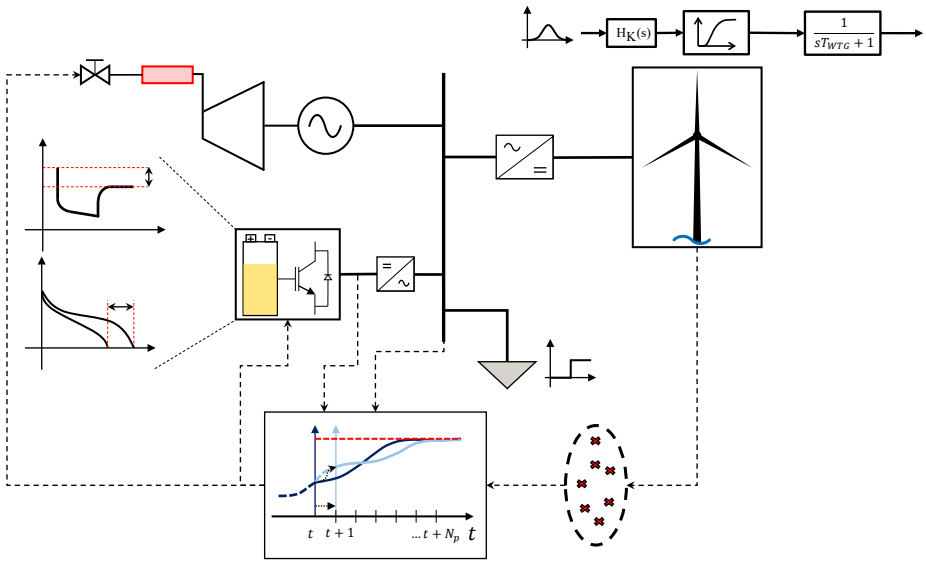

FIGURE 2.10. Overall power system model and proposed control framework

cause it to deviate from its SoC reference. Meanwhile, it should also be weighted so that its cycling behavior and corresponding degradation are minimum. Control and control deviation bounds were integrated into the controller for both the GT and ESS, modelling power and power ramping constraints. In addition, to quantify the effect of the control law parametrization, various SMPC versions were developed where the control law was either implicitly calculated from the numerical optimization problem SMPC-*No Parametrization*) (NP) or was expressed through a feedback mechanism. This was either an affine function of the disturbance SMPC-*Full Parametrization* (FP) or an affine function of the states using a constant *LQR* feedback law SMPC-*State Feedback* parametrization (SF). The performance of the various SMPC controllers was compared against a deterministic MPC version and against a robust control design based on H_∞ method, explained in section 2.1.4.

Initially, the different controllers were compared in terms of their nominal performance assuming no plant or disturbance uncertainty by simulating their responses in a load step variation. In this case, it was found that the SMPC-NP achieved the most dumped and fastest frequency response compared to the SMPC-SF and H_∞ controllers. Additionally, it performed better in terms of SoC tracking compared to SMPC-SF while the H_∞ ensured the tightest SoC tracking with the least dynamic deviation. Nevertheless, the SMPC-SF was accompanied by more conservative control effort/action (i.e., peak GT and BESS power demand) compared to SMPC-SF. Then, even though H_∞ resulted in the worst frequency nadir, it also achieved the best SoC tracking. Such effects revealed the inherent preferences and increased tuning requirements from each controller, meaning that SF eventually offered smoother control actions at the cost of slower responses while the robust controller ensured the best satisfaction for the BESS objectives, putting more stress on the GT and at the cost of the worst frequency regulation.

Then, again for the same specified load step variation, the developed controllers were compared under the presence of both plant and disturbance uncertainty. The disturbance uncertainty was due to random wind power realizations at each time step (based on an average wind speed value and the higher resolution model of wind speed variations described in Chapter B.1, while a 10% uncertainty was considered over the nominal parameters values. For this analysis, two evaluations studies were conducted, one expressing the expected performance of the controllers and another based on an *MC* approach to quantify their constraint violation probabilities and estimate the full ECDF of some defined key performance indicators. For the expected performance analysis, similar results with the nominal performance comparison were observed, with the most important being the similarity in the achieved performance among the DMPC, SMPC-NP, and SMPC-FP controllers, justified by their quite similar internal structure compared to SMPC-SF and H_∞. In terms of constraint violation probability, as expected, the SMPC versions resulted in less violation of the maximum allowable frequency deviation compared to the DMPC. In addition, since the impact of the disturbance uncertainty is directly on the system's frequency and

not on the SoC, it is noteworthy that all controllers could respect the SoC bounds without violations, although again the DMPC would saturate the constraint (reach the SoC limit value) more often compared to the SMPC versions. In addition, the SMPC-NP and SMPC-FP achieved less frequency nadir violation and maximum SoC deviations compared to SMPC-SF, which had similar violation distribution with the DMPC. The worst violation distribution was observed for H_∞ controller, meaning that the impact of the disturbance uncertainty was much more important compared to the parametric uncertainty for which the H_∞ controller was designed. Nevertheless, H_∞ achieved the best distribution in terms of BESS cycling (in accordance with its nominal behavior), while it was associated with the worst distribution in terms of the GT control effort, for which the SMPC-SF had the best one. Finally, different factors related to the C-rate capabilities of the ESS were studied and their impact on the DMPC performance. Summarizing the above, we can state that:

Achieving simultaneous tight frequency regulation and SoC tracking for isolated grids that include a GT, a BESS, and stochastic wind power is possible and better achieved by using SMPC, preferably with an affine disturbance feedback controller parametrization. This enables the smooth integration with higher level EMS algorithms that give optimal SoC reference trajectories, addressing the difficulties due to the time-scale separation in power systems.

2.2.4 Adaptive frequency and energy constrained primary control design embedding in the EMS

It is now evident that the complexity in decision making for an EMS comes not only from the multiple objectives, but also from the coupling of multiple time scales with different requirements. An optimal operation can be decided upon a higher time scale ($\sim$ minutes), but the reliable and safe system operation is decided on a lower time scale ($\sim$ seconds) during the continuous system operation. As seen before (section 2.2.3), a typical way to consider that active power balance is not only achieved at the discrete scheduled times but during the whole operation, is to regulate the frequency of the ac system. In the previous section (section 2.2.3), a method for continuous frequency regulation was presented assuming that one of the conventional units (GT) will be the master unit operating in isochronous mode and will be supported by the ESS. However, this option puts all the stress on a single GT (despite being relieved by the ESS in the proposed setup).

An alternative way that has been traditionally adopted in large interconnected power systems is to distribute the control effort among the several interconnected units and decouple the effects of an active power imbalance in different time intervals employing a hierarchical frequency regulation structure. In particular, there exist dedicated procedures defined by national/international authorities and system operators (TSO) to follow a *divide and conquer* approach in which the frequency response is

partitioned in time and different control requirements are set at each partition. The first and quickest requirement is to arrest the frequency response, which comes as a natural effect from the rotating inertia of the generators (assuming that those exist in the system). Then, during the first seconds after the disturbance, primary frequency control is implemented, being responsible to bound and contain the frequency deviation from its nominal value. Then, the secondary frequency control is employed to bring the frequency back to its nominal value. At this stage, since the various generators participating in this hierarchical control structure have deviated from their scheduled dispatch values, an additional control layer is employed (tertiary control) to reschedule the generators to new optimal operating points while releasing any amount of power capability reserved for primary or secondary control. Separate and dedicated markets exist for each of the above services where different types of generators provide (bid) their capability/willingness to support the grid after disturbances. This capability is labeled as *reserves* and, depending on if it is provided for primary or secondary control, is further characterized as *primary / secondary reserves*, respectively. This hierarchical structure has the benefit of splitting the control effort among the participating units and relying on simple but effective enough control laws. As an example we mention the primary control, which is typically implemented through proportional laws to the frequency deviation, the so-called *droop* control.

The situation becomes more complicated when trying to limit the operation of conventional units and replace them with RES. Then their contribution is limited and the rotating inertia of the system reduced, making the grid vulnerable to large-scale disturbances. In addition, the optimal operation of the conventional units (coming from the UC and Energy Dispatch (ED) problems) does not necessarily mean that the security of the system will be ensured, and therefore, special reformulations are needed. This becomes particularly critical regarding the operation of isolated power systems, such as the offshore wind-powered O&G platforms that are the main application target of this thesis. Following the distributed control approach, the online generators (GTs) take the responsibility of dealing with Active Power Disturbances (APDs) in a collective way through their rotational masses and predefined droop control laws. Additionally, since properly sized ESS solutions are already considered for the optimal EMS as presented throughout section 2.2 and in particular in section 2.2.2, the natural extension is to use this as a *virtual generator* supporting the grid's frequency (as also explored in section 2.2.3). Then, the question that arises is how to integrate the design of the droop control mechanism and the ESS participation in the EMS algorithm, so that *i)* minimum GTs contribution is required, *ii)* the ESS does not deviate much from its originally planned (by the EMS) optimal SoC schedule, and *iii)* allocated reserves are enough to withstand near-future uncertain APDs.

To solve the above-mentioned problems, an upgraded version of the EMS is proposed (w.r.t. section 2.2.2) with the following additional enhancements. Initially, the non-linear dynamics of the ac power system are used to provide bounds on the frequency deviation given a particular APD value. Such a relation defines the minimum

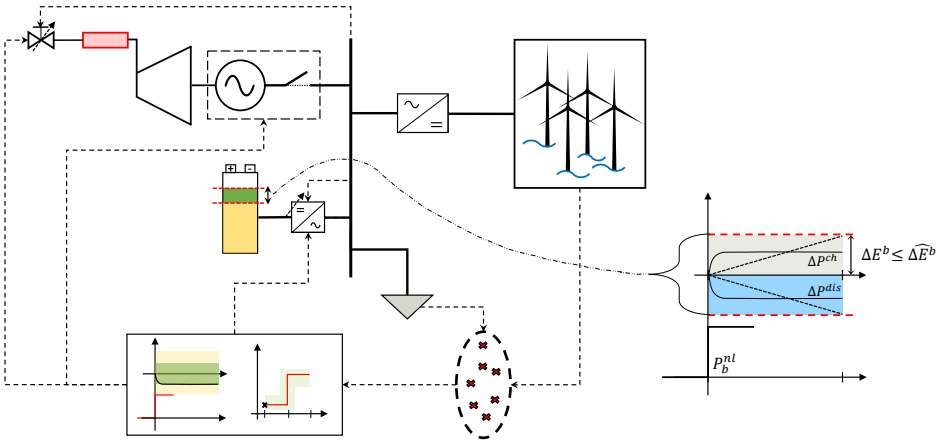

FIGURE 2.11. Overall power system model with proposed Energy Management System and adaptive control framework

required damping of the system and conversely, defining an acceptable range for the frequency after an APD, we may find the minimum required system damping. Similarly, it is possible to define the minimum required system inertia to limit the rate of change of frequency (RoCoF) below a particular defined value. Besides the GT units that provide inertia and damping (by the droop control), a virtual inertia and virtual droop control law is employed for the ESS to emulate a GT and contribute to the minimum required inertia and damping values. Then, since the ESS will be participating in the inertial and primary control layers, meaning that it will provide or absorb an unscheduled amount of energy, this should be small enough to limit its impact on the optimally scheduled State of Energy (SoE) trajectory. A method for reformulating the aforementioned logic into a set of linear constraints was derived, enabling the smooth integration with MILP-based EMS. Nevertheless, for such an implementation, a value of the APD is required. Since perfect forecast is impossible and given the possibility from the developed SMPC-EMS algorithm (section 2.2.2) to quantify uncertainty of load and wind power in an adaptive way, then a probabilistic representation of APD constraints could be imposed. Then, combining this with a risk-dependent probabilistic satisfaction of the induced constraints using a modified version of the *sa*, it was possible to reformulated the chance-constrained optimisation problem into a finite sample *ro* problem. To efficiently solve the robust MILP reformulation, a pattern-based technique was employed (equivalently to the pattern-based solution of the famous *cutting-stock problem*), avoiding the extensive tree search resulting from the *Branch-and-Bound* method, and thus it was possible to solve the problem in a recursive way through an MPC framework. The main concepts of the proposed algorithm are illustrated in Figure 2.11. With the proposed modified EMS, it was possible to co-optimize the system's efficient operation, the droop control of the

GTs, and the ESS frequency support contribution under uncertain disturbances and guarantees on the frequency variations. Since probabilistic forecasts could capture sudden net load variations, the optimal schedules derived with the enhanced EMS were different from the original *security-ignorant* EMS (section 2.2.2), securing safe system operation (i.e., the frequency staying inside the allowable range and its rate of change being no greater than the acceptable value). It was interesting to observe that the allocation of reserves was following the pattern on the net load where a possible future large variation would be secured by scheduling more reserves and inertia compared to cases where relatively flat conditions were expected. The security enforcing feature came at a relatively small cost compared to the *security-ignorant* EMS, where the largest difference was the amount of time and the GT units that should be kept on by each version. Notably, the coordination of the ESS and GTs acts as an alternative to the $N + 1$ redundancy, since if the ESS was not used to provide frequency response, additional GT units would be required to be "ON" at some instants, to ensure the minimum requirements. Finally, the constraints on the use of the ESS were validated by two versions of the EMS algorithm; in the first, such constraints were ignored and in the second, they were enforced. It was found that ignoring such constraints could lead to violations of the desired energy reserves bounds allocated for the EMS for some instants, while with the second version bounds were respected for the whole simulated period.

2.3 REFERENCES

[1] M. C. Campi and S. Garatti, *Introduction to the Scenario Approach*. Philadelphia, PA: Society for Industrial and Applied Mathematics, Nov. 2018. [Online]. Available: https://epubs.siam.org/doi/book/10.1137/1.9781611975444 Cited on page/s 16.

[2] S. Küçükyavuz and S. Sen, "An Introduction to Two-Stage Stochastic Mixed-Integer Programming," in *The Operations Research Revolution*, R. Batta, J. Peng, J. C. Smith, and H. J. Greenberg, Eds. INFORMS, Sep. 2017, pp. 1–27. [Online]. Available: http://pubsonline.informs.org/doi/10.1287/educ.2017.0171 Cited on page/s 17, 19.

[3] M. J. Sklar, "Fonctions de repartition a n dimensions et leurs marges," 1959. Cited on page/s 22.

[4] L. Breiman, "Random Forests," *Machine Learning*, vol. 45, pp. 5–32, Oct. 2001. Cited on page/s 25, 26.

[5] N. Meinshausen, "Quantile Regression Forests," *J. Mach. Learn. Res.*, vol. 7, pp. 983–999, Dec. 2006. Cited on page/s 25.

[6] A. Bemporad and M. Morari, "Control of systems integrating logic, dynamics, and constraints," *Automatica*, vol. 35, no. 3, pp. 407–427, Mar. 1999. [Online]. Available: https://linkinghub.elsevier.com/retrieve/pii/S0005109898001782 Cited on page/s 30.

[7] "Hywind Tampen." [Online]. Available: https://www.equinor.com/energy/hywind-tampen Cited on page/s 32, 34.

[8] M. Kaut and S. W. Wallace, *Evaluation of scenario-generation methods for stochastic programming*, J. L. Higle, W. Römisch, and S. Sen, Eds. Humboldt-Universität zu Berlin, Mathematisch-Naturwissenschaftliche Fakultät II, Institut für Mathematik, 2003. Cited on page/s 36.

Part II

PAPERS

Chapter 3

Techno-Economic Evaluation of the Sizing and Operation of Battery Storage for Isolated Oil and Gas Platforms with High Wind Power Penetration

Spyridon Chapaloglou[1,*], Damiano Varagnolo[2] and Elisabetta Tedeschi[1]

First published in: *IECON 2019* - 45th Annual Conference of the IEEE Industrial Electronics Society.
DOI: 10.1109/IECON.2019.8926739

Abstract

According to the plans of one of the global O&G industry leaders, the integration of offshore wind power into offshore O&G platforms will become reality within the next three years. Although this implementation is going to set the standards for a cleaner platform operation, the intermittency of wind power generation does not favor the provision of scheduled constant and reliable power for the loads. To cope with this limitation, this paper proposes a configuration that integrates a BESS in the O&G platform. The manuscript focuses on how to appropriately size the BESS through a techno-economic study that considers both investment and operation costs, along with the possibility for economic benefits in terms of fuel savings and CO2 emissions reductions. The results, obtained using aggregated field data from a real platform, indicate that the sized BESS enables fuel savings and higher levels of wind power penetration. This confirms the intuition that BESSs may positively contribute towards renewable-based offshore O&G platforms.

3.1 Introduction

The global O&G industry is deemed amongst the most emissions intensive, with the production and use of O&G accounting for over half of global greenhouse gas emissions associated with energy consumption [1]. In Norway, which is the third larger exporter of gas in the world and covers about 2% of the global oil demand, a considerable need to

[1]Department of Electric Power Engineering, Norwegian University of Science and Technology (NTNU), Trondheim, Norway. [2]Department of Engineering Cybernetics, Norwegian University of Science and Technology (NTNU), Trondheim, Norway. *e-mail: spyridon.chapaloglou@ntnu.no, damiano.varagnolo@ntnu.no and elisabetta.tedeschi@ntnu.no

maximize the O&G resources utilization, minimize environmental impact, and reduce its GHG emissions is felt and now also stated on the Norwegian OG21 strategic vision for the petroleum sector [2]. Offshore O&G platforms are typically isolated, implying that their operations are supported by conventional power generation systems, namely diesel generators and GTs. These systems add a significant proportion to the total generated emissions that result from the operation of the various processing systems typically found in an O&G platform. Therefore, to control and reduce the high emission levels associated with the operation of O&G platforms, one way is to find alternatives for the power generation system. Such alternatives could include long-distance power transmission (at the cost of facing several technical and environmental challenges related to the deployment of these lines) and the integration of renewable energy to the O&G platform [3]. Following the recent progress of the offshore wind energy sector [4], Equinor has recently announced their plan to interconnect two offshore O&G platforms with a co-located floating wind farm and to explore the possibility for integrating large amounts of renewable power to the platforms power systems [5]. However, this introduces the problem of coupling the intermittent behavior of the wind power production with the high criticality and reliability requirements of the supplied loads. The critical point from a technical perspective is that the uncertainties associated to the energy supply and production processes can lead to system-wide power fluctuations, which can, in their turn, threaten the stability and reliability of the platform's operations [6, 7]. Facing this problem requires flexible solutions that may include advanced energy resources scheduling [8], efficient coordination of the various subsystems [9] and integrating an energy storage system in the platforms grid. However, none of the above-mentioned studies investigated the benefits of integrating ESSs into O&G platforms, despite their proven abilities to provide ancillary services, aid improving scheduling, and help increasing renewable penetration. To this respect, battery ESSs provide interesting possibilities, due to their constantly decreasing installation and operation costs.

3.2 Problem Formulation

We first describe and model the system in Subsection 3.2.1, and then use this information to formulate our BESS sizing problem.

3.2.1 System Description and Quantitative Models

The O&G platform under consideration is located in the North Sea; its power supply comes from 2 identical GTs that are operated in load sharing mode, with a capability to cover the load just by using one of them. The platform is also supplied from locally generated offshore wind power, rated at a 50% power penetration (i.e., the maximum wind power production over the peak load of the platform). For the smooth and safe operation of the system, a dump load is also included for dissipating excess power when total generation is greater than total consumption. The proposed configuration,

which is depicted in Figure 3.1, integrates two key components: a) a BESS with its corresponding balance of power components, and b) a controllable dump load. Including the controllable dump load adds essential flexibility in how to design and operate the storage system: being enforced to store surplus energy under any conditions could indeed lead to an economically unjustifiably large battery size. The wind power generation was modeled based on the tools from [10]. Thus, it was possible to simulate the hourly wind power production for a whole year, based on realistic wind conditions. Figure 3.2 presents the power consumption profiles of the offshore platform, along

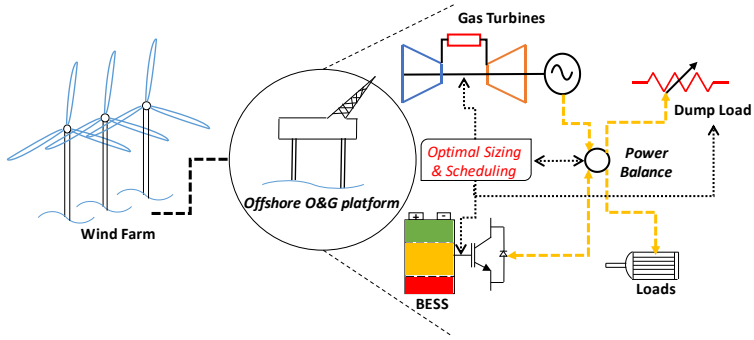

FIGURE 3.1. The proposed system configuration

with the wind power generation at the selected site, on an hourly basis for a whole year. The location is characterized by extreme offshore wind conditions: more than 50% of the year the wind power generation is greater equal than 80% of its rated power, with a yearly Capacity Factor (CF) of 67%. The last, is in line with actual performance of offshore floating wind farms [11]. The wind farm operates thus at its rated capacity most of the time, but it also experiences several deep wind drops and steep ramp-ups concentrated in a few hours. At the same time, the O&G platform consumption profile is mostly constant along the different days, as it is dominated by large and scheduled loads (i.e., drilling and oil pumping equipment). However, the platform load curve presents short-term power spikes due to the startup and disconnection of individual heavy loads (i.e. compressors, cranes, thermal process equipment). The combined effects of these events lead to a constantly varying correlation between the wind power generation and the platform's consumption; to maintain reliable operations of the overall system there is thus the need for introducing appropriate power management strategies that, depending on the situation, divert or extract electrical power to / from the BESS. Designing the BESS control strategy calls then for solving the associated BESS sizing problem. Sizing the BESS shall in its turn take into account both operation costs (i.e., the operational costs of the power generation system, including fuel consumption, operation and maintenance (O&M), and additional CO2 generation taxes) and investment costs (i.e., installation, commissioning and de-commissioning, potential loans). The remainder of this section will thus introduce the various models of the

costs above, i.e., the atomic components of what will be our BESS sizing optimization problem. The first model relates then to the GTs operation costs, modeled based on

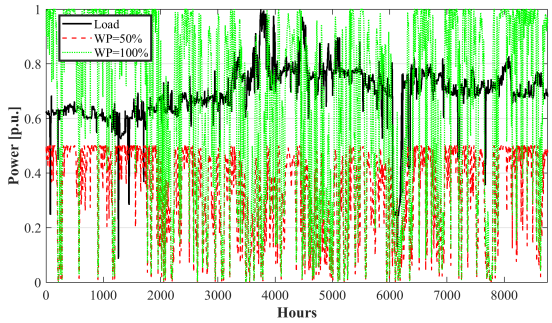

FIGURE 3.2. Platform power consumption and wind power generation (a year)

field data about power generation and thermal efficiency of the GTs of the considered platform. More specifically, for each operation point the model estimates the fuel mass flow $\dot{m}_f(i)$ [kg/h] as

$$\dot{m}_f(i) = \frac{P_{GT}}{\eta(i) \cdot LHV} \tag{3.1}$$

where i indicates the operating point, $\eta(i)$ is the thermal efficiency of the GTs [adim.], $P_{GT}(i)$ the GT power [MW], and LHV is the lower heating value of natural gas [MJ/kg]. The dataset indicates an almost linear relationship between fuel mass flow and GTs power, so that in the following we will approximate this model with the commonly used affine map $\dot{m}_f = a \cdot P_{GT} + b$. Note moreover that in our analyses we consider dt = 1 hour, so that the average power production (in MW) is numerically equal to the hourly produced energy (in MWh). The same is valid for the fuel consumption.

The second model is relative to the produced CO2 emissions, that can be estimated from the fuel flows for each operation point by considering the ideal combustion process of natural gas through a conversion coefficient $\mu_{NG\rightarrow CO2}$. Thus, from the fuel sale value C_{NG}, the fuel density at standard temperature and pressure conditions ρ_N, the estimated O&M cost [12] and the CO2 tax $C_{co2,tax}$ estimated from [13], it is possible to calculate the levelized cost of the power produced from the GTs, C_f as

$$C_f\left[\frac{€}{MWh}\right] = \left(\frac{C_{NG}\left[\frac{€}{Nm^3}\right]}{\rho_N\left[\frac{kg}{Nm^3}\right]} + C_{CO_2 tax}\left[\frac{€}{kg_{CO_2}}\right] \cdot \mu_{NG\rightarrow CO2}\left[\frac{kg_{CO_2}}{kg_{fuel}}\right]\right) \cdot \alpha\left[\frac{kg}{MWh}\right] + C_{O\&M}\left[\frac{€}{MWh}\right] \tag{3.2}$$

The third model regards the total BESS investment cost, that is divided as in [14] into two factors, i.e., its capacity $C_E[MWh]$ and its power conversion rating $C_P[MW]$. The battery type has been selected based on the lifetime duration [15,

16], power density and the possibility for deep charge/discharge cycles. Moreover, since deep-water offshore O&G platforms are typically far from the shore, replacing equipment corresponds to costly and time-consuming operations. Considering the cost and maintenance trends of various battery technologies (summarized in [17]), we thus considered *Li-Ion* batteries as the most viable option for a BESS in a deep-water O&G platform. Finally, the amortization of the initial investment cost C_{BESS} is split into a daily basis cost (i.e., the Capital Recovery Factor (CRF)) as in [18], and thus as

$$CRF = \frac{r \cdot (1+r)^p}{(1+r)^p - 1} \tag{3.3}$$

$$C_{BESS} = CRF \cdot (C_P \cdot \hat{P}_B + C_E \cdot \hat{E}_B) \tag{3.4}$$

where r is the daily interest rate (derived from the annual interest rate), p is the recouping periods ($p = 365 \cdot L$), where L is the investment lifetime and $\hat{P}_B$ and $\hat{E}_B$ are the BESS power rating and maximum capacity, respectively. For the sake of reproducibility of our results, we collect the values of the abovementioned parameters in Table 3.1.

TABLE 3.1. Technical and economical parameters

Parameter	Value
Fuel and Combustion Characteristics	
LHV [MJ/kg]	44.19
NG sale value C_{NG} $\left[\frac{€}{Sm^3}\right]$	0.24 [12]
$\mu_{NG \to CO2}$ $\left[\frac{kg_{co2}}{kg_{fuel}}\right]$ (NG to CO2 combustion ratio)	2.53
CO2 TAX: $C_{co2,tax}$ $\left[\frac{€}{kg_{CO_2}}\right]$	0.07 [13]
Levelized CO2 TAX $\left[\frac{€}{MWh}\right]$	30.55
Gas Turbine Characteristics	
Max GT Power $P_{GT,max}$ $[MW]$	15
Min GT power $P_{GT,min}$ $[MW]$ (@ Tech. Min. = 20%)	3
Min GT power $P_{GT,min}$ $[MW]$ (@ Tech. Min. = 30%)	4.5
Linear Interpolation coefficient a $\left[\frac{kg}{MWh}\right]$	172.5
Linear Interpolation constant b $\left[\frac{kg}{h}\right]$	729.2
O&M cost of GT $C_{O\&M}$ $\left[\frac{€}{MWh}\right]$	11.42
Fuel Cost C_{NG} $\left[\frac{€}{MWh}\right]$	57.74
Levelized cost of GT power C_f $\left[\frac{€}{MWh}\right]$	99.71
Battery Energy Storage System Characteristics	
Investment Lifetime L	15 [15, 16]
Annual Interest Rate	7% [12]
BESS Capacity Cost C_E $\left[\frac{€}{MWh}\right]$	70 [17]
BESS Power Cost C_P $\left[\frac{€}{MWh}\right]$	40 [17]

3.2.2 Formulating the BESS sizing and operation problem as a linear optimization problem

To define the BESS sizing problem we consider solving the UC problem using a simplified two stage stochastic LP formulation based on deterministic scenarios that emerge from expert knowledge contained in the available dataset of hourly measured load and wind power profiles for a whole year. The two-stage formulation allows for two different stages of decision variables, the first containing the sizing problem variables ($\hat{P}_B, \hat{E}_B$) and the second containing the operating variables that are different based on each operational scenario, as described below. In this way, it is possible to take into account a summary of the possible future weather conditions, so that the many possible outcomes of the platform consumption and wind power generation are considered as equiprobable scenarios to be realized. Then, the scenarios are simultaneously taken into account and included in the objective function through the evaluation of the expected cost based on the SAA [19].The envisioned approach to design the maximum capacity of the storage system $\hat{E}_{bat} \geq 0$ and its power rating $\hat{P}_{bat} \geq 0$ for every possible scenario s (N=365) and examined case c (C=40), becomes thus the following: first of all, the UC problem shall consider the following as controllable variables:

- The aggregated hourly power generation from the GTs, i.e., $P^s_{GT}(t)$ for t=1,…,24, s=1,…,365;
- The hourly charging/discharging power profile of the BESS, i.e., $P^s_{bat}(t)$ for t=1,…,24, s=1,…,365 (with $P^s_{bat}(t) > 0$ indicating that the BESS discharges and acts as a generation unit, and $P^s_{bat}(t) < 0$ vice versa);
- The hourly dissipated dump load power, i.e., $P^s_{dump}(t)$ for t=1,…,24, s=1,…,365. Moreover, the approach shall guarantee the following series of constraints:
- the system depicted in Figure 3.1 needs to be always in power balance, that means

$$P^s_{bat}(t) + P^s_{GT}(t) = P^s_L(t) - P^s_w(t) + P^s_{dump}(t)\,,\ t = 1 \div 24, s = 1 \div N \quad (3.5)$$

- The GTs need to always satisfy box constraints of the form

$$P^c_{GT,min}(t) \leq P_{GT}(t) \leq P_{GT,max},\ c = 1 \div C \quad (3.6)$$

- the platform power demand $P^s_L(t)$ demand needs to be always met;
- the dynamics of the BESS shall be respected. Relative to this, we model the energy levels for the BESS as

$$E^s_{bat}(t) = E^c_{bat,0} + \sum_{i=1}^{t} P^s_{bat}(i),\ t = 1 \div 24, s = 1 \div N, c = 1 \div C \quad (3.7)$$

where $E^{s}_{bat}(t)$ is the remaining energy capacity of the BESS at any instant t, for every scenario s and $E^{case}_{bat,0}$ is the initial energy capacity of the BESS for every case examined, the latter calculated from a selected initial SoC_0 as

$$E^{case}_{bat,0} = SoC^{case}_{0} \cdot \hat{E}_{bat} \tag{3.8}$$

- the energy capacity and the power exchanges of the BESS need also to be box constrained, i.e.,

$$0 \leq E^{s}_{bat}(t) \leq \hat{E}_{bat}, |P^{s}_{bat}(t)| \leq \hat{P}_{bat}, \; t = 1 \div 24, s = 1 \div N \tag{3.9}$$

- finally, a cycling behavior of the storage system shall be enforced. For this we use the common constraint such that the initial SoC shall be equal to the final one, i.e.,

$$\sum_{i=1}^{24} P^{s}_{bat}(i) = 0, \;\; s = 1 \div N \tag{3.10}$$

Importantly, this implies that the initial state of charge SoC_0 becomes a decision variable that may affect the final results on the design variables $\hat{E}_{bat} \geq 0$ and $\hat{P}_{bat} \geq 0$. This issue will be discussed in detail in Section 3.3. The cost function to be minimized for this approach is

$$J = \frac{1}{N} \sum_{s=1}^{N} \sum_{t=1}^{24} C_f P^{s}_{GT}(t) \cdot \delta t + C_p \cdot \hat{P}_B + C_E \cdot \hat{E}_B \tag{3.11}$$

3.3 QUANTITIVE RESULTS AND DISCUSSION

The optimization problem described in the previous section was used to study the impact of the different system parameters, in particular: 1) the technical minimum (TM) associated to the GTs on the O&G platform operation, 2) the size and number of available GTs and 3) the initial state of charge of the BESS. As for the first parameter, TMs indicate the lowest operation level for the GTs: going under this minimum limit should be avoided due to increased mechanical wear [20], in addition to the inability to supply the heat demand, if any. As for the last parameter, we note that most of the studies reported in literature that consider a scenario-based approach for optimization (such as in our case) and that rely on assumption 3.10 do not provide deep investigations on the impact of its initial numeric value on the final results. However, our ansatz is that SoC_0 is a sensitive quantity that shall be investigated in details, because of the following intuition: the constraint (3.10) limits the cycling behaviors that the BESS may follow; different values of the SoC may lead to dramatically different strategies of how to charge and discharge the batteries (e.g., assume that all the scenarios start with high wind conditions and low platform power requirements; starting then fully charged is likely to be worse than starting fully discharged). For this we simulate and

compare two basic scenarios, one with a lower wind power penetration (WP=50%) and one with a high one (WP=100%), a strategy that enables to examine the effects of increasing wind power integration levels. In particular, the parameter SoC_0 is varied along five equally spaced discrete values that range from initially empty ($SoC_0 = 0\%$) to initially full ($SoC_0 = 100\%$). As for the GTs, we assume that there may be either one or two GTs in operation (i.e., $N_{GT} = 1$, or $N_{GT} = 2$, respectively). Note that the second approach is common in offshore O&G platforms, as having two generators increases the system reliability and the possibility of serving critical loads even during emergencies. This reliability need is however diminished when integrating BESSs, since the platform may rely on the BESS remaining capacity for emergency power provision while operating with just one GT. Finally, we specify that the proposed configuration (with the BESS) is compared against the base case where wind power is integrated in the platform, but no storage is included. Consequently, when we refer to the term CO2 "reduction", we imply that an additional CO2 reduction (compared to the case of wind integration) is achieved by introducing the BESS to the platform (when this is instructed form the optimization results) for any WP level, and when we refer to "Daily Benefit" we imply that the daily operational cost of the proposed system (including BESS) is already smaller compared to the one without the BESS. The same concept applies also to the term "Dumped energy reduction". The results can qualitatively be summarized through the following series of considerations: 1) Increasing the wind penetration rate typically implies smaller BESS, when 2 GTs are operating. This is consistent with the intuition that, given that the load of the platform to be covered is limited, with a simultaneous large base load coverage from the 2 GTs, and given that in our formulation dumping excess power is not penalized, then the more wind power is available the less there is the need to store it. Therefore, it can be preferably dumped at no cost (Figure 3.3). The opposite case is valid when we operate just with 1 GT and thus reduced operating costs. Then a bigger BESS could be promoted despite its increasing investment cost, because the operating cost is already reduced by using 1 GT. (Figure 3.4) 2) Increasing the number of GTs or their

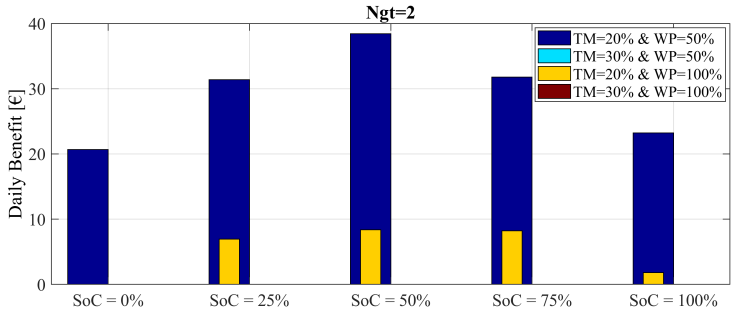

Figure 3.3. Expected daily benefit for the cases examined with two GTs in operation

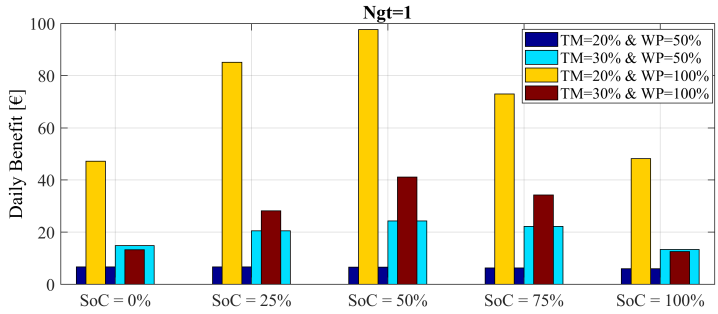

FIGURE 3.4. Expected daily benefit for the cases examined with one GT in operation

TM (that, in practice, corresponds to increase the minimum guaranteed load supplied by the GTs) is, from a BESS sizing point of view, equivalent to having higher wind penetration rate. This means that when the wind farm connected to the O&G platform and/or the GT generated power is sufficiently large, then implementing a BESS is not economically meaningful. This is depicted in Figure 3.5 and Figure 3.6 where for both cases of WP level we do not get a BESS size for the case of increased number of GTs and *TM* ($N_{GT} = 2$ & *TM*=30%). Especially from Figure 3.6 it is possible to observe that we do not get a BESS size even for the case with 2 GTs and lower *TM* (*TM*=20%) when we start at zero initial state of charge, while for the remaining values we get a result. This can be interpreted as follows: based on our dataset, it is better to start with some initial energy because the system should be able to discharge power before charging, most of the times. On top of that, the higher the wind penetration, the larger the maximum possible expected daily CO2 and dump energy reduction are, with respect to the different cases considered for each WP level. As both variables are directly linked to the fuel consumption of the GT and, hence, to the operational cost, they also follow similar trends as the ones expressed in terms of the "Daily Benefit" variable, as depicted in Figure 3.5 and Figure 3.6. 3) The more balanced the initial

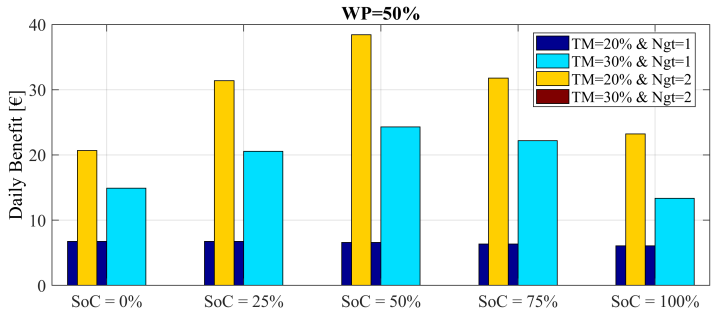

FIGURE 3.5. Expected daily benefit for the cases examined with lower WP

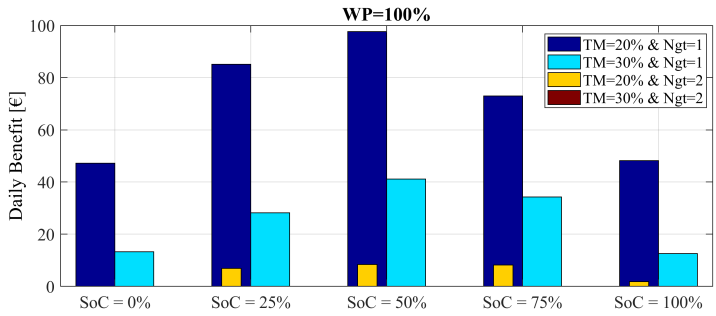

FIGURE 3.6. Expected daily benefit for the cases examined with higher WP

SoC for the BESS is (i.e., more towards 50% than 0% or 100%), the larger the capacity of the sized BESS becomes and - at the same time - the better economic benefits can be obtained (Figure 3.3 to Figure 3.6). Our intuitive explanation, driven by inspecting the temporal evolution of the SoC during the various daily scenarios, is that the more the BESS can follow positive and negative swings (i.e., can both charge and discharge by serving the simultaneous variations of the platform's load and wind power production) the better economic benefits one gets. The computed power rating of the BESS seems instead almost insensitive to changes in the initial SoC parameter. The reason may be that the platform load and wind power production have fixed maximum ramps amplitudes. Since the load following capabilities are provided by the BESS and the GTs simultaneously, the minimum BESS power rate parameter is more dependent on the GTs power rate rather than the BESS initial SoC. 4) The costlier the BESS is (both in terms of investment and deployment) with respect to the fuel for the GTs, the smaller the final sized BESS becomes. This is intuitive, and as expected. Moreover, the bigger the BESS, the less the overall system will dump energy and the higher the possible CO2 reduction is - again, as expected. Concluding (and summarizing the intuitions above), if one desires to dump less energy, then the best option seems to have more wind capacity, a larger battery storage, use initial SoC levels around 50%, and decrease the usage of the GTs by either reducing their size and/or (if technically possible) their TM. Considering that typically the GTs in an O&G platform are two, due to redundancy reasons, the main conclusion that can be extracted by all the intuitions above is that for the considered platform, and looking only from an electrical energy perspective, there exist combinations of wind capacity and GTs sizing for which may it be economically meaningful to substitute one of the GTs with a BESS. The numeric results of the capacity and power rating sizing are summarized in Table 3.2 and Table 3.3.

Table 3.2. BESS sizing results for WP=50%

	WP=50%							
	Ngt=1				Ngt=2			
	TM=20%		*TM=30%*		*TM=20%*		*TM=30%*	
SoC	**P** *[MW]*	**E** *[MWh]*	**P** *[MW]*	**E** *[MWh]*	**P** *[MW]*	**E** *[MWh]*	**P** *[MW]*	**E** *[MWh]*
0	0.193	0.272	0.193	0.579	0.259	0.773	-	-
0.25	0.193	0.272	0.212	0.799	0.357	1.155	-	-
0.50	0.193	0.272	0.261	0.930	0.374	1.444	-	-
0.75	0.193	0.271	0.262	0.845	0.375	1.164	-	-
1	0.193	0.271	0.193	0.498	0.308	0.853	-	-

Table 3.3. BESS sizing results for WP=100%

	WP=100%							
	Ngt=1				Ngt=2			
	TM=20%		*TM=30%*		*TM=20%*		*TM=30%*	
SoC	**P** *[MW]*	**E** *[MWh]*	**P** *[MW]*	**E** *[MWh]*	**P** *[MW]*	**E** *[MWh]*	**P** *[MW]*	**E** *[MWh]*
0	0.576	1.727	0.207	0.507	-	-	-	-
0.25	0.874	3.217	0.361	1.084	0.102	0.272	-	-
0.50	0.925	3.701	0.451	1.619	0.110	0.329	-	-
0.75	0.833	2.698	0.359	1.372	0.109	0.327	-	-
1	0.627	1.808	0.164	0.493	0.034	0.067	-	-

3.4 Conclusions

This paper stems from the trend for which wind power and other renewable energy sources will eventually be integrated into offshore O&G platforms, with the objective of reducing their environmental impact. Implementing an energy system that is based on non-dispatchable RESs, in its turn, may benefit from integrating a storage system. This study considered thus the problem of sizing and integrating BESSs into such RESs-oriented platforms (in our numerical case study, a wind-based one). The sizing problem was cast and solved in terms of optimizing a linear objective function that

Table 3.4. CO2 and Dump Energy Reduction Results for WP=50%

	WP=50%							
	Ngt=1				Ngt=2			
	TM=20%		*TM=30%*		*TM=20%*		*TM=30%*	
SoC	CO_2 *[kg]*	E_{dump} *[MWh]*	CO_2 *[kg]*	E_{dump} *[MWh]*	CO_2 *[kg]*	E_{dump} *[MWh]*	CO_2 *[kg]*	E_{dump} *[MWh]*
0	29.6	0.068	65.2	0.150	90.5	0.207	-	-
0.25	29.6	0.068	89.9	0.206	137.4	0.315	-	-
0.50	28.8	0.066	106.3	0.244	168.1	0.385	-	-
0.75	27.7	0.064	97.0	0.223	139.2	0.319	-	-
1	26.6	0.061	58.4	0.134	101.6	0.233	-	-

Table 3.5. CO2 and dump energy reduction results for WP=100%

	WP=100%							
	Ngt=1				Ngt=2			
	TM=20%		*TM=30%*		*TM=20%*		*TM=30%*	
SoC	CO_2 *[kg]*	E_{dump} *[MWh]*	CO_2 *[kg]*	E_{dump} *[MWh]*	CO_2 *[kg]*	E_{dump} *[MWh]*	CO_2 *[kg]*	E_{dump} *[MWh]*
0	206.7	0.474	58.0	0.133	-	-	-	-
0.25	372.7	0.854	123.6	0.283	30.3	0.069	-	-
0.50	427.3	0.979	180.0	0.413	36.7	0.084	-	-
0.75	319.6	0.732	150.2	0.344	36.0	0.083	-	-
1	211.2	0.483	54.8	0.126	7.9	0.018	-	-

weights costs and benefits of both operations and investments. More precisely, as for the operation costs we considered that the platform-wide power system needs to provide both electrical and thermal power, and remains always in power balance (i.e., we imposed the platform's gas turbines (GTs) and BESS to serve the load following needs, and considered that the RESs shall typically respect the minimum power production levels due to efficiency, maintenance reasons and possible heat supply needs). In the formulation, moreover, dumping excess power is not penalized. The performed numerical simulations investigated the dependency of the plant's operational cost to the storage system size, and how these sizing solutions depend on the multiple variables that define the problem, i.e., the wind power penetration rate, the number of the GTs and the technical minimum of them. Two main conclusions can be drawn from our quantitative results: first, with the used parameters (that, incidentally, are in line with current techno-economic evaluations of typical O&G platform systems) it results that implementing a BESS for a platform connected with an existing wind farm is often economically meaningful in terms of reducing operational cost. Moreover, increasing the wind power penetration by 100% (i.e., from WP=50% to WP=100%) leads to 156.3% bigger BESS and a 154.2% decrease of the fuel consumption, which is in turn translated in correspondingly reduced CO2 emissions, dumped energy and increased mean daily benefits. The results moreover suggest an interesting possibility: in platforms that are connected to opportunely big wind farms, instead of using two GTs to serve the electrical loads it may be economically meaningful to consider a configuration with a single operating GT and a BESS.

3.5 References

[1] L. F. . T. C. . J. S. . K. Marcell, "Beyond the cycle," CDP Investor Research Team, Tech. Rep., Nov. 2018. Cited on page/s 57.

[2] N. M. of Petroleum and Energy, "Norway's oil and gas technology strategy for the 21st century-strategy document," OG21, techreport, 2016. [Online]. Available: https://www.og21.no/en/strategy-and-analyses/the-og21-strategy/ Cited on page/s 58.

[3] M. G. Abidi, M. B. Smida, M. Khalgui, Z. Li, and N. Wu, "Multi-agent oriented solution for forecasting-based control strategy with load priority of microgrids in an island mode – case study: Tunisian petroleum platform," *Electric Power Systems Research*, vol. 152, pp. 411 – 423,

2017. [Online]. Available: http://www.sciencedirect.com/science/article/pii/S0378779617302985 Cited on page/s 58.

[4] WindEurope, "Wind in power 2017: Annual combined onshore and offshore wind energy statistics," WindEurope, Tech. Rep., 2018. Cited on page/s 58.

[5] Equinor. (2018, Aug.) Wind farm being considered at snorre and gullfaks. Press Release. [Online]. Available: https://www.equinor.com/en/news/27aug2018-hywind-tampen.html Cited on page/s 58.

[6] A. Zhang, H. Zhang, M. Qadrdan, W. Yang, X. Jin, and J. Wu, "Optimal planning of integrated energy systems for offshore oil extraction and processing platforms," *Energies*, vol. 12, no. 4, 2019. [Online]. Available: https://www.mdpi.com/1996-1073/12/4/756 Cited on page/s 58.

[7] S. Sanchez, E. Tedeschi, J. Silva, M. Jafar, and A. Marichalar, "Smart load management of water injection systems in offshore oil and gas platforms integrating wind power," *IET Renewable Power Generation*, vol. 11, no. 9, pp. 1153–1162, 2017. Cited on page/s 58.

[8] M. Sedghi, A. Ahmadian, and M. Aliakbar-Golkar, "Optimal storage planning in active distribution network considering uncertainty of wind power distributed generation," *Transactions on Power Systems*, vol. 31, no. 1, pp. 304–316, Jan 2016. Cited on page/s 58.

[9] A. Ahmadian, M. Sedghi, M. Aliakbar-Golkar, A. Elkamel, and M. Fowler, "Optimal probabilistic based storage planning in tap-changer equipped distribution network including pevs, capacitor banks and wdgs: A case study for iran," *Energy*, vol. 112, pp. 984 – 997, 2016. [Online]. Available: http://www.sciencedirect.com/science/article/pii/S0360544216309069 Cited on page/s 58.

[10] I. Staffell and S. Pfenninger, "Using bias-corrected reanalysis to simulate current and future wind power output," *Energy*, vol. 114, pp. 1224 – 1239, 2016. [Online]. Available: http://www.sciencedirect.com/science/article/pii/S0360544216311811 Cited on page/s 59.

[11] Equinor. (2018, Feb.) World class performance by world's first floating wind farm. Press Release. Equinor. [Online]. Available: https://www.equinor.com/en/news/15feb2018-world-class-performance.html Cited on page/s 59.

[12] R. Chokhawala, "Powering platforms: Connecting oil and gas platforms to mainland power grids," ABB, techreport, 2008. Cited on page/s 60, 61.

[13] Norwegian-Petroleum. (2018) Emissions to air. Norwegian Ministry of Petroleum and Energy. [Online]. Available: https://www.norskpetroleum.no/en/environment-and-technology/emissions-to-air/ Cited on page/s 60, 61.

[14] J. P. Fossati, A. Galarza, A. Martín-Villate, and L. Fontán, "A method for optimal sizing energy storage systems for microgrids," *Renewable Energy*, vol. 77, pp. 539 – 549, 2015. [Online]. Available: http://www.sciencedirect.com/science/article/pii/S0960148114008660 Cited on page/s 60.

[15] IRENA, "Electricity storage and renewables: Costs and markets to 2030," International Renewable Energy Agency, Abu Dhabi, Tech. Rep., Oct. 2017. Cited on page/s 60, 61.

[16] H. Chen, T. N. Cong, W. Yang, C. Tan, Y. Li, and Y. Ding, "Progress in electrical energy storage system: A critical review," *Progress in Natural Science*, vol. 19, no. 3, pp. 291 – 312, 2009. [Online]. Available: http://www.sciencedirect.com/science/article/pii/S100200710800381X Cited on page/s 60, 61.

[17] M. Wilshire, "Future trends in energy, bloomberg new energy finance," Wärtsilä Flexible Power Symposium, Portland, Aug. 2018, bloomberg BESS costs. [Online]. Available: https://about.bnef.com/blog/behind-scenes-take-lithium-ion-battery-prices/ Cited on page/s 61.

[18] J. Cervantes and F. Choobineh, "Optimal sizing of a nonutility-scale solar power system and its battery storage," *Applied Energy*, vol. 216, pp. 105 – 115, 2018. [Online]. Available: http://www.sciencedirect.com/science/article/pii/S0306261918301363 Cited on page/s 61.

[19] T. H. de Mello and G. Bayraksan, "Monte carlo sampling-based methods for stochastic optimization," *Surveys in Operations Research and Management Science*, vol. 19, no. 1, pp. 56 – 85, 2014. [Online]. Available: http://www.sciencedirect.com/science/article/pii/S1876735414000038 Cited on page/s 62.

[20] W. He, G. Jacobsen, T. Anderson, F. Olsen, T. D. Hanson, M. Korpås, T. Toftevaag, J. Eek, K. Uhlen, and E. Johansson, "The potential of integrating wind power with offshore oil and gas platforms," *Wind Engineering*, vol. 34, no. 2, pp. 125–137, 2010. [Online]. Available: https://doi.org/10.1260/0309-524X.34.2.125 Cited on page/s 63.

Chapter 4

Data-Informed Scenario Generation for Statistically Stable Energy Storage Sizing in Isolated Power Systems

Spyridon Chapaloglou[1,*], Damiano Varagnolo[2,5], Francesco Marra[3] and Elisabetta Tedeschi[1,4]

Published in: *Journal of Energy Storage* **51**, 104311 (2022).
DOI: 10.1016/j.est.2022.104311

Highlights

- *so* energy storage sizing methodology for isolated power systems
- Optimal uncertainty space exploration considering coupled uncertainty sources
- Minimum cardinality scenario subsets for statistically stable MILP sizing solutions
- Techno-economic investigation of battery system for wind-powered O&G platforms

[1]Department of Electric Power Engineering, Norwegian University of Science and Technology (NTNU), Trondheim, Norway. [2]Department of Engineering Cybernetics, Norwegian University of Science and Technology (NTNU), Trondheim, Norway. [3]Equinor R&T Electrical Technology Department, Arkitekt Ebbels 10, 7005, Trondheim, Norway. [4]Department of Industrial Engineering, University of Trento, Via Sommarive, 9, 38123 Povo, Italy. [5]Department of Information Engineering, University of Padova, Via 8 Febbraio 2, 35122 Padova, Italy. [#]e-mail: spyridon.chapaloglou@ntnu.no, damiano.varagnolo@ntnu.no, fmarr@equinor.com and elisabetta.tedeschi@ntnu.no

Abstract

We consider the problem of how to generate uncertainty scenarios to be used in energy storage sizing problems in isolated power systems. More precisely, we consider storage sizing formulations where both loads and generation are stochastic, where no closed form analytical expression is available, and where the presence of multiple discrete RVs makes the sizing problem mixed integer and with combinatorial search spaces. We thus propose and characterize a data-driven scenarios selection strategy that mitigates the computational issues associated with these types of storage sizing problem formulations while guaranteeing statically stable optimal solutions. Specifically, the approach works by first learning the distribution of the uncertainties of the loads and generation starting from field data, and then generating, through the learned distribution, an optimal set of uncertainty scenarios that are subsequently used in a two-stage SP reformulation of the original sizing problem. The workflow does not impose arbitrary structures to the correlation among the uncertainties, nor does it lump these in a single parameter; thus, it is suitable for systems with any load characteristics. Moreover, the approach ensures to reach a solution that is statistically close to the one that would be computed if the original problem was solvable and not computationally intractable. As a case study, we analyze the problem of designing an energy storage system for a wind powered O&G platform to minimize the expected daily system operational costs. Numerical simulations showed that the proposed methodology leads to higher quality solutions compared with other scenario selection strategies. This reveals realistic estimations of the expected benefits, while also highlighting the risk-management limitations, when solving the risk-constrained version of the problem.

4.1 Introduction

Modern power systems are characterized by high levels of uncertainty and operational complexity. This stems from the interaction of intermittent energy production from RESs with electricity consumption patterns. Under this perspective, and to achieve a more reliable, cost-effective and environmentally friendly operation, ESS are recognized as an essential component of future grids [1, 2] and are especially valuable for non-interconnected systems. However, determining the optimal size of an ESS when considering the expected future system operational patterns is not a trivial task [3–5]. This is because the problem should account not only for costs and other important limiting factors, but also for the fact that the uncertainties (especially load requirements and generation) are statistically distributed, and their distribution cannot be learned perfectly.

A potential strategy to deal with the presence of such uncertainties is to employ stochastic optimization formulations [6, 7]. When integrating uncertainty into the storage sizing problem by assuming parametric distributions [6, 8], there exist inherent limitations on how well the available data can be described and generalized. On the

contrary, data-based methods have shown the ability to better generalize and replicate more complex patterns found in historical datasets [9]. Energy storage sizing problems that consider the expected daily system operation are often formulated as two-stage MILP problems where day-ahead UC and/or ED are determined over a scenario set that includes uncertainty realizations [9–11]. These approaches are indeed inherently less conservative than worst-case alternatives [12]. However, they often lead to problem formulations that are computationally intractable [13] because the cost to be optimized should consider all the scenarios that have been observed in the past. In other words, assuming for example we have a dataset comprising years of measured loads and disturbances. Here, such formulations would naturally embed all the scenarios, leading to a computationally intractable combinatorial problem. However, in cases where the resulting problems are linear, (LPs) [14] such issues do not exist and one is not typically constrained by computational tractability.

To mitigate this issue, one potential approach is reducing the number of scenarios to be considered in the stochastic optimization formulation [11, 15]. However, the algorithm for selecting such alternative subsets of scenarios should lead to a final sizing solution that has low sensitivity to the considered subset. Otherwise, the quality of the final solution is intuitively of less value since it is arbitrated by the scenarios selection algorithm and not by the dataset itself (see also [16] for a more formal discussion of this point). For that reason, to guarantee the reliability of the final sizing, the scenarios selector should not only properly generate/select such scenarios, but also keep a sufficient number of them to minimize the inevitable information loss due to the scenarios sampling procedure [15, 17].

In the literature, one may thus find various ways of selecting scenarios subsets, e.g., [9, 11, 18–25]. Highlighting the main categories that most of these methods fall, we have *sg* by: random sampling of historical data, optimal *sr*, moments matching, and clustering to representative patterns [9, 11, 25]. As another example, [17] proposed the scenario map method as an alternative *sr* technique that considers RES and load uncertainty through the system net load. However, net load data do not capture the whole uncertainty space since they represent a conditional slice of it, especially when the underlying individual uncertain profiles present high variance (such as in isolated industrial power systems with wind power). In addition, specific correlation values between RES and load were imposed in [26–28] and Cholesky decomposition was then used to model dependent profiles, as commonly done in several studies. To the best of our knowledge, all available literature reports that when dealing simultaneously with both RES and load uncertainties, these factors are either lumped together in a single parameter before using some scenarios reduction method (namely the net-load as in [29, 30]), or the proposed approach imposes some specific structure to the correlation among the uncertainties. However, the validity of such assumptions is debatable, as they depend on the specific power system application. Those assumptions typically rely on conclusions from specific analyses [31] which *i)* targeted large interconnected power systems (implying that such scenarios selection strategies are not suitable for

the specific case of isolated power systems with non-standard load patterns) and *ii)* are not guaranteed to be time-invariant. In fact [32] showed that, for wind energy, the observed correlation levels are much lower than the ones observed between load and solar energy, due to its less consistent and predictable behavior.

As mentioned although it is possible to generate high quality profiles for individual uncertain parameters (i.e., RES or load individually), most of the state-of-the-art *so* formulations for the sizing problem do not effectively explore the whole space of combined uncertainties and often do not investigate how big this exploration should be to ensure that the final computed size is statistically close to what one would get by solving the original problem, including all possible scenarios from the available datasets.

As such, to the best of our knowledge, there is currently no literature that addresses, in a general way, how to select and combine RES and load profiles (and their associated uncertainties) over each other from a dataset that is too large to be used in its entirety, which is typical for two-stage MILP sizing formulations.

4.1.1 Contributions

This paper proposes a methodology for performing this selection that considers different rearrangements of profiles from the reduced subsets (samples) as conditional draws (instances) of the total uncertainty space (population). Therefore, the proposed approach intuitively aims to perform more accurate modelling/exploration of the combined uncertainty space than the approaches existing in the literature. This will make the sizing solution statistically closer to what would be computed (if we had the computational capability) with the whole dataset.

In summary, we propose an integrated methodology that can be applied to ESS sizing problems under *so* frameworks, and that generates subsets of scenarios that intrinsically consider the relationship between the optimization problem and the input data. The novelty of the approach is that it generates minimum-cardinality subsets that implicitly account for the effect of coupling load and RES uncertainties through opportune statistical evaluations of the solutions to the original optimization problem. In addition, the entire methodology is purely data-driven, and it avoids any strong assumptions on the individual uncertainties and their coupling. The proposed methodology is compared against other scenario subset generation methods, demonstrating its superiority to achieve preferable statistical properties for the obtained optimization solutions. As a test case study, we address the sizing of a techno-economically feasible ESS for an isolated offshore O&G platform, that includes onsite power generation from GTs and integrates wind power.

The remainder of the paper is organized as follows: Section 4.2 formulates the optimization problem, Section 4.3 describes the proposed *sg* methodology, and Section 4.4 presents the numerical results and an investigation of which effects the worst-case scenarios included in the reduced subset have on the solutions. Finally, Section 4.5

presents an overall summary and concluding remarks.

4.2 BESS SIZING OPTIMIZATION PROBLEM

This section formulates the BESS sizing problem as a SP that integrates considerations on risks by introducing a risk-aversion user-defined parameter. The following subsections introduce the quantities needed to arrive at the formulation that is summarized at the end of the section.

4.2.1 Objective function and cost modelling

Let in general $\boldsymbol{x}$ be the first-stage decision variables expressing the BESS size in terms of power and capacity rating with cost $\boldsymbol{c}$, $\boldsymbol{y}$ the second-stage optimal decision about how to operate a plant with cost $\boldsymbol{q}$, and $\tilde{\boldsymbol{\xi}}$ the stochastic process variables introducing uncertainty into the parameters of the problem. Note that we explicitly consider two types of uncertainty: $\tilde{\boldsymbol{\xi}}^{\ell}$ to model randomness in the platform's load, and $\tilde{\boldsymbol{\xi}}^{w}$ to model randomness in the wind speed at the specified offshore location. Notation-wide, we let $\tilde{\boldsymbol{\xi}} = \begin{bmatrix} \tilde{\boldsymbol{\xi}}^{\ell} & \tilde{\boldsymbol{\xi}}^{w} \end{bmatrix}^T$. Given this notation, the BESS *so* sizing can be initially phrased as

$$\begin{aligned} \text{SP:} \quad & \min_{\boldsymbol{x}} \{\mathbb{E}[f(\boldsymbol{x}; \tilde{\boldsymbol{\xi}})]\} \\ \text{where,} \quad & f(\boldsymbol{x}; \tilde{\boldsymbol{\xi}}) = \boldsymbol{c}^T \boldsymbol{x} + \min_{\boldsymbol{y}} \{\boldsymbol{q}^T \boldsymbol{y}\} \\ \text{s.t.} \quad & \boldsymbol{A}\boldsymbol{x} + \boldsymbol{B}\boldsymbol{y} + \boldsymbol{C}\tilde{\boldsymbol{\xi}} \leq \boldsymbol{0}. \end{aligned} \tag{4.1}$$

Note this formulation includes all the randomness related to the stochastic process variables, leading to coupled constraints through data matrices $\boldsymbol{A}, \boldsymbol{B}, \boldsymbol{C}$.

This problem can be formulated as a MILP by deriving the deterministic equivalent of (4.1) and discretizing the continuous stochastic process $\tilde{\boldsymbol{\xi}}$ over a set Ω containing all the possible realizations of the uncertain parameters (scenarios). The discretized process is denoted as $\widehat{\boldsymbol{\xi}}$. Through this, thus, we can derive the MILP

$$\begin{aligned} \text{SP:} \quad & \min_{\boldsymbol{x}, \boldsymbol{y}(\omega)} \{\boldsymbol{c}^T \boldsymbol{x} + \sum_{\omega \in \Omega} \pi_{\omega} \, \boldsymbol{q}^T(\omega) \boldsymbol{y}(\omega)\} \text{ where,} \\ & \boldsymbol{q}^T \boldsymbol{y}(\omega) = \sum_{g \in N_G} \sum_{t \in T} C_{GT} P^{g}_{GT,t,\omega} + C^{on}_{GT} u^{g}_{t,\omega} + C^{start}_{GT} z^{g}_{t,\omega} \\ \text{s.t.} \quad & \boldsymbol{A}(\omega)\boldsymbol{x} + \boldsymbol{B}(\omega)\boldsymbol{y}(\omega) + \boldsymbol{H}(\omega)\widehat{\boldsymbol{\xi}}(\omega) \leq \boldsymbol{0}, \ \forall \, \omega \in \Omega \, . \end{aligned} \tag{4.2}$$

Note then that the structure of (4.2) is such that the first stage investment cost for the BESS decision (i.e., $\boldsymbol{c}^T \boldsymbol{x}$) can be divided into distinct capacity-related ($C_{B,E}$) and power-related ($C_{B,P}$) components. Moreover, the investment is amortized into a daily basis through CRF [33] as

$$\boldsymbol{c}^T \boldsymbol{x} = \frac{r \cdot (1+r)^p}{(1+r)^p - 1} \begin{bmatrix} C_{B,P} & C_{B,E} \end{bmatrix} \begin{bmatrix} P_B \\ E_B \end{bmatrix} \tag{4.3}$$

where r is the daily interest rate (derivable from an annual interest rate), p is the recouping period ($p = 365L$), L is the investment lifetime, and P_B and E_B are the BESS power rating and capacity, respectively. At this point we highlight that even though an accurate and case specific description of the BESS aging mechanism is out of scope of the paper, this is reflected through the selection of the BESS investment lifetime L which is implicitly linked with the storage lifetime expectancy. To account for this dependency, an overall reserved/pessimistic L value was considered (see Section 4.6), thus penalizing the BESS (a priori) sizing decision to gain a safety margin for its actual (a posteriori) cycling degradation. The second stage decision $\boldsymbol{q}^T(\omega)\boldsymbol{y}(\omega)$ relates to the operation of the platform's GTs for each scenario ω (whose occurrence probability is assumed to be π_ω). Each scenario represents a daily system operation (i.e., a 24 hour optimization horizon), as commonly adopted by system operators for solving the UC and ED problems for the day-ahead scheduling [1, 5, 6, 23, 34]. The second stage control variables $\boldsymbol{y}(\omega)$ and corresponding costs $\boldsymbol{q}^T(\omega)$ are given as

$$
\begin{aligned}
\boldsymbol{y}(\omega) &= \left[\boldsymbol{P}_{B,\omega}\ \boldsymbol{P}^g_{GT,\omega}\ \boldsymbol{u}^g_\omega\ \boldsymbol{z}^g_\omega\ \boldsymbol{P}_{D,\omega}\right]^T \quad \forall\, \omega \in \Omega \\
\boldsymbol{q}^T(\omega) &= \left[\mathbf{0}\ \mathbf{C_{GT}}\ \mathbf{C^{on}_{GT}}\ \mathbf{C^{start}_{GT}}\ \mathbf{0}\right] \quad \forall\, \omega \in \Omega \ \text{ where,} \\
\mathbf{C_{GT}} &= \left\{\left(\frac{C_{NG}}{\rho} + \mu C_{CO_2}\right)\alpha_g + C_{O\&M}\right\}_{t\in T} \\
\mathbf{C^{on}_{GT}} &= \left\{\left(\frac{C_{NG}}{\rho} + \mu C_{CO_2}\right)\beta_g\right\}_{t\in T}, \\
\mathbf{C^{start}_{GT}} &= \left\{C^{start}_{GT}\right\}_{t\in T}
\end{aligned}
\tag{4.4}
$$

where $\boldsymbol{P}_{B,\omega}$ and $\boldsymbol{P}_{D,\omega}$ are the BESS and (controllable) dump power vectors respectively; $\boldsymbol{P}^g_{GT,\omega}$, $\boldsymbol{u}^g_\omega$, $\boldsymbol{z}^g_\omega$, are the GT power, ON/OFF status and startup indicator variables for each generator g and all time periods T respectively; μ is the ideal combustion coefficient of natural gas (NG) to CO_2; C_{NG} is the fuel (NG) sale value per normal cubic meter; ρ is the NG density at standard temperature and pressure conditions; C_{CO_2} is the CO_2 tax per kg of released CO_2; $C_{O\&M}$ is the estimated operation and maintenance (O&M) costs per generated kWh; C^{start}_{GT} is the estimated startup cost of a generator per event; and α_g and β_g are the estimated regression parameters of the fitted model to data explaining fuel consumption ($\dot{m}_f$) as a function of the GT loading (P_{GT}), approximated with the commonly used affine map $\dot{m}_f = \alpha_g \cdot P_{GT} + \beta_g$.

To complete the formulation of the optimization problem, we then proceed with describing its constraints.

4.2.2 *Energy system operation constraints*

The daily system operation (i.e., for a 24-hour optimization horizon) can be explicitly considered in the optimization problem (4.2) by constraining the feasible solution space. From a methodological perspective, these constraints can be derived from

modelling the operation of each sub-component, for a given scenario tree Ω, as shown in the following.

The GT operation is represented through the following set of equations, where

$$u^g_{t,\omega}\gamma\overline{P}^g_{GT} \leq P^g_{GT,t,\omega} \leq u^g_{t,\omega}\overline{P}^g_{GT}, \quad \forall\, t \in T,\ g \in N_G,\ \omega \in \Omega \tag{4.5}$$

is the box constraint for the GT power, $\overline{P}^g_{GT}$ is the maximum operation capacity of each GT, and γ is the allowed minimum technical operational ratio. To model the realistic case of an offshore O&G platform, we consider the presence of four identical GTs with the same maximum rating and the same technical minimum γ set to be 20%. The GT power ramping constraint was described as

$$\left|P^g_{GT,t,\omega} - P^g_{GT,t-1,\omega}\right| \leq R,\ \forall\, t \in T,\ g \in N_G,\ \omega \in \Omega \tag{4.6}$$

where R is the allowed ramping rate of the GT. Recalling that this study considers an hourly discretization of the time series, we set R as $\overline{P}_{GT}$ for all four generators. The minimum required time to start-up a GT after a shut down is modeled as

$$\begin{gathered} u^g_{GT,t-1,\omega} - u^g_{GT,t,\omega} \leq 1 - u^g_{GT,k,\omega}, \quad \forall\, t \in T,\ g \in N_G,\ \omega \in \Omega, \\ k = \{t+1, \ldots, \min(t + T_{off} - 1, T)\} \end{gathered} \tag{4.7}$$

where T_{off} is the minimum GT off-time after a shutdown (here set to 4 hours, to the best of our knowledge a value representing typical field setups). The startup events of the GTs are modelled as

$$u^g_{GT,t,\omega} - u^g_{GT,t-1,\omega} \leq z^g_{GT,t,\omega}, \quad \forall\, t \in T,\ g \in N_G,\ \omega \in \Omega \tag{4.8}$$

The BESS inter-temporal and cycling constraints are instead modeled as

$$E_{B,t,\omega} = E_{B,0} + \sum_{k=1}^{t} P_{B,k,\omega},\ \forall\, t \in T,\ \omega \in \Omega \tag{4.9}$$

$$0 \leq E_{B,t,\omega} \leq E_B, \quad |P_{B,t,\omega}| \leq\ P_B\ \forall\, t \in T,\ \omega \in \Omega \tag{4.10}$$

$$\sum_{t \in T} P_{B,t,\omega} = 0,\ \forall\, \omega \in \Omega \tag{4.11}$$

where $E_{B,t,\omega}$ is the remaining energy capacity of the BESS at any instant t, for every scenario ω. Moreover, $E_{B,0,\omega} = 0$ shall be considered as the initial capacity of the BESS for every scenario ω. This condition combined with eq. (4.11) enforces a specific cycling behavior to the BESS, removing the dependency of consecutive days of operation on the initial *SoC* at each day, represented as scenario ω. We note that the demonstration of the methodology proposed in the paper considers a rather simplistic (although general) energy storage model, since a detailed technology-dependent and

case-specific description of degradation mechanisms is out of scope of the paper. The goal of this manuscript is indeed to propose a general framework to solve the ESS sizing problem under system-wise uncertainties (i.e., load and RES), independently of the ESS technology itself or the considered power system operation. However, any arbitrary ESS aging/degradation mechanism may be included into the optimization problem formulation, as long as it is formulated as a MILP, without impacting the proposed methodology. The wind power generation is then modeled after the basic power curve of the reference case wind turbines, i.e., as

$$W\left(\widehat{\xi}_t^w(\omega)\right) = \begin{cases} 0, & \widehat{\xi}_t^w(\omega) \leq w_{ci} \\ N_w P_w^n \left(\frac{\widehat{\xi}_t^w(\omega)}{w_n}\right)^3, & w_{ci} \leq \widehat{\xi}_t^w(\omega) \leq w_n \\ N_w P_w^n, & w_n \leq \widehat{\xi}_t^w(\omega) < w_{co} \\ 0, & w_{co} \leq \widehat{\xi}_t^w(\omega) \end{cases} \quad \forall\, t \in T,\ \omega \in \Omega \tag{4.12}$$

where w_{ci} is the cut-in wind speed; w_n is the nominal wind speed; w_{co} is the cut-off wind speed; P_w^n is the nominal power of each wind turbine; and N_w is the number of wind turbines in the considered wind farm. Finally, the sub-components interaction is modelled through the power balance equation as

$$\sum_{g\,\in\, N_G} P_{GT,t,\omega}^g + P_{B,t,\omega} - P_{D,t,\omega} = \widehat{\xi}_t^{\ell}(\omega) - W\left(\widehat{\xi}_t^w(\omega)\right) \quad \forall\, t \in T,\ \omega \in \Omega \tag{4.13}$$

4.2.3 Risk-management formulation

So far, the formulation of problem (4.1) allows for minimizing the cost under a specific probabilistic disturbance model. However, it does not inherently consider the effects of extreme disturbances [35]. To account for these, we follow the common strategy, e.g., see [36], of penalizing these extreme realizations using the Conditional Value-at-Risk (CVaR) risk measure [10, 26, 34, 37]. In practice, this means that CVaR represents the expected value of the cost for the $1-\alpha$ percentage of worst scenarios. In other words, given an α-quantile, the random cost variable $f\left(\boldsymbol{x};\tilde{\boldsymbol{\xi}}\right)$ from SP (4.1), and a decision $\boldsymbol{x}$, the $CVaR$ can be calculated after [37] as

$$CVaR_\alpha(\boldsymbol{x}) = \mathbb{E}_{\tilde{\boldsymbol{\xi}}}\left[f(\boldsymbol{x}) \middle| f(\boldsymbol{x}) \geq VaR_\alpha(\boldsymbol{x})\right]. \tag{4.14}$$

Note that, as soon as the distribution of the RV is known, eq. (4.14) can be efficiently computed by solving the linear program [37], i.e.,

$$\begin{aligned} CVaR_\alpha(\boldsymbol{x}) = \min_{\zeta,\ s(\omega)\in\mathbb{R}_{\geq 0}} & \left\{\zeta + \frac{1}{1-\alpha}\cdot\sum_{\omega\in\Omega}\pi_\omega s(\omega)\right\} \\ \text{s.t.}\ \ & f(\boldsymbol{x};\widehat{\boldsymbol{\xi}}(\omega)) - \zeta \leq s(\omega),\ \ \forall\,\omega\in\Omega\,. \end{aligned} \tag{4.15}$$

where $s(\omega)$ are scenario-dependent slack variables and ζ is a helper variable indicating the lowest value of the worst-cases costs. The structure of (4.15) implies that at the optimal point it holds that $\zeta^* = VaR_\alpha(\boldsymbol{x})$. Finally, the optimization problem (4.2) can integrate risk by introducing a risk-aversion control parameter β, and by reformulating the original problem as

$$\min_{\boldsymbol{x},\boldsymbol{y}(\omega),\zeta,s(\omega)} F\left(\boldsymbol{x};\widehat{\boldsymbol{\xi}}\right) \ , \text{ s.t. } eq.\,(4.12)-(4.13) \text{ and } (4.15)$$

where,

$$F\left(\boldsymbol{x};\widehat{\boldsymbol{\xi}}\right) = (1-\beta)\left(\boldsymbol{c}^T\boldsymbol{x} + \sum_{\omega\,\in\,\Omega} \pi_\omega\ \boldsymbol{q}^T(\omega)\boldsymbol{y}(\omega)\right) \tag{4.16}$$
$$+\beta\left(\zeta + \frac{1}{1-\alpha}\cdot\sum_{\omega\in\Omega}\pi_\omega s(\omega)\right)$$

We note once again that this formulation includes all the scenarios that may have been recorded from historical data. This means that for large datasets, this MILP is computationally unsolvable; consequently, an approach like the one proposed in this paper is needed that selects which scenarios should be included in the formulation in a statistically meaningful way.

4.3 METHODOLOGY

Our goal is to select a number of opportune scenarios that assist in solving a reduced version of eq. (4.16) such that the solution of the reduced problem is statistically close to the solution of the original (computationally intractable) one, leveraging an accurate representation of the annual behavior of the power system through samples of daily operation, with a computationally tractable MILP formulation. From an intuitive perspective, this requires selecting scenarios that are distributed within the uncertainty space in a way that captures the statistical properties of the potential scenarios that the plant may encounter. In this way, daily sampling profiles that effectively explore different possible conditions that could arise during the system operation are generated, and considered for the BESS sizing problem. Thus, this section proposes an algorithm that serves this selection purpose.

4.3.1 Accounting for Time Dependencies

To obtain accurate representations of uncertainties, we consider that the generated scenarios must reproduce the cyclostationarity of the historical field data. To infer these, one may consider a dataset $\{\xi^p\}_{i=1:N}$ composed of one-year long hourly *i)* aggregated load ($p = \ell$) time-series from an existing offshore platform (load at 50 MW power range) and *ii)* wind speed ($p = w$) time-series for the same location.

The first step of inferring the probability functions from such historical field data is to infer the structure of the marginal distributions, before inferring the joint ones.

Importantly, in our proposed methodology we make no assumptions on the parametric structure of the marginals of the physical variables ($p = \{\ell, w\}$), and rather infer it through a Kernel Density Estimation method [36, 38], i.e., independently compute non-parametric smooth representations of the time-dependent marginal empirical distributions of load and wind speed as

$$\widehat{F}^p_{h,t}(\tilde{\xi}^p_t) = \frac{1}{N h_p} \sum_{i=1}^{N} \frac{1}{\sqrt{2\pi}} e^{-\frac{\left(\tilde{\xi}_t - \xi^p_i\right)^2}{2h_p^2}} \quad \forall\, t \in T. \tag{4.17}$$

To capture the statistical dependency of the load or wind process along its temporal dimension, we then propose to use a copula-based approach, i.e., express the joint distribution of the load or wind vector as an opportune combination of the marginals at the various times t and a copula function for $p = \{\ell, w\}$, so that the joint distribution becomes, consistent with Sklar's theorem,

$$F^p\left(\tilde{\boldsymbol{\xi}}^p\right) = C^p\left(F^p_{h,1}\left(\tilde{\xi}^p_1\right), \cdots, F^p_{h,T}\left(\tilde{\xi}^p_T\right)\right). \tag{4.18}$$

Assuming then a Gaussian copula for C^p, known to have the potential of adequately modelling temporal dependencies [22], leads to the possibility of using MLE inference to estimate such temporal correlations.

We then propose to leverage copula-based approaches to generate independent profiles from F^p. Specifically, considering that $u^p_t = \widehat{F}^p_{h,t} \sim unif\,[0,1]$, plus using *MC* sampling and probability inverse transforms (PIT), we propose the generation steps to be:

i. a sampling as $\boldsymbol{z} \sim N\left(0, \widehat{\rho}^p_{ML}\right)$,

ii. a unit cube transformation as $\tilde{u}^p_t = \Phi\left(z_t\right), \quad \forall\, t \in T$,

iii. an inverse transformation as $\tilde{\xi}^p_t = \widehat{F}^{p^{-1}}_{h,t}(\tilde{u}^p_t), \quad \forall\, t \in T$.

Here, Φ is the CDF of a standard normal and N is a $\mathcal{MVN}$. Following the proposed procedure, one can generate sample sets Ω containing representative profiles $\tilde{\boldsymbol{\xi}}^p(\omega)$ where $\omega = 1 \ldots |\Omega|$. For $p = w$, the profiles can be directly transformed to wind power through eq. (4.12). After sampling 100 random profiles from F^ℓ and comparing them with the initial dataset (Figure 4.1), it is possible to observe that the sampled data reproduce the qualitative properties of the original dataset, effectively spanning the variation throughout annual system operation. We note that the corresponding learned distribution does not consider conditional effects, i.e., the plant conditions the day before, or the month of the year. Learning such effects may be performed effectively increasing the complexity of the model, at the cost though of requiring typically a bigger training set, to avoid risks of poorly fitting the parameters added to the model. Thus, the estimated F^p can be well approximated through a random sampling approach to generate, arbitrarily, many synthetic profiles.

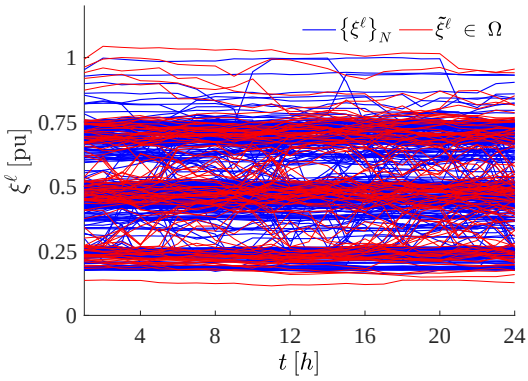

FIGURE 4.1. Random load profiles sampling after learning the temporal correlation structure from the dataset and qualitative validation of the capability to reproduce the dataset properties (case for $p = \ell$)

4.3.2 *Selecting the Scenarios for the considered BESS SP*

As indicated above, our goal is to construct scenarios $\tilde{\boldsymbol{\xi}} \in \Omega$ by combining generated profiles $\tilde{\boldsymbol{\xi}}^p(\omega)$ in a way that characterizes the system's uncertainty as well as possible, given a fixed number of scenarios to be included in the sizing Stochastic Problem. To achieve this, the first step is to introduce mathematical tools to assess the usefulness of a given scenario for characterizing the system's uncertainty (Ranking the scenarios). The second step is to understand how many scenarios are needed to achieve sufficiently good characterization (A Clustering Approach for Selecting the Scenarios).

Ranking the scenarios

Assume Ω to be populated with a number of sampled profiles, and assume our goal to be selecting a subset Ω_s of them. Before delving into details, the overarching structure of our proposed approach is: *i)* rank the samples within Ω based on how representative they are of their kind ($p = \{\ell, w\}$), *ii)* use these ranking scores to map the sampled profiles into a low-dimensional space, *iii)* discretize this space in some statistically optimal way, *iv)* use the scenarios $\widehat{\boldsymbol{\xi}} \in \Omega_s$ from this discretization and solve a computationally tractable version of eq. (4.16). This whole procedure is illustrated graphically in Figure 4.2.

We propose starting by ranking the profiles $\tilde{\boldsymbol{\xi}}^p \in \Omega$ using a Kantorovich distance, i.e., using

$$
\begin{aligned}
D_K^p &= \sum_{\omega \in \Omega \setminus \Omega_k} \pi_\omega \min_{\omega, \omega_k} v^p(\omega, \omega_k), \quad \text{where,} \\
v^p(\omega, \omega_k) &= ||\tilde{\boldsymbol{\xi}}^p(\omega) - \tilde{\boldsymbol{\xi}}^p(\omega_k)|| = \sum_{t=1}^{T} |\tilde{\xi}_t^p(\omega) - \tilde{\xi}_t^p(\omega_k)|
\end{aligned}
\tag{4.19}
$$

where Ω_k is the dynamically updated set including the k most representative profiles (note that when $k = |\Omega|$, then Ω_k will be an ordered version of Ω). The usage of a Kantorovich distance is due to its simplicity in providing good and quick heuristic solutions to the optimal transportation problem for *sr* algorithms (i.e. *FFS*) [9, 18].

Note now that the rank value of a profile ranked k^{th} out of $|\Omega|$ can be expressed as the scalar $t\left(\tilde{\boldsymbol{\xi}}^p(\omega_k)\right) = \frac{|\Omega|-k}{|\Omega|-1}, \quad p = \{\ell, w\}$ where $t(\omega_k) \to 1$ for profiles that can be thought as "more representative/typical" and $t(\omega_k) \to 0$ for profiles profiles that capture non-casual/non-typical events. In this way, a mapping is enforced, which not only preserves information spanning the whole support of the distribution of each individual *RV* (load, wind), but also indicates different possible profile combinations that could actually happen, despite not being observed before. In other words, this mapping expresses a generalized combinatorial space, showing possible ways that "typical" profiles from one uncertain parameter (i.e., load) can happen together with "typical" profiles from the other (i.e., wind) and similarly for "non-casual/non-typical" ones. We note that having the capability of coupling different uncertainties without imposing a particular structure on their covariances is one of the motivations behind this work, since this capability is, to the best of our knowledge, an important component that has not been addressed in the literature until now.

A Clustering Approach for Selecting the Scenarios

Finally, to optimally select the scenarios that *i)* will extend the whole uncertainty space and *ii)* are the minimum (optimal) amount needed, we propose the following procedure.

From the mechanism described in Subsection 4.3.1, the multivariate data points $(\tilde{\boldsymbol{\xi}}^\ell, \tilde{\boldsymbol{\xi}}^w)$ representing a sampled scenario, are mapped into a unique 2-dimensional space (Figure 4.3), which contains coupled information for $p = \{\ell, w\}$. We can then sample this space by clustering the data in K groups and considering the centroids of these groups. Assuming that field data is homogeneous (something that empirically is known to hold for wind and load profiles, e.g., Figure 4.3, given their practical statistical independence), the $\widehat{\boldsymbol{\xi}} \in \Omega_s$ can be determined from any clustering algorithm. In the following considerations we use *k-means*, even if some other algorithms (e.g., DBSCAN) may be used. Thus, our setup is

$$\begin{aligned} &\min_{r,\mu} \sum_{i=1}^{|\Omega|} \sum_{k=1}^{K} r_{ik} \, ||\boldsymbol{x}_i - \boldsymbol{\mu}_k|\,|_2^2, \\ &\text{s.t.,} \quad \boldsymbol{x}_i = \left(t_i\left(\tilde{\boldsymbol{\xi}}^\ell(\omega)\right), t_i\left(\tilde{\boldsymbol{\xi}}^w(\omega)\right)\right) \end{aligned} \tag{4.20}$$

where $r_{ik} \in \{0, 1\}$. Solving eq. (4.20) returns a set of clusters and the associated centroids $\boldsymbol{\mu}_k$ (marked as black crosses in Figure 4.3). This enables selecting the data points that are closest to these centroids as scenarios $\widehat{\boldsymbol{\xi}} \in \Omega_s$ that may be used to

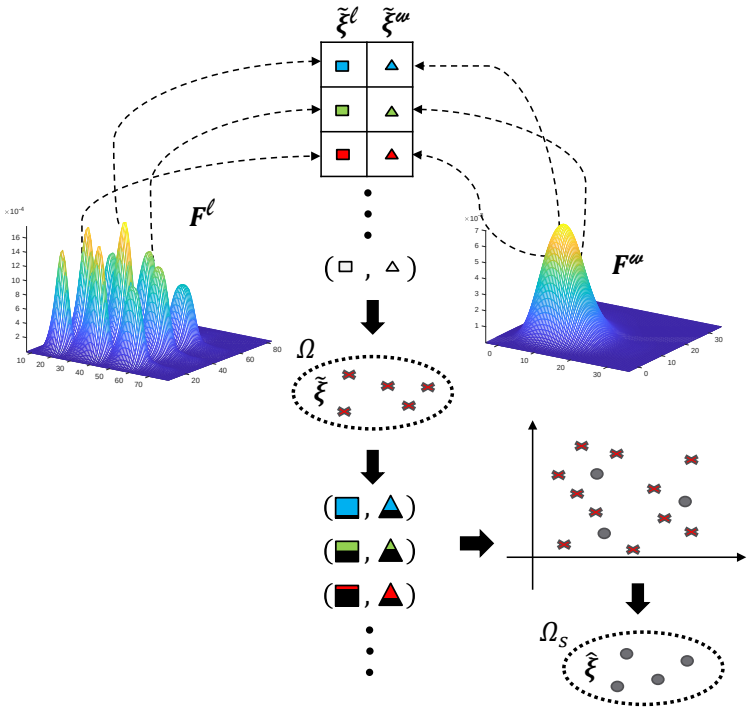

FIGURE 4.2. A graphical summary of the proposed procedure for generating the reduced scenario subset Ω_s from the sample space Ω. The starting point is sampling the joint distributions F^p, then joining the load (square) and wind (triangle) realizations together to form scenarios $\tilde{\boldsymbol{\xi}}$. These multi-dimensional vectors are then reduced to 2-dimensional points that are furthermore grouped in $|\Omega_s|$ clusters. The centroids of such clusters are then used as representatives of each such cluster, and thus used to populate the reduced subset of scenarios $\hat{\boldsymbol{\xi}} \in \Omega_s$. Note that here the distributions F^p have been visualized just for the first two dimensions out of 24

formulate the optimization problem eq. (4.16). This approach enables the coupling of the various uncertainties present in the setup, as well as the ability to find scenarios that statistically cover the whole combinatory space (note that the probability of the various $\hat{\boldsymbol{\xi}}$ can be computed based on the mass of its corresponding cluster). The approach then needs to be completed by defining a data-driven way for selecting the number of clusters K such that the solution of problem eq. (4.15) statistically depends on Ω as little as possible (given a tolerance level of choice). For this, we propose applying bootstrapping techniques to assess the sample statistics of the estimated parameter, namely the problem's objective value for varying K [16]. To summarize, we propose performing tests on the stability of the sizing results based on the following considerations: 1) the stochastic process $\tilde{\boldsymbol{\xi}} \in \Omega$ is approximated by M randomly drawn sample spaces $\tilde{\boldsymbol{\xi}}_m \in \Omega_m$, from which the reduced subspaces $\hat{\boldsymbol{\xi}}_m \in \Omega_{m,s}$ can be derived as described earlier and illustrated in Figure 4.2 and $|\Omega_{m,s}| = |\Omega_s| = K$. 2) the optimal

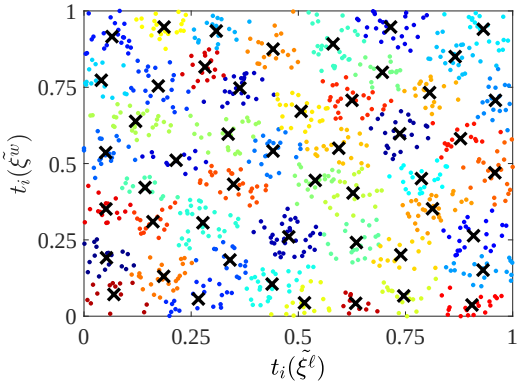

Figure 4.3. Snapshot of the iterative procedure for deciding $|\Omega_s^*|$. Randomly sampled profiles (load and wind) are represented as points on the 2-dimensional rank space and clustered in $|\Omega_s|$ groups, the centroids of which will populate Ω_s. Different colors correspond to different clusters (like a Voronoi diagram)

number $K^* = |\Omega_s^*|$ is such that $F(\boldsymbol{x}_m^*; \Omega_{m,s}) \approx F(\boldsymbol{x}_n^*; \Omega_{n,s}) \ \forall \ m, n \in 1 \dots M$, where $F\left(\boldsymbol{x}; \widehat{\boldsymbol{\xi}}\right)$ from eq. (4.16). This means that by choosing $|\Omega_s| = |\Omega_s^*|$ we diminish the sensitivity of the solution of the optimization problem on the subsets Ω_s.

In order to estimate Ω_s^*, numerical simulations can then be performed, for example, to obtain the results in figs. 4.4a and 4.4b. To assess the statistical dependence of the final sizing solutions on the scenarios selection algorithm, we propose to monitor the statistical properties (range Rg, interquartile range IQR and sample standard deviation s) of the M scenario trees that were created for each $|\Omega_s|$. In our considered field case, results indicate that $|\Omega_s^*| = 50$. At this point, one has all the components to code the resulting MILP problem, that in our field case was modeled in *Matlab R2020a* and solved with *Gurobi 9.0.3* in a 28 physical core multi-node cluster with Intel(R) Xeon(R) CPU E5-2690 v4 @ 2.60 Hz, 25 GB RAM.

4.4 Results

4.4.1 Analysing the quality of the solution and associated expected benefits

One of our aims was to demonstrate the effectiveness of the proposed strategy and its advantage over logically simpler alternatives. To do so, we considered the risk-neutral problem ($\beta = 0$ in (4.16)) and performed numerical tests where several scenario subsets were produced by different typically used strategies [9, 11, 25]. These compared in terms of the stability requirement expressed in A Clustering Approach for Selecting the Scenarios. For a fair comparison $|\Omega_s| = |\Omega_s^*|$ was set for all methods. We specify that scenario reduction and selection was a necessary process, since using the whole available dataset to solve eq. (4.16) is computationally intractable. Thus, one needs to create a criterion for selecting scenarios that is statistically more meaningful than

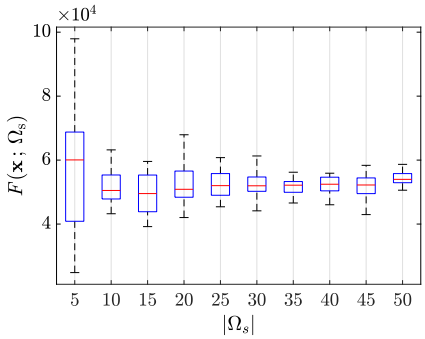

(a) Dispersion of the objective values for increasing scenario set cardinality.

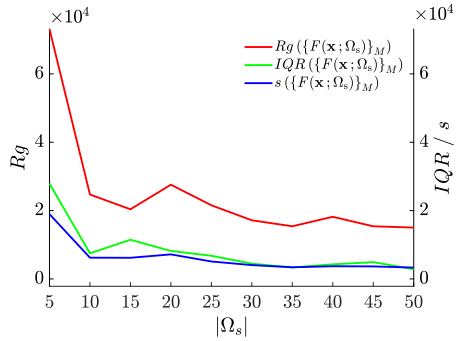

(b) Convergence of the statistical indices, indicating the proper scenario set cardinality.

FIGURE 4.4. Statistical stability tests for the optimization problem objective and convergence plots for determining $|\Omega_s^*|$ through the proposed iterative procedure

just random selection. That said, the following strategies were compared with the one proposed in this paper:

i. *Data*: under this naïve but straightforward strategy, we performed a random selection of combinations of load and wind profiles as observed in the available dataset. Thus, scenarios were composed of profiles combinations that were uniquely defined by the available historical dataset. As such, we represented uncertainty by conditional draws where a load pattern implies a unique wind pattern.

ii. *Random*: this is a generalization of the *Data* method, where load and wind profiles are allowed to be randomly permuted so that different combinations of load and wind are explored. Again, we used the available datasets (load and wind) but here, different profile combinations can emerge.

iii. *FFS*: this method applies a commonly used optimal *sr* algorithm (*FFS*). The historical profiles (load and wind) found in their corresponding datasets were individually reduced to sets of specified cardinality while redistributing the probability mass of the discarded to the preserved ones, according to their distance. Then, different random profile combinations were explored, considering their relative probabilities.

iv. *H-cl*: with this method, the individual profiles of each *RV* (load / wind) were again reduced but this time using an established clustering algorithm: hierarchical clustering. The dominant patterns were distinguished from each variable and stand as representatives of their clusters, the probabilities of which are weighted based on how many profiles are assigned to each group. Then those profiles

were again randomly combined to consider their relative probabilities to form scenarios.

v. *SetCorr*: this method was employed to demonstrate the effect of imposing arbitrary correlation between the *RV*s load and wind, as has been done in several studies [26–28, 31]. The estimated multivariate probabilities of each variable were used to generate pairs of *MC* samples (pairs of load and wind profiles) which were then ranked based on the distance of their correlation (Pearson correlation coefficient) from the nominal one. The nominal value was selected in accordance with [26–28, 31] and was set equal to 0.28. Then, the first $\left|\Omega_s^*\right|$ scenarios (pairs of load and wind profiles) with correlations closest to the nominal value were selected, weighted by the inverse of their distance from it.

vi. *Proposed*: this is the method proposed in this paper and described in Section 4.3.

The results of the comparison are summarized in Figure 4.5 and Table 4.1. Figure 4.5 shows that not only is the variation of the solutions gained with the proposed strategy smaller, but the extreme values are also much closer. Those effects are numerically expressed through the statistical indices defined in section 4.3.2 and presented in Table 4.1.

From the direct sampling methods *Data, Random* we observed the high dependence of the optimal objective value to the specific subset used as input to the optimization problem, highlighting the need for a better subset selection methodology. As evident, random permutations may produce different results meaning that the optimal value may be different when using different samples. Similar effects are noticed from methods *FFS*, *H-cl*. In particular, *FFS* shows higher bias of the optimal values that may be related to the fact that *sr* tends to prefer particular profiles that dominate the problem solution. From *H-cl* we observed a different trend characterized by the higher variance of the optimal values, meaning that the problem is very dependent on the way profiles are combined. Even though profiles can be fairly representative of their own clusters, we observed that for the specified subset cardinality, no representative combinations were identified by this methodology. From *SetCorr* we observed once more the pattern of high variability of the optimal values making clear that considering specific correlation between load and RES does not necessarily imply stable sizing solutions. This is because there could be many different profile combinations with the same correlation that lead to different optimal objective values. Finally, we saw that from our method (*Proposed*) the subset selection was performed in such a way that the dependency of the solution to the input data was minimized. This is because of the optimal exploration of the uncertainty space that was induced by considering all the different possible patterns of load, wind and their combinations. In other words, using the proposed methodology makes the optimization problem solution less sensitive (robust) to the scenario subset selection.

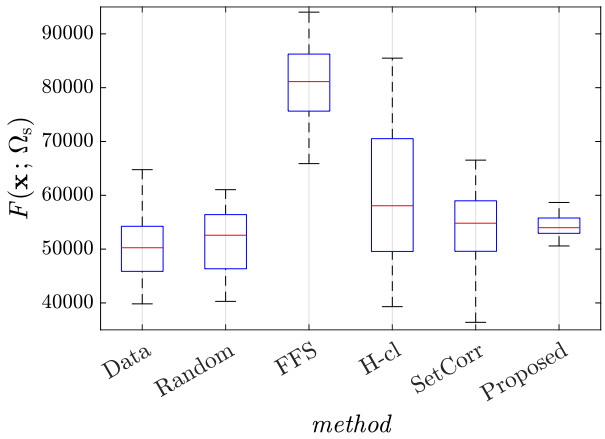

FIGURE 4.5. Comparison of optimization solution quality achieved by the proposed methodology against alternative methods of defining reduced scenarios set (load and wind) for the calculated $|\Omega_s^*|$

TABLE 4.1. Statistics of the stability tests comparison

Statistic	Method					
	Data	*Random*	*FFS*	*H-cl*	*SetCorr*	*Proposed*
Rg	24,937	20,758	45,572	72,009	57,653	15,033
IQR	8,376	10,061	10,602	20,958	9,384	2,851
s	6,082	6,210	11,539	16,969	14,893	3,319

We also assessed the value of incorporating uncertainty as proposed in this paper. Here, we calculated the *Value of Stochastic Solution* (*VSS*), commonly used in MILP formulations [10, 11]. For that, the expected (average) scenario was first calculated from the generated Ω_s^* set, then the deterministic problem was solved and finally the first stage solution was used to solve the original stochastic problem. It is noteworthy that with the optimal decision from the deterministic problem there was no BESS size that could diminish the expected operational costs, i.e., $\boldsymbol{x}_d^* = 0$ (d stands for deterministic and s for stochastic). Then the *VSS* was equal to

$$VSS = F\left(\boldsymbol{x}_d^*; \Omega_s^*\right) - F\left(\boldsymbol{x}_s^*; \Omega_s^*\right) = 1,044 \text{ €} / \text{ day} \tag{4.21}$$

which means that sizing the storage under the proposed stochastic framework has the potential to reduce the daily operating costs in the reference O&G platform by €$1,044$. In summary, for the whole set Ω_s^* we got the following performance indices

results:

$$\begin{aligned} \frac{F\left(\boldsymbol{x}_d^*;\Omega_s^*\right)-F\left(\boldsymbol{x}_s^*;\Omega_s^*\right)}{F\left(\boldsymbol{x}_d^*;\Omega_s^*\right)} &= 2.09\% \\ \frac{\mathbb{E}\left[V_{CO_2}\left(\boldsymbol{x}_d^*;\Omega_s^*\right)\right]-\mathbb{E}\left[V_{CO_2}\left(\boldsymbol{x}_s^*;\Omega_s^*\right)\right]}{\mathbb{E}\left[V_{CO_2}\left(\boldsymbol{x}_d^*;\Omega_s^*\right)\right]} &= 3.64\% \\ \frac{\mathbb{E}\left[E_D\left(\boldsymbol{x}_d^*;\Omega_s^*\right)\right]-\mathbb{E}\left[E_D\left(\boldsymbol{x}_s^*;\Omega_s^*\right)\right]}{\mathbb{E}\left[E_D\left(\boldsymbol{x}_d^*;\Omega_s^*\right)\right]} &= 6.89\% \end{aligned} \tag{4.22}$$

That is, we expect reduction not only in the daily operational costs (2.09%) but also in daily V_{CO_2} emissions (3.64%) and daily dumped energy E_D (6.89%).

4.4.2 *Analysing the effects on the management of the risk*

To analyze the impact of extreme (worst-case) events captured by the proposed *sg* methodology within Ω_s^* on the solution of (4.16), we performed a comparative analysis by holding the same confidence level $\alpha = 0.8$ and varying $\beta \in [0, 1]$.

The results showed that, as the decision maker becomes more risk-averse, the optimal BESS size is decreased, limiting the capability of the storage to be operated such that it reduces the operational costs. A counter-benefit here is that one gets better (reduced) $CVaR$ values (Table 4.2). However, this reduction is considerably smaller than the variation of the optimal storage decision and its impact on the expected cost. This is illustrated in Figure 4.6 where the CDF of the cost values $\forall\ \omega = 1 \ldots |\Omega_s^*|$ are plotted for two extreme cases: $\beta = 0$ (risk-neutral) and $\beta = 1$ (risk-averse). We observed that although the $\boldsymbol{x}^*$ decision changes drastically (and this directly impacts the shape of the cost distributions), they are very close (similar) after the given confidence level α is reached and consequently the expectation of the cost for that region ($CVaR$) essentially remains the same.

The reasoning for this can be revealed from Figure 4.7, where the scenarios are ranked based on their associated cost value and plotted as a contour depending on the value of $\widehat{\xi^p}$. Scenarios associated with low costs ($\omega \to 1$ after sorting) are generally associated with a combination of low loads and high wind power profiles and vice-versa (i.e., for scenarios associated with high costs, $\omega \to 50$). This indicates, in accordance with our expectations, that in cases of high demand and low wind conditions, several GTs need to be operated anyway and whatever decision one makes on the BESS size, this cannot greatly reduce the daily operational cost. Thus, provided that the dataset includes scenarios capable of capturing this phenomenon, a risk-informed decision for the storage size is not very meaningful, as worst cases cannot be avoided (faced) with any storage.

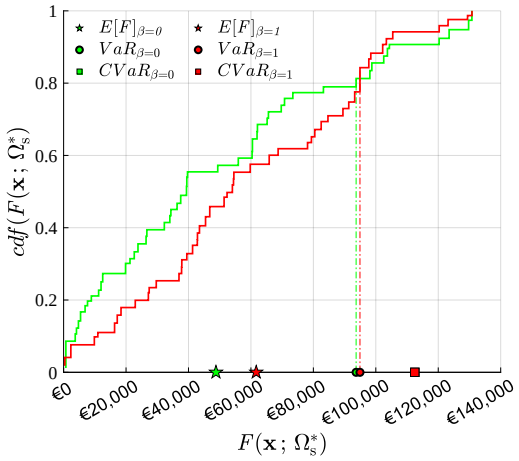

FIGURE 4.6. Cumulative distribution of the daily costs for the risk-neutral (green) and risk-averse (red) sizing problem for the optimal scenario subset. Even though risk management affects the shape of the cost distribution changing the mean value, it does not significantly affects the worst-cases tail

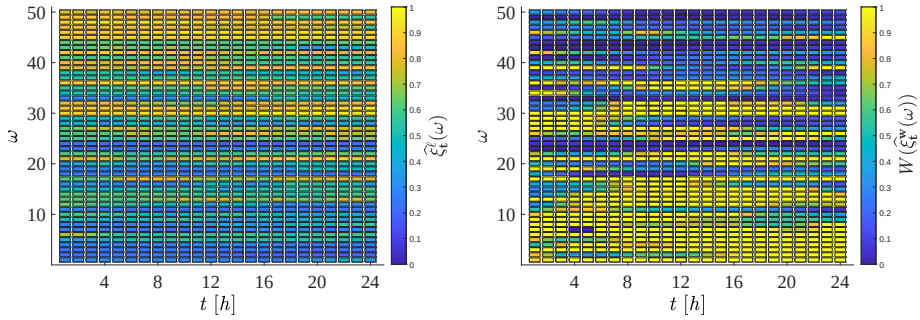

(a) Load profiles

(b) Wind power profiles

FIGURE 4.7. Optimally selected scenarios $\widehat{\boldsymbol{\xi}} \in \Omega_s^*$ from the proposed methodology, ranked based on the corresponding induced cost

TABLE 4.2. Risk management study

Variable	*Units*	*No BESS*	*With BESS*		
			$\beta = 0$	$\beta = 0.8$	$\beta = 0.95$
E_B	MWh	-	8.252	6.281	3.950
P_B	MW	-	4.873	4.802	3.526
F	€$/day$	49,844	48,718	48,801	49,053
$\mathbb{E}\left[V_{CO_2}\right]$	tn/day	247.21	238.59	239.09	241.21
$\mathbb{E}\left[E_D\right]$	MWh/day	84.822	78.972	79.565	80.745
VaR	€$/day$	94,892	93,691	93,555	94,925
$CVaR$	€$/day$	112,738	112,545	112,505	112,463

4.4.3 *Analysing the sensitivity of the results on the price of the battery*

Finally, in order to address the impact of the sizing parameter values on the decision $\boldsymbol{x}^*$ and on the performance indices referred to Subsection 4.4.1, we performed a sensitivity analysis on $C_{B,E}$ while preserving the same $C_{B,E}/C_{B,P}$ ratio. Quantifying the effect of the BESS price is important, considering the latest and constantly decreasing trend of the cost [39–41] and the fact that the system of this case study will be implemented in the near future. Figure 4.8 shows the results from this analysis. As expected, increasing

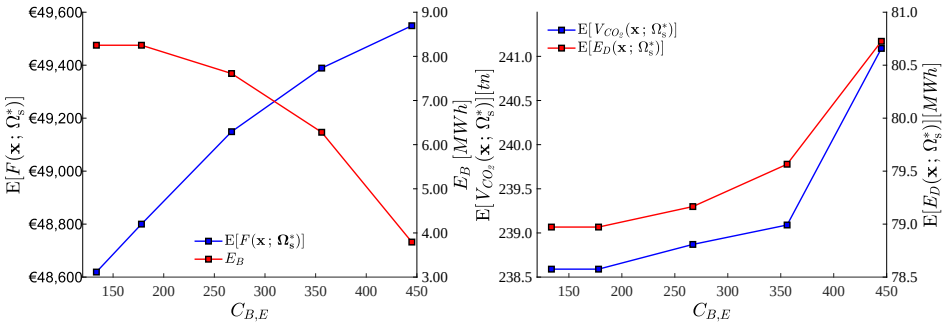

(a) Cost (b) Emissions and dumped energy

Figure 4.8. Sensitivity analysis on battery price $C_{B,E}$ [€/kWh]

the battery price led to smaller size and in turn higher expected daily operational costs. However, even for the highest battery price (that refers to the conservative future price estimations), the expected costs were better than the no BESS case. The direct effect of the battery price-size dependency was also evident in the daily expected emissions and curtailed energy. Both the latter indices increased more drastically (almost exponentially) compared to the operational costs, especially following a particular battery price. Finally, below a specific battery price level we saw no significant change in the size decision and therefore in the performance indices.

4.5 Conclusions

Deciding the techno-economically optimal size of an energy storage for isolated power systems gives rise to combinatorially hard optimization problems when considering UC decisions, load and renewable uncertainties and their interactions without any arbitrary assumption. Considering all available historical data to solve the uncertain optimization problem leads to computational intractability issues, hence there is the need to reduce the number of scenarios that are used in the optimization problem. However, the scenarios selection algorithm should be such that the solution obtained is statistically as close as possible to the one that would be computed if there were no computational issues. This can be of high significance because if the final decision is highly dependent on the selected scenarios, then the confidence of the expected

benefits from the energy storage is low. To deal with this problem, this paper proposes a data-informed methodology that designs and selects minimum scenarios subsets such that the solutions gained are of guaranteed statistical quality, while optimally exploring the combinatorial space of different uncertainty outcomes. The proposed methodology was benchmarked against alternative ways of deriving reduced scenario sets and achieved more stable solutions for the same problem complexity. Thus, it provided more realistic estimates of the expected benefits of integrating an energy storage system into a wind powered O&G platform, accounting for a reduction of -2.09% in daily operational costs, -3.64% in daily produced emissions and -6.89% in daily curtailment. In addition, it was demonstrated that the subsets of scenarios that are generated with the proposed methodology include instances of uncertainty that do not favor the use of energy storage, proving that risk-constrained decisions may promote smaller investments for the storage sizing problem in isolated O&G applications without significant risk reductions.

As for future work, we envision two distinct directions. The first is towards extending the method's applicability for further practical problems by including additional types of RESs (increasing the dimensionality of the uncertainty space) and by applying the proposed methodology for sizing energy storage for interconnected micro-grids where an additional uncertain variable is the energy pricing profiles. There is then the need to verify if the favorable properties we found for our test case hold true in other power systems with different profile characteristics. In addition, the impact of different initial operating conditions across different scenarios on the resulting BESS sizing decision, could be alleviated by considering those as an additional source of (parametric) uncertainty and integrate them into the proposed methodology. The second direction is to find analytical results on the properties of the methodology. The most important one is likely finding results that couple the number of scenarios to be used in the programs with the statistical stability of the sizing results. These theorems may indeed be useful to decide the number of scenarios to be used without performing time consuming stability simulations, but rather using theoretically grounded formula.

4.6 Appendix

See Table 4.3.

4.7 References

[1] Y. Yang, S. Bremner, C. Menictas, and M. Kay, "Battery energy storage system size determination in renewable energy systems: A review," *Renewable and Sustainable Energy Reviews*, vol. 91, pp. 109–125, Aug. 2018. [Online]. Available: https://linkinghub.elsevier.com/retrieve/pii/S1364032118301436 Cited on page/s 72, 76.

[2] R. Machlev, N. Zargari, N. R. Chowdhury, J. Belikov, and Y. Levron, "A review of optimal control methods for energy storage systems - energy trading, energy balancing and electric vehicles," *Journal of Energy Storage*, vol. 32, p. 101787, Dec. 2020. [Online]. Available: http://www.sciencedirect.com/science/article/pii/S2352152X20316248 Cited on page/s 72.

Table 4.3. Parameter values

Parameter	Symbol	Value	Units
Natural Gas and Gas Turbines			
Natural Gas density	ρ	0.77	$\left[\frac{kg}{m^3}\right]$
CO_2 combustion coefficient	μ	2.682	$\left[\frac{kg_{CO_2}}{kg_f}\right]$
maximum GT power	$\overline{P}^g_{GT}$	20.2	$[MW]$
affine fuel consumption coefficient	α_g	172.50	$\left[\frac{kg_f}{MW}\right]$
affine fuel consumption constant	β_g	729.20	$\left[\frac{kg_f}{h}\right]$
operation and maintenance cost	$C_{O\&M}$	5.53	$\left[\frac{€}{MW}\right]$
GT startup cost	C^{start}_{GT}	1217	$\left[\frac{€}{\text{start}}\right]$
CO_2 emissions tax	C_{CO_2}	0.07	$\left[\frac{€}{kg_{CO_2}}\right]$
Natural gas wholesale price	C_{NG}	0.24	$\left[\frac{€}{m^3}\right]$
Wind Farm			
cut in speed	w_{ci}	3	$\left[\frac{m}{s}\right]$
cut off speed	w_{ci}	25	$\left[\frac{m}{s}\right]$
rated wind speed	w_n	12	$\left[\frac{m}{s}\right]$
rated wind turbine power	P^n_w	8	$\left[\frac{m}{s}\right]$
wind farm turbines	N_w	5	$[-]$
Battery Energy Storage System			
interest rate	r	7	$[\%]$
battery lifetime	L	8	$[years]$
battery energy cost	$C_{B,E}$	178.00	$\left[\frac{€}{kWh}\right]$
battery power cost	$C_{B,P}$	89.00	$\left[\frac{€}{kW}\right]$

[3] A. Soroudi and T. Amraee, "Decision making under uncertainty in energy systems: State of the art," *Renewable and Sustainable Energy Reviews*, vol. 28, pp. 376–384, Dec. 2013. [Online]. Available: https://linkinghub.elsevier.com/retrieve/pii/S1364032113005790 Cited on page/s 72.

[4] L. A. Wong, V. K. Ramachandaramurthy, P. Taylor, J. Ekanayake, S. L. Walker, and S. Padmanaban, "Review on the optimal placement, sizing and control of an energy storage system in the distribution network," *Journal of Energy Storage*, vol. 21, pp. 489–504, Feb. 2019. [Online]. Available: https://linkinghub.elsevier.com/retrieve/pii/S2352152X18303803 Cited on page/s 72.

[5] M. Hannan, M. Faisal, P. Jern Ker, R. Begum, Z. Dong, and C. Zhang, "Review of optimal methods and algorithms for sizing energy storage systems to achieve decarbonization in microgrid applications," *Renewable and Sustainable Energy Reviews*, vol. 131, p. 110022, Oct. 2020. [Online]. Available: https://linkinghub.elsevier.com/retrieve/pii/S1364032120303130 Cited on page/s 72, 76.

[6] M. Cao, Q. Xu, J. Cai, and B. Yang, "Optimal sizing strategy for energy storage system considering correlated forecast uncertainties of dispatchable resources," *International Journal of Electrical Power & Energy Systems*, vol. 108, pp. 336–346, Jun. 2019. [Online]. Available: https://linkinghub.elsevier.com/retrieve/pii/S0142061518324773 Cited on page/s 72, 76.

[7] C. Wang, Z. Zhang, O. Abedinia, and S. G. Farkoush, "Modeling and analysis of a microgrid considering the uncertainty in renewable energy resources, energy storage systems and demand management in electrical retail market," *Journal of Energy Storage*, vol. 33, p. 102111, Jan. 2021. [Online]. Available: https://linkinghub.elsevier.com/retrieve/pii/S2352152X20319411 Cited on page/s 72.

[8] V. Jani and H. Abdi, "Optimal allocation of energy storage systems considering wind power

uncertainty," *Journal of Energy Storage*, vol. 20, pp. 244–253, Dec. 2018. [Online]. Available: https://linkinghub.elsevier.com/retrieve/pii/S2352152X18303761 Cited on page/s 72.

[9] J. Li, J. Zhou, and B. Chen, "Review of wind power scenario generation methods for optimal operation of renewable energy systems," *Applied Energy*, vol. 280, p. 115992, Dec. 2020. [Online]. Available: https://linkinghub.elsevier.com/retrieve/pii/S0306261920314380 Cited on page/s 73, 82, 84.

[10] A. J. Conejo, M. Carrión, and J. M. Morales, *Decision making under uncertainty in electricity markets*, ser. International series in operations research & management science. New York: Springer, 2010, oCLC: ocn662409210. Cited on page/s 73, 78, 87.

[11] C. Li and I. E. Grossmann, "A Review of Stochastic Programming Methods for Optimization of Process Systems Under Uncertainty," *Front. Chem. Eng.*, vol. 2, 2021, publisher: Frontiers. [Online]. Available: https://www.frontiersin.org/articles/10.3389/fceng.2020.622241/full Cited on page/s 73, 84, 87.

[12] X. Kong, J. Xiao, D. Liu, J. Wu, C. Wang, and Y. Shen, "Robust stochastic optimal dispatching method of multi-energy virtual power plant considering multiple uncertainties," *Applied Energy*, vol. 279, p. 115707, Dec. 2020. [Online]. Available: https://linkinghub.elsevier.com/retrieve/pii/S0306261920312010 Cited on page/s 73.

[13] M. Aghamohamadi, A. Mahmoudi, and M. H. Haque, "Two-Stage Robust Sizing and Operation Co-Optimization for Residential PV–Battery Systems Considering the Uncertainty of PV Generation and Load," *IEEE Transactions on Industrial Informatics*, vol. 17, no. 2, pp. 1005–1017, Feb. 2021, conference Name: IEEE Transactions on Industrial Informatics. Cited on page/s 73.

[14] Z. Guo, W. Wei, L. Chen, R. Xie, and S. Mei, "Sizing energy storage to reduce renewable power curtailment considering network power flows: a distributionally robust optimisation approach," *IET Renewable Power Generation*, vol. 14, no. 16, pp. 3273–3280, 2020, _eprint: https://ietresearch.onlinelibrary.wiley.com/doi/pdf/10.1049/iet-rpg.2020.0354. [Online]. Available: https://ietresearch.onlinelibrary.wiley.com/doi/abs/10.1049/iet-rpg.2020.0354 Cited on page/s 73.

[15] M. Zhang, X. Ai, J. Fang, W. Yao, W. Zuo, Z. Chen, and J. Wen, "A systematic approach for the joint dispatch of energy and reserve incorporating demand response," *Applied Energy*, vol. 230, pp. 1279–1291, Nov. 2018. [Online]. Available: https://www.sciencedirect.com/science/article/pii/S0306261918313539 Cited on page/s 73.

[16] M. Kaut and S. W. Wallace, "Evaluation of scenario-generation methods for stochastic programming," *Pacific Journal of Optimization*, vol. 3, no. 2, pp. 257–271, 2007. Cited on page/s 73, 83.

[17] E. Du, N. Zhang, C. Kang, and Q. Xia, "Scenario Map Based Stochastic Unit Commitment," *IEEE Transactions on Power Systems*, vol. 33, no. 5, pp. 4694–4705, Sep. 2018, conference Name: IEEE Transactions on Power Systems. Cited on page/s 73.

[18] J. Dupačová, N. Gröwe-Kuska, and W. Römisch, "Scenario Reduction in Stochastic Programming: An Approach Using Probability Metrics," 2003. Cited on page/s 73, 82.

[19] J. Hu and H. Li, "A New Clustering Approach for Scenario Reduction in Multi-Stochastic Variable Programming," *IEEE Transactions on Power Systems*, vol. 34, no. 5, pp. 3813–3825, Sep. 2019, conference Name: IEEE Transactions on Power Systems. Cited on page/s 73.

[20] J. Wang, M. Shahidehpour, and Z. Li, "Security-Constrained Unit Commitment With Volatile Wind Power Generation," *IEEE Transactions on Power Systems*, vol. 23, no. 3, pp. 1319–1327, Aug. 2008, conference Name: IEEE Transactions on Power Systems. Cited on page/s 73.

[21] A. Jalali and M. Aldeen, "Risk-Based Stochastic Allocation of ESS to Ensure Voltage Stability Margin for Distribution Systems," *IEEE Transactions on Power Systems*, vol. 34, no. 2, pp. 1264–1277, Mar. 2019, conference Name: IEEE Transactions on Power Systems. Cited on page/s 73.

[22] P. Pinson, G. Papaefthymiou, B. Klockl, and J. Verboomen, "Dynamic sizing of energy storage for hedging wind power forecast uncertainty," in *2009 IEEE Power & Energy Society General Meeting*. Calgary, Canada: IEEE, Jul. 2009, pp. 1–8. [Online]. Available: http://ieeexplore.ieee.org/document/5275816/ Cited on page/s 73, 80.

[23] H. Valizadeh Haghi and S. Lotfifard, "Spatiotemporal Modeling of Wind Generation for Optimal Energy Storage Sizing," *IEEE Transactions on Sustainable Energy*, vol. 6, no. 1, pp. 113–121, Jan. 2015, conference Name: IEEE Transactions on Sustainable Energy. Cited on page/s 73, 76.

[24] Y. Chen, Y. Wang, D. Kirschen, and B. Zhang, "Model-Free Renewable Scenario Generation Using Generative Adversarial Networks," *IEEE Trans. Power Syst.*, vol. 33, no. 3, pp. 3265–3275, May 2018. [Online]. Available: http://ieeexplore.ieee.org/document/8260947/ Cited on page/s 73.

[25] P. Seljom, L. Kvalbein, L. Hellemo, M. Kaut, and M. M. Ortiz, "Stochastic modelling of variable renewables in long-term energy models: Dataset, scenario generation & quality of results," *Energy*, p. 121415, Jul. 2021. [Online]. Available: https://linkinghub.elsevier.com/retrieve/pii/S0360544221016637 Cited on page/s 73, 84.

[26] X. Yang, C. Xu, H. He, W. Yao, J. Wen, and Y. Zhang, "Flexibility Provisions in Active Distribution Networks With Uncertainties," *IEEE Transactions on Sustainable Energy*, pp. 1–1, 2020, conference Name: IEEE Transactions on Sustainable Energy. Cited on page/s 73, 78, 86.

[27] M. R. M. Cruz, D. Z. Fitiwi, S. F. Santos, S. J. P. S. Mariano, and J. P. S. Catalão, "Multi-Flexibility Option Integration to Cope With Large-Scale Integration of Renewables," *IEEE Transactions on Sustainable Energy*, vol. 11, no. 1, pp. 48–60, Jan. 2020, conference Name: IEEE Transactions on Sustainable Energy. Cited on page/s 73, 86.

[28] S. F. Santos, D. Z. Fitiwi, M. Shafie-Khah, A. W. Bizuayehu, C. M. P. Cabrita, and J. P. S. Catalão, "New Multistage and Stochastic Mathematical Model for Maximizing RES Hosting Capacity—Part I: Problem Formulation," *IEEE Transactions on Sustainable Energy*, vol. 8, no. 1, pp. 304–319, Jan. 2017, conference Name: IEEE Transactions on Sustainable Energy. Cited on page/s 73, 86.

[29] F. Pourahmadi, J. Kazempour, C. Ordoudis, P. Pinson, and S. H. Hosseini, "Distributionally Robust Chance-Constrained Generation Expansion Planning," *IEEE Transactions on Power Systems*, vol. 35, no. 4, pp. 2888–2903, Jul. 2020, conference Name: IEEE Transactions on Power Systems. Cited on page/s 73.

[30] J. H. Yi, R. Cherkaoui, and M. Paolone, "Optimal Allocation of ESSs in Active Distribution Networks to achieve their Dispatchability," *IEEE Transactions on Power Systems*, pp. 1–1, 2020, conference Name: IEEE Transactions on Power Systems. Cited on page/s 73.

[31] G. Sinden, "Characteristics of the UK wind resource: Long-term patterns and relationship to electricity demand," *Energy Policy*, vol. 35, no. 1, pp. 112–127, Jan. 2007. [Online]. Available: https://www.sciencedirect.com/science/article/pii/S0301421505002752 Cited on page/s 73, 86.

[32] Z. Shu and P. Jirutitijaroen, "Latin Hypercube Sampling Techniques for Power Systems Reliability Analysis With Renewable Energy Sources," *IEEE Transactions on Power Systems*, vol. 26, no. 4, pp. 2066–2073, Nov. 2011, conference Name: IEEE Transactions on Power Systems. Cited on page/s 74.

[33] Z. Yang, M. Ghadamyari, H. Khorramdel, S. M. Seyed Alizadeh, S. Pirouzi, M. Milani, F. Banihashemi, and N. Ghadimi, "Robust multi-objective optimal design of islanded hybrid system with renewable and diesel sources/stationary and mobile energy storage systems," *Renewable and Sustainable Energy Reviews*, vol. 148, p. 111295, Sep. 2021. [Online]. Available: https://linkinghub.elsevier.com/retrieve/pii/S1364032121005827 Cited on page/s 75.

[34] O. Sadeghian, A. Oshnoei, R. Khezri, and S. Muyeen, "Risk-constrained stochastic optimal allocation of energy storage system in virtual power plants," *Journal of Energy Storage*, vol. 31, p. 101732, Oct. 2020. [Online]. Available: https://linkinghub.elsevier.com/retrieve/pii/S2352152X20315693 Cited on page/s 76, 78.

[35] J. Liu, C. Chen, Z. Liu, K. Jermsittiparsert, and N. Ghadimi, "An IGDT-based risk-involved optimal bidding strategy for hydrogen storage-based intelligent parking lot of electric vehicles," *Journal of Energy Storage*, vol. 27, p. 101057, Feb. 2020. [Online]. Available: https://linkinghub.elsevier.com/retrieve/pii/S2352152X19309429 Cited on page/s 78.

[36] X. Xu, Z. Yan, M. Shahidehpour, Z. Li, M. Yan, and X. Kong, "Data-Driven Risk-Averse Two-Stage Optimal Stochastic Scheduling of Energy and Reserve With Correlated Wind Power," *IEEE Transactions on Sustainable Energy*, vol. 11, no. 1, pp. 436–447, Jan. 2020, conference Name: IEEE

Transactions on Sustainable Energy. Cited on page/s 78, 80.

[37] R. T. Rockafellar and S. Uryasev, "Optimization of conditional value-at-risk," *JOR*, vol. 2, no. 3, pp. 21–41, 2000. [Online]. Available: http://www.risk.net/journal-of-risk/technical-paper/2161159/optimization-conditional-value-risk Cited on page/s 78.

[38] Z. Zhang, H. Qin, J. Li, Y. Liu, L. Yao, Y. Wang, C. Wang, S. Pei, P. Li, and J. Zhou, "Operation rule extraction based on deep learning model with attention mechanism for wind-solar-hydro hybrid system under multiple uncertainties," *Renewable Energy*, vol. 170, pp. 92–106, Jun. 2021. [Online]. Available: https://linkinghub.elsevier.com/retrieve/pii/S0960148121001221 Cited on page/s 80.

[39] M. Wilshire, "Future trends in energy - Bloomberg New Energy Finance," Wärtsilä Flexible Power Symposium, Aug. 2018. Cited on page/s 90.

[40] I. R. E. Agency, "Electricity storage and renewables: Costs and markets to 2030," IRENA, Abu Dhabi, Tech. Rep., Oct. 2017. Cited on page/s 90.

[41] "Battery storage to drive the power system transition," ECOFYS Germany GmbH, Summary, 2018. [Online]. Available: https://ec.europa.eu/energy/sites/ener/files/report-_battery_storage_to_drive_the_power_system_transition.pdf Cited on page/s 90.

Chapter 5

Data-Driven Energy Management of Isolated Power Systems Under Rapidly Varying Operating Conditions

Spyridon Chapaloglou[1,*], Damiano Varagnolo[2,5], Francesco Marra[3] and Elisabetta Tedeschi[1,4]

Published in: *Applied Energy* **314**, 118906 (2022).
DOI: 10.1016/j.apenergy.2022.118906

Highlights

- SMPC for energy management of isolated power systems
- Auto-regressive QRFs for irregular events prediction
- Optimal system operation under load steps variations and wind power trend reversals
- Minimization of battery degradation, GTs ON/OFF commands and dumped energy

[1]Department of Electric Power Engineering, Norwegian University of Science and Technology (NTNU), Trondheim, Norway. [2]Department of Engineering Cybernetics, Norwegian University of Science and Technology (NTNU), Trondheim, Norway. [3]Equinor R&T Electrical Technology Department, Arkitekt Ebbels 10, 7005, Trondheim, Norway. [4]Department of Industrial Engineering, University of Trento, Via Sommarive, 9, 38123 Povo, Italy. [5]Department of Information Engineering, University of Padova, Via 8 Febbraio 2, 35122 Padova, Italy. [#]e-mail: spyridon.chapaloglou@ntnu.no, damiano.varagnolo@ntnu.no, fmarr@equinor.com and elisabetta.tedeschi@ntnu.no

Abstract

We propose an energy management algorithm for isolated industrial power systems that integrate uncertain renewable generation and energy storage. The proposed strategy is designed to ensure sustainable and cost-effective operations by managing the energy flows in the grid, and is structured so to cope with: *1)* high levels of renewable power penetration, and *2)* load profiles characterized by non-smooth patterns and irregular events (i.e., events such as those occurring from connections/disconnections of large scale equipment, or from large wind speed ramps). The proposed algorithm leverages a stochastic economic MPC scheme capable of dealing simultaneously with the dispatch and scheduling of the local generation units. More precisely, the scheme embeds a MILP optimal control policy formulation together with a stochastic programming approach. Moreover, the optimization problem accounts for multiple techno-economical objectives, such as minimization of operational costs, battery degradation, and non-utilized energy. We test the algorithm on a case study of an isolated offshore O&G platform producing energy onsite with conventional GTs and a local wind farm, while integrating a BESS. The results show that the proposed approach can issue ensemble predictions that successfully capture the potential irregular variations just by using recent past information of the associated RV, even when no particular sudden events are anticipated in the near-future (i.e., step changes/trend reversals). In this way, the approach provides useful future information for the optimal management of the grid. This effect is numerically quantified via simulations that compare the performance of the proposed *so* approach against its deterministic MPC version in several realistic operating conditions. The empirical results suggest that the stochastic version leads to better scheduling of the conventional generators, with up to 12.86% reductions of the operating cost, 2.56% reduction in fuel consumption and emissions, and 35.29% reduction in status transitions (on/off) of the GTs, while keeping dumped energy and battery degradation as low as possible.

5.1 Introduction

Operating resiliently and efficiently islanded microgrids and isolated power systems is believed to require not only integrating energy storage technologies, but also efficiently controlling these [1]. This is especially true for isolated industrial power systems such as remote offshore facilities [2], where specialized EMSs are required. Following the recent trends in the offshore O&G industry [3], BESSs are expected to significantly contribute toward the decarbonization of the O&G sector. However, to achieve this goal in a cost-efficient and safe way, the particular characteristics of these grids, such as the intermittent load patterns and abrupt load steps [4, 5], need to be taken into account. On top of that, integrating RES in these grids adds one more level of complexity due to uncertainty in the power supply. Therefore, appropriate EMS strategies that consider these effects are required. In addition, another important aspect that needs

to be captured by the EMS algorithm is the accurate representation of potential time-dependent characteristics of the system's resources, such as BESS degradation [6]. In this way, multiple objectives come together, complicating the calculation of an optimal control policy. Adding then the presence of flexible conventional units with binary operation modes (ON/OFF) makes the energy management optimization problem combinatorial, complicating the numerical search for the optimal solution. As shown in the literature review below, these issues have already been the subject of investigation by the scientific community.

5.1.1 Literature Review

Most of the time, EMS algorithms are formulated either as rule-based strategies or mathematical optimization problems [7–10]. However, such methods do not account for uncertainty in the operating conditions. Recent trends have suggested the consideration of *so* techniques [1] together with advanced probabilistic forecasting [11, 12]. These two components have indeed shown a good potential in dealing with the energy management specifications/requirements under partially known information. A popular approach in integrating uncertainty in the EMS has indeed been the feedback mechanism provided by the MPC framework [13–15], which can be further enhanced by using MILP [16–18]. Yet, such formulations still do not explicitly consider the uncertainty of future events. Nevertheless, MPC strategies are especially useful for handling energy management problems when combined with *so* as in [19, 20]. However, for better performance and more realistic modelling, such formulations should also consider battery degradation, as we instead do in this paper.

We shall also note that a common way to express uncertainty in *so* models is through the use of sample paths, called *scenarios*. To be representative of the true random processes, the marginal distribution of each RV should describe historical data accurately, and at the same time, the joint distribution should also be modelled accurately enough to capture temporal and multivariate correlations [21, 22]. The latter requirement is commonly ensured using Cholesky decompositions [23–25]. However, the distribution of each individual RV is commonly assumed to follow some kind of typical parametric structure [23, 24, 26], an assumption that should be avoided when arbitrary load characteristics are considered (such as loads including irregular events). An alternative is to learn these distributions from available data. In [27, 28], stochastic load and RES are modelled using discrete values and probability mass functions. However, such formulations are prone to the curse of dimensionality, especially when the number of loads or the RES resources in the system increase.

In other studies, quantile forecasting is used as a data-driven method to generate auto-correlated scenarios [25, 29, 30]. However, in most studies where probabilistic forecasts are issued for RES uncertainty quantification, e.g., [22, 30–32], future information about weather conditions is used as input from specialized NWP models. In this way, such forecasts heavily depend on the availability of these models, which are

limited in time resolution, making the forecasting of sudden irregular events (i.e., step changes/trend reversals) extremely challenging.

Then, by combining probabilistic forecasting with scenarios, *so*, and MPC, an enhanced class of MPC algorithms emerges (SMPC-EMS). In [14, 33–35] such strategies were proposed to optimally manage HVAC equipment in the built environment. In [36] a similar method was proposed for the market-based optimal power dispatch, demonstrating the potential application of SMPC-EMS in the power sector. Then, in [25] an SMPC-EMS was proposed for the economic optimization of a grid-connected microgrid integrating PV power.

As evident from the above analysis, state-of-the-art energy management is achieved by combining advanced forecasting and optimization methods. However, to the best of our knowledge, no integrated SMPC-EMS has been proposed for the management of isolated power systems that are subject to irregular load patterns and rapidly varying renewable generation.

5.1.2 Statement of contributions

It is now clear that the cost-efficient and environmentally sustainable operation of isolated industrial power systems integrating high amounts of renewable resources combined with dispatchable conventional power generation units, is a challenging problem. This is due to: 1) the combined effects of very short-term uncertainties coming from both power generation and consumption sides, and 2) the combinatorial nature of the UC decisions. Limitations related to the existing methods are found mainly in an accurate and adaptive probabilistic description of future disturbances to be used along with predictive control, in capturing irregular events without any prior future knowledge, and in dealing with multiple objectives when both continuous and binary decisions need to be taken for the optimal energy management problem. We thus propose to overcome such limitations by formulating and testing an algorithm that

i. is capable of better quantifying load uncertainty and sudden operation changes just by using lagged values of the load time-series and has an increased performance in predicting trend reversals in wind power generation compared to point forecasts, again by using just lagged values and no future information (i.e., NWP);

ii. is formulated as an optimal feedback control problem through employing a MILP that is numerically solvable, in contrast with other schemes that bypass numerical intractability by means of sub-optimal heuristics;

iii. includes multiple objectives in its formulation, considering not only the cost-efficient operation of the system, but also its environmental performance by minimizing the wasted (dumped) energy and the optimal usage of the BESS; and

iv. uses a detailed degradation model for the BESS, leading thus to operations that do not over-strain this subsystem.

The remainder of this paper is therefore organized as follows: Section 5.2 presents how to embed the SMPC-EMS with forecasting capabilities, Section 5.3 formulates the optimal control problem, and Section 5.4 presents the numerical results from the simulations. Finally, Section 5.5 presents an overall summary of the main findings and some concluding remarks.

5.2 DISTURBANCE UNCERTAINTY QUANTIFICATION THROUGH PROBABILISTIC FORECASTING

The objective of this section is to build an auto-regressive model that can effectively predict the occurrence of irregular events such as sudden steps and ramps. This capability is especially important in control strategies with fine time discretizations, especially when model-based predictions are either not available or available at higher time resolutions to the point that interpolating such model-based predictions would lead to missing the steps and ramps of our interest. As an example, this applies to load profiles that are characterized by frequent ON/OFF switching of the equipment: in this case, the exact schedule of on or off states might be unknown in advance, since depending on rapidly changing operating conditions, and interpolating coarse model-based predictions of their operations may lead to missing some of these switches.

In the following two subsections, we thus first propose the forecasting method, and then discuss a sensible way to tune its hyper-parameters.

5.2.1 Quantile Regression Forests as Auto-regressive Models

We propose to use QRFs, that were introduced in [37] and that, to the best of our knowledge, comprise one of the best-performing supervised learning algorithms for quantile regression [38]. This approach has proven useful in providing probabilistic forecast for both RES [11, 22] and load [39] time-series, making it suitable for the application considered here. This method makes use of a RF structure - i.e., an ensemble of $|\mathcal{T}|$ trees - and this makes it particularly useful for probabilistic forecasting. This is because, besides the prediction of a point value of the response y as in common regression, the whole distribution of the response can be estimated as a function of the predictor input x.

The method is thus formulated so that, in general, at time t one may use the last $L+1$ measured values as input features $x = [P_t, P_{t-1}, \ldots, P_{t-L}]$ to then estimate the conditional empirical distribution $\hat{F}$ of a particular response value $y \in \mathcal{R}$ as

$$\hat{F}(y \mid X = x) = \sum_{j}^{N} \sum_{t \in \mathcal{T}} \frac{1}{|\mathcal{T}|} w_{tj}(x) \mathbb{1}\{Y_j \leq y\}. \tag{5.1}$$

In our specific field case $L = 5$ is the hyperparameter that empirically led to the best results.

To enhance the reproducibility of our results, we note that here X represents the random input feature taking the specific value x, and Y_j are the values of the random response variable for the N observations. Each observation Y_j, $j = 1, \ldots, N$ is instead associated with an input sample X_j that belongs to the dedicated bootstrapped training set of the tree $t \in \mathcal{T}$. Then, for each available observation $j = 1, \ldots, N$, a weight $w_{tj}(x)$ is assigned, given the specific (new) input x, indicating the fraction of training samples X_j that belong to the same leaf $\mathcal{S}_t(x)$ (set of values in a terminal node) as the one that the new input x falls in. In other words, it expresses how much each observation Y_j from the set of values in the terminal node where $x \in \mathcal{S}_t(x)$, from each tree $t \in \mathcal{T}$, should be accounted (used) for the final prediction of y. In our proposed approach, the weights are then calculated as

$$w_{tj}(x) = \frac{\mathbb{1}\{X_j \in \mathcal{S}_t(x)\}}{\sum_{n}^{N} \mathbb{1}\{X_n \in \mathcal{S}_t(x)\}}. \tag{5.2}$$

Note that each tree $t \in \mathcal{T}$ uses different bootstrapped samples from N training observations. Gathering these weights together, it is possible to construct the empirical conditional relative frequency distributions of the response variable, which can then be used for the prediction of different quantiles. The prediction of a single tree can then be computed as

$$\hat{y}_{t,j}(x) = \sum_{j}^{N} w_{tj}(x) Y_j. \tag{5.3}$$

To use the whole RF, consisting of trees trained on different bootstrapped samples X_j, one can then estimate the expected value of the response as

$$\hat{y}_j(x) = \mathbb{E}(Y \mid X = x) = \sum_{j}^{N} w_j(x) Y_j \tag{5.4}$$

where

$$w_j(x) = \frac{1}{\mid \mathcal{T} \mid} \sum_{t \in \mathcal{T}} w_{tj}(x), \ \forall\, j = 1, 2, \ldots, N \tag{5.5}$$

Then the conditional quantile functions can be estimated for quantile probability levels τ as

$$Q_\tau(x) = \inf\{y : \hat{F}(y \mid X = x) \geq \tau\}. \tag{5.6}$$

We note that to assess the quality of the developed forecasting models and avoid overfitting to the training observations, performance metrics shall be calculated based on the *Out-Of-Bag* (*oob*) samples [37]. During the training procedure with RF, in our coding of the technique, the available data are sampled with replacement, creating bootstrap samples specific to each individual learner of the ensemble. Then, the prediction errors

are estimated using the samples that do not belong to the specific bootstrapped samples used for training tree $t \in \mathcal{T}$ (*oob* samples). In this way the *oob* ensemble error estimator is unbiased for the true ensemble error. Therefore, the tuning of the RF parameters can be done based on this, instead of implementing cross-validation.

Finally, we note that our case considers two random response variables, y: the load (power consumption P^{ℓ}) of the platform, and the wind power produced by the wind farm P^{w}. In the following, we thus consider two separate QRF models, one for each of these *RV*s.

5.2.2 Model Selection and Performance

RFs have a low number of hyper-parameters, the main one being the number of trees $|\mathcal{T}|$ that compose the forest. A common data-driven strategy for selecting $|\mathcal{T}|$ is to analyse statistical performance indexes that are commonly used for regression metrics, such as MSE and Normalized Root Mean Squared Error (NRMSE) for the *oob* samples, i.e.,

$$MSE(k) = \frac{1}{\sum_{j=1}^{N} w_{j,k}} \sum_{j=1}^{N} w_{j,k} \left(Y_j(k) - \hat{y}_j(k)\right)^2 \tag{5.7}$$

and

$$NRMSE(k) = \frac{1}{P_n} \sqrt{\frac{1}{N} \sum_{j=1}^{N} w_{j,k} \left(Y_j(k) - \hat{y}_j(k)\right)^2}. \tag{5.8}$$

For example, following this approach leads to results for the *RV* P^{ℓ} such as in figs. 5.1a and 5.1b. In particular, in fig. 5.1a we observe that increasing the number of trees inside the forest generally results in decreasing the resulting MSE for all the lead times $k \in \mathcal{K}$. This decrease is bigger and significant for low trees number, and it becomes less significant as the ensemble of trees grows, until it levels off around $|\mathcal{T}| = 20$. A similar trend is noticed in fig. 5.1b, plotting the relation between the number of trees and lead times. This figure shows that, in general, smaller lead times are associated with smaller NRMSE, meaning that (as intuition would say) short-term predictions are better compared to longer-term ones. However, as the number of trees approaches 20, the NRMSE improvement becomes negligible, as we observe from the increased density of the curves at the lower part of the diagram. Let us note that the scope of this paper is not to improve the QRF method, but rather to demonstrate its applicability and suitability as a good non-linear probabilistic estimator for regression problems with intricate non-linear patterns and how this can be integrated into the optimal energy management, leading to potential benefits (as presented in detail in Section 5.4).

To demonstrate the performance of the developed forecasting models for each random variable, a reference period was selected and the output of the forecasting results for different lead times was monitored, as illustrated in Figure 5.2. As we observe

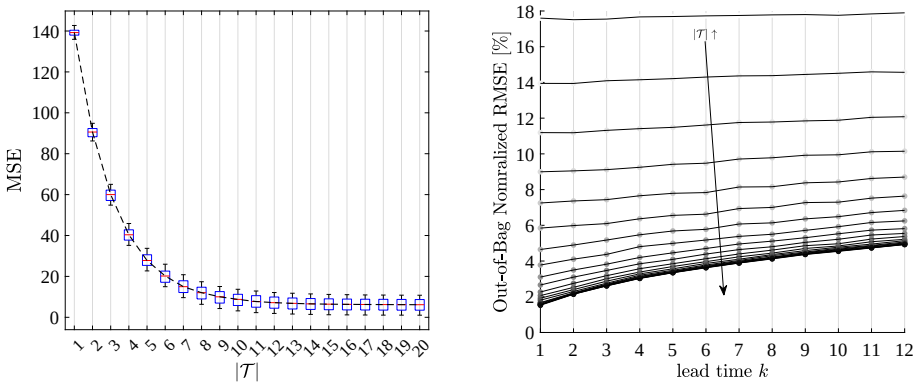

(a) MSE metric for all lead times and increasing the number of trees in the Random Forest.

(b) NRMSE for different numbers of trees in the Random Forest and increasing lead time.

Figure 5.1. Regression model selection based on *oob* performance metrics for different lead times and number of trees in the Random Forest

from fig. 5.2a, the one step ahead forecasting model ($k = 1$) can accurately predict the expected value of the true response, despite the step variations (i.e., within 15 minutes) of the load profile. However, as the lead time increases ($k = 6$), the predictions become less accurate (especially when close to the steps). This demonstrates the challenge of performing precise and detailed prediction of steps for further look ahead times.

We can also note the following interesting behavior of the forecaster: when load profiles tend to be constant, the predictions become more noisy for larger look ahead times, reflecting the deterioration of the forecasts as we look further steps ahead. Similar patterns can also be noticed from figs. 5.2c and 5.2d, where for $k = 1$ the predictions follow accurately the data, while $k = 6$ leads to a remarkably worse quality of the predictions, especially close to the local minima and maxima resulting from wind power ramps-up and ramps-down.

5.3 Power system and SMPC

This section introduces the model of the system to be controlled, i.e., the isolated power system integrating a wind farm and energy storage. A schematic of the consider system is presented in Figure 5.3.

5.3.1 Control system

The control system under consideration is composed of a continuous state, related to the BESS subsystem and discrete ones (binaries) related to the operational status (on/off) of the GTs. The system state can be expressed as

$$\mathbf{x} = \left[x^{SoC}, \mathbf{x}^{gt}_{1:N_g}\right]^T \quad \forall\, g = 1, \ldots, N_g \tag{5.9}$$

where the control input is again hybrid composed of continuous variables (charging and discharging power) and discrete (binary) signals indicating turning on/off of a GT unit. This is expressed as

$$\mathbf{u} = \left[P^{ch}, P^{dis}, b_1^{gt,on}, b_1^{gt,off}, \ldots, b_{N_g}^{gt,on}, b_{N_g}^{gt,off}\right]^T \tag{5.10}$$

Then, given an initial condition

$$\mathbf{x}_0 = \left[x_0^{SoC}, \mathbf{x}_{0,1:N_g}^{gt}\right]^T \tag{5.11}$$

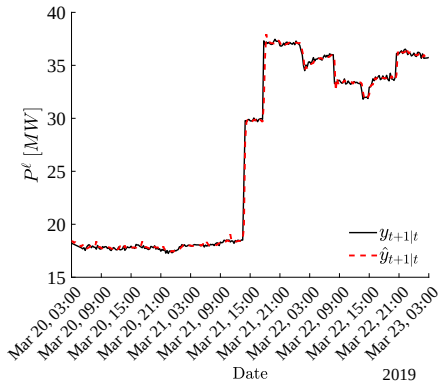

(a) forecasted vs actual load signals for $k = 1$

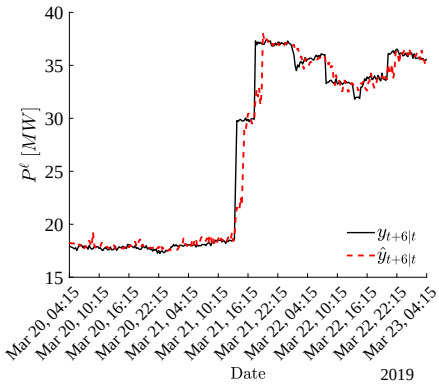

(b) forecasted vs actual load signals for $k = 6$

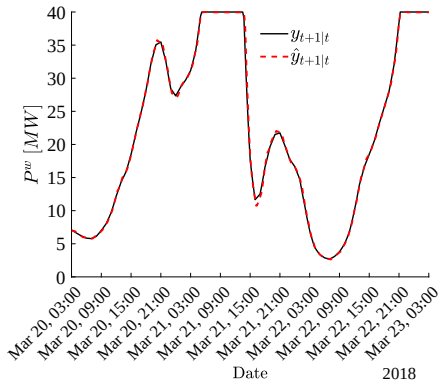

(c) forecasted vs actual wind power signals for $k = 1$

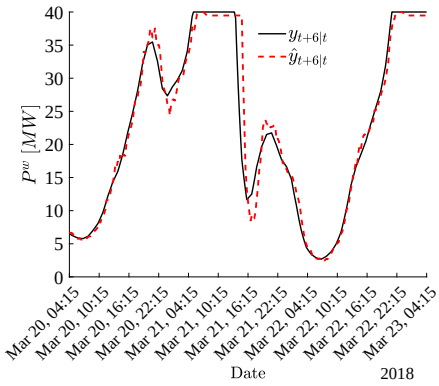

(d) forecasted vs actual wind power signals for $k = 6$

FIGURE 5.2. Forecasted (red) vs actual (black) load and wind power signals using the corresponding developed auto-regressive Random Forest models for different prediction horizons ($k = 1$, $k = 6$)

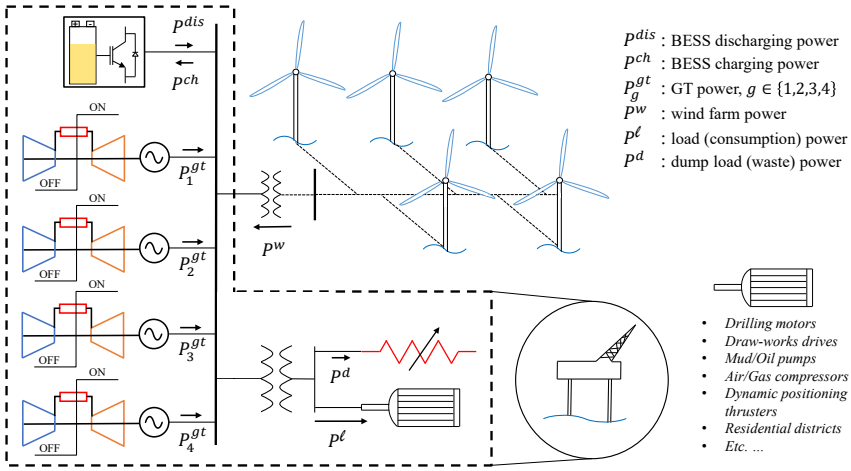

FIGURE 5.3. Simplified single-line diagram of the O&G installation integrates wind power from a local wind farm, a BESS, a controllable load for excess energy dumping, and an aggregated load representing the total load to be covered by the power generation systems

and an optimal control action at $k = 0$

$$\mathbf{u}_0 = \left[P_0^{ch,*}, P_0^{dis,*}, b_{0,1}^{gt,on,*}, b_{0,1}^{gt,off,*}, \ldots, b_{0,N_g}^{gt,on,*}, b_{0,N_g}^{gt,off,*}\right]^T \tag{5.12}$$

we can express the updated state as

$$\mathbf{x}_+ = \boldsymbol{A}_0\mathbf{x}_0 + \boldsymbol{B}_0\mathbf{u}_0 \tag{5.13}$$

where the system matrices are defined as

$$\boldsymbol{A}_0 = diag\left\{\mathbb{1}_{\{1:|\mathcal{K}|\}}^T\right\} \tag{5.14}$$

$$\boldsymbol{B}_0 = \begin{bmatrix} \begin{bmatrix} \frac{\eta_{ch}T_s}{60\overline{E}^b}, & \frac{\eta_{dis}^{-1}T_s}{60\overline{E}^b} \end{bmatrix} & \mathbf{0}_{1\times N_g} \\ \mathbf{0}_{2\times N_g} & \boldsymbol{G}_0 \end{bmatrix} \tag{5.15}$$

where $\boldsymbol{G}_0$ is a $4 \times N_g$ matrix (i.e., the dimensions defined by the number of GTs and associated control actions) defined as

$$\boldsymbol{G}_0 = \begin{bmatrix} 1 & -1 & 0 & \cdots & 0 \\ 0 & 0 & \ddots & 0 & 0 \\ 0 & 0 & \cdots & 1 & -1 \end{bmatrix} \tag{5.16}$$

The setpoints of the GT (continuous) and of the dumping power (continuous), which are outputs of the economic optimal control law, are inputs to the power system but are not considered as part of control system, since they do not affect the state as defined

in eq. (5.9). Thus, for notational consistency, they are not included in the vector u but they are defined as

$$\mathbf{v} = \left[P_1^{gt}, \ldots, P_{N_g}^{gt}, P^d\right]^T \tag{5.17}$$

In the following, the control system variables (eqs. (5.9), (5.10) and (5.17)) are associated with the islanded power grid components, through the modeling of each subsystem's operation.

5.3.2 Gas turbines operation

To capture the detailed operation of the GT units, the fuel/efficiency curve needs to be accurately modeled. The non-linear curve $\mathcal{F}_{fuel}$ is approximated though *Piece-Wise Linear* (PWL) functions as in [40] (details in Section 5.7). Then $\forall\ k \in \mathcal{K},\ g = 1, \ldots, N_g,\ \omega = 1, \ldots, N_\omega$ we have

$$P_{k,\omega,g}^{gt} = \mathbf{D}_P^{gt^T} \mathbf{w}_{k,\omega,g}^{fuel} \tag{5.18}$$

$$x_{k,\omega,g}^{gt} - x_{k-1,g}^{gt} \leq b_{k,\omega,g}^{gt,on} \tag{5.19}$$

$$x_{k-1,g}^{gt} - x_{k,\omega,g}^{gt} \leq b_{k,\omega,g}^{gt,off} \tag{5.20}$$

$$x_{k,\omega,g}^{gt} = x_{k-1,\omega,g}^{gt} + b_{k,\omega,g}^{gt,on} - b_{k,\omega,g}^{gt,off} \tag{5.21}$$

$$b_{k,\omega,g}^{gt,on} + b_{k,\omega,g}^{gt,off} \leq 1 \tag{5.22}$$

$$\mid P_{k,\omega,g}^{gt} - P_{k-1,\omega,g}^{gt} \mid \leq 4\frac{T_s}{60} RR \tag{5.23}$$

$$P_{k,\omega,g}^{gt} \leq \overline{P}^{gt} x_{k,\omega,g}^{gt} \tag{5.24}$$

$$\underline{P}^{gt} x_{k,\omega,g}^{gt} \leq P_{k,\omega,g}^{gt} \tag{5.25}$$

Following [25] we model the common control action at $k = 0$ as

$$P_{0,\omega,g}^{gt} = P_{0,g}^{gt} \quad \forall\ g = 1, \ldots, N_g,\ \omega = 1, \ldots, N_\omega \tag{5.26}$$

Note that no additional variables are needed to bind the binary variables $b_{k,\omega}^{gt,on}$ to be the same at $k = 0,\ \forall\ \omega = 1, \ldots, N_\omega$ because this is enforced by eq. (5.26).

5.3.3 Battery Energy Storage System

Dynamics

The charging/discharging power is modelled through the following set of linear equations

$$P_{k,\omega}^{dis} \leq \overline{P}^b b_{k,\omega}^{dis} \tag{5.27}$$

$$P_{k,\omega}^{ch} \leq \overline{P}^b (1 - b_{k,\omega}^{dis}) \tag{5.28}$$

Following again [25], we model the common control action at $k = 0$ as

$$P_{0,\omega}^{ch} = P_0^{ch} \quad \forall\, \omega = 1, \ldots, N_\omega \tag{5.29}$$

$$P_{0,\omega}^{dis} = P_0^{dis} \quad \forall\, \omega = 1, \ldots, N_\omega \tag{5.30}$$

We can then express the charging and discharging variables $\forall\ k \in \mathcal{K},\ \omega = 1, \ldots, N_\omega$ in compact form as

$$\mathbf{P}^{dis} = \left[P_{0,1}^{dis}, \ldots, P_{|\mathcal{K}|,1}^{dis}, \ldots P_{0,N_\omega}^{dis}, \ldots, P_{|\mathcal{K}|,N_\omega}^{dis}\right]^T \tag{5.31}$$

$$\mathbf{P}^{ch} = \left[P_{0,1}^{ch}, \ldots, P_{|\mathcal{K}|,1}^{ch}, \ldots P_{0,N_\omega}^{ch}, \ldots, P_{|\mathcal{K}|,N_\omega}^{ch}\right]^T \tag{5.32}$$

Then the continuous state of the BESS can be expressed as

$$x_{k,\omega}^{SoC} = 1 - DoD_{k,\omega} \tag{5.33}$$

where $DoD_{k,\omega}$ represents the depth-of-discharge $\ \forall\ k \in \mathcal{K},\ \omega = 1, \ldots, N_\omega$ and given the initial condition $E_0^b = x_0^{SoC}\overline{E}^b$ we can express its time evolution as

$$\begin{aligned} \mathbf{1} - \left(\frac{E_0^b}{\overline{E}^b} diag\left\{\mathbb{1}_{\{1:|\mathcal{K}|\times N_\omega\}}^T\right\} + \frac{T_s}{60\overline{E}^b}\boldsymbol{B}\left(\eta_{ch}\mathbf{P}^{ch} - \eta_{dis}^{-1}\mathbf{P}^{dis}\right)\right) = \\ diag\left\{\mathbb{1}_{\{1:|\mathcal{K}|\times N_\omega\}}^T\right\}\mathbf{DoD} \end{aligned} \tag{5.34}$$

where

$$\mathbf{DoD} = \left[DoD_{0,1}, \ldots, DoD_{|\mathcal{K}|,1}, \ldots DoD_{0,N_\omega}, \ldots, DoD_{|\mathcal{K}|,N_\omega}\right]^T \tag{5.35}$$

subject to

$$\begin{aligned} E_0^b diag\left\{\mathbb{1}_{\{1:|\mathcal{K}|\times N_\omega\}}^T\right\} + \frac{T_s}{60}\boldsymbol{B}\left(\eta_{ch}\mathbf{P}^{ch} - \eta_{dis}^{-1}\mathbf{P}^{dis}\right) \preceq \\ diag\left\{\mathbb{1}_{\{1:|\mathcal{K}|\times N_\omega\}}^T\right\} SoC_{max}\overline{E}^b \end{aligned} \tag{5.36}$$

$$\begin{aligned} E_0^b diag\left\{\mathbb{1}_{\{1:|\mathcal{K}|\times N_\omega\}}^T\right\} + \frac{T_s}{60}\boldsymbol{B}\left(\eta_{ch}\mathbf{P}^{ch} - \eta_{dis}^{-1}\mathbf{P}^{dis}\right) \succeq \\ diag\left\{\mathbb{1}_{\{1:|\mathcal{K}|\times N_\omega\}}^T\right\} SoC_{min}\overline{E}^b \end{aligned} \tag{5.37}$$

where $\boldsymbol{B}$ is defined in Section 5.7.

Battery degradation

Similarly, following [41] and again using PWL approximations [40] for the curve $\mathcal{F}_{deg}$, the battery degradation can be expressed as a combination of linear equations (details in section 5.7). Then, $\forall\ k \in \mathcal{K},\ \omega = 1, \ldots, N_\omega$ we have

$$DoD_{k,\omega} = \mathbf{D}_{dod}^{deg^T} \mathbf{w}_{k,\omega}^{deg} \tag{5.38}$$

$$\rho_{k,\omega} = \mathbf{D}_{cyc}^{deg^T} \mathbf{w}_{k,\omega}^{deg} \tag{5.39}$$

$$d_{k,\omega} \geq \frac{1}{2} \mid \rho_{k,\omega} - \rho_{k-1,\omega} \mid \tag{5.40}$$

$$D_{\omega}^{cyc} \geq \sum_{k \in \mathcal{K}} d_{k,\omega} \quad \forall\ \omega = 1, \ldots, N_\omega \tag{5.41}$$

5.3.4 Wind turbines

The wind power generation is then modeled after the basic power curve of the reference case wind turbines, i.e., as

$$P_{k,\omega}^{w}(w_{k,\omega}) = \begin{cases} 0, & w_{k,\omega} \leq w_{ci} \\ N_w P_n^w \left(\frac{w_{k,\omega}}{w_n}\right)^3, & w_{ci} \leq w_{k,\omega} \leq w_n \\ N_w P_n^w, & w_n \leq w_{k,\omega} < w_{co} \\ 0, & w_{co} \leq w_{k,\omega} \end{cases} \quad \forall\ k \in \mathcal{K},\ \omega = 1, \ldots, N_\omega \tag{5.42}$$

where w_{ci} is the cut-in wind speed; w_n is the nominal wind speed; w_{co} is the cut-off wind speed; P_w^n is the nominal power of each wind turbine; and N_w is the number of wind turbines in the considered wind farm.

5.3.5 Stochastic Model Predictive Controller Design

Then, by interconnecting the control system with its sub-components, as defined in sections 5.3.1 to 5.3.3 with the power system including the stochastic disturbance as described below, we can formulate the proposed SMPC.

Power system

The grid dynamics are expressed through the power balance as

$$\sum_{g}^{N_g} P_{k,\omega,g}^{gt} = P_{k,\omega}^{ch} - P_{k,\omega}^{dis} + P_{k,\omega}^{d} + \xi_{k,\omega} \quad \forall\ k \in \mathcal{K},\ \omega = 1, \ldots, N_\omega \tag{5.43}$$

where $\xi_{k,\omega}$ is the random disturbance composed of load and wind power values at lead time k, formed by scenarios $\omega = 1, \ldots, N_\omega$, as described in section 5.3.5. By iteratively evaluating eq. (5.13) we can then forecast the trajectory

$\mathbf{X}_+ = \left[\mathbf{x}_{t+0|t}, \ldots, \mathbf{x}_{t+k|t}, \ldots, \mathbf{x}_{t+|\mathcal{K}||t}\right]^T$ for the BESS and GT states that are associated with a particular realization ω of the random disturbance signal $\boldsymbol{\xi}_\omega = \left[\xi_{1,\omega}, \ldots, \xi_{|\mathcal{K}|,\omega}\right]^T$ (see eq. (5.48)).

Scenario generation

We now describe a statistically motivated data-driven strategy for generating the scenarios that shall then be used within the stochastic control strategy proposed by this paper.

To arrive at the formulation of the scenarios generation mechanism, we start then by assuming that the predictive QRF models for the *RV*s P^p, with $p = \{\ell, w\}$, have been estimated as proposed in section 5.2. We then note that by using Probability Inverse Transforms, Cholseky decompositions [25, 42], and Gaussian copulas [43], it is possible to generate scenarios and populate the random disturbance signals $\boldsymbol{\xi}_\omega$ as follows: for each *RV* (i.e., both wind and load power), we can get the quantile function (inverse CDF) by interpolating among the set of pre-calculated quantile values as

$$\hat{F^p}^{-1}_{t+k|t}\left(P^p_{t+k} \mid \left[P^p_t, P^p_{t-1}, \ldots, P^p_{t-L}\right]\right) = \left\{Q^p_{\tau,k}\left(\left[P^p_t, P^p_{t-1}, \ldots, P^p_{t-L}\right]\right)\right\}_{\tau\in[0,1]} \quad \forall\ k\ \in\ \mathcal{K}. \tag{5.44}$$

Then, by applying the ECDF to the quantile function, we get a new *RV* U^p_{t+k} uniformly distributed and then by using the inverse Gaussian CDF, we can generate *RV*s that are normally distributed as

$$\mathcal{X}^p_{t+k} = \Phi^{-1}(U^p_{t+k})\ \forall\ k\ \in\ \mathcal{K}. \tag{5.45}$$

Defining $\mathcal{X}^p_t = \left\{\mathcal{X}^p_{t+k}\right\}_{k\in\mathcal{K}}$ as a vectorized *RV*, we can calculate its empirical co-variance for each time step t in an adaptive and recursive way as in [42] by means of

$$\Sigma^p_t = \mu\Sigma^p_{t-1} + (1-\mu)\mathcal{X}^p_t\mathcal{X}^{pT}_t, \tag{5.46}$$

where μ is the forgetting factor of the exponential forgetting scheme, as in [42]. Then, the empirical co-variance can be scaled to get the corresponding correlation matrix R^p_t from which, using a standard normal $\mathbf{z} \sim \mathcal{N}(0,1)$ and the Cholesky decomposition $R^p_t = P^p_t P^{pT}_t$, it is possible to generate normal *RV*s, correlated as in R^p_t, by $\mathbf{z}_c = \mathbf{z}P^p_t$. Finally, by using the Gaussian copula technique, we can generate correlated samples of the *RV*s P^p as

$$\mathcal{Y}^p = \hat{F^p}^{-1}_{t+k|t}\left(\Phi(\mathbf{z}_c)\right),\ \forall\ k \in \mathcal{K}. \tag{5.47}$$

where $\mathcal{Y}^p = \left\{y^p_{t+k|t}\right\}_{k\in\mathcal{K}}$ and $y^p_{t+k|t} \sim \hat{F^p}_{t+k|t}$. In this way we can generate auto-correlated realizations (scenarios)

$$\xi_{k,\omega} = y^{\ell,(\omega)}_{t+k|t}s_r - y^{w,(\omega)}_{t+k|t}\ \ \forall\ k \in \mathcal{K},\ \omega = 1, \ldots, N_\omega \tag{5.48}$$

where s_r is the spinning reserve (percentage). Such scenarios will then be used in the *so* problem defined below.

Objective function

To formulate an optimization problem, one must also define the objective function, that in our case will correspond to an optimal control law whose decision variables are $\mathbf{U}_\mathbf{t}^* = \left[\mathbf{u}_{t+0|t}, \ldots, \mathbf{u}_{t+k|t}, \ldots, \mathbf{u}_{t+|\mathcal{K}||t}\right]^T$ and $\mathbf{V}_\mathbf{t}^* = \left[\mathbf{v}_{t+0|t}, \ldots, \mathbf{v}_{t+k|t}, \ldots, \mathbf{v}_{t+|\mathcal{K}||t}\right]^T$ for any given time step t, where $\mathbf{V_t}$ is the vector of additional optimization variables not considered as inputs to the control system as defined in eq. (5.17) (i.e., GT setpoints and dumping power). More precisely, we consider an optimization problem corresponding to the economic SMPC

$$\begin{aligned} \text{SP:} \quad & \min_{\mathbf{U_t},\mathbf{V_t}} \left\{\mathbb{E}_\omega \left[f(\mathbf{X}_+; \mathbf{U_t}; \mathbf{V_t}; \boldsymbol{\xi}_\omega)\right]\right\} \\ \text{where,} \quad & f\left(\mathbf{X}_+; \mathbf{U_t}; \mathbf{V_t}; \boldsymbol{\xi}_\omega\right) = C_\omega^{fuel} + C_\omega^{gt,str} + C_\omega^{gt,on} + C_\omega^{deg} + C_\omega^{d} \\ \text{s.t.} \quad & \boldsymbol{K}\mathbf{X}_+ + \boldsymbol{L}\mathbf{U_t} + \boldsymbol{M}\mathbf{V_t} + \boldsymbol{N}\boldsymbol{\xi}_\omega \preceq \mathbf{0}, \\ & \boldsymbol{K}_{eq}\mathbf{X}_+ + \boldsymbol{L}_{eq}\mathbf{U_t} + \boldsymbol{M}_{eq}\mathbf{V_t} + \boldsymbol{N}_{eq}\boldsymbol{\xi}_\omega = \mathbf{0}, \quad \forall\, \omega = 1, \ldots, N_\omega. \end{aligned} \tag{5.49}$$

where $\boldsymbol{K}, \boldsymbol{L}, \boldsymbol{M}, \boldsymbol{N}, \boldsymbol{K}_{eq}, \boldsymbol{L}_{eq}, \boldsymbol{M}_{eq}, \boldsymbol{N}_{eq}$ are matrices of appropriate size expressing the linear constraints eqs. (5.13) to (5.43), and the terms of the cost functions are defined as

$$C_\omega^{fuel} = \frac{T_s}{60} c_f \sum_{k\in\mathcal{K}} \sum_{g\in N_g} \mathbf{D}_f^{gt\,T} \mathbf{w}_{k,\omega,g}^{fuel} \tag{5.50}$$

$$C_\omega^{gt,str} = c_{gt}^{str} \sum_{k\in\mathcal{K}} \sum_{g\in N_g} b_{k,\omega,g}^{gt,on} \tag{5.51}$$

$$C_\omega^{gt,on} = \frac{T_s}{60} c_{gt}^{on} \sum_{k\in\mathcal{K}} \sum_{g\in N_g} x_{k,\omega,g}^{gt} \tag{5.52}$$

$$C_\omega^{deg} = \left(c_{b,rpl} - c_{b,res}\right) D_\omega^{cyc} \tag{5.53}$$

$$C_\omega^{d} = \frac{T_s}{60} c_d \sum_{k\in\mathcal{K}} P_{k,\omega}^{d}. \tag{5.54}$$

We note that the cost function defined in eq. (5.49) can be numerically approximated using SAA and equiprobable scenarios issued by the developed probabilistic forecasting model described in Section 5.2. Considering the real time applicability of the proposed method and the solution time of the *so* problem at each time step, the number of scenarios was set equal to 10. Under the lack of generalized theoretical instructions for the exact number of scenarios to be used in the non-convex MILP optimization problems, this number was selected as a trade-off among practical implementation,

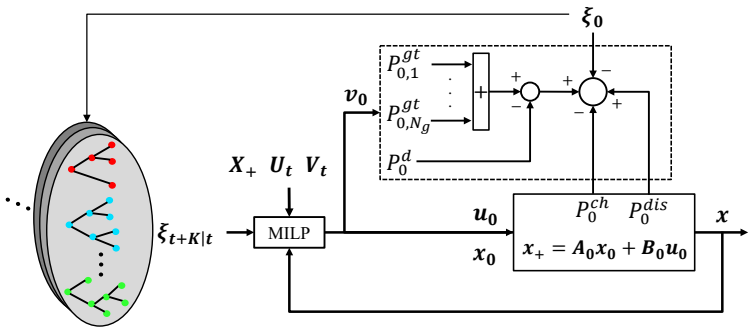

FIGURE 5.4. Control schematic

computational complexity, and solution quality (tight termination criteria for branch-and-cut methods).

Under the proposed framework, the optimal control action $\mathbf{u}_0$ to be applied at time step t is found as $\mathbf{u}_0 = \mathbf{U}_{\mathbf{t},\mathbf{1}}^*$. Correspondingly, the state of the system is updated through eq. (5.13), and the optimal setpoints of the GT and dumped power are given by $\mathbf{v}_0 = \mathbf{V}_{\mathbf{t},\mathbf{1}}^*$. The control schematic diagram is illustrated in Figure 5.4.

5.4 SIMULATION RESULTS AND ANALYSIS

This section assesses the potential benefits of applying the proposed methodology to the case of an isolated wind-powered O&G platform with energy storage, against a deterministic MPC strategy counterpart (DMPC). The approach is thus first investigating the performance of the integrated forecasting algorithm proposed in Section 5.2, and then comparing the control performance of the proposed SMPC-EMS against its deterministic counterpart.

To make such comparisons realistic and valuable, actual load measurements were used from the available datasets (with 15 minutes time resolution), while the wind power generation data were derived from hourly wind speed timeseries data, publicly available at [44, 45] for the specific offshore location of the platform. These measurements were linearly interpolated to match the load timeseries resolution (15 minutes), allowing for the use of a $T_s = 15$ minutes simulation timestep for the rest of the considered components as well (i.e., BESS and GTs).

5.4.1 Assessing the capability of the scenario generation mechanism in capturing irregular events

The proposed stochastic control scheme cannot be effective if its integrated forecasting capability is not effective. To assess this last effectiveness, the performance of the forecaster is here assessed based on commonly used metrics first, and then also by examining specific cases of particularly interesting irregular events.

Continuously Ranked Probability Score

Since the QRF model developed in Subsection 5.2.1 is used to perform probabilistic forecasting, we assess its performance based on the commonly used metric of Continuously Ranked Probability Score (CRPS) [25, 46, 47] and by comparing it against a benchmark method. Respectively, this score is defined as a function of k, for an observation y_{t+k} of the random response variable Y_{t+k} with ECDF $\hat{F}_{t+k|t}(y) = \mathbf{P}[Y_{t+k} \leq y]$ as

$$CRPS(\hat{F}_{t+k|t}, y_{t+k}) = \int_{supp(Y_{t+k})} \left(\hat{F}_{t+k|t}(y) - \mathbb{1}\{y_{t+k} \leq y\}\right)^2 dy \tag{5.55}$$

and is numerically calculated for a test time period $t \in T_{test}$ as

$$CRPS(t,k) = \sum_{\underline{y}_{t+k}}^{y_{t+k}} \hat{F}^2_{t+k|t}(y)dy + \sum_{y_{t+k}}^{\overline{y}_{t+k}} \left(\hat{F}_{t+k|t}(y) - 1\right)^2 dy \tag{5.56}$$

where $supp(Y_{t+k}) = [\underline{y}_{t+k}, \overline{y}_{t+k}]$ is the support of RV Y_{t+k} and dy a fine discretization of the values that the RV can take, given its support.

As for the benchmark algorithm, we perform comparisons against the method from [48], named *CH-PeEn*, which to our knowledge is often used as a universal benchmarking method for a fair comparison. This method basically uses the whole historical dataset to construct distributions of the RVs first, and then uses this information to produce probabilistic forecasts. Note that we constructed a separate model for each lead time $k \in \mathcal{K}$; its CRPS was then calculated as in eq. (5.56), and then compared against the one produced by the QRF method for the selected test period ($t \in T_{crps}$, which was set equal to a whole month, i.e., September).

From Figure 5.5 we can observe the results of the comparison in a dimensionless form, i.e., after the power values of each variable were rescaled to $[0, 1]$. As it is evident from fig. 5.5a, the proposed QRF models, as applied to their corresponding RV (load/wind power), not only improve significantly the probabilistic forecasts compared to *CH-PeEn*, but also achieve very low CRPS values for all the lead times, with the values becoming slightly worse as the lead time increases. From 5.5b we observe again the superiority of the QRF method over *CH-PeEn* (which, actually, is characterized by particularly high values). This means that the distributions produced by the proposed model are much closer to the observations and less spread around it. Finally, the overall relative improvement for the average CRPS across the lead times and for the models concerning the two RVs (load and wind power), is presented in terms of the skill score [25, 46], defined as

$$Sk_{sc} = 1 - \frac{\sum_{t \in T_{test}} \sum_{k \in \mathcal{K}} CRPS_{QRF}(t,k)}{\sum_{t \in T_{test}} \sum_{k \in \mathcal{K}} CRPS_{CH-PeEn}(t,k)}. \tag{5.57}$$

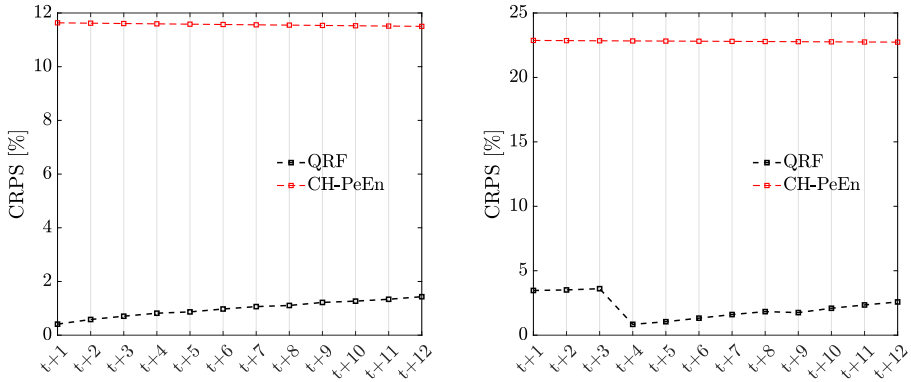

(a) Load (b) Wind power

FIGURE 5.5. CRPS for September

The numerical results are then presented in Table 5.1.

Assessing the capability of capturing irregular events

Typical demanding situations for the efficient operation of isolated grids that are dominated by intermittent power supply and rapidly varying loads, are those that are characterized by non-smooth and/or sudden net load trend variations (irregular events). This means that we need to assess the performance of the proposed forecasting model in capturing irregular events, since capturing them means enabling the proposed SMPC counteracting them, ensuring efficient grid operation. Such events can then be generated using the proposed copula method. For the load profiles, step variations were considered as a test case, while for the wind power, specific points of curvature reversal or saturation were selected. Curvature variations can happen in cases where the trend is reversed, so a wind ramp-down is followed by a wind-ramp-up and vice versa. The saturation occurs when the wind farm reaches its nominal power production capacity.

In Figure 5.6 we see the results of the forecasting capabilities of the proposed approach for different characteristic load patterns. In these diagrams we observe both the true data (black line), the expected forecast (mean prediction - dashed red

TABLE 5.1. Skill score improvement

	$\overline{CRPS}$ [%]	
	P^{ℓ}	P^{w}
CH-PeEn	11.56	22.80
QRF	0.98	2.17
Sk_{sc} [%]	91.51	90.50

line), prediction intervals at various percentiles (green areas), and also the generated scenarios from the proposed method (dashed purple lines). As we observe, the proposed approach is capable to quantify the uncertainty around a forecast by increasing or decreasing the width of the prediction intervals. In particular, from fig. 5.6a we see that when there is low uncertainty and the forecasted profile pattern is quite simple (almost constant), this is followed by a set of generated scenarios where all these scenarios follow the same trend. However, when we are heading towards a load step instant, the uncertainty becomes larger and the prediction intervals more spread (figs. 5.6b and 5.6c). As a result, the anticipated step variation is included in the prediction intervals and as a result, there are scenarios that actually resemble the true variation. This is an important feature, since these scenarios will provide the SMPC information about the existence of possible alternatives for the possible future load patterns. In this way, we get around the inertia problem that characterizes the deterministic forecast, i.e., the tendency for forecasters in the literature to produce patterns that are too similar to the previous values, and do not anticipate deviations. The same is illustrated in fig. 5.6d for a step decrease in load where we can see that scenarios very close to the actual step can be generated.

Similar results can be noted from Figure 5.7 and Figure 5.8. In particular, from Figure 5.7 we see how the uncertainty interval automatically adapts to the time instant of the issued forecasts. This means that it can understand when a change in the signal shape (wind power profile) is happening. Starting with fig. 5.7a, we already observe how the mean forecast (red dashed line) is much affected by the previous values and is not close to the actual curvature. Nevertheless, scenarios very close to the actual shape can be generated. Then, as time moves forward, as we observe from figs. 5.7b to 5.7d, the uncertainty interval constantly becomes larger to include the abrupt curvature change and as a result, even when this change is big enough (fig. 5.7d), scenarios close to reality can be generated. The same characteristics are illustrated in Figure 5.8 for a case where the wind power reaches the saturation level.

5.4.2 Stochastic MPC (SMPC) for Energy Management Under Irregular Events

We then move to assessing the ensemble of the proposed strategies, i.e., the performance of the integration of the forecasting models developed in section 5.2.1 with the proposed MPC formulation described in section 5.3.5. The assessment of the proposed method (SMPC) was realized by comparing it against the performance of its deterministic MPC version (DMPC), through numerical simulations. In addition, a benchmark rule-based method was included in the results to better demonstrate/illustrate the effectiveness of the MPC framework for the EMS.

It is noteworthy that the datasets related to our specialized power system application (offshore O&G platform with wind power integration) are characterized by a significant variety of patterns, resulting in different net load profiles. Therefore, to (correctly) assess the proposed method and compare it against other alternatives while

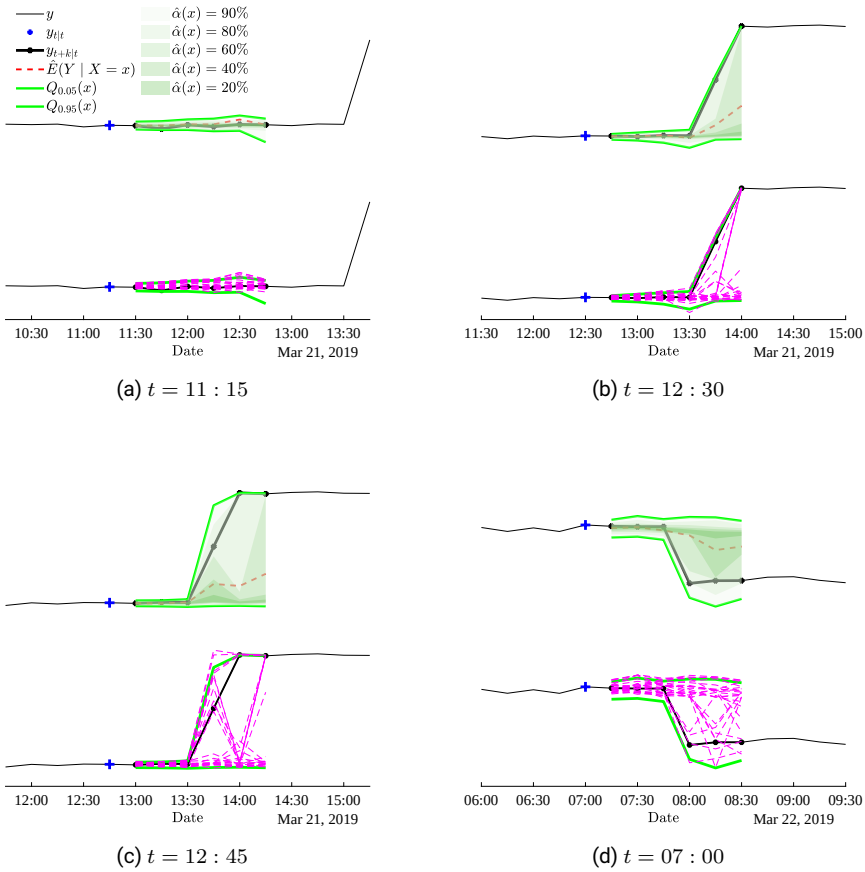

(a) $t = 11:15$ (b) $t = 12:30$

(c) $t = 12:45$ (d) $t = 07:00$

FIGURE 5.6. Various types of an O&G platform's load patterns, reflecting both normal operation and irregular events, such as step variations in both directions. (a) Normal operation (constant loading conditions) (b) Sudden load increase in the near future. Scenarios that accurately capture the variation gradient are generated through the updated (increased) uncertainty interval (c) Moving closer toward the sudden upwards load variation, the updated scenarios closely resemble the shape of the forthcoming load step (d) An example of similar sudden variation, where the load is step-like decreased and the generated scenarios capture this event

capturing the main characteristics of our datasets, different combinations of platform load and wind power generation were considered as case studies. Nevertheless, testing the whole available dataset is computationally intractable, given the restriction of the computational resources and the solution time of the MILP problem on a rolling horizon basis. In this study, the optimization problems were modeled in *Matlab R2020* and solved with *Gurobi 9.1.0* in a 28 physical core multi-node cluster with Intel(R) Xeon(R) CPU E5-2690 v4 @ 2.60 Hz, 25 GB RAM.

However, for the purpose of assessing our method and investigating the potential

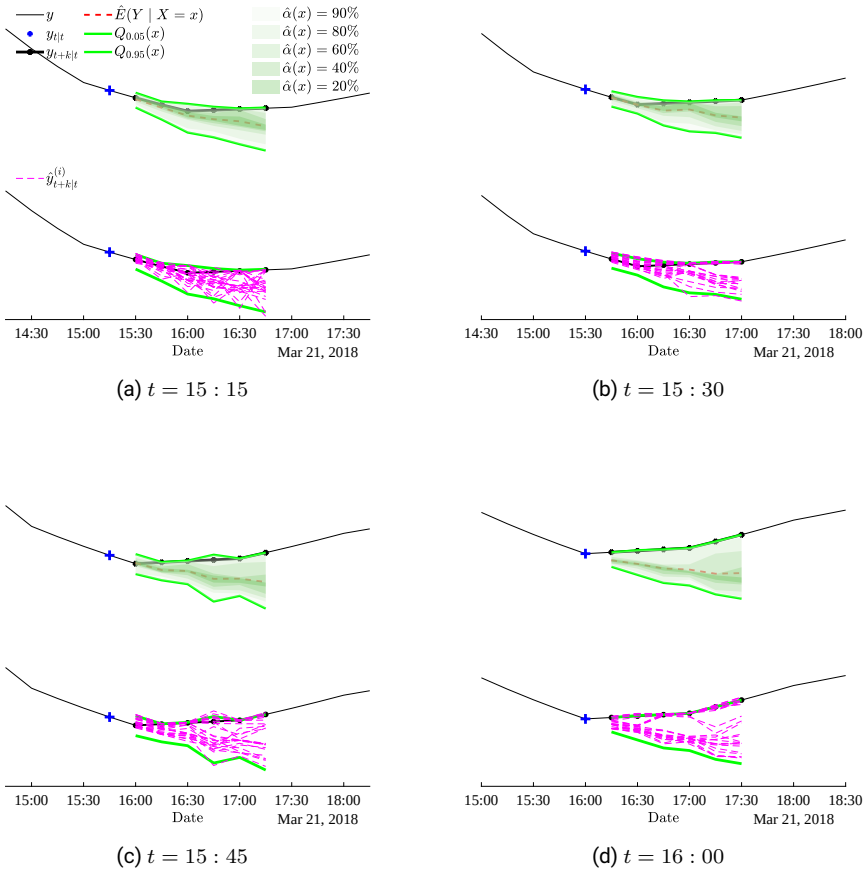

(a) $t = 15:15$ (b) $t = 15:30$

(c) $t = 15:45$ (d) $t = 16:00$

FIGURE 5.7. Example of a trend reversal situation for wind power on 21 March, 15:00 - 18:00 and successive probabilistic forecasts. Following the sub-figures from top to bottom, we see the updated uncertainty intervals associated with each forecast issue time and the generated scenarios that are able to capture the sudden change from a wind power ramp-down to a ramp-up

benefits, some representative daily net load patterns were identified and selected as case studies. They describe typical behaviors present throughout the whole datasets (both load and wind power), capturing in detail the irregular events that are the main target for our method. Such irregular events include sudden transitions from lower to higher loading conditions resembling step-like perturbations that demand the startup or shutdown of an extra GT unit, wind power trend reversals from lower average values ramping up to higher ones and vice versa, or even net load conditions where the operating GT units are marginal, and several switching actions would be required for relatively small net load variation. Capturing case studies with these characteristics allows us to make a more accurate assessment of the proposed method and its applica-

bility to the target applications. The following basic patterns were then considered as case studies.

i. ***LL-SU-WD***: *low* loading conditions including load step *up* under wind ramping *down*

ii. ***ML-SD-WU***: *medium* loading conditions including load step *down* under wind ramping *up*

iii. ***HL-SUD-WU***: *high* loading conditions including load steps *up and down* and wind ramping *up*

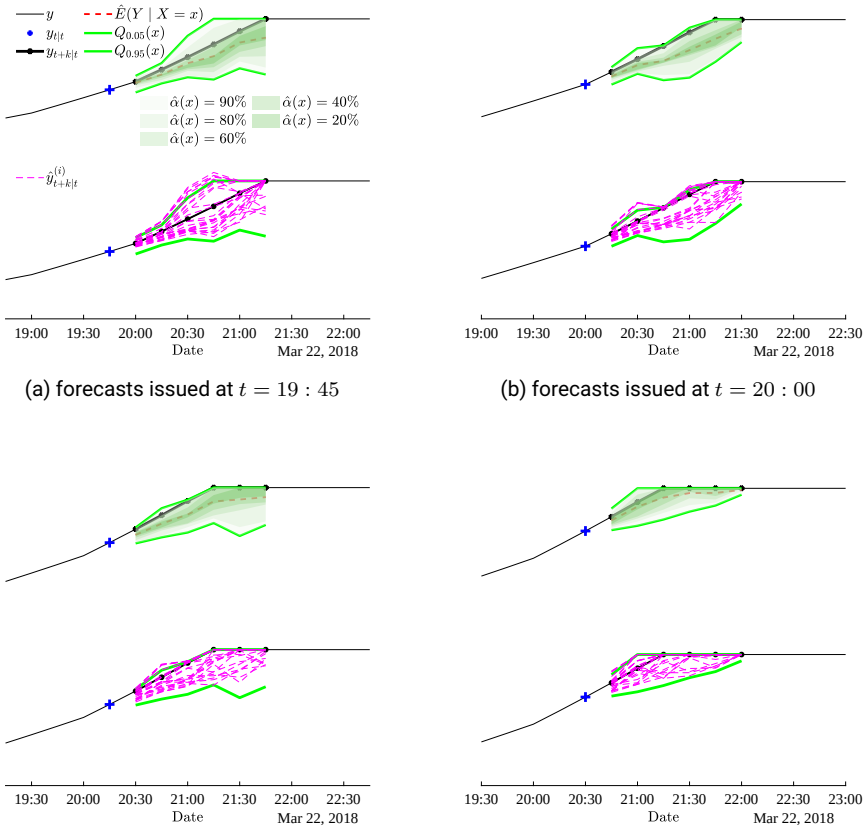

(a) forecasts issued at $t = 19:45$

(b) forecasts issued at $t = 20:00$

(c) forecasts issued at $t = 20:15$

(d) forecasts issued at $t = 20:30$

FIGURE 5.8. Example of a wind power saturation situation on 22 March, 19:00 - 22:00 and successive probabilistic forecasts. Following the sub-figures from top to bottom, we see how the updated uncertainty intervals associated with each forecast issue time, keep on narrowing down, identifying a saturation event

iv. ***LL-SDU-WU***: *low* loading conditions including load steps *down and up* and wind ramping up

v. ***HL-SDU-WD***: *high* loading conditions including load steps *down and up* and wind ramping *down*

vi. ***HL-WD***: *high* loading conditions (almost steady) and wind ramping *down*

Those cases span different operational regimes such as low (L), medium (M), or high (H) loading (L) conditions relative to the total aggregated platform load, capture different types of irregular events such as load steps up (SU), load steps down (SD), or both in any order (SUD, SDU), and also include the effects of wind power ramping up (WU) and down (WD). To assess the performance and compare the proposed controller (SMPC) with the deterministic (DMPC) version, numerical simulations were performed for the above test periods with duration T_t per case. The methods were evaluated and compared in terms of the key performance indices (KPIs) defined in eqs. (5.58) to (5.62). Those reflect the cumulative costs (eq. (5.59)) and emissions production (eq. (5.58)) from the platform operation, the amount of curtailed energy (eq. (5.61)), and the lifetime degradation of the controllable components. The latter can be expressed by the cycling behavior for the BESS (eq. (5.62)) and the number of switching signals (on/off) for the GTs (eq. (5.60)).

$$I_f(\mathbf{x}_+(t), \mathbf{v}_0(t)) = \frac{T_s}{60} \sum_{t \in T_t} \sum_{g \in N_g} \mathcal{F}_{fuel}(P_{0,g}^{gt}(t)) P_{0,g}^{gt}(t) + c_f^{idle} x_{0,g}^{gt}(t) \tag{5.58}$$

$$I_c(\mathbf{x}_+(t), \mathbf{u}_0(t), \mathbf{v}_0(t)) = I_f(\mathbf{x}_+(t), \mathbf{v}_0(t)) c_f + c_{gt}^{str} \sum_{t \in T_t} \sum_{g \in N_g} b_{0,g}^{gt,on}(t) \tag{5.59}$$

$$I_{sw}(\mathbf{u}_0(t)) = \sum_{t \in T_t} \sum_{g \in N_g} b_{0,g}^{gt,on}(t) + \sum_{t \in T_t} \sum_{g \in N_g} b_{0,g}^{gt,off}(t) \tag{5.60}$$

$$I_{de}(\mathbf{u}_0(t), \mathbf{v}_0(t)) = \frac{T_s}{60} \sum_{t \in T_t} \sum_{g \in N_g} P_{0,g}^{gt}(t) - \left(P_0^{ch}(t) - P_0^{dis}(t) \right) - \xi_0(t) \tag{5.61}$$

$$I_{dg}(\mathbf{x}_+(t), \mathbf{u}_0(t)) = \sum_{t \in T_t} D^{cyc}(t) \tag{5.62}$$

where I_f is the total fuel consumption (which can be directly associated with CO_2 emissions because of the linear dependency on the combustion reaction), I_c represents the operational expenditure resulting from the indicated operation of the GTs, I_{sw} accounts for the switching signals turning on or shutting down the GTs expressing the binary control actions, I_{de} is the amount of the actual dumped energy (including the shifted load because of the spinning reserve and safety requirement), and I_{dg} represents the degradation of the BESS as a consequence of the cycling induced by the control action. Those indices encapsulate the effects of the EMS on the operation of the power system under consideration and reflect both economic and environmental aspects.

Case studies assessment

For the analysis of the case studies, we employ the following procedure. First, the actual load, wind power, and resulting net load profiles are plotted together. Net load represents the sequence of values of the disturbance $\xi_0(t),\ \forall\ t = 0, \ldots, T_t$ that acts on the platform power system and needs to be estimated by the proposed forecasting method (section 5.3.5). Then, different colored areas are used on the same plots to indicate different ranges of the values $\xi_0(t)$. These areas highlight the different numbers of operating (turned ON) GTs that would be required to cover the corresponding net load value $\xi_0(t)$ under the following simple benchmark rule-based strategy

if $\xi_0(t) \leq 0$ **then**
  $\mathbf{x}^{gt}_{1:N_g}(t) = 0$
else if $\xi_0(t) \leq P^{gt}_n$ **then**
  $\mathbf{x}^{gt}_{1}(t) = 1 \wedge \mathbf{x}^{gt}_{2:N_g}(t) = 0$
else if $\xi_0(t) \leq 2P^{gt}_n$ **then**
  $\mathbf{x}^{gt}_{1:2}(t) = 1 \wedge \mathbf{x}^{gt}_{3:N_g}(t) = 0$
else if $\xi_0(t) \leq 3P^{gt}_n$ **then**
  $\mathbf{x}^{gt}_{1:3}(t) = 1 \wedge \mathbf{x}^{gt}_{4:N_g}(t) = 0$
else
  $\mathbf{x}^{gt}_{1:N_g}(t) = 1$
end if

In addition, in the same plot on the right axis we can identify the number of on GTs with each proposed method (DMPC/SMPC) and, in this way, we can compare the number of GTs that would be required by each method. This is expressed as

$$I^{gt}_{on}(\mathbf{x}_+(t)) = \sum_{g \in N_g} x^{gt}_g(t) \tag{5.63}$$

Then, the resulting state of charge trajectories with the DMPC and SMPC methods are plotted together with the common disturbance signal on separate figures and finally, the KPIs defined in eqs. (5.58) to (5.62) are calculated.

Case: LL-SU-WD

First, a case of low loading conditions with a load step up and wind ramp down is demonstrated (Figure 5.9). As can be noticed from fig. 5.9a, the load step and the low wind power generation cause the net load to change regime and based on the rule-based strategy, 2 GTs would be required to operate. However, we see from the same figure that under both control algorithms, DMPC and SMPC, after the step, there are some instants where the platform could operate with just a single GT, obtaining the rest

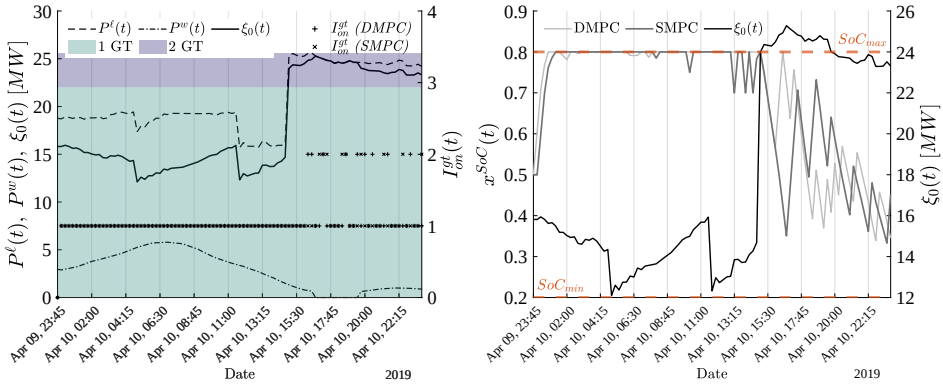

(a) Load, wind power, and net load patterns vs number of on GTs

(b) Net load pattern vs SoC evolution

FIGURE 5.9. Disturbance and optimal states trajectories (discrete and continuous) with DMPC and SMPC controllers, for the case LL-SU-WD

energy from the BESS. This is also illustrated in fig. 5.9b from the SoC trajectories. Initially and up to the load step, both DMPC and SMPC would result in a similar behavior, with the BESS reaching its maximum SoC while charging to provide higher efficiency operating point for the GT. After the step though, the available capacity of the BESS is being used (again by both methods), discharging the battery and providing some extra time for the 1 GT operational regime. From the same figure we also see that at the moment of the step, the proposed SMPC makes better use of the BESS, providing a deeper discharge and thus some extra time to the 1 GT regime. Then, some oscillations are induced by both methods while trying to minimize the number of on GTs but also operating them as efficiently as possible not to significantly increase the emissions level. Of course, this behavior increases the BESS degradation, but it highly depends on the weighting of the corresponding cost term (eq. (5.53)), in the objective function (eq. (5.49)) which in our case was set based on the investment and residual costs of the battery (see Table 5.9) as in [41]. Different values for the weight would induce different behaviors with possibly fewer oscillations. As the effect of the net load transient vanishes, the SoC trajectories become more similar and converge approaching the end of the day. The improved performance of the SMPC during the (unavoidable) oscillatory behavior is reflected in the fewer GT switching signals (Table 5.2), avoiding startup costs and eventually resulting in reduced cost at the expense of a slightly higher BESS degradation. In addition, despite these benefits, the proposed SMPC does not significantly deteriorate the energy dumping and the fuel consumption (Table 5.2).

TABLE 5.2. LL-SU-WD KPIs

KPI	MPC Method		Net
	DMPC	SMPC	
I_c [€]	54,277	51,922	2,354
I_f $[tn]$	143.53	145.69	-0.266
I_{sw} $[-]$	17	13	4
I_{de} $[MWh]$	24.05	24.09	-0.049
I_{dg} [%]	0.311	0.387	-0.076

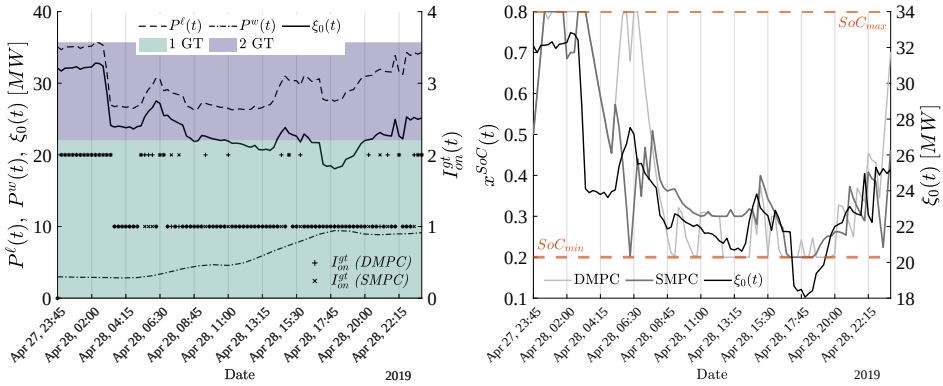

(a) Load, wind power, and net load patterns vs number of on GTs

(b) Net load pattern vs SoC evolution

FIGURE 5.10. Disturbance and optimal states trajectories (discrete and continuous) with DMPC and SMPC controllers, for the case ML-SD-WU

Case: ML-SD-WU

Next, a case with medium loading conditions, a load step down, and a wind power ramp up is presented (Figure 5.10). In this case, although a clear step down is observed on the load (early times), after that it is still highly variable alternating between the regimes of 1 and 2 on GTs (fig. 5.10a). Again, we notice that under the optimal policies of both MPC controllers, we decrease the number of operating GT compared to the rule-based strategy. Even though DMPC and SMPC result in similar SoC trajectories initially, at the first load upwards rise right after the step down, the SMPC realizes that it can operate with a single GT for a bit longer and thus discharges the BESS to provide the additional energy (fig. 5.10b). After this event, the trajectories deviate but both follow similar trends. In this case, the superiority of the proposed control scheme resulted in significant cost savings coming from both fuel consumption reduction and much fewer GT startups again at the small cost of marginally higher BESS degradation (Table 5.3).

TABLE 5.3. ML-SD-WU KPIs

KPI	MPC Method		Net
	DMPC	SMPC	
I_c [€]	71,154	66,105	5,049
I_f $[tn]$	185.74	181.04	4.693
I_{sw} $[-]$	25	19	6
I_{deg} $[MWh]$	34.55	34.50	0.051
I_{dg} $[\%]$	0.347	0.452	-0.105

TABLE 5.4. HL-SUD-WU KPIs

KPI	MPC Method		Net
	DMPC	SMPC	
I_c [€]	153,815	152,438	1,377
I_f $[tn]$	487.72	487.18	0.539
I_{sw} $[-]$	11	9	2
I_{de} $[MWh]$	82.16	89.12	-6.961
I_{dg} $[\%]$	0.095	0.070	0.025

Case: HL-SUD-WU

Then, an interesting case of high loading conditions with both up and down steps and low to medium wind conditions is examined (Figure 5.11). This represents a case where all GTs would be required to provide the necessary power (fig. 5.11a). As the capacity of the systems is close to its limits (more GTs required), the potential benefits decrease since the flexibility provided by the BESS depends on its (limited) size and how this compares with the power capability of a single GT unit. However, again in this case, the SMPC demonstrated its capability to reduce costs by properly controlling the timing and number of on/off commands to the GTs. As we can see in fig. 5.11b, interestingly the SoC trajectories deviate from the first moment while the SMPC chooses to discharge the BESS. As such, and in contrast with the DMPC which chose to have maximum SoC during the early stage, the BESS can later be used to react on the load step up (SU), providing higher efficiency operating points for the additional GT that starts almost simultaneously with this event. However, this action is unavoidably associated with somewhat higher energy dumping compared to the DMPC method, as noticed in Table 5.4. From fig. 5.11b, we also see that although both methods discharge the BESS equally close to the SD event, the SMPC can better forecast the rapid load increase right afterwards and in contrast with the DMPC, avoids recharging the BESS. In this way, it can get more time with 1 less GT on, resulting in fewer GT startups and degrading the BESS less. The effects are quantified in Table 5.4.

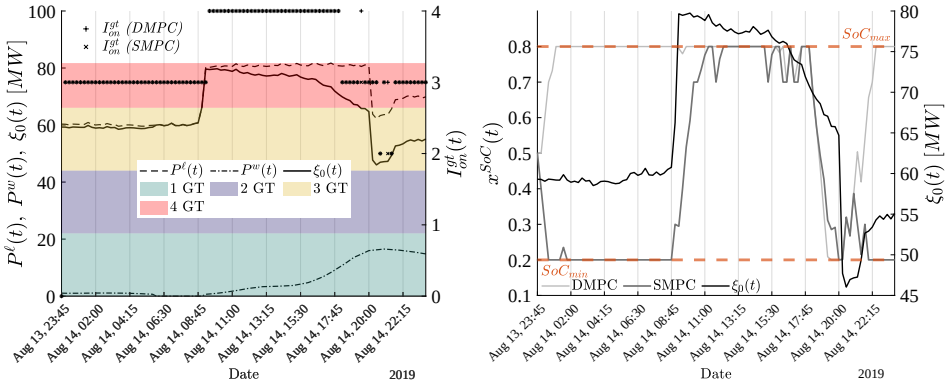

(a) Load, wind power, and net load patterns vs number of on GTs

(b) Net load pattern vs SoC evolution

FIGURE 5.11. Disturbance and optimal states trajectories (discrete and continuous) with DMPC and SMPC controllers, for the case HL-SUD-WU

TABLE 5.5. LL-SDU-WU KPIs

KPI	MPC Method		Net
	DMPC	SMPC	
I_c [€]	60,633	57,937	2,696
I_f $[tn]$	170.85	169.97	0.881
I_{sw} $[-]$	14	11	3
I_{de} $[MWh]$	28.26	28.24	0.02
I_{dg} [%]	0.317	0.212	0.105

Case: LL-SDU-WU

Benefits with the proposed SMPC are also noticed from a case with low loading conditions, step transitions from the 2 GTs to 1 GT on regime and vice versa, and wind power ramping up (Figure 5.12). From fig. 5.12a we observe that with both MPC algorithms, we can achieve longer period of times (i.e., in the morning) with 1 GT on while the net load is on the 2 GTs regime. Also, from fig. 5.12b we observe that initially both SoC trajectories follow similar trends, with the one from SMPC presenting deeper discharging. Then, the trajectories deviate again after the second load step variation (step up) where the SMPC trajectory remains at high SoC levels, allowing the single on GT to operate closer to its maximum efficiency point (net load around closer to P^{gt}_n), anticipating for the wind ramping up. In this way, not only lower cost is achieved and fewer GT startups, but also less BESS degradation (Table 5.5).

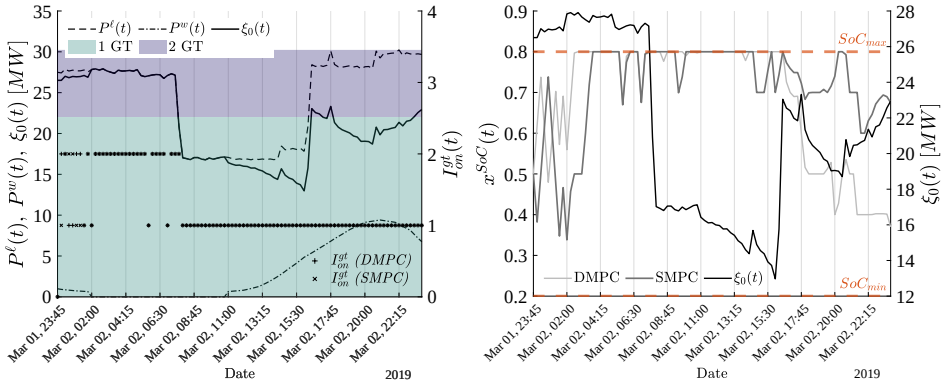

(a) Load, wind power, and net load patterns vs number of on GTs

(b) Net load pattern vs SoC evolution

FIGURE 5.12. Disturbance and optimal states trajectories (discrete and continuous) with DMPC and SMPC controllers, for the case LL-SDU-WU

TABLE 5.6. HL-SDU-WD KPIs

KPI	MPC Method		Net
	DMPC	SMPC	
I_c [€]	31,797	27,708	4,089
I_f $[tn]$	69.97	68.49	1.472
I_{sw} $[-]$	17	11	6
I_{de} $[MWh]$	52.45	52.28	0.169
I_{dg} [%]	0.416	0.440	-0.024

Case: HL-SDU-WD

Another interesting case happens when the loading conditions are high but still enough wind power is being generated, resulting in fewer GTs required and almost zero net load (Figure 5.13). From fig. 5.13a we observe once more the capability of the MPC to operate with fewer GTs on, compared to the rule-based benchmark method. In particular, the BESS is used similarly in both methods to discharge power over the period of time right after the load step down, providing the necessary reliability and capacity to the platform and keeping the GTs down for the very low net load values (fig. 5.13b). However, after the load steps up again, even though both methods result in an oscillatory SoC behavior similarly as in the case *LL-SU-WD*, eventually the trajectories deviate. As a result, the SMPC achieves significant cost and fuel reduction (Table 5.6).

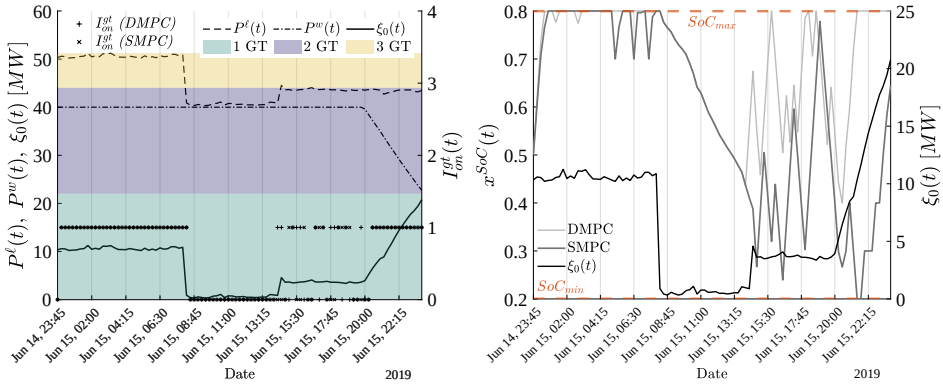

(a) Load, wind power, and net load patterns vs number of on GTs

(b) Net load pattern vs SoC evolution

Figure 5.13. Disturbance and optimal states trajectories (discrete and continuous) with DMPC and SMPC controllers, for the case HL-SDU-WD

Table 5.7. HL-WD KPIs

KPI	MPC Method		Net
	DMPC	SMPC	
I_c [€]	69,799	66,510	3,289
I_f [tn]	201.61	198.75	2.870
I_{sw} [$-$]	14	10	4
I_{de} [MWh]	63.31	63.83	-0.518
I_{dg} [%]	0.375	0.359	0.016

Case: HL-WD

Finally, similar benefits can be noticed from a case where loading conditions are relatively more stable compared to the rest cases, without large and abrupt steps (Figure 5.14). Again, from fig. 5.14a we can see the superiority of the MPC methods compared to the rule-based one, where the platform can be operated with fewer GTs. Interestingly, the SoC trajectories defined by DMPC and SMPC deviate from the beginning of the day and eventually, when the net load transits from the 1 GT to the 2 GTs regime, the SMPC method manages to hold only 1 GT in operation longer than the DMPC. As a result, significant cost and fuel reductions were achieved again (Table 5.7).

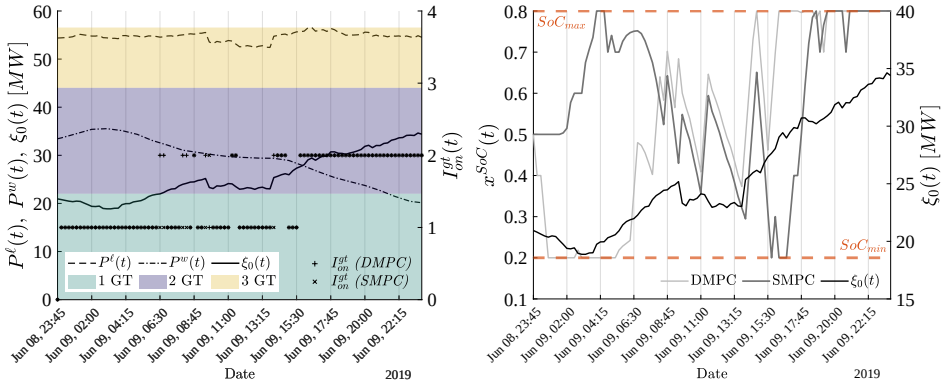

(a) Load, wind power, and net load patterns vs number of on GTs

(b) Net load pattern vs SoC evolution

FIGURE 5.14. Disturbance and optimal states trajectories (discrete and continuous) with DMPC and SMPC controllers, for the case HL-WD

Cases comparison

The cumulative results for the performance comparison of the DMPC and SMPC methods, for all the cases considered, are given in Table 5.8. From this table, we can identify the capability of the proposed method to achieve lower fuel consumption, significant cost reduction, and much smoother GT operation, depending on the loading level of the platform and the combination of load and wind power patterns. In particular, we see that the maximum cost reduction (case *HL-SDU-WD*) is associated with the maximum improvement in GT turn ups/downs, while the minimum cost reduction (case *HL-SUD-WU*) is associated with the smallest improvement in GT turn ups/downs. It is also important to clarify that fuel reduction percentages are also equal to the CO_2 emissions reduction percentages, coming from the normal operation of the GTs. However, there are additional environmental benefits resulting from the fewer GT start ups, which are associated with high emissions that would add up to the improvement of the emissions coming from the normal GT operation.

TABLE 5.8. Comparison of the DMPC and SMPC methods with relative KPIs

Case	ΔI_c [%]	ΔI_f [%]	$\Delta I_{on/off}$ [%]
LL-SU-WD	4.338	-0.180	23.53
ML-SD-WU	7.096	2.526	24.00
HL-SUD-WU	0.896	0.111	18.18
LL-SDU-WU	4.447	0.515	21.43
HL-SDU-WD	12.861	2.104	35.29
HL-WD	4.712	1.423	28.57

5.5 Conclusions and future works

It is challenging to operate isolated power systems that integrate renewable sources together with flexible conventional generating units and energy storage, while solving the task efficiently and cost-optimally. This gets even harder for industrial systems or small scale isolated grids where the load intermittency is increased compared to large power systems where load aggregation has a smoothing effect. Short-term abrupt step variations combined with the stochastic nature of renewable sources make it hard to accurately forecast the near future power imbalance. Thus, the power scheduling solution from the energy management system may be sub-optimal. In addition, the existence of binary operational status of conventional thermal units and the multiple conflicting objectives pose an additional challenge to preforming optimal energy management.

This paper proposed a SMPC scheme aimed at solving the EMS problem under uncertainty for isolated power systems that are characterized by abrupt load variations and lack of future events information. The developed controller is designed to solve an optimal control problem on a rolling horizon basis, using stochastic mixed-integer linear programming and considering the minimization of operational costs, battery degradation, and dumped energy simultaneously. The proposed EMS framework integrates a data-driven mechanism to represent future uncertainty by means of quantile regression and scenario generation, providing useful information for the expected uncertainty bounds over the load and renewable generation. With the proposed probabilistic forecasting framework, significant skill score improvement was achieved for both load forecasts (91.50%) and wind power forecasts (90.50%). This made it possible to better anticipate near-future irregular events just by using past information.

We thus considered the specific case study of an offshore O&G platform that integrates wind power. The performance of the proposed algorithm was then evaluated and benchmarked against a deterministic version to assess the benefits of making the optimization problem stochastic. For this reason, several case studies capturing the high variation of loading conditions (characterizing O&G platforms) and the intermittency of wind power were considered. The results showed that, under the proposed SMPC-EMS, in all the patterns examined, better planning of the resources could be achieved leading to daily operational cost savings up to 12.86%, fuel consumption and emissions reduction from normal GT operation up to 2.56%, and less switching of the GTs up to 35.29%.

Even though the proposed SMPC-EMS deals with the optimal techno-economic operation of the isolated grid, it does not explicitly consider operational constraints related to the smaller time-scale stability of the system when rapid net load variations occur. Such a limitation could be overcome by integrating adaptive state of charge limits, ensuring the additional provision of ancillary services by the energy storage system, supporting the local grid. The proposed method could be easily adapted to other cases of isolated power systems (i.e., any kind of industrial plants or small-scale

physical islands) that integrate various and multiple kinds of RESs (i.e., solar energy) by re-purposing the QRF models on the corresponding datasets and including more stochastic scenarios representing disturbances from each RV, to cover a possibly more diverse situation.

5.6 Appendix A

Table 5.9. Nomenclature

Description	Symbol
Random Forest	
tree in set of trees bag	$t \in \mathcal{T}$
lead time in prediction horizon	$k \in \mathcal{K}$
observations in dataset	$Y_j,\ j = 1, \cdots, N$
predictor (input feature)	$x = [P_t, P_{t-1}, \ldots, P_{t-L}]$
power value at time t	P_t
leaf set of values of a tree t containing predictor x	$x \in \mathcal{S}_t(x)$
induced weight of tree t for observation j	$w_{tj}(x)$
induced weight of observation j	$w_j(x)$
mean response value of the random forest	$\hat{y}_j(x)$
percentile	τ
quantile of predictor x	$Q_\tau(x)$
estimated prediction interval given x	$\hat{\alpha}(x)$
observation value (input predictor)	$x \in \mathcal{X}$
future values (data)	$y_{t+k\|t}$
scenario generated	$i \in \mathcal{N}_s$
response value (prediction)	$\hat{y}_{t+k\|t}$
response value (prediction) for scenario i	$\hat{y}^{(i)}_{t+k\|t}$
power consumption random variable	P^ℓ
wind power random variable	P^w
SMPC	
PWL approximations	$p = 1, \ldots, N_{pwl}$
set of available synchronous generators	$g = 1, \ldots, N_g$
set of scenarios	$\omega = 1, \ldots, N_\omega$
set of lead times for the forecasting models	$k = 1, \ldots, \mid \mathcal{K} \mid$
fuel curve X data values (P^{gt} [MW])	$\mathbf{D}^{gt}_P$
fuel curve Y data values (f^{gt} [kg/MWh])	$\mathbf{D}^{gt}_f$
fuel curve	$\mathcal{F}_{fuel}$
battery degradation curve X values	$\mathbf{D}^{deg}_{dod}$
battery degradation curve Y values	$\mathbf{D}^{deg}_{cyc}$
battery degradation curve	$\mathcal{F}_{deg}$
SoC	x^{SoC}
GT status	$\mathbf{x}^{gt}_{1:N_g}$
control input	$\mathbf{u}$
charging power	P^{ch}

Continued on next page

Table 5.9 – continued from previous page

Description	Symbol
discharging power	P^{dis}
GT turn ON command	$b_g^{gt,on}$
GT turn OFF command	$b_g^{gt,off}$
GT power	P^{gt}
random disturbance	ξ
Random Variable at time t	$P^p_{t+k},\ p = \{\ell, w\}$
estimated inverse conditional CDF	$\hat{F^p}^{-1}_{t+k\|t}\left(P^p_{t+k} \mid x\right)$
inverse normal CDF	Φ^{-1}

TABLE 5.10. Parameter values

Parameter	Symbol	Value	Units
Sets			
GTs	N_g	4	[-]
Scenarios	N_ω	10	[-]
PWL points	N_{pwl}	11	[-]
prediction horizon (SMPC)	$\mid \mathcal{K} \mid$	6	[-]
Non-linear curves			
fuel curve coefficient	α_f	0.5109	[-]
fuel curve coefficient	β_f	-20.933	[-]
fuel curve coefficient	γ_f	433.83	[-]
degradation curve coefficient	k_0	1591.1	[-]
degradation curve coefficient	k_1	2.089	[-]
BESS			
max battery power	$\overline{P}^b$	5	[MW]
battery capacity	$\overline{E}^b$	10	[MWh]
max SoC	SoC_{max}	0.8	[p.u.]
min SoC	SoC_{min}	0.2	[p.u.]
charging efficiency	η_{ch}	0.95	[p.u.]
discharging efficiency	η_{dis}	0.95	[p.u.]
GT			
nominal GT power	P_n^{gt}	20.200	[MW]
max GT power	$\overline{P}^{gt}$	22.018	[MW]
min GT power	$\underline{P}^{gt}$	4.040	[MW]
GT ramping rate	RR	22.018	[MW/15 min]

Continued on next page

Table 5.10 – continued from previous page

Parameter	Symbol	Value	Units
spinning reserve	s_r	5	[%]
idling (no-load) fuel consumption	c_f^{idle}	1,679	[kg/h]
cost coefficients			
fuel cost	c_f	0.2979	[€/kg]
startup cost	c_{gt}^{str}	1,217	[€/startup]
fixed on cost	c_{gt}^{on}	5,000	[€/on time]
battery replacement cost	$c_{b,rpl}$	445,000	[€]
battery residual cost	$c_{b,res}$	44,500	[€]
energy dumping cost	$c_{b,res}$	1,000	[€/MW]
Wind Turbine Power Curve			
cut in speed	w_{ci}	3	$\left[\frac{m}{s}\right]$
cut off speed	w_{co}	25	$\left[\frac{m}{s}\right]$
rated wind speed	w_n	12	$\left[\frac{m}{s}\right]$
rated power	P_n^w	8	[MW]
wind turbines	N_w	5	[-]
simulation time step	T_s	15	[min]
case studies duration	T_t	24	[h]

5.7 Appendix B

List of sets used in the proposed models:

i. $p = 1, \ldots, N_{pwl}$: points used in the PWL approximations of non-linear functions

ii. $g = 1, \ldots, N_g$: set of available GTs (conventional generators)

iii. $\omega = 1, \ldots, N_\omega$: set of scenarios

iv. $k = 1, \ldots, \mid \mathcal{K} \mid$: set of lead times for the forecasting models

List of sets of data points:

i. $\mathbf{D}_P^{gt} = \left[D_{P,1}^{gt}, \ldots, D_{P,N_{pwl}}^{gt}\right]^T$: fuel curve X data values (P^{gt} [MW])

ii. $\mathbf{D}_f^{gt} = \left[D_{f,1}^{gt}, \ldots, D_{f,N_{pwl}}^{gt}\right]^T$: fuel curve Y data values (f^{gt} [kg/MWh])

iii. $\mathbf{D}_f^{gt} = \mathcal{F}_{fuel}(\mathbf{D}_P^{gt})$ transformation (fuel curve)

iv. $\mathcal{F}_{fuel}(x) = \alpha_f x^2 + \beta_f x + \gamma_f$ fuel curve definition

v. $\mathbf{D}^{deg}_{dod} = \left[D^{deg}_{dod,1}, \ldots, D^{deg}_{dod,N_{pwl}}\right]^T$: battery degradation curve X values

vi. $\mathbf{D}^{deg}_{cyc} = \left[D^{deg}_{cyc,1}, \ldots, D^{deg}_{cyc,N_{pwl}}\right]^T$: battery degradation curve Y values

vii. $\mathbf{D}^{deg}_{cyc} = \mathcal{F}_{deg}(\mathbf{D}^{deg}_{dod})$ transformation (degradation curve)

viii. $\mathcal{F}_{deg}(x) = \frac{100}{k_0 x^{-k_1}}$ degradation curve definition

Fuel curve PWL approximation

$$\mathbb{1}^T_{\{1:N_{pwl}\}} \cdot \mathbf{w}^{fuel}_{k,\omega,g} = x^{gt}_{k,\omega,g} \tag{5.64}$$

$$w^{fuel}_{k,\omega,g,1} \leq \lambda^{fuel}_{k,\omega,g,1} \tag{5.65}$$

$$w^{fuel}_{k,\omega,g,p} \leq \lambda^{fuel}_{k,\omega,g,p-1} + \lambda^{fuel}_{k,\omega,g,p} \tag{5.66}$$

$$w^{fuel}_{k,\omega,g,N_{pwl}} \leq \lambda^{fuel}_{k,\omega,g,N_{pwl}-1} \tag{5.67}$$

$$\mathbb{1}^T_{\{1:N_{pwl}-1\}} \cdot \boldsymbol{\lambda}^{fuel}_{k,\omega,g} = x^{gt}_{k,\omega,g} \tag{5.68}$$

We define $\boldsymbol{B}_\omega$ as a square matrix of dimension $\mid \mathcal{K} \mid$ as

$$\boldsymbol{B}_\omega = \begin{bmatrix} 1 & 0 \cdots & 0 \\ 1 & 1 \cdots & 0 \\ & \vdots & \\ 1 & 1 \cdots & 1 \end{bmatrix} \quad \forall\, \omega = 1, \ldots, N_\omega \tag{5.69}$$

and

$$\boldsymbol{B} = \begin{bmatrix} \boldsymbol{B}_1 & 0 & 0 \\ 0 & \ddots & 0 \\ 0 & 0 & \boldsymbol{B}_{N_\omega} \end{bmatrix} \tag{5.70}$$

Degradation curve PWL approximation

$$\mathbb{1}^T_{\{1:N_{pwl}\}} \cdot \mathbf{w}^{deg}_{k,\omega} = 1 \tag{5.71}$$

$$w^{deg}_{k,\omega,1} \leq \lambda^{deg}_{k,\omega,1} \tag{5.72}$$

$$w^{deg}_{k,\omega,p} \leq \lambda^{deg}_{k,\omega,p-1} + \lambda^{deg}_{k,\omega,p} \tag{5.73}$$

$$w^{deg}_{k,\omega,N_{pwl}} \leq \lambda^{deg}_{k,\omega,N_{pwl}-1} \tag{5.74}$$

$$\mathbb{1}^T_{\{1:N_{pwl}-1\}} \cdot \boldsymbol{\lambda}^{deg}_{k,\omega} = 1 \tag{5.75}$$

5.8 References

[1] R. Machlev, N. Zargari, N. R. Chowdhury, J. Belikov, and Y. Levron, "A review of optimal control methods for energy storage systems - energy trading, energy balancing and electric vehicles," *Journal of Energy Storage*, vol. 32, p. 101787, Dec. 2020. [Online]. Available: http://www.sciencedirect.com/science/article/pii/S2352152X20316248 Cited on page/s 98, 99.

[2] R. Itiki, S. G. Di Santo, C. Itiki, M. Manjrekar, and B. H. Chowdhury, "A comprehensive review and proposed architecture for offshore power system," *International Journal of Electrical Power & Energy Systems*, vol. 111, pp. 79–92, Oct. 2019. [Online]. Available: http://www.sciencedirect.com/science/article/pii/S014206151930095X Cited on page/s 98.

[3] S. Settemsdal, L. Barstad, and W. Voss, "Hybrid power plants can help decarbonize offshore drilling rigs and vessels," *Endeavor Business Media*, no. Offshore, p. 4, May 2020. Cited on page/s 98.

[4] M. G. Abidi, M. Ben Smida, M. Khalgui, Z. Li, and N. Wu, "Multi-agent oriented solution for forecasting-based control strategy with load priority of microgrids in an island mode – Case study: Tunisian petroleum platform," *Electric Power Systems Research*, vol. 152, pp. 411–423, Nov. 2017. [Online]. Available: https://linkinghub.elsevier.com/retrieve/pii/S0378779617302985 Cited on page/s 98.

[5] D. Pavković, A. Sedić, and Z. Guzović, "Oil drilling rig diesel power-plant fuel efficiency improvement potentials through rule-based generator scheduling and utilization of battery energy storage system," *Energy Conversion and Management*, vol. 121, pp. 194–211, Aug. 2016. [Online]. Available: https://linkinghub.elsevier.com/retrieve/pii/S0196890416303909 Cited on page/s 98.

[6] M. Jafari, A. Botterud, and A. Sakti, "Estimating revenues from offshore wind-storage systems: The importance of advanced battery models," *Applied Energy*, vol. 276, p. 115417, Oct. 2020. [Online]. Available: https://www.sciencedirect.com/science/article/pii/S0306261920309296 Cited on page/s 99.

[7] N. Anglani, G. Oriti, and M. Colombini, "Optimized energy management system to reduce fuel consumption in remote military microgrids," p. 9. Cited on page/s 99.

[8] A. Berrueta, M. Heck, M. Jantsch, A. Ursúa, and P. Sanchis, "Combined dynamic programming and region-elimination technique algorithm for optimal sizing and management of lithium-ion batteries for photovoltaic plants," *Applied Energy*, vol. 228, pp. 1–11, Oct. 2018. [Online]. Available: https://linkinghub.elsevier.com/retrieve/pii/S0306261918309279 Cited on page/s 99.

[9] M. F. Roslan, M. A. Hannan, P. Jern Ker, R. A. Begum, T. Indra Mahlia, and Z. Y. Dong, "Scheduling controller for microgrids energy management system using optimization algorithm in achieving cost saving and emission reduction," *Applied Energy*, vol. 292, p. 116883, Jun. 2021. [Online]. Available: https://www.sciencedirect.com/science/article/pii/S0306261921003718 Cited on page/s 99.

[10] M. Restrepo, C. A. Cañizares, J. W. Simpson-Porco, P. Su, and J. Taruc, "Optimization- and Rule-based Energy Management Systems at the Canadian Renewable Energy Laboratory microgrid facility," *Applied Energy*, vol. 290, p. 116760, May 2021. [Online]. Available: https://www.sciencedirect.com/science/article/pii/S0306261921002671 Cited on page/s 99.

[11] Y. Zhang, J. Wang, and X. Wang, "Review on probabilistic forecasting of wind power generation," *Renewable and Sustainable Energy Reviews*, vol. 32, pp. 255–270, Apr. 2014. [Online]. Available: https://www.sciencedirect.com/science/article/pii/S1364032114000446 Cited on page/s 99, 101.

[12] R. P. Worsnop, M. Scheuerer, T. M. Hamill, and J. K. Lundquist, "Generating wind power scenarios for probabilistic ramp event prediction using multivariate statistical post-processing," *Wind Energ. Sci.*, vol. 3, no. 1, pp. 371–393, Jun. 2018. [Online]. Available: https://www.wind-energ-sci.net/3/371/2018/ Cited on page/s 99.

[13] A. Parisio and L. Glielmo, "Energy efficient microgrid management using Model Predictive Control," in *2011 50th IEEE Conference on Decision and Control and European Control Conference*, Dec. 2011, pp. 5449–5454, iSSN: 0743-1546. Cited on page/s 99.

[14] A. Parisio, L. Fabietti, M. Molinari, D. Varagnolo, and K. H. Johansson, "Control of

HVAC systems via scenario-based explicit MPC," in *53rd IEEE Conference on Decision and Control*. Los Angeles, CA, USA: IEEE, Dec. 2014, pp. 5201–5207. [Online]. Available: http://ieeexplore.ieee.org/document/7040202/ Cited on page/s 99, 100.

[15] T. I. Bø, E. Vaktskjold, E. Pedersen, and O. Mo, "Model Predictive Control of Marine Power Plants With Gas Engines and Battery," *IEEE Access*, vol. 7, pp. 15 706–15 721, 2019, conference Name: IEEE Access. Cited on page/s 99.

[16] A. Richards and J. How, "Mixed-integer programming for control," in *Proceedings of the 2005, American Control Conference, 2005.* Portland, OR, USA: IEEE, 2005, pp. 2676–2683. [Online]. Available: http://ieeexplore.ieee.org/document/1470372/ Cited on page/s 99.

[17] A. Parisio, E. Rikos, and L. Glielmo, "A Model Predictive Control Approach to Microgrid Operation Optimization," *IEEE Transactions on Control Systems Technology*, vol. 22, no. 5, pp. 1813–1827, Sep. 2014, conference Name: IEEE Transactions on Control Systems Technology. Cited on page/s 99.

[18] G. Cardoso, T. Brouhard, N. DeForest, D. Wang, M. Heleno, and L. Kotzur, "Battery aging in multi-energy microgrid design using mixed integer linear programming," *Applied Energy*, vol. 231, pp. 1059–1069, Dec. 2018. [Online]. Available: https://linkinghub.elsevier.com/retrieve/pii/S0306261918315058 Cited on page/s 99.

[19] A. Parisio, E. Rikos, and L. Glielmo, "Stochastic model predictive control for economic/environmental operation management of microgrids: An experimental case study," *Journal of Process Control*, vol. 43, pp. 24–37, Jul. 2016. [Online]. Available: https://www.sciencedirect.com/science/article/pii/S0959152416300324 Cited on page/s 99.

[20] J. Silvente, G. M. Kopanos, V. Dua, and L. G. Papageorgiou, "A rolling horizon approach for optimal management of microgrids under stochastic uncertainty," *Chemical Engineering Research and Design*, vol. 131, pp. 293–317, Mar. 2018. [Online]. Available: https://www.sciencedirect.com/science/article/pii/S0263876217304665 Cited on page/s 99.

[21] C. Tang, Y. Wang, J. Xu, Y. Sun, and B. Zhang, "Efficient scenario generation of multiple renewable power plants considering spatial and temporal correlations," *Applied Energy*, vol. 221, pp. 348–357, Jul. 2018. [Online]. Available: https://linkinghub.elsevier.com/retrieve/pii/S0306261918304203 Cited on page/s 99.

[22] S. Camal, F. Teng, A. Michiorri, G. Kariniotakis, and L. Badesa, "Scenario generation of aggregated Wind, Photovoltaics and small Hydro production for power systems applications," *Applied Energy*, vol. 242, pp. 1396–1406, May 2019. [Online]. Available: https://linkinghub.elsevier.com/retrieve/pii/S0306261919305203 Cited on page/s 99, 101.

[23] Y. Lei, D. Wang, H. Jia, J. Chen, J. Li, Y. Song, and J. Li, "Multi-objective stochastic expansion planning based on multi-dimensional correlation scenario generation method for regional integrated energy system integrated renewable energy," *Applied Energy*, vol. 276, p. 115395, Oct. 2020. [Online]. Available: https://www.sciencedirect.com/science/article/pii/S0306261920309077 Cited on page/s 99.

[24] F. Hafiz, A. Rodrigo de Queiroz, P. Fajri, and I. Husain, "Energy management and optimal storage sizing for a shared community: A multi-stage stochastic programming approach," *Applied Energy*, vol. 236, pp. 42–54, Feb. 2019. [Online]. Available: https://linkinghub.elsevier.com/retrieve/pii/S0306261918317963 Cited on page/s 99.

[25] D. van der Meer, G. C. Wang, and J. Munkhammar, "An alternative optimal strategy for stochastic model predictive control of a residential battery energy management system with solar photovoltaic," *Applied Energy*, vol. 283, p. 116289, Feb. 2021. [Online]. Available: https://linkinghub.elsevier.com/retrieve/pii/S0306261920316767 Cited on page/s 99, 100, 107, 108, 110, 113.

[26] S. Talari, M. Yazdaninejad, and M.-R. Haghifam, "Stochastic-based scheduling of the microgrid operation including wind turbines, photovoltaic cells, energy storages and responsive loads," *Transmission Distribution IET Generation*, vol. 9, no. 12, pp. 1498–1509, 2015, conference Name: Transmission Distribution IET Generation. Cited on page/s 99.

[27] D. Giaouris, A. I. Papadopoulos, C. Patsios, S. Walker, C. Ziogou, P. Taylor, S. Voutetakis,

S. Papadopoulou, and P. Seferlis, "A systems approach for management of microgrids considering multiple energy carriers, stochastic loads, forecasting and demand side response," *Applied Energy*, vol. 226, pp. 546–559, Sep. 2018. [Online]. Available: https://www.sciencedirect.com/science/article/pii/S030626191830833X Cited on page/s 99.

[28] J. A. A. Silva, J. C. López, N. B. Arias, M. J. Rider, and L. C. P. da Silva, "An optimal stochastic energy management system for resilient microgrids," *Applied Energy*, vol. 300, p. 117435, Oct. 2021. [Online]. Available: https://www.sciencedirect.com/science/article/pii/S0306261921008254 Cited on page/s 99.

[29] L. Torossian, V. Picheny, R. Faivre, and A. Garivier, "A Review on Quantile Regression for Stochastic Computer Experiments," Feb. 2019. [Online]. Available: https://hal.archives-ouvertes.fr/hal-02010735 Cited on page/s 99.

[30] C. A. Correa-Florez, A. Gerossier, A. Michiorri, and G. Kariniotakis, "Stochastic operation of home energy management systems including battery cycling," *Applied Energy*, vol. 225, pp. 1205–1218, Sep. 2018. [Online]. Available: https://linkinghub.elsevier.com/retrieve/pii/S0306261918306597 Cited on page/s 99.

[31] C. Poolla, A. K. Ishihara, and R. Milito, "Designing near-optimal policies for energy management in a stochastic environment," *Applied Energy*, vol. 242, pp. 1725–1737, May 2019. [Online]. Available: https://www.sciencedirect.com/science/article/pii/S0306261919302570 Cited on page/s 99.

[32] D. Han and J. H. Lee, "Two-stage stochastic programming formulation for optimal design and operation of multi-microgrid system using data-based modeling of renewable energy sources," *Applied Energy*, vol. 291, p. 116830, Jun. 2021. [Online]. Available: https://www.sciencedirect.com/science/article/pii/S0306261921003299 Cited on page/s 99.

[33] A. Parisio, D. Varagnolo, M. Molinari, G. Pattarello, L. Fabietti, and K. H. Johansson, "Implementation of a Scenario-based MPC for HVAC Systems: an Experimental Case Study," *IFAC Proceedings Volumes*, vol. 47, no. 3, pp. 599–605, 2014. [Online]. Available: https://linkinghub.elsevier.com/retrieve/pii/S1474667016416800 Cited on page/s 100.

[34] A. Parisio, M. Molinari, D. Varagnolo, and K. H. Johansson, "A scenario-based predictive control approach to building HVAC management systems," in *2013 IEEE International Conference on Automation Science and Engineering (CASE)*. Madison, WI, USA: IEEE, Aug. 2013, pp. 428–435. [Online]. Available: http://ieeexplore.ieee.org/document/6654024/ Cited on page/s 100.

[35] A. Parisio, D. Varagnolo, D. Risberg, G. Pattarello, M. Molinari, and K. H. Johansson, "Randomized Model Predictive Control for HVAC Systems," in *Proceedings of the 5th ACM Workshop on Embedded Systems For Energy-Efficient Buildings - BuildSys'13*. Roma, Italy: ACM Press, 2013, pp. 1–8. [Online]. Available: http://dl.acm.org/citation.cfm?doid=2528282.2528299 Cited on page/s 100.

[36] P. Patrinos, S. Trimboli, and A. Bemporad, "Stochastic MPC for real-time market-based optimal power dispatch," in *IEEE Conference on Decision and Control and European Control Conference*. Orlando, FL, USA: IEEE, Dec. 2011, pp. 7111–7116. [Online]. Available: http://ieeexplore.ieee.org/document/6160798/ Cited on page/s 100.

[37] N. Meinshausen, "Quantile Regression Forests," *J. Mach. Learn. Res.*, vol. 7, pp. 983–999, Dec. 2006. Cited on page/s 101, 102.

[38] F. Golestaneh, H. B. Gooi, and P. Pinson, "Generation and evaluation of space–time trajectories of photovoltaic power," *Applied Energy*, vol. 176, pp. 80–91, Aug. 2016. [Online]. Available: https://linkinghub.elsevier.com/retrieve/pii/S0306261916306079 Cited on page/s 101.

[39] S. Zhang, Y. Wang, Y. Zhang, D. Wang, and N. Zhang, "Load probability density forecasting by transforming and combining quantile forecasts," *Applied Energy*, vol. 277, p. 115600, Nov. 2020. [Online]. Available: https://www.sciencedirect.com/science/article/pii/S0306261920311065 Cited on page/s 101.

[40] C. D'Ambrosio, A. Lodi, and S. Martello, "Piecewise linear approximation of functions of two variables in MILP models," *Operations Research Letters*, vol. 38, no. 1, pp. 39–46, Jan. 2010. [Online]. Available: https://www.sciencedirect.com/science/article/pii/S0167637709001072

Cited on page/s 107, 109.

[41] Y. Wang, Z. Zhou, A. Botterud, K. Zhang, and Q. Ding, "Stochastic coordinated operation of wind and battery energy storage system considering battery degradation," *J. Mod. Power Syst. Clean Energy*, vol. 4, no. 4, pp. 581–592, Oct. 2016. [Online]. Available: http://link.springer.com/10.1007/s40565-016-0238-z Cited on page/s 109, 121.

[42] P. Pinson, H. Madsen, H. A. Nielsen, G. Papaefthymiou, and B. Klöckl, "From probabilistic forecasts to statistical scenarios of short-term wind power production," *Wind Energy*, vol. 12, no. 1, pp. 51–62, 2009, _eprint: https://onlinelibrary.wiley.com/doi/pdf/10.1002/we.284. [Online]. Available: https://onlinelibrary.wiley.com/doi/abs/10.1002/we.284 Cited on page/s 110.

[43] G. Papaefthymiou and D. Kurowicka, "Using Copulas for Modeling Stochastic Dependence in Power System Uncertainty Analysis," *IEEE Transactions on Power Systems*, vol. 24, no. 1, pp. 40–49, Feb. 2009, conference Name: IEEE Transactions on Power Systems. Cited on page/s 110.

[44] S. Pfenninger and I. Staffell, "Long-term patterns of European PV output using 30 years of validated hourly reanalysis and satellite data," *Energy*, vol. 114, pp. 1251–1265, Aug. 2016. [Online]. Available: https://www.sciencedirect.com/science/article/pii/S0360544216311744 Cited on page/s 112.

[45] I. Staffell and S. Pfenninger, "Using bias-corrected reanalysis to simulate current and future wind power output," *Energy*, vol. 114, pp. 1224–1239, Nov. 2016. [Online]. Available: http://www.sciencedirect.com/science/article/pii/S0360544216311811 Cited on page/s 112.

[46] P. Pinson and R. Girard, "Evaluating the quality of scenarios of short-term wind power generation," *Applied Energy*, vol. 96, pp. 12–20, Aug. 2012. [Online]. Available: https://linkinghub.elsevier.com/retrieve/pii/S0306261911006994 Cited on page/s 113.

[47] M. B. Bjerregård, J. K. Møller, and H. Madsen, "An introduction to multivariate probabilistic forecast evaluation," *Energy and AI*, vol. 4, p. 100058, Jun. 2021. [Online]. Available: https://www.sciencedirect.com/science/article/pii/S2666546821000124 Cited on page/s 113.

[48] D. Yang, "A universal benchmarking method for probabilistic solar irradiance forecasting," *Solar Energy*, vol. 184, pp. 410–416, May 2019. [Online]. Available: https://www.sciencedirect.com/science/article/pii/S0038092X19303457 Cited on page/s 113.

Chapter 6

Data dependent concurrent storage sizing and control design for frequency support in isolated power systems

Spyridon Chapaloglou[1,*], Damiano Varagnolo[2,5], Francesco Marra[3] and Elisabetta Tedeschi[1,4]

Published in: 2021 European Control Conference (*ECC*).
DOI: 10.23919/ECC54610.2021.9655025

Abstract

As more intermittent energy sources are integrated into isolated power systems, maintaining nominal frequency under the uncertain power fluctuations becomes even more challenging. For that, properly controlled ESSs are commonly used to provide frequency support. However, the design of such controllers typically does not rely on system operation data, leading to oversized storage systems and in turn overpriced investments. This paper addresses this problem and presents a methodology for deriving controllers that optimally use a specified storage capability to achieve a target compensation level, given past information of the disturbances. To leverage between uncertainty and actuation (storage) magnitude, the manuscript proposes a data-based approach for deciding alternative combinations of storage size and corresponding control laws that ensure risk constrained robust frequency regulation. The proposed designs are capable of providing additional virtual-inertia services to the isolated system against a guaranteed level of security over all possible uncertainty realizations. An application to an offshore oil and gas platform with onsite GTs and locally produced wind power is presented to highlight the numerical properties of the proposed methodology.

[1]Department of Electric Power Engineering, Norwegian University of Science and Technology (NTNU), Trondheim, Norway. [2]Department of Engineering Cybernetics, Norwegian University of Science and Technology (NTNU), Trondheim, Norway. [3]Equinor R&T Electrical Technology Department, Arkitekt Ebbels 10, 7005, Trondheim, Norway. [4]Department of Industrial Engineering, University of Trento, Via Sommarive, 9, 38123 Povo, Italy. [5]Department of Information Engineering, University of Padova, Via 8 Febbraio 2, 35122 Padova, Italy. [#]e-mail: spyridon.chapaloglou@ntnu.no, damiano.varagnolo@ntnu.no, fmarr@equinor.com and elisabetta.tedeschi@ntnu.no

6.1 Introduction

The operation of modern isolated power systems is becoming less safe and resilient due to the constantly increasing level of converter-interfaced RES [1]. The problem arises from the combined effects of lower system inertia available to face power fluctuations [2] and uncertainties of the relevant signals [3]. Such effects, that can result in excessive frequency variations, can be attenuated with proper Load Frequency Control (LFC) and storage systems providing virtual-inertia [4].

In this context, to deal with different sources of uncertainty in isolated systems the literature offers a series of robust control strategies based on linearized dynamics. For example, [5–7] propose two-degrees of freedom Internal Model Control (IMC) - PID controllers for LFC of power systems, and show that better performance can be achieved compared to conventional PIDs. However, [5–7] arbitrarily select the disturbance signals without considering any information related to the system under study. Also model order reduction had to be performed for the control design purpose, leading to simplified estimates of the true dynamics. [8] instead proposes a fractional order PID LFC design via an opportune IMC tuning, leading to better results compared to the aforementioned studies. The design in [8] is shown to be robust enough to be resilient against parametric uncertainties but, as in [5–7], no disturbance information was considered in the control design. In addition, in all the above mentioned methodologies, no control saturation limits were considered.

[9] proposes a fractional order fuzzy controller for LFC of a power system that includes storage system. The approach exhibits robust performance under both linear and non-linear operation regimes, the last ones owing to rate limiters. However, this design does not consider inherently those non-linear regimes, and uses simplified probabilistic models for the RES and the load uncertain power signals. [10], instead, proposes a time-varying fuzzy based PI controller that shows improved robustness under different operating conditions. However, also this approach does not inherently consider saturation limits of the specific storage system in the design phase.

Other authors like [11, 12] propose instead H_∞ controllers with the purpose of improving frequency profiles and the virtual-inertia capabilities of storage elements, but omit providing statistical analyses for quantifying the disturbances. Such design methodologies typically consider the performance of a worst-case plant that may never be realized and use over-conservative uncertainty assumptions (norm - bounded descriptions) [13]. However, for power system applications where at least one synchronous generator ensures frequency stability, sizing the storage system for a highly unlikely or even non-realizable worst case, would make any investment economically infeasible. [14] instead considers a simplified statistical model of the disturbances to determine the capacity of a storage system and its effect on frequency control. However, the paper employs simple probability density models that do not capture the time-dependency of the uncertain signals. Other authors then investigate machine-learning oriented strategies: for example [15] employs a deep-learning based control

technique, and shows that this approach may lead to marginally slightly better results compared to worst-case based controllers. However, the power disturbance signals are here considered to be random, without taking any information of the particular system under study into account.

As it is evident from the aforementioned studies, the existing literature on the LFC design problem usually ignores the physical limits of the system (i.e., the capacity limits of the storage), and this leads to either suboptimal use of the storage or over-conservative control laws. *We here aim at developing a methodology for designing a LFC that is as conservative as needed, and that uses the storage in an efficient way, so that this is not over-sized.* For this reason we employ the *sa* for control design [16] for the concurrent sizing and control design for a storage system. This is achieved through the use of realistic data of the system under study together with the Variable Robustness Control (VRC) methodology [17]. This enables to explore different robustness levels and gain greater insights into the system uncertainty and leveraging the controller decision against the risk.

Based on the recent breakthroughs in floating offshore wind and the need for cleaner offshore operations (see, e.g., [18]), we consider an isolated offshore O&G platform with significant wind power penetration and a dedicated storage system as a case study for the proposed methodology.

6.2 METHODOLOGY

The analysed system, whose complete configuration is presented in fig. Figure 6.1, is composed of: a droop controlled GT, a wind farm of 3 identical wind turbines controlled to their maximum power point, and an ESS. As field data, we consider time series of aggregated load data and wind speed measurements from a selected offshore location.

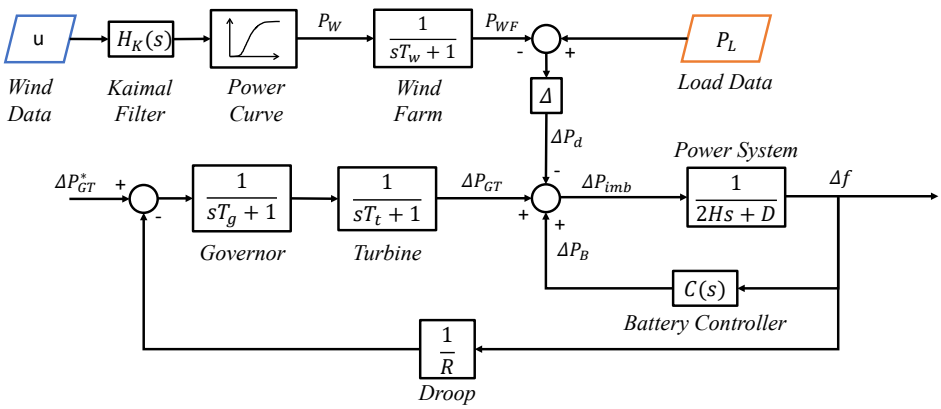

FIGURE 6.1. Schematic configuration of the system analysed in the paper

6.2.1 System modelling

This section describes the linearized small-signal model of the isolated power system. In more details, the power system dynamics are modelled though the commonly used swing equations (see [1]), i.e., as

$$\frac{2H_0}{f_n}\frac{df}{dt} + \frac{D_0}{S_b}f = \frac{P_{imb}}{S_b} \tag{6.1}$$

where H_0 $[s]$ is the rotating mass inertia, D_0 $[MW/Hz]$ the load dependent damping provided by the various induction motors on the platform, f $[Hz]$ the actual frequency of the AC grid, f_n $[Hz]$ the nominal one, S_b $[MW]$ is the base power and P_{imb} $[MW]$ the imbalance power. Considering the Laplace transform of eq. (6.1) and the variation of imbalance power P_{imb} $[MW]$ as the input signal leads to

$$\frac{\Delta f}{\Delta P_{imb}} = G(s) = \frac{1}{2Hs + D}\,. \tag{6.2}$$

Considering the system configuration presented in Figure 6.1 the complete dynamics are then described by

$$\Delta P_{imb} = \frac{\left(\Delta P^*_{GT} - \frac{1}{R}\Delta f\right)}{(sT_g + 1)\,(sT_t + 1)} - \Delta P_d + \Delta P_B \tag{6.3}$$

$$\Delta P_d = \Delta\left(P_L - P_{WF}\right) \tag{6.4}$$

where P_L is the load of the power system and P_{WF} the power coming from the wind farm. From eqs. (6.2) to (6.4) one can then derive

$$\begin{aligned}\Delta f = \Delta P^*_{GT}\frac{\dfrac{G(s)}{(sT_g + 1)\,(sT_t + 1)}}{1 + \dfrac{G(s)}{R\,(sT_g + 1)\,(sT_t + 1)}} + \\ (\Delta P_B - \Delta P_d)\,\frac{G(s)}{1 + \dfrac{G(s)}{R\,(sT_g + 1)\,(sT_t + 1)}}\end{aligned} \tag{6.5}$$

that eventually imply

$$\begin{aligned}&\Delta f = \Delta P^*_{GT} S_r(s) + \Big(\Delta P_B - \Delta P_d\Big) S_d(s)\,, \\ &\text{where} \qquad S_d(s) = \frac{G(s)}{1 + \dfrac{G(s)}{R\,(sT_g + 1)\,(sT_t + 1)}}\end{aligned} \tag{6.6}$$

is a causal and stable system (invertible). Summarizing, eq. (6.6) can be considered as the equivalent dynamics of the system under consideration.

Our aim is then to find an outer control loop $C(s)$ that rejects the net load disturbance ΔP_d in eq. (6.6). For this purpose, we propose to follow a *discrete design* strategy for synthesizing this control law. Thus, we discretize the continuous-time LTI representation $S_d(s)$ through a Tustin approach with a sampling period of $t_s = 0.01\ s$, deemed sufficiently accurate for our purposes, and then design a discrete controller directly on top of the obtained discrete-time system $S_d(z)$. In the following $u(k)$ is the discrete control signal at time step k, indicating the commanded storage power deviation $\Delta P_B(k)$ and $y(k)$ is the output of the plant, indicating the system frequency deviation $\Delta f(k)$.

The output feedback controller $C(z)$ shall cancel the dynamics caused by the disturbance. To this aim we use an IMC approach (see, e.g., [19]) where an the internal plant model is used and for which we require

$$u(k) = Q(z)\Delta P_d(k) \tag{6.7}$$

where $Q(z)$ is a strictly stable transfer function. Since the internal model principle outputs proactive control actions using the assumed internal model, [19], the output feedback control action is equivalent to a disturbance feed-forward action (eq. (6.7)) from the storage when this is revealed.

As for the strictly stable $Q(z)$, we select a commonly used FIR parametrization as in [16] and the control law in eq. (6.7) can be re-written as

$$u(k) = \Delta P_B(k) = q_0\Delta P_d(k) + q_1\Delta P_d(k-1) = \langle \phi_k, \boldsymbol{q} \rangle \tag{6.8}$$

where $\boldsymbol{q} = [q_0 \quad q_1]^T$ and $\boldsymbol{\phi}_k = [\Delta P_d(k) \quad \Delta P_d(k-1)]^T$.

We then reformulate the ro problem as minimizing the worst-case disturbance effect to our output signal. For this purpose we build our cost function on top of the upper bound h of the commonly used ISE of the frequency deviations. Since real-word disturbance dynamics are hard to model, in the proposed approach historical data are used as the best available representation. For that we define the uncertainty set Δ as

$$\delta_i : \{\Delta \boldsymbol{P_d}\}_i, \quad i \in \{1, \ldots, N_d\}\ . \tag{6.9}$$

as the set of all possible disturbance realizations δ_i (net load deviations profiles $\Delta \boldsymbol{P_d}$, sequences of $\Delta P_d(k)$ values for specified time horizon $t_h = 10\ s$). Realistic wind speed timeseries $v(t, \delta_i)$ were generated from local measurements and a Kaimal filter [20] that models the smaller time scale turbulence related phenomena, after the Normal Turbulence Model [21]. The wind power profiles were calculated through the commonly used cubic power curve transformation, considering the wind turbine dynamics as

$$P_{WF}(v(\delta_i)) = \frac{P_W(v(\delta_i))}{sT_w + 1} \quad \forall\ \delta_i \in \Delta\ . \tag{6.10}$$

6.2.2 Optimization problem formulation

The control design for compensation of frequency fluctuations under uncertain disturbances is cast as the *ro* problem

$$\begin{aligned} &\underset{h,\, \boldsymbol{q} \in R^3}{\text{minimize}} \quad h \\ \text{subject to} \quad &\sum_{k=1}^{M=\frac{t_h}{t_s}} \Delta f^2(k) \leq h, \forall\ \Delta \boldsymbol{P_d} \in \Delta \\ &\left|\Delta P_B(k)\right| \leq \overline{u}, \forall\ k = 0, \ldots, t_h. \end{aligned} \tag{6.11}$$

where $\overline{u}$ is the saturation level of the storage system (i.e., its maximum charge/discharge power rate). Now consider $\Delta P^*_{GT} = 0$, i.e., assume the GT to be scheduled to produce a fixed reference value. Given this assumption we can derive the constraints leveraging on eq. (6.3), eq. (6.7) and eq. (6.8), and obtain

$$\sum_{t=1}^{M} y^2(k) = \sum_{k=1}^{M} [S_d(z)(u(k) - \Delta P_d(k))]^2 = \sum_{k=1}^{M} [S_d(z)\phi_k^T \boldsymbol{q} - S_d(z)\Delta P_d(k)]^2 \tag{6.12}$$

Where we call $\phi_k = [\Delta P_d(k) \quad \Delta P_d(k-1)]^T$, $\psi_k = S_d(z)\phi_k$. In this way eq. (6.12) becomes

$$\begin{aligned} &\sum_{k=1}^{M} y^2(k) = \sum_{k=1}^{M} \left[\psi_k^T \boldsymbol{q} - S_d(z)\Delta P_d(k)\right]^2 = \\ &\sum_{k=1}^{M} \left(\boldsymbol{q}^T \psi_k \psi_k^T \boldsymbol{q} - 2S_d(z)\Delta P_d(k)\psi_k^T \boldsymbol{q} + \left(S_d(z)\Delta P_d(k)\right)^2\right) . \end{aligned} \tag{6.13}$$

Note then that if we choose the decision variables vector as $\boldsymbol{x} = [\boldsymbol{q} \quad h]^T = [q_0 \quad q_1 \quad h]^T$ the constraints of eq. (6.13) can be rewritten as

$$\boldsymbol{x}^T A \boldsymbol{x} + B\boldsymbol{x} + C \leq 0 \tag{6.14}$$

where the coefficients A, B and C can be calculated as

$$\begin{aligned} A &= \sum_{k=1}^{M} [\psi_k \quad 0]\,[\psi_k \quad 0]^T \\ B &= 2\sum_{k=1}^{M} -\Delta P_d(k) S_d(z)\,[\psi_k \quad 0]^T - [0 \quad 0 \quad 1] \\ C &= \sum_{k=1}^{M} (-\Delta P_d(k) S_d(z))^2 . \end{aligned} \tag{6.15}$$

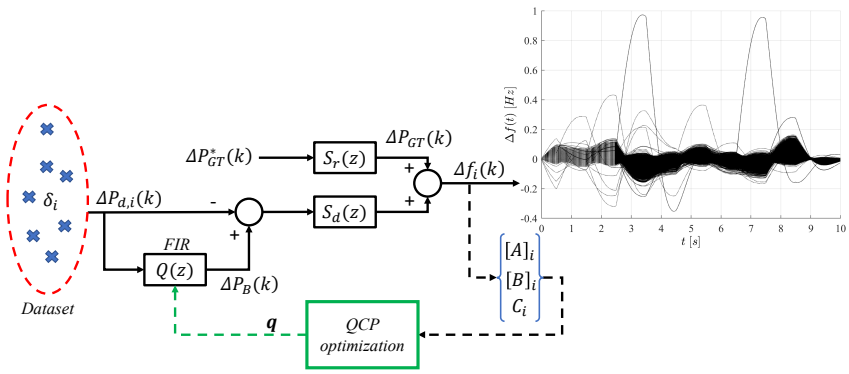

FIGURE 6.2. Graphical summary of the proposed methodology

This means that a quadratic constraint that is formulated from eq. (6.14) and eq. (6.15) corresponds to each instance of the uncertain disturbance δ_i. Note though that to calculate the coefficients A, B and C of each of these constraints we first need to simulate the system S_d with the appropriate inputs, a process that we graphically illustrate in Figure 6.2. Then, based on the scenario approach [22], we can select to disregard a portion of the set of disturbances Δ that from a probabilistic standpoint accounts in total for a probability ε out of the whole probability metric over Δ. This is done by selecting an appropriate number of scenarios N_s so that the optimality of the solution of eq. (6.11) is $1-\beta$ level guaranteed against all other unseen instances of uncertainty from Δ. In other words, the designer can select a risk level ε from which she/he can compute a number of scenarios (i.e., constraints) N_s such that the confidence of not violating the unseen constraints is at least $1-\beta$. The commonly used values $\varepsilon = 0.01$ and $\beta = 10^{-7}$ were selected for this study. Finally, the optimization problem is set as

$$\begin{aligned} &\underset{\boldsymbol{x}\in R^3}{\text{minimize}} \;\; c^T\boldsymbol{x} \\ &\text{subject to} \\ &\{\boldsymbol{x}^T A\boldsymbol{x} + B\boldsymbol{x} + C\}_i \le 0, \;\; \forall\, \delta_i \in \Omega, \\ &\left\{ \left| \begin{bmatrix} \phi_k \\ 0 \end{bmatrix}^T \boldsymbol{x} \right| \le \overline{u} \right\}_i, \;\; \forall\, \delta_i \in \Omega, \;\; k = 0, \ldots, t_h. \end{aligned} \tag{6.16}$$

where $\boldsymbol{x} = [\boldsymbol{q} \quad h]^T = [q_0 \quad q_1 \quad h]^T$ and $c = [0 \quad 0 \quad 1]^T$. Note that the quadratically constrained problem (QCP) eq. (6.16) can be numerically solved using standard numerical solvers. More specifically, to derive the constraints in eq. (6.14) we used the *Matlab-Simulink* parallel computing toolbox [23] and solved eq. (6.16) with the commercial mathematical optimization solver *Gurobi 9.0.3* [24].

6.3 Simulation results

6.3.1 *Effects of choosing different storage sizes*

To investigate the dependency between the control action and the storage capability, we find appropriate controllers $Q(z)$ for different values of the saturation level of the storage system $\overline{u}$. More precisely, we initially set the upper bound to the relatively high value of $\overline{u} = 0.4$, so that basically the storage saturation constraint is not active in eq. (6.16). The worst case disturbance and the associated control action required $\widehat{u}$ are then presented in Figure 6.3. Here we can identify the unsaturated peak value of the control action as $\overline{u} = 0.3222 < 0.4$, with the control parameters leading to such design being $q_0 = 1.0023$, $q_1 = -0.0023$ (see also Table 6.1) meaning that the full range of the disturbance signals can be counteracted from the proposed storage controller (see also eq. (6.8)). As can be noticed from Figure 6.3 such a design is basically able to almost perfectly compensate the worst case disturbance. This means that this controller will also compensate all the other measured disturbances, given the chosen confidence level and risk.

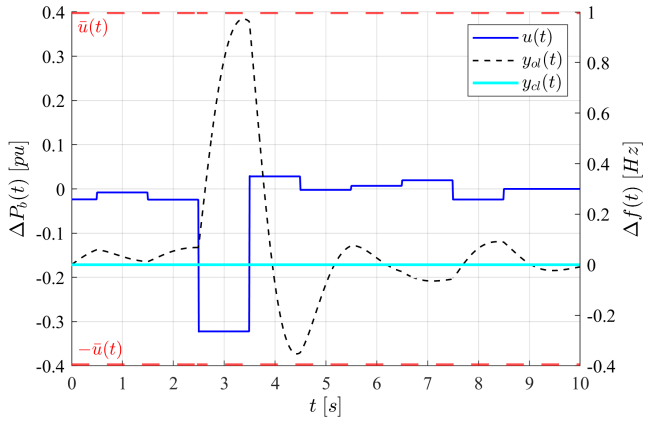

Figure 6.3. System response and control action for the worst case scenario - unsaturated design case

Changing the saturation level $\overline{u}$ parameter it is then possible to get different designs that compensate the worst case frequency fluctuations in different ways. The cumulative results, summarized in Table 6.1, show that decreasing the saturation level (i.e., choosing a smaller and thus less expensive storage system) increases the optimal value of the ISE performance index h^*. Intuitively, as $\overline{u}$ diminishes the worst case disturbance first and then, one by one, all the consequent next-worst cases cannot be effectively compensated any more. To this point we note that we observe a distinct pattern: while the q_0 parameter is decreasing as $\overline{u}$ decreases, $q_1 = 0$ most of the times, leading to a controller purely proportional to the disturbance. This indicates that the optimal compensator (QCP optimization eq. (6.16)), for the particular parametrization

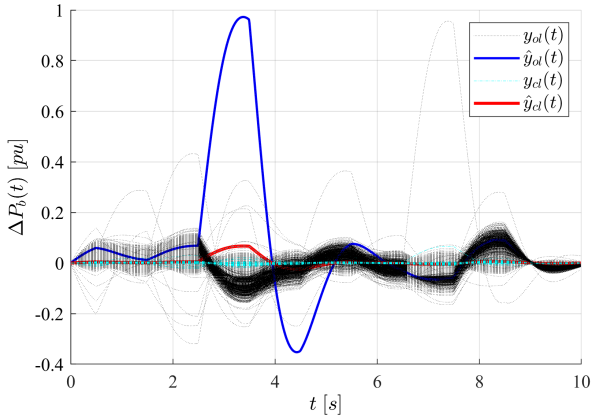

(a) y

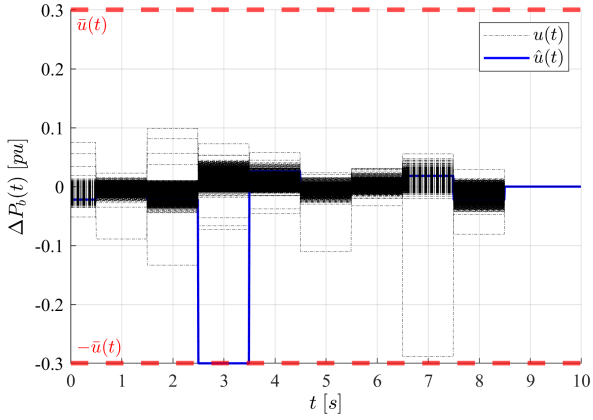

(b) u

FIGURE 6.4. System response and control action for $\overline{u} = 0.3$

(eq. (6.7)), depends mostly on the present value of the disturbance, and little on the previous one. Despite such a simple controller structure, this is in agreement with the basic *loop-shaping* recommendations for rejecting disturbances entering directly at the plant input [13]. Then, in order to respect the physical saturation limits of the storage, the optimizer selects an appropriate (lower) gain value, meaning that the proportion of the worst disturbance that the specific control design can effectively compensate, is decreased. This effect can be noticed in Figure 6.4, where we present the results for $\overline{u} = 0.3$. Note that this design is smaller compared to the non-saturated case $\overline{u} = 0.4$; we expect thus that some disturbances will saturate the control output, so that the disturbance will not be perfectly compensated. From fig. 6.4b we can observe this event, where the controller is saturated just for one case $\widehat{u}$, the one that dominated the

Table 6.1. Summary of the control design results

$\overline{u}$ $[pu]$	q_0	q_1	h^*
0.4	1.0023	-0.0023	78.0604
0.3	0.9310	0	78.0642
0.2	0.6206	0	78.1738
0.1	0.3104	0	78.4354
0.09	0.2793	0	78.4699

initial design. The impact of this effect is presented in fig. 6.4a, where we compare the corresponding open loop and closed loop outputs y_{ol} and y_{cl}. We can see that even though the worst-case open loop response $\widehat{y}_{ol}$ (depicted in blue) cannot be compensated as effectively as in the other scenarios, the proposed optimal control design leads to a much improved worst-case closed loop response $\widehat{y}_{cl}$ (depicted in red).

6.3.2 *Effects of choosing different levels of robustness*

Based on the results of section 6.3.1, it is evident that for any meaningful storage sizing $\overline{u}$ the control design is dominated by a few specific realizations of the disturbances δ_i. To quantify the effect of these specific δ_i's, and eventually characterize their impact of the data-based uncertainty structure of our problem, we apply the VRC algorithm. For this we employ the *FFS* [25] as a means to identify the support scenarios (which are intuitively thought as the ones that are more "different" compared the rest of the sampled dataset) and remove them in turns.

At every iteration k the *FFS* algorithm preserves the most "equidistant" scenarios, and discards the most "different" ones. The number of the scenarios $N_s^{'}$ to be considered for the VRC algorithm is decided as in [17]. Then, at each iteration k, we can calculate the upper bound ε_k on the probability of violating the unseen δ_i instances (i.e., the risk-level) for k removed scenarios out of $N_s{}'$ as

$$\binom{d+k}{k} \sum_{i=0}^{d+k} \binom{N_s^{'}}{i} \varepsilon_k^i \left(1-\varepsilon_k\right)^{N_s^{'}-i} = \frac{\beta}{\overline{k}+1} \; \forall \; k = 0, \ldots, \overline{k} \tag{6.17}$$

where $d = 2$ is the number of the design variables.

Applying the *FFS* procedure to the specific case $\overline{u} = 0.09$ leads to the results shown in Figure 6.5 and Table 6.2. From Figure 6.5 we can observe that as we keep removing scenarios the optimal value h_k^* decreases, while the risk increases from its initial value $\varepsilon = 0.01$. We also note that every time removing a scenario leads to a better solution, this is because a different control design is decided (see also Table 6.2). In most cases we get once again $q_1 = 0$, while we find also that the gain q_0 increases for increasing k. This has the following interpretation: as the support scenarios are identified and removed, the storage (whose size is now fixed) can be operated in a way that does not need to account for (and thus reject) these "bad" realizations of the

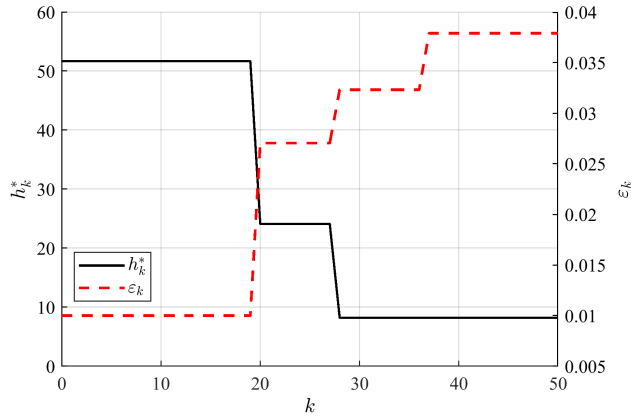

FIGURE 6.5. Dependency of the optimal value h_k^* and of the risk parameter ε_k on the number of scenarios removed through the FFS procedure

disturbances. In addition, from Table 6.2 we can observe that the removal of particular scenarios may have a great effect on the improvement of h_k^*, with the best improvement found at $k = 29$. For our particular system, we see that after that k it is not worth to keep removing scenarios, because the relative improvement is small, at the cost though of increasing risks. Last but not least, it is of high importance to notice from Figure 6.5 that in general removing a scenario does not necessarily mean improving h_k^*. For example, after $k = 38$ the results did not change. That means that in general there are just a few disturbance scenarios that are dictating the optimal design process; just by increasing our risk we may even neglect them on the initial sizing of the storage system. However, if the storage system is decided (fixed $\overline{u}$), a meaningful risk-averse decision for the controller $Q(z)$ would be $q_0 = 0.7959$ and $q_1 = -0.2131$ with risk level 3.23 times bigger than the initial one.

6.4 CONCLUSIONS

This study presents a data-based methodology for the concurrent design of the size and control law of a storage system to be operated in isolated power systems with low inertia and intermittent non-dispatchable energy sources. The results showed that the proposed method can effectively improve the dynamic characteristics of an isolated

TABLE 6.2. Results about the effects of choosing different levels of robustness

k	q_0	q_1	ε_k [%]	h_k^*	Δh_k^* [%]
0-20	0.3542	0	1.00	51.6588	-
21-28	0.5111	0	2.71	24.1094	-53.33
29-37	0.7959	-0.2131	3.23	8.2075	-65.96
38-79	1.0000	0	3.23	8.1931	-0.18

offshore O&G power system which integrates significant amount of wind power. The proposed design methodology can be considered as a guideline for risk-dependent decision support, and for the selection of storage system and its optimal controller, given information specific to the system under study. The case study presented in this paper demonstrates the contribution of appropriately sizing storage to provide frequency support. It is also shown that smaller storage sizes may still effectively compensate uncertain disturbances, at the cost of relatively small risk increment. As future possible work, parametric uncertainty could also be integrated to construct the uncertainty set, while the method could be even used in a rolling horizon way, deciding a control law, given recent past observations and parameters values.

6.5 Appendix

Table 6.3. Summary of the main parameters defining the power system considered in our numerical analyses

Parameter	*Value*	*Units*
Base power value	$S_b = 60$	[MW / puMW]
Nominal system frequency	$f_n = 60$	[Hz]
Droop constant	$R = 2.4$	[Hz / puMW]
Power system inertia constant	$H = 0.083$	[puMW s / Hz]
Power system damping constant	$D = 0.0083$	[puMW / Hz]
Governor time constant	$T_g = 0.08$	[s]
GT time constant	$T_t = 0.3$	[s]
Wind turbine time constant	$T_w = 1.5$	[s]
Nominal wind turbine power	$P_{wt}^n = 15$	[MW]
Number of scenarios in Δ	$N_d = 52560$	[-]
Number of scenarios	$N_s = 2158$	[-]
Number of scenarios for VRC	$N_s^{'} = 2631$	[-]

6.6 References

[1] K. S. El-Bidairi, H. D. Nguyen, T. S. Mahmoud, S. D. G. Jayasinghe, and J. M. Guerrero, "Optimal sizing of Battery Energy Storage Systems for dynamic frequency control in an islanded microgrid: A case study of Flinders Island, Australia," *Energy*, vol. 195, p. 117059, Mar. 2020. [Online]. Available: http://www.sciencedirect.com/science/article/pii/S0360544220301663 Cited on page/s 140, 142.

[2] A. Pepiciello, A. Vaccaro, D. Villacci, and F. Milano, "A Method to Evaluate the Inertial Response of Frequency Controlled Converter-Interfaced Generation," in *2020 IEEE International Conference on Environment and Electrical Engineering and 2020 IEEE Industrial and Commercial Power Systems Europe (EEEIC / I CPS Europe)*, Jun. 2020, pp. 1–6. Cited on page/s 140.

[3] Y. Levron and J. Belikov, "Control of Energy Storage Devices Under Uncertainty Using Nonlinear Feedback Systems," p. 5. Cited on page/s 140.

[4] H. Golpîra, A. Atarodi, S. Amini, A. R. Messina, B. Francois, and H. Bevrani, "Optimal Energy Storage System-Based Virtual Inertia Placement: A Frequency Stability Point of View," *IEEE Transactions on Power Systems*, vol. 35, no. 6, pp. 4824–4835, Nov. 2020, conference Name: IEEE Transactions on Power Systems. Cited on page/s 140.

[5] Wen Tan, "Unified Tuning of PID Load Frequency Controller for Power Systems via

TABLE 6.4. Summary of the quantities involved in the models

Variable	*Symbol*
Platform load	P_L
Wind farm power	P_{WF}
Frequency deviation	Δf
Storage power deviation	ΔP_B
GT power deviation	ΔP_{GT}
Net load power deviation	ΔP_d
Imbalance power deviation	ΔP_{imb}
Control action	$u = \Delta P_B$
System output	$y = \Delta f$
Open loop ($S_d(z)$) output	y_{ol}
Closed loop ($S_d(z),\ C(z)$) output	y_{cl}
Control saturation level	$\overline{u}$
Worst case control action	$\widehat{u}$
Worst case system output	$\widehat{y}$
Number of removed scenarios	k
Bound of violation probability	ε_k
Optimal ISE upper bound	h_k^*

IMC," *IEEE Trans. Power Syst.*, vol. 25, no. 1, pp. 341–350, Feb. 2010. [Online]. Available: http://ieeexplore.ieee.org/document/5361327/ Cited on page/s 140.

[6] S. Saxena and Y. V. Hote, "Load Frequency Control in Power Systems via Internal Model Control Scheme and Model-Order Reduction," *IEEE Trans. Power Syst.*, vol. 28, no. 3, pp. 2749–2757, Aug. 2013. [Online]. Available: http://ieeexplore.ieee.org/document/6476046/ Cited on page/s 140.

[7] J. Singh, K. Chattterjee, and C. Vishwakarma, "Two degree of freedom internal model control-PID design for LFC of power systems via logarithmic approximations," *ISA Transactions*, vol. 72, pp. 185–196, Jan. 2018. [Online]. Available: https://linkinghub.elsevier.com/retrieve/pii/S0019057817306213 Cited on page/s 140.

[8] S. Jain and Y. V. Hote, "Design of fractional PID for Load frequency control via Internal model control and Big bang Big crunch optimization," *IFAC-PapersOnLine*, vol. 51, no. 4, pp. 610–615, 2018. [Online]. Available: https://linkinghub.elsevier.com/retrieve/pii/S2405896318304609 Cited on page/s 140.

[9] I. Pan and S. Das, "Fractional order fuzzy control of hybrid power system with renewable generation using chaotic PSO," *ISA Transactions*, vol. 62, pp. 19–29, May 2016. [Online]. Available: https://linkinghub.elsevier.com/retrieve/pii/S001905781500083X Cited on page/s 140.

[10] M.-H. Khooban, T. Niknam, F. Blaabjerg, P. Davari, and T. Dragicevic, "A robust adaptive load frequency control for micro-grids," *ISA Transactions*, vol. 65, pp. 220–229, Nov. 2016. [Online]. Available: https://linkinghub.elsevier.com/retrieve/pii/S001905781630146X Cited on page/s 140.

[11] V. P. Singh, S. R. Mohanty, N. Kishor, and P. K. Ray, "Robust H-infinity load frequency control in hybrid distributed generation system," *International Journal of Electrical Power & Energy Systems*, vol. 46, pp. 294–305, Mar. 2013. [Online]. Available: https://linkinghub.elsevier.com/retrieve/pii/S0142061512005789 Cited on page/s 140.

[12] T. Kerdphol, F. S. Rahman, Y. Mitani, M. Watanabe, and S. K. Küfeoğlu, "Robust Virtual Inertia Control of an Islanded Microgrid Considering High Penetration of Renewable Energy," *IEEE Access*, vol. 6, pp. 625–636, 2018, conference Name: IEEE Access. Cited on page/s 140.

[13] P. I. Skogestad S., *MULTIVARIABLE FEEDBACK CONTROL Analysis and design*. Cited on page/s 140, 147.

[14] H. Jia, Y. Mu, and Y. Qi, "A statistical model to determine the capacity of battery–supercapacitor hybrid energy storage system in autonomous microgrid," *International Journal of Electrical*

Power & Energy Systems, vol. 54, pp. 516–524, Jan. 2014. [Online]. Available: https://linkinghub.elsevier.com/retrieve/pii/S0142061513003220 Cited on page/s 140.

[15] V. Skiparev, J. Belikov, and E. Petlenkov, "Reinforcement Learning Based Approach for Virtual Inertia Control in Microgrids with Renewable Energy Sources," p. 6. Cited on page/s 140.

[16] M. C. Campi, S. Garatti, and M. Prandini, "The scenario approach for systems and control design," *Annual Reviews in Control*, vol. 33, no. 2, pp. 149–157, Dec. 2009. [Online]. Available: https://linkinghub.elsevier.com/retrieve/pii/S1367578809000479 Cited on page/s 141, 143.

[17] S. Garatti and M. C. Campi, "Modulating robustness in control design: Principles and algorithms," *IEEE Control Systems Magazine*, vol. 33, no. 2, pp. 36–51, Apr. 2013, conference Name: IEEE Control Systems Magazine. Cited on page/s 141, 148.

[18] S. Settemsdal, L. Barstad, and W. Voss, "Hybrid power plants can help decarbonize offshore drilling rigs and vessels," p. 4. Cited on page/s 141.

[19] J. C. Kantor, "Robust process control. By Manfred Morari and Evanghelos Zafiriou, Prentice-Hall, Inc., Englewood Cliffs, NJ, 1989, 488 pp., $55.00," *AIChE Journal*, vol. 37, no. 12, pp. 1905–1906, 1991, _eprint: https://aiche.onlinelibrary.wiley.com/doi/pdf/10.1002/aic.690371216. [Online]. Available: https://aiche.onlinelibrary.wiley.com/doi/abs/10.1002/aic.690371216 Cited on page/s 143.

[20] C. Gavriluta, S. Spataru, I. Mosincat, C. Citro, I. Candela, and P. Rodriguez, "Complete methodology on generating realistic wind speed profiles based on measurements," *REPQJ*, pp. 1757–1762, Apr. 2012. [Online]. Available: http://www.icrepq.com/icrepq'12/828-gavriluta.pdf Cited on page/s 143.

[21] "INTERNATIONAL STANDARD IEC 61400-1," Tech. Rep. [Online]. Available: http://dlbargh.ir/mbayat/46.pdf Cited on page/s 143.

[22] M. C. Campi and S. Garatti, *Introduction to the Scenario Approach*. Philadelphia, PA: Society for Industrial and Applied Mathematics, Nov. 2018. [Online]. Available: https://epubs.siam.org/doi/book/10.1137/1.9781611975444 Cited on page/s 145.

[23] MATLAB, *9.8.0.1380330 (R2020a) Update 2*. Natick, Massachusetts: The MathWorks Inc., 2020. Cited on page/s 145.

[24] L. Gurobi Optimization, "Gurobi optimizer reference manual," 2020. [Online]. Available: http://www.gurobi.com Cited on page/s 145.

[25] J. Dupačová, N. Gröwe-Kuska, and W. Römisch, "Scenario Reduction in Stochastic Programming: An Approach Using Probability Metrics," 2003. Cited on page/s 148.

Chapter 7

Multi-objective control of isolated power systems under different uncertainty approaches

Spyridon Chapaloglou[1,*], Andreas Faanes[2], Damiano Varagnolo[2,4] and Elisabetta Tedeschi[1,3]

Published in: *Sustainable Energy, Grids and Networks (SEGAN)* **32**, 100853 (2022).
DOI: 10.1016/j.segan.2022.100853

Highlights

- Multi-objective optimal MIMO control of isolated power systems with energy storage
- Simultaneous grid frequency regulation and SoC schedule tracking
- Performance metrics for robust and predictive control assessment under uncertainty
- Comparison of control parametrizations for scenario-based stochastic control

[1]Department of Electric Power Engineering, Norwegian University of Science and Technology (NTNU), Trondheim, Norway. [2]Department of Engineering Cybernetics, Norwegian University of Science and Technology (NTNU), Trondheim, Norway. [3]Department of Industrial Engineering, University of Trento, Via Sommarive, 9, 38123 Povo, Italy. [4]Department of Information Engineering, University of Padova, Via 8 Febbraio 2, 35122 Padova, Italy. [#]e-mail: spyridon.chapaloglou@ntnu.no, andreas.faanes96@gmail.com, damiano.varagnolo@ntnu.no and elisabetta.tedeschi@ntnu.no

Abstract

This paper proposes and compares a set of multi-objective supervisory controllers for an isolated power system including a GT operating in load following mode as a dominant source of generation, a BESS, and stochastic renewable generation. It analyzes their capability to coordinate the GT and energy storage to provide isochronous speed control, achieving Fast Frequency Regulation (FFR) for the local grid, while the GT can still operate with minimum deviation from its optimal loading and the storage system can follow a pre-scheduled reference SoC trajectory. In more detail, we consider and compare different control strategies to handle model and disturbance uncertainties, including SMPC under various parametrizations of the sa, and robust control under the H_∞ paradigm. The various controllers are compared against a benchmark, i.e., a deterministic predictive control strategy. Instead of point-to-point comparisons for some arbitrary cases (i.e., worst-case or expected), empirical distributions of the controller's performance for the whole probability spectrum are derived, leading to more accurate and representative comparisons. The analyzed performance indicators are nominal dynamic performance, constraint violation probabilities, and expected system operation performance. The results indicate the clear superiority of stochastic control over both robust and deterministic control in dealing with both parametric and disturbance uncertainty. Moreover, choosing an appropriate parametrization is shown to be essential to achieve both good nominal performance and lower violations probability, indicating that the superiority of stochastic control comes with the drawback of needing user-defined tuning from the designer.

7.1 Introduction

Due to constantly stricter regulations towards increasing renewable penetration, maintaining a stable and efficient operation for isolated power systems has become challenging [1]. Based on recent advances in offshore technologies [2], more and more such isolated grids with high renewable penetration are about to be realized [3], and this highlights the need for efficient controls.

The stochastic nature of RES and the low system inertia, induced by replacing traditional synchronous machines with converter interfaced generators, makes the operation of such grids vulnerable to large frequency variations[4–6]. A common and accepted way to mitigate such issues is the integration of ESSs such as BESSs [4, 7–12]. However, increasing the number of controllable components in the grid complicates the MIMO nature of these systems, exacerbating the chances of encountering multiple contradictory objectives, additional constraints due to safety, and optimal operation requirements. On top of that, uncertainty poses an additional level of difficulty for controlling such grids [13].

In [14, 15] the fundamental methods to provide frequency control in isolated power systems by controlling the generator units, are explained in detail. Two main

categories are identified, one being the well-known traditional droop control and the other the isochronous control. With the first, generators modify the active power provision in correspondence to the system's frequency deviation and based on the set droop curve, whereas in isochronous mode the rotational speed and thus the frequency of a single or master unit are tightly regulated to their reference values. It is noteworthy that even though droop control facilitates the load sharing among several units, the frequency will not be restored to its nominal value. To achieve that in the absence of interconnection, frequency restoration will depend only on the local generator capabilities and requires that one of them be in isochronous mode. In other words, from a control perspective, droop control corresponds to a proportional controller whereas isochronous operation corresponds to controllers with integral action. In further detail and from a system dynamics perspective, droop control is the main source of damping, necessary for the stability of the system and isochronous control the term encapsulating error accumulation effects and responsible for achieving zero steady state deviation.

For the isochronous case, a frequency variation will be immediately compensated by the generating unit, providing a service equivalent to the secondary frequency restoration in large interconnected systems. However, in contrast to the isochronous operation of a generator for an isolated system, in large interconnected systems such a service is achieved by the system operator, assigning different activation signals and participation factors to all available generators participating in the Frequency Restoration Reserve market. Such services are typically activated after the provision of primary control to stabilize the system after a disturbance and on the scale of several seconds to minutes. We also highlight that the actual speed of frequency restoration will depend on the amount of power imbalance and the operational limits of the involved units (ramp constraints and technical maximum).

In [16] GT dynamics are studied along with power systems frequency dynamics, demonstrating the fast-acting behavior of such generators and the isochronous operation capability (response time in the range of seconds). Such a practical case study for an islanded plant (industrial isolated power system) is also provided in [17].

Various types of advanced control methods for LFC of isolated power systems have been proposed in literature. In [18] optimal PID controllers were designed to provide LFC in microgrid clusters, in [19] a swarm-optimized fuzzy logic was used for robust secondary frequency control of islanded systems, in [20–22] the H_∞ synthesis concept was used to provide robust secondary frequency control in islanded microgrids, in [23] an MPC controller was investigated to provide LFC, in [1] a Grey Wolf Optimization was used to provide frequency support by a BESS for an island power system, in [24] a Linear Quadratic Regulator stochastic based control was proposed to provide secondary frequency regulation in an independent microgrid, in [25, 26] fractional order MPC and PID were designed correspondingly to provide frequency control for an islanded microgrids or for single area power systems, in [27] an IMC-PID design was investigated for LFC.

In the aforementioned studies, the (isolated) power system is modeled as a continuous time LTI dynamical system and the control performance is typically assessed through load step variations considering either average or worst cases disturbances. However, the actual empirical distributions are not derived, possibly leading to biased/over-conservative or rather optimistic conclusions. Nevertheless, all the proposed load frequency controllers include an integral part that brings the steady state error to zero in just a few seconds. Such action resembles the isochronous operation provided by single generators when speed and thus frequency are tightly regulated in stand-alone isolated systems. The system's response time highly depends on the various time constants involved (primarily the inertia) and the operational limits (power provision /absorption capability) of the related units. Therefore, for low inertia isolated power systems, response can be faster than large interconnected systems. We note that when secondary level control is designed and assessed (frequency restoration), primary control loops (i.e., droop) can be included in the dynamics of the power system, by modifying the system's damping.

Different approaches can be found in literature for dealing with uncertainty in frequency control of isolated grids. In [7] a standard MPC algorithm based on a convex Quadratic Programming problem is employed to control an isolated power system containing critical and non-critical loads, diesel generators, BESS, and RES in the form of photovoltaics and wind power generation. The results demonstrates how MPC can effectively manage several objectives, like preserving power balance in the grid and reducing the fuel consumption of the diesel generators. However, this work integrates uncertainty in a simplistic way, by using scenarios with different level of accuracy for the load profile predictions ranging from a perfect forecast and up to approximately 10% deviation. In [10] authors develop a scheduling algorithm for an isolated power system with high penetration of RES which controls the energy production from fossil sources and the power transactions with the main grid in order to maintain power balance and maximize the RES penetration. This yields an alternative strategy to the MPC algorithm and shows good simulation results with a time frame of a day with uncertain forecasts of wind speeds and load profiles. In [28] a SMPC approach that uses scenarios-based description of uncertainties is employed to optimize the fossil energy production and power transactions in the real time market. Such scenarios are generated from a scenario tree designed explicitly to capture the additive feature of uncertainty and avoid infeasibility. The authors of this work compare their algorithm to a so-called prescient optimal control strategy that assumes perfect knowledge of future realizations of the uncertainty, and a certainty equivalent MPC where the uncertain parameters are substituted by average values identified from historical data. Results demonstrate the superiority of the scenario based approach in decreasing costs. [29] performs a comparative study of what they call SMPC and Scenario Model Predictive Control (SCMPC). The difference between the two methods is that the SMPC method converts the probabilistic constraints into deterministic ones using knowledge of the co-variance of the random variables and their propagation along the prediction

horizon; the SCMPC approach computes scenarios and forms a scenario tree from the probability distribution of the uncertain variables, as in [28]. The results show that SCMPC generates more realistic scenarios than SMPC because it uses information gathered online to adjust scenario predictions rather than exploiting knowledge on second moments. This accuracy comes though at the cost of increased computational requirements. In [30], the authors develop a scenario SMPC for hybrid vehicles with the goal of improving fuel efficiency while obeying constraints on the SoC of the battery and the power exchanged with it. However, the SCMPC is modified to only generate scenarios that are feasible and likely. The disturbance, i.e., the power requested by the driver, is instead estimated via a Markov chain that predicts the future driver inputs by learning the previous request pattern in real time. Results from [30] show that their SCMPC with learning may outperform classical MPC formulations, and that in many simulations the SMPC performs almost as an MPC with perfect knowledge of future realizations of the disturbances. Other methods consider then a robust control design approach to mitigate uncertain frequency variations [20]. For example, in [31] the authors apply both an H_∞ and μ synthesis approaches for robust frequency control in islanded microgrids. Results show that the two control algorithms may outperform an "optimally tuned" PID controller in the presence of structured uncertainty in the form of wind power generation, solar power generation and uncertain load conditions.

The review above highlights the presence of a plethora of different MPC based methods for either optimal scheduling in isolated power systems or for frequency regulation under uncertainty, either based on robust or stochastic control algorithms. To the best of our knowledge there is though a lack of publicly available studies that analyse how to integrate both tasks into the same control strategy, and thus analyse how control strategies may satisfy optimal schedule tracking while simultaneously ensuring continuous, tight, and FFR. The goals of this paper are thus two:

i. propose a series of control formulations and parametrizations (stochastic, robust and deterministic *in primis*) that are all capable of coordinating a master GT and an energy storage to achieve FFR for the local grid, while the GT can still operate with minimum deviation from its optimal loading and the storage system can follow a pre-scheduled reference SoC trajectory;

ii. understand which one best handles uncertainties while guaranteeing control performance, and their tradeoffs.

For this purpose, the paper is organized as follows: Section 7.2 introduces the dynamic MIMO model of the isolated power system, Section 7.3 describes the design of the controllers we compare, and Section 7.4 performs the in silico analyses that lead to the main messages given by the paper, i.e., the comparative analysis of the proposed controllers. Lastly, Section 7.5 draws some final conclusions.

7.2 Power System Modelling

We consider an isolated power system that includes a GT generator in isochronous mode, a wind turbine generator, a BESS, and an aggregated load. The GT is mainly responsible to stabilize the system by arresting the frequency deviation after a disturbance and simultaneously cooperate with the BESS to restore it to its nominal value. The following subsections describe then each of these elements in details, assuming the state of the system to be a six-dimensional vector where x_1 and x_2 are states related to the GT (governor and turbine subsystems respectively), x_3 is the power deviation coming form the battery storage system, x_4 is the grid's frequency variation, and x_5, x_6 are the states describing the internal dynamics of the batteries (relaxation and rate capacity effects).

7.2.1 Modelling of the grid dynamics

Given the scope of this paper, we choose to model the dynamics of the isolated power system as a first order transfer function from power balance to frequency deviation [14, 15, 32]. The transfer function, derived from the swing equation, is thus

$$M \cdot \frac{d\Delta f(t)}{dt} = -D \cdot \Delta f(t) + \Delta P_g(t) - \Delta P_\ell(t) \tag{7.1}$$

where M is the inertia constant (due to the generator's rotating mass), D is the damping constant (which encapsulates the combined effects of primary control layer (droop) and load damping, and ΔP_g and ΔP_ℓ the generated and consumed power deviations with respect to the operating point, respectively.

7.2.2 Gas turbine dynamics

To capture the dynamics of both the turbine and its governor, we model the dispatchable generation system as two first order low pass filters connected in series, giving the equivalent system

$$\begin{bmatrix} \dot{x}_1 \\ \dot{x}_2 \end{bmatrix} = \begin{bmatrix} -\frac{1}{T_g} & 0 \\ \frac{1}{T_t} & -\frac{1}{T_t} \end{bmatrix} \begin{bmatrix} x_1 \\ x_2 \end{bmatrix} + \begin{bmatrix} \frac{1}{T_g} \\ 0 \end{bmatrix} u_1 \tag{7.2}$$

where T_g is the governor time constant, T_t the turbine time constant, $u_1 = P_{gt}$ the power command to the GT, relatively to its steady state operating point $u_{1|t=0} = \Delta P^*_{gt} = 0$. The input to eq. (7.2) is defined as $u_{1|t} = u_{1|t-1} + \Delta u_{1|t}$, from which we see that the part associated to the small signal dynamics of the GT is Δu_1.

7.2.3 Wind turbine dynamics

The electromechanical conversion on the wind turbine generator is modeled as a first order filter [14, 15] from the input (mechanical wind power) to the output (electric

power injected into the grid). More precisely, we assume

$$w_1(s) = \frac{\Delta P_w(s)}{sT_{wt} + 1} \tag{7.3}$$

where T_{wt} is the wind turbine generator time constant, $\Delta P_w(s)$ is the uncertain wind power variation and $w_1(s) = \Delta P_{wt}(s)$ is the corresponding uncertain electric power injections from the wind turbine generator. As for modelling the stochastic process corresponding to the input, or in other words to implement the disturbance model used in our case, we consider wind speed scenarios from a wind speed generator that creates, starting from an average wind speed given as parameter, a realistic set of wind speed samples by means of a physics-driven model of the hydrodynamic effects occurring locally around wind turbines and rotor blades. Such a wind speed samples generator makes use of normal random variables and Kaimal distributions that better capture the small time scale wind intermittency. More details can be found in [33, 34].

7.2.4 Battery energy storage system dynamics

To model the dynamics of the power converter interfacing the BESS with the grid and capture the internal dynamics of the battery cells during charging and discharging processes, we consider the system

$$\begin{bmatrix} \dot{x}_3 \\ \dot{x}_5 \\ \dot{x}_6 \end{bmatrix} = \begin{bmatrix} -\frac{1}{T_B} & 0 & 0 \\ 0 & -\frac{c_r}{c_W} & \frac{c_r}{1-c_W} \\ 0 & \frac{c_r}{c_W} & -\frac{c_r}{1-c_W} \end{bmatrix} \begin{bmatrix} x_3 \\ x_5 \\ x_6 \end{bmatrix} + \begin{bmatrix} \frac{1}{T_B} \\ C_b^{-1} \\ 0 \end{bmatrix} u_2 \tag{7.4}$$

where $SoC = x_5 + x_6$ is the SoC, $u_2 = P_b = u_{2|t=0} + \Delta P_b$ the reference power to the BESS (since $u_{2|t=0} = \Delta P_b^* = 0$ at the steady state), T_B the time constant related to the power conversion and c_r, c_w the coefficients related to the linear modified KiBaM model, illustrated in fig. Figure 7.1 and which we assume as sufficiently detailed for our purposes [35–37]. Here it follows a detailed derivation of the proposed simplified battery model based on the modified KiBAM model. The battery charge dynamics (rate capacity and charge relaxation effects) can be approximated by an equivalent dynamic system of two interconnected water tanks with different volumes. If Q_b is the total charge of the battery at full capacity, Q_1 and Q_2 the total charge of tank 1 and 2 and their widths c_w and $1 - c_w$ correspondingly we have that $h_1 = \frac{q_1}{c_w}$ and $h_2 = \frac{q_2}{1-c_w}$, where q_1 and q_2 are normalized variables defined as $q_1 = \frac{Q_1}{Q_b}$ and $q_2 = \frac{Q_2}{Q_b}$ and h_1, h_2 represent the normalized water column heights (head) of each tank. Then, considering that the flow across the valve is proportional to the head difference between the two tanks, we can write

$$\dot{Q}_{21} = c_r' \left(h_2 - h_1\right) \Rightarrow \dot{q}_{21} = c_r \left(h_2 - h_1\right). \tag{7.5}$$

where c_r' is the valve's coefficient and $c_r = \frac{c_r'}{Q_b}$. Remembering that the output current is defined as $I_b = \dot{Q}_b$ and based on the above definitions we can write the tanks system

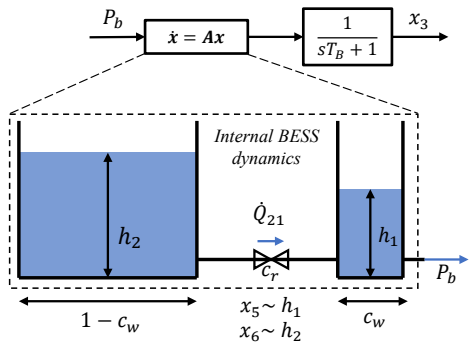

FIGURE 7.1. Modified kinetic battery storage system model (KiBAM) - analogy to coupled water tanks dynamics

equations as

$$\begin{cases} \frac{dQ_1}{dt} &= \dot{Q}_{21} - \dot{Q}_b \\ \frac{dQ_2}{dt} &= -\dot{Q}_{21} \end{cases} \Rightarrow \begin{cases} \dot{q}_1 &= -\frac{c_r}{c_w} q_1 + \frac{c_r}{1-c_w} q_2 - I_b Q_b \\ \dot{q}_2 &= \frac{c_r}{c_w} q_1 - \frac{c_r}{1-c_w} q_2 \end{cases}. \tag{7.6}$$

which can be compactly expressed as

$$\begin{bmatrix} \dot{x}_5 \\ \dot{x}_6 \end{bmatrix} = \begin{bmatrix} -\frac{c_r}{c_W} & \frac{c_r}{1-c_W} \\ \frac{c_r}{c_W} & -\frac{c_r}{1-c_W} \end{bmatrix} \begin{bmatrix} x_5 \\ x_6 \end{bmatrix} - \begin{bmatrix} Q_b^{-1} \\ 0 \end{bmatrix} I_b \tag{7.7}$$

where $x_5 = q_1 \sim h_1$ and $x_6 = q_2 \sim h_2$. Then, under the assumption of constant (average) open circuit voltage $\bar{V}_{oc}$ we can express the battery power as $P_b = \bar{V}_{oc} I_b$ and that the battery energy capacity can be written as $C_b = Q_b \bar{V}_{oc}$ [36, 37] we have

$$Q_b^{-1} I_b = C_b^{-1} P_b. \tag{7.8}$$

Finally, neglecting the charge/discharge efficiencies and considering a series-connected first-order delay for the power conversion stage (see Figure 7.1) we end up in eq. (7.4) where battery power $-\bar{P}_b \leq P_b \leq \bar{P}_b$ is the system input.

7.2.5 Dynamics of the whole interconnected system

Combining subsystems eqs. (7.1) to (7.4) as depicted in Figure 7.2, letting $x_4 = \Delta f$, and renaming the uncertain power demand as $w_2 = \Delta P_\ell$, eq. (7.1) can be rewritten as

$$\dot{x}_4 = -\frac{D}{M} x_4 + \frac{1}{M} \left(x_2 + x_3 + w_1 - w_2 \right). \tag{7.9}$$

This means that the system's model can be written in the state space form

$$\dot{\mathbf{x}} = A\boldsymbol{x} + B\boldsymbol{u} + H\boldsymbol{w} \tag{7.10}$$

$$\mathbf{y} = C^T \boldsymbol{x} \tag{7.11}$$

where $\boldsymbol{x}^T = [x_1, x_2, x_3, x_4, x_5, x_6]$, $\boldsymbol{u}^T = [u_1, u_2] = [P_{gt}, P_b]$, $\boldsymbol{w}^T = [w_1, w_2] = [\Delta P_{wt}, \Delta P_\ell]$, and

$$A = \begin{bmatrix} -\frac{1}{T_g} & 0 & 0 & 0 & 0 & 0 \\ \frac{1}{T_t} & -\frac{1}{T_t} & 0 & 0 & 0 & 0 \\ 0 & 0 & -\frac{1}{T_B} & 0 & 0 & 0 \\ 0 & \frac{1}{M} & \frac{1}{M} & -\frac{D}{M} & 0 & 0 \\ 0 & 0 & 0 & 0 & -\frac{c_r}{c_W} & \frac{c_r}{1-c_W} \\ 0 & 0 & 0 & 0 & \frac{c_r}{c_W} & -\frac{c_r}{1-c_W} \end{bmatrix} \tag{7.12}$$

$$B = \begin{bmatrix} \frac{1}{T_g} & 0 \\ 0 & 0 \\ 0 & \frac{1}{T_B} \\ 0 & 0 \\ 0 & -\frac{1}{C_b} \\ 0 & 0 \end{bmatrix}, \; C^T = \begin{bmatrix} 0 & 0 \\ 0 & 0 \\ 0 & 0 \\ 1 & 0 \\ 0 & 1 \\ 0 & 1 \end{bmatrix}, \; H = \begin{bmatrix} 0 & 0 \\ 0 & 0 \\ 0 & 0 \\ \frac{1}{M} & -\frac{1}{M} \\ 0 & 0 \\ 0 & 0 \end{bmatrix}. \tag{7.13}$$

From a block-scheme perspective, the overall system is thus modelled as in Figure 7.2.

7.3 CONTROL DESIGN

7.3.1 *Deterministic Model Predictive Control*

To achieve optimal operation and reduced fuel usage in isolated power systems, supervisory power management is typically used to deliver the optimal scheduling set points to the local controllers of the different subsystems, such as the BESS and the GTs [8, 38]. In this study we consider integrating the local control objectives of these subsystems along with the frequency regulation of the isolated power system. Local objectives mean that the GT can still operate with minimum deviation from its optimal loading and provide primary grid stabilization while the BESS can still follow a SoC reference trajectory coming from a tertiary dispatch level, and at the same time work together to restore and tightly regulate the system's frequency. For this purpose we propose using a Model Predictive multi-objective MIMO control that, on top of the basic requirements, aims at minimizing the control effort so to promote reduced actuator wear, and cycling energy storage so to promote longer battery lifetime. To integrate the several control objectives considering the state space model developed section 7.2 into a MPC formulation we first use a recursive elimination approach to express the states for the selected prediction horizon N_p as

$$\boldsymbol{X} = A_e \boldsymbol{x}_0 + B_0 \boldsymbol{u}_0 + B_e \boldsymbol{\Delta U} + H_e \boldsymbol{W} \tag{7.14}$$

where $\boldsymbol{x}_0$ is the initial condition, $\boldsymbol{u}_0^T = \left[\Delta P_{gt}^*, \Delta P_b^*\right]$ is the initial operating point of the subsystems and $\boldsymbol{X}$, $\boldsymbol{\Delta U}$, $\boldsymbol{W}$, A_e, B_0, B_e, and H_e are defined in section 7.6. Hence, we define the following qualitative control objectives:

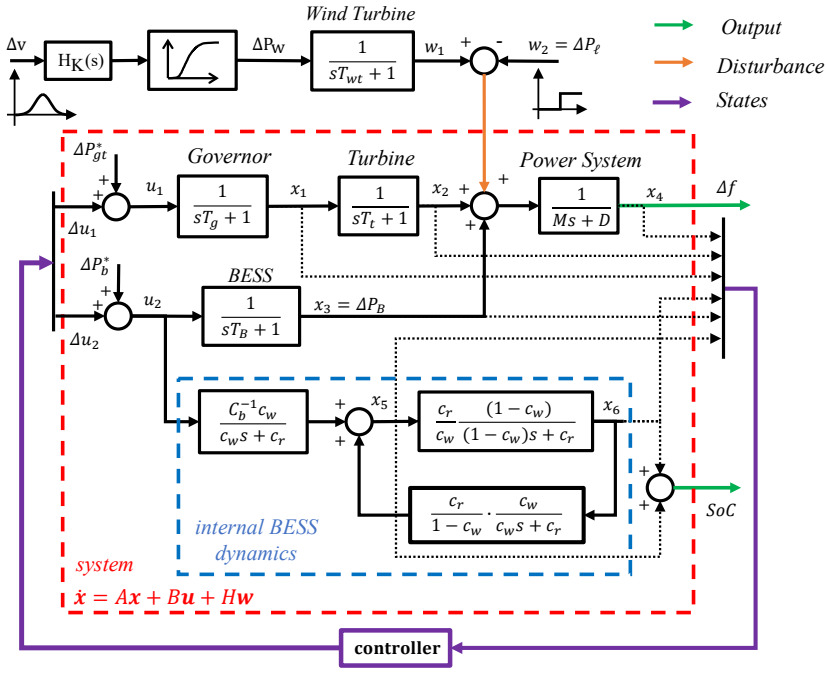

FIGURE 7.2. Schematic representation and modelling of the interconnected system considered in this paper

- minimize the frequency deviation (to achieve FFR purposes);
- minimize the amplitude of the control signal (to minimize the fuel consumption associated to GT usage);
- perform an optimal system operation (to follow the reference schedule);
- reduce BESS degradation (to minimize replacement costs).

We then translate the above qualitative targets into quantitative ones as follows: first, penalize the states with the Q-norm $\boldsymbol{x}^T Q \boldsymbol{x}$, with Q diagonal and positive definite, so to promote small frequency deviations. Then penalize deviations from operating the GT at its maximum efficiency, and thus penalizing Δu_1 through the norm $\boldsymbol{\Delta u}^T R \boldsymbol{\Delta u}$ to minimize the GT fuel consumption. To follow the reference schedule, penalize the deviations of the SoC from the reference value using the affine plus quadratic cost $\ell\left(s^T \boldsymbol{x} - SoC_{ref}\right)^2$. Penalizing the BESS degradation can be then promoted in several ways. Typically, the degradation of a battery is modelled as caused by two distinct effects [39], namely the calendar aging and the cycling effect. Since the cycling degradation is dependent on the number of cycles and the depth of the cycles, a common approach is to discourage cycling by minimizing the standard deviation of the SoC

for the prediction horizon as $\mu\sqrt{\frac{1}{N_p}\sum_{k=1}^{N_p}\left(SoC_k - \frac{1}{N_p}\sum_{k=1}^{N_p} SoC_k\right)^2}$.

Then, by considering the augmented states $\boldsymbol{X}$ and control variables $\boldsymbol{U}$ for the prediction and control horizons (N_p and N_c respectively), and expressing the evolution of SoC as $\boldsymbol{X}_{soc} = \boldsymbol{S}\boldsymbol{X}$, we can formulate the objective function for the finite horizon optimal control problem as

$$J = \boldsymbol{X}^{\boldsymbol{T}}\boldsymbol{Q}\boldsymbol{X} + \left(\boldsymbol{S}\boldsymbol{X} - \boldsymbol{X}_{\boldsymbol{soc}}^{\boldsymbol{ref}}\right)^{\boldsymbol{T}} \boldsymbol{L}\left(\boldsymbol{S}\boldsymbol{X} - \boldsymbol{X}_{\boldsymbol{soc}}^{\boldsymbol{ref}}\right) + \frac{\mu}{\sqrt{N_p - 1}}\left\|\left(\boldsymbol{S}\boldsymbol{X} - \frac{1}{N_p}\|\boldsymbol{S}\boldsymbol{X}\|_1\right)\right\|_2 + \boldsymbol{\Delta U}^{\boldsymbol{T}}\boldsymbol{R}\boldsymbol{\Delta U} \tag{7.15}$$

J in eq. (7.15) is convex in $\boldsymbol{X}$ and $\boldsymbol{\Delta U}$ by construction (since a sum of basic convex functions. The constraints associated to the problem of optimizing J shall then include the physical limits of the components (like the allowable BESS SoC range, minimum and maximum governor opening, BESS power limits, and ramp rates for the changes of the manipulated variables), and the maximum allowable deviations from the nominal frequency and SoC. Summarizing, the constraints can be expressed mathematically as

$$\boldsymbol{P}\cdot\boldsymbol{X} + \boldsymbol{c} \preceq \boldsymbol{0} \tag{7.16}$$

$$\boldsymbol{U}_{\boldsymbol{min}} \preceq \boldsymbol{U} \preceq \boldsymbol{U}_{\boldsymbol{max}} \tag{7.17}$$

$$\boldsymbol{\Delta U}_{\boldsymbol{min}} \preceq \boldsymbol{\Delta U} \preceq \boldsymbol{\Delta U}_{\boldsymbol{max}} \tag{7.18}$$

where $\boldsymbol{P}$ and $\boldsymbol{c}$ contain information of the hard limits on the states and are presented in Section 7.6. Here we note that in practice, different battery cell types and technologies would have different C-rate limitations, resulting in different and tighter bounds on the allowed charge/discharge power. However, such limits can be directly integrated in eqs. (7.17) and (7.18) without affecting the formulation of the problem proposed in this paper. To simplify our analysis while preserving generality, and since the focus of the paper is not on the comparison of different battery types and technologies, we chose to restrict charge/discharge power based on the rated power, as commonly done. This is a simplifying assumption which eventually does not alter the methodology proposed in this paper or the comparative analysis presented later, since all comparisons are performed under the same generic battery model and same constraints. In this way we intend to provide upper theoretical bounds on the performance, while further case specific studies are needed depending on the selected battery technology. As a complement, an additional sensitivity analysis focusing on the different factors that affect the resulting charge/discharge rate is provided in Subsection 7.4.5. eqs. (7.14) to (7.18) define then the DMPC that will then be compared against the stochastic one defined in the next subsection.

7.3.2 Stochastic Model Predictive Control

One of the objectives of this manuscript is to investigate which strategy best handles uncertainties while guaranteeing control performance. To account for uncertainties in the control design we then adopt the commonly used sa-SMPC [28–30, 40, 41], where the cost eq. (7.15) from the DMPC scheme is replaced by an expectation over the possible outcomes defined from the scenarios. The implementation of such cost function is done through the SAA [42] as

$$\mathbb{E}[J(u,w)] \approx \frac{1}{N}\sum_{\omega=1}^{N} J(u_\omega, w_\omega) \tag{7.19}$$

Where N is the number of scenarios considered. As explained in [41], different constraints are induced by eqs. (7.16) to (7.18) for each random realization of the uncertainty from the randomly sampled uncertainty set. Those can be described as

$$\boldsymbol{P}\cdot\boldsymbol{X}_\omega + \boldsymbol{c} \preceq \boldsymbol{0}, \quad \omega \in \{1,\dots,N\} \tag{7.20}$$

$$\boldsymbol{U_{min}} \preceq \boldsymbol{U_\omega} \preceq \boldsymbol{U_{max}}, \quad \omega \in \{1,\dots,N\} \tag{7.21}$$

$$\boldsymbol{\Delta U_{min}} \preceq \boldsymbol{\Delta U_\omega} \preceq \boldsymbol{\Delta U_{max}}, \quad \omega \in \{1,\dots,N\} \tag{7.22}$$

We highlight, that there is not specific requirement on the distribution of the RVs, or the disturbance model used for the sa, as long as number of samples used is chosen based on the main theorem [43] and the same risk criteria. Another interesting feature related to the SMPC is the different choices for the parametrization of the control input [41], an aspect which is also investigated in this study. In this paper we thus employ different commonly reported controller parametrizations for the SMPC formulation eqs. (7.19) to (7.22), and compare their performance in terms of handling uncertainties and system performance. More specifically, we consider the following parametrizations:

Open loop policy (no parametrization)

The direct open loop policy is also considered as a possible choice for the controller, meaning that the direct output of the solution of the numerical optimization problem eqs. (7.19) to (7.22) is applied to the plant, i.e.,

$$u_i = \gamma_i. \tag{7.23}$$

The non-parameterized control action (SMPC-NP) is also included as a benchmark alternative to better understand and illustrate the effects of the control action parameterization, relatively to a less constrained open loop solution. Here we specify, that still under this parametrization, the controller is of the standard rolling horizon MPC type, which means that feedback of the system's response is given back to the controller

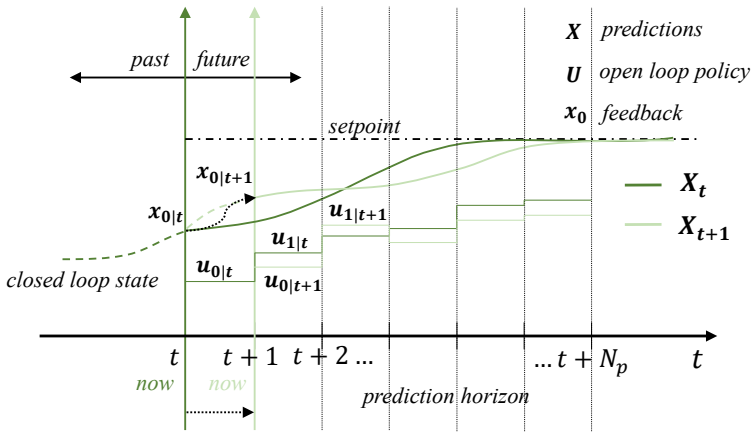

FIGURE 7.3. Feedback mechanism of the open loop MPC policy

in the form of the constantly updated initial condition for each step's optimization problem [44, 45]. In that way, no substantial error is accumulated over time. This concept is illustrated in Figure 7.3

Affine disturbance feedback

The disturbance feedback full parametrization (SMPC-FP) adjusts the control action directly based on past values of disturbance realizations. By using this strategy, the disturbance history is fed into the controller while preserving the convexity of eq. (7.19). More in details, such full parametrization is defined as

$$u_i = \gamma_i + \sum_{j}^{i-1} \theta_{i,j} w_{0+j}. \tag{7.24}$$

With such a parametrization, we include constant terms γ_i and terms $\theta_{i,j}$ proportional to past disturbance realizations w_j, for the specified control horizon. In this way the resulting optimization problem is convex with respect to the control parameters which are iteratively updated on each MPC iteration. Note that, by reorganizing this into a recursive eliminated vector form, and by integrating the number of states, control actions, and disturbances, one obtains

$$\boldsymbol{U} = \Gamma + \Theta \boldsymbol{W} \tag{7.25}$$

where $\boldsymbol{U}, \boldsymbol{W}, \Gamma, \Theta$ are defined as in Section 7.6.

State feedback

Another commonly used controller parametrization for state space formulations is the state feedback parametrization (SMPC-SF), defined as

$$u_i = \gamma_i - K_{lqr} x_i \tag{7.26}$$

where K_{lqr} is a fixed constant. In contrast with SMPC-FP, this particular parametrization suffers from the fact that the feedback gain parameter cannot be treated as an optimization variable, since this would result in a non-convex problem [41]. To avoid this issue, K_{lqr} may be chosen to be the infinite horizon optimal gain (see [41] for more details).

7.3.3 Robust Control

To compare the stochastic control approach described in Subsection 7.3.2 against a robust control design approach, we also design a mixed synthesis H_∞ controller for the system eqs. (7.10) and (7.11). More precisely we design the H_∞ controller by applying the principles of loop shaping, designing appropriate weights W_p and W_d for acceptable nominal performance and robust stability for the lumped unstructured output multiplicative uncertainty, and finally solving a linear matrix inequality (LMI) optimization problem that minimizes the cost

$$\left\| \begin{bmatrix} W_p S \\ W u K S \\ W_d T \end{bmatrix} \right\|_\infty \leq \gamma \leq 1 \tag{7.27}$$

where W_p, Wu, and W_d are the disturbance-rejection performance, controller effort and robustness weights respectively. Selecting proper weights for $W_p(s), W_d(s)$ allows then to upper bound the sensitivity $S(s)$ and complementary sensitivity $T(s)$ functions, finding an overall satisfactory controller $K(s)$. This paper follows the basic guidelines from [46] on how to select these weights for robust disturbance rejection; after an iterative procedure we set

$$W_p(s) = \begin{bmatrix} \frac{\frac{2}{3}s+0.01}{s+3.15*10^{-6}} & \frac{\frac{2}{3}s+0.01}{s+3.15*10^{-6}} \\ \frac{\frac{2}{3}s+0.50}{s+4.99*10^{-6}} & \frac{0.32s+0.05}{s+4.74*10^{-6}} \end{bmatrix} \tag{7.28}$$

$$W_u(s) = 1 \tag{7.29}$$

$$W_d(s) = \begin{bmatrix} \frac{0.32s+0.018}{s+1.77} & \frac{10s+3.33}{s+33.34} \\ \frac{s+1.00*10^{-8}}{s+100} & \frac{s+3.17}{s+31.65} \end{bmatrix}. \tag{7.30}$$

From Figure 7.4, we notice how the robustness weight selected as

$$W_d(s) = \frac{0.32s + 0.018}{s + 1.77} \tag{7.31}$$

bounds all realizations of the relative model error of the uncertain plant, validating the required specification for a robust controller design. Note that this type of robust control only considers parametric uncertainty being integrated as output multiplicative.

7.4 SIMULATION RESULTS AND ANALYSIS

To analyze the effect of the proposed multi-objective MIMO control strategies, we compare the various control designs described in sections 7.3.1 to 7.3.3 in terms of their dynamic response and capabilities of handling uncertainty. We note that our proposed formulations adopt the simplified but generic battery model described in eq. (7.4) where no particular technology-dependent maximum C-rates are enforced besides the power rating limits (eqs. (7.17) and (7.18)). Since the focus of the study is on the comparative analysis and not on the different technologies' comparison, for the purpose of the analysis presented in sections 7.4.1 to 7.4.4 we therefore assume no further technology-dependent battery power constraints, but we ensure the same model and limits for all controllers, for a fair comparison. However, a detailed discussion on the various factors affecting the battery charge/discharge rate and the resulting C-rate is given in Subsection 7.4.5. In addition, we note that for the nominal case, the controller assumes no mismatch to the plant model, as to have a benchmark upper bound performance, for comparison with the proposed controllers that assume no knowledge of the nominal plant by considering both the uncertain plant parameters and the unmodeled dynamics. The following key performance indices are defined on the output signals to serve the relative comparison:

- Max frequency deviation:

$$M_f = \|\Delta f(t)\|_\infty \tag{7.32}$$

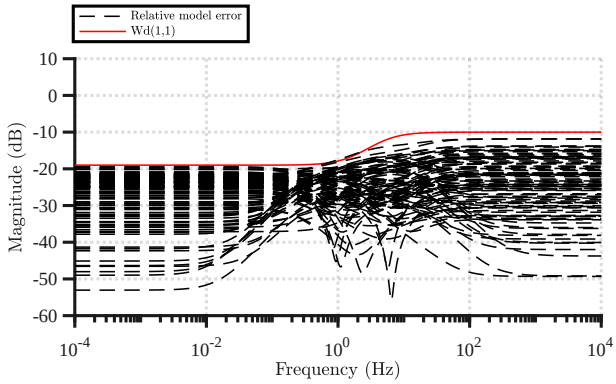

FIGURE 7.4. Frequency response of the relative model error for random realization of uncertainty and robustness weight $W_d(s)$ covering the responses

- Average (expected) frequency deviation:

$$A_f = \frac{1}{N_{sim}} \sum_{k=1}^{N_{sim}} |\Delta f(k)| \tag{7.33}$$

- Total fuel usage:

$$T_{u_1} = \sum_{k=1}^{N_{sim}} |\Delta P_{gt}(k)| \tag{7.34}$$

- Max SoC deviation:

$$M_{soc} = \left\| \boldsymbol{SX} - \boldsymbol{X_{soc}^{ref}} \right\|_{\infty} \tag{7.35}$$

- Average (expected) SoC deviation:

$$A_{soc} = \frac{1}{N_{sim}} \sum_{k=1}^{N_{sim}} \left| \left(\boldsymbol{SX} - \boldsymbol{X_{soc}^{ref}} \right)_{\boldsymbol{k}} \right| \tag{7.36}$$

- SoC standard deviation (storage cycling indicator):

$$STD_{soc} = \frac{\left\| \left(\boldsymbol{SX} - \frac{1}{N_{sim}} \|\boldsymbol{SX}\|_1 \right) \right\|_2}{\sqrt{N_{sim} - 1}} \tag{7.37}$$

where N_{sim} is the number of simulated time steps.

7.4.1 Nominal dynamic performance

Initially, we compare the performance of designs DMPC, SMPC-FP, SMPC-SF, SMPC-NP, H_∞ at the nominal conditions, that is for the nominal set of plant parameters (see Table 7.1) and for a deterministic knowledge of the disturbance signal (i.e., assuming the uncertain wind power generation to be constant). This means that in this specific case the different versions of the SMPC controllers consider only one scenario implying that the DMPC, SMPC-FP, SMPC-NP formulations are in this case equivalent. However, the design of the SMPC-SF is different since it depends on the state feedback gain K_{lqr} which is calculated independently of the uncertainty realization, thus resulting in a different performance.

The comparison of the dynamic performance of the various designs is illustrated through Figure 7.5. In particular, from fig. 7.5a we can observe the frequency response of the isolated power system, from fig. 7.5b the SoC regulation to the scheduled value, and from fig. 7.5c the control effort required from the two subsystems (BESS and GT)

to achieve the multiple objectives. From fig. 7.5a it is clear that the *DMPC/SMPC-FP/SMPC-NP* design achieves the fastest regulation with the smallest peak deviation, the SMPC-SF design has the smallest damping and the largest peak deviation while the H_∞ design results in a slower but less oscillatory response. Then, from fig. 7.5b we observe that H_∞ achieves the best tracking of the reference value with negligible dynamics, while DMPC/SMPC-FP/SMPC-NP once more performs better than SMPC-SF. However, the performance of H_∞ can be justified by fig. 7.5c where we can observe the unbalanced use of GT and battery power to achieve the multiple goals. As it is observed, DMPC/SMPC-FP/SMPC-NP and SMPC-SF split the power usage between the two units whereas H_∞ achieves the same goals by using almost exclusively the GT in a way that avoids the power overshoot in contrast with the others. This sub-optimal response is associated with the tuning of the performance weights, a difficulty which inherently associated with the mixed sensitivity design procedure, since the calculation of the most appropriate weights is a notoriously challenging and tedious task.

7.4.2 Mixed model and disturbance uncertainty

To further compare the performance of the controllers introduced in Subsection 7.4.1 for the nominal conditions, we include a 10% uncertainty in the model parameters, so to capture imperfect knowledge one may have when identifying the system plant parameters. Dynamic simulations were performed for random values of the plant parameters and the corresponding responses as in Figure 7.5 where recorded for each design: DMPC, SMPC-FP, SMPC-SF, SMPC-NP. The dynamic responses of the system under the various controllers are derived for random realizations of the uncertain parameters and disturbances and compared. By observing Figure 7.6 to Figure 7.10 we see the following patterns:

i. The response profiles of DMPC is very similar to the ones of SMPC-FP, SMPC-NP since these controllers are somehow equivalent in the absence of disturbance uncertainty.

ii. Performance of the SMPC-SF are different relatively to the other stochastic controllers, achieving in general less overshoot at the requested GT power, at the cost of slower frequency regulation and an overshot in the SoC tracking.

iii. The robust H_∞ controller achieves the best SoC tracking at the presence of small overshoot at the frequency regulation and higher usage of GT power. In addition the GT actuation depends significantly on the plant parameters compared to the other controllers.

7.4.3 Monte-Carlo simulations and constraint violation

To assess the ability of the stochastic controllers SMPC-FP, SMPC-SF, SMPC-NP in integrating all kinds of uncertainties under the sa, the various designs from Subsec-

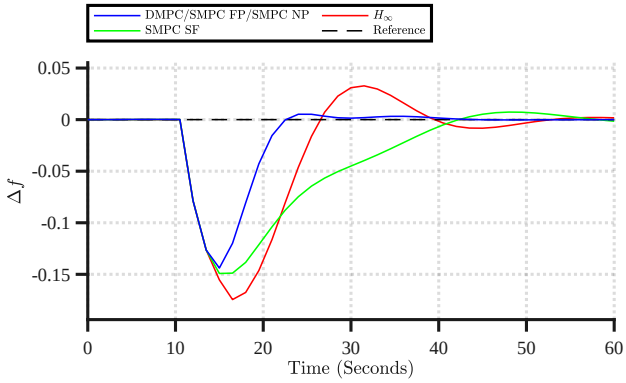

(a) Frequency deviation

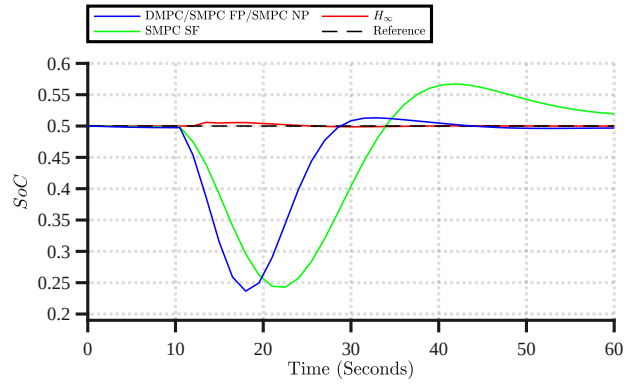

(b) SOC

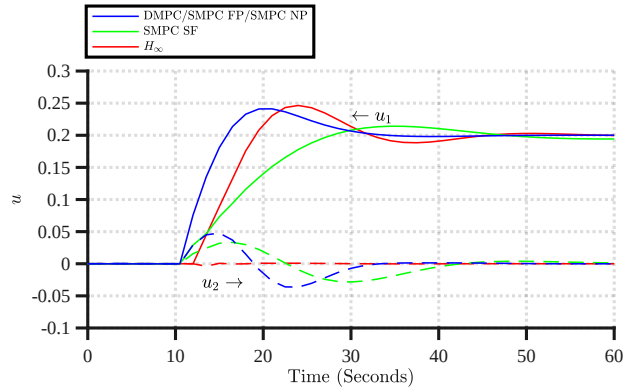

(c) control action

FIGURE 7.5. Response without disturbance and parametric uncertainty

tion 7.4.1 were compared under a *MC* simulation framework [23, 47]. By performing numerous simulations and considering both parametric and disturbance uncertainty, the ECDFs of the constrain violations and of the indices eqs. (7.32) to (7.37) were calculated.

We note that from the *sa*, the constraint satisfaction is meant on a probabilistic sense, that is by using specific number of scenarios we can have theoretical guarantees (bound) on the maximum violation probability when the original distribution is used. To demonstrate this effect, the SMPC-FP design was considered with different values of scenarios (small number: 250, big number: 750) and corresponding guaranteed violation probabilities. Increasing the number of scenarios generally results in a smaller violation probability, a fact which is numerically validated through Figure 7.11 where we observe that for larger number of scenarios the constraint violation probability decreases. From the same figure it is also remarkable to notice the superiority of stochastic control over the deterministic version (DMPC) which is always associated with a higher probability of constraint violation. In addition, we can observe that the combined effect of disturbance uncertainty and 10% parametric uncertainty has a greater impact on the max frequency deviation constraint fig. 7.11a compared to the max SoC deviation constraint fig. 7.11b. From the latter we can see that even though enough cases would imply the maximum allowable deviation, none of them would

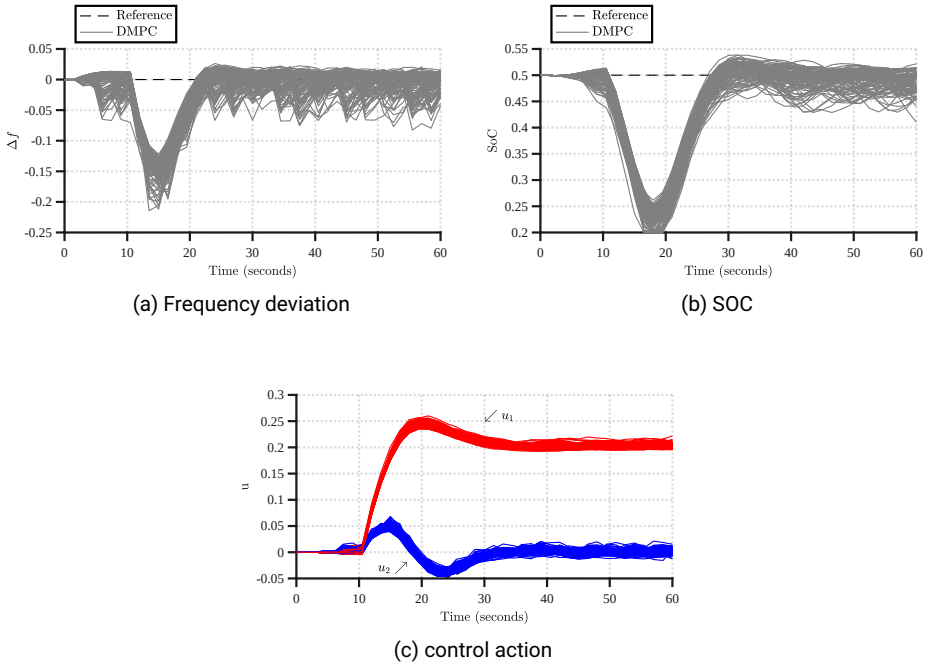

(a) Frequency deviation

(b) SOC

(c) control action

FIGURE 7.6. Response with disturbance and 10% parametric uncertainty for DMPC

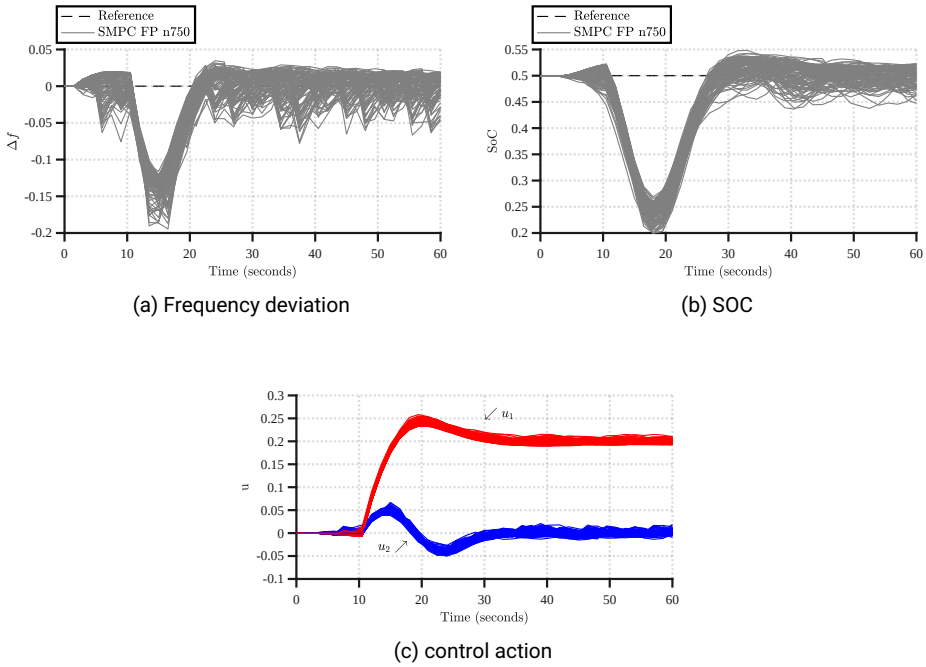

(a) Frequency deviation

(b) SOC

(c) control action

FIGURE 7.7. Response with disturbance and 10% parametric uncertainty for SMPC-FP 750 scenarios

cause an actual violation.

Then, for the large number of scenarios (750) we compared the max constraint violation probabilities for the different controllers (deterministic, stochastic with different parametrizations, and robust). From Figure 7.12 we observe that SMPC-FP and SMPC-NP achieve lower constraint violations for the max frequency and SoC deviations compared to DMPC whereas DMPC performs better for the max frequency constraint than SMPC-SF. This is an interesting result demonstrating *i)* the incapability of state feedback to adapt its control law based on disturbance information and *ii)* the unexpectedly good performance of the DMPC, considering an expected behavior as the deterministic equivalent. However, the trends seem to be different for the max SoC deviation, where SMPC-FP and SMPC-SF seem to perform better than SMPC-NP and DMPC, meaning that the state feedback parametrization has a better capability of handling the parametric uncertainty related to the SoC variations relatively to DMPC. Finally, from fig. 7.12a and fig. 7.12b we observe that the robust design is associated with the highest violation probability in max frequency deviations and the smallest in SoC deviation respectively. This fact is in agreement with the fact that H_∞ considers the parametric uncertainty, minimizing the impact on the SoC deviation but does not considers disturbances that could cause higher frequency variations.

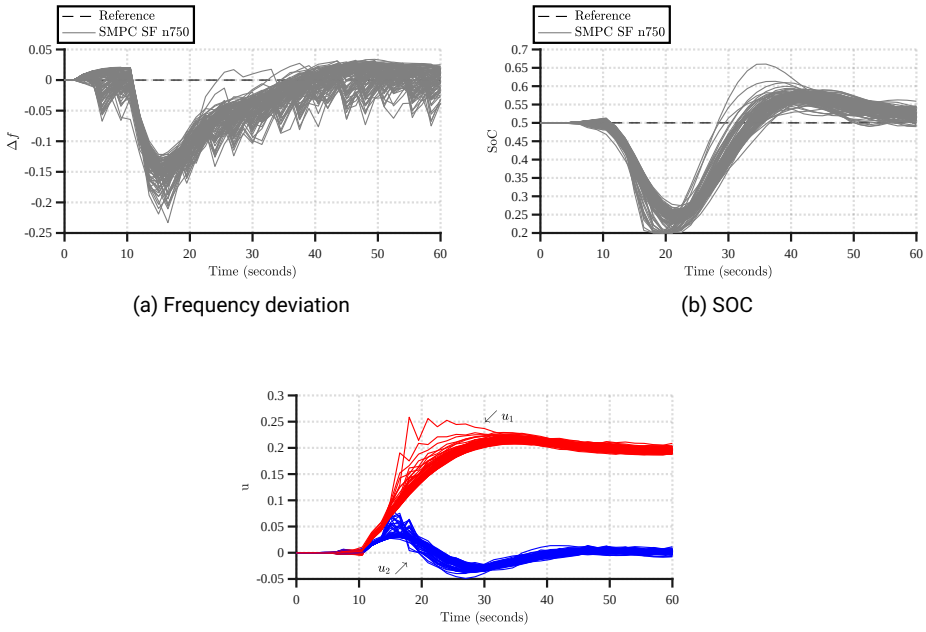

(a) Frequency deviation

(b) SOC

(c) control action

FIGURE 7.8. Response with disturbance and 10% parametric uncertainty for SMPC-SF 750 scenarios

7.4.4 Expected performance and operation

Finally, the different control designs were compared in terms of their average constraint violation performance, the fuel usage of the gas turbine and the battery cycling. In particular from Figure 7.13 we can observe the ECDFs of the average frequency deviation defined in eq. (7.33) and the average SoC deviation as defined in eq. (7.36). From fig. 7.13a we can see that SMPC-FP, SMPC-NP, DMPC significantly outperform the SMPC-SF, H_∞, with DMPC having a bit more violations compared to the best stochastic designs. A similar trend is observed from fig. 7.13b, from which we can see that the average performance of the state feedback control is much worse compared to the other stochastic controllers. From these figures we can also see once more the pattern associated to robust control, where the average frequency violations are even worse than the worst stochastic design while the average SoC deviations are much better compared to the rest.

From Figure 7.14 we can observe the effect of each controller on the battery degradation levels. As expected, since the robust control makes minimum use of the storage system, its degradation is the smallest with significant difference from the rest, while for the other controllers we can see again that SMPC-FP, SMPC-NP designs have a better degradation performance than SMPC-SF, DMPC with SMPC-SF again being the worst. However, interestingly the trends reverse for the total fuel usage

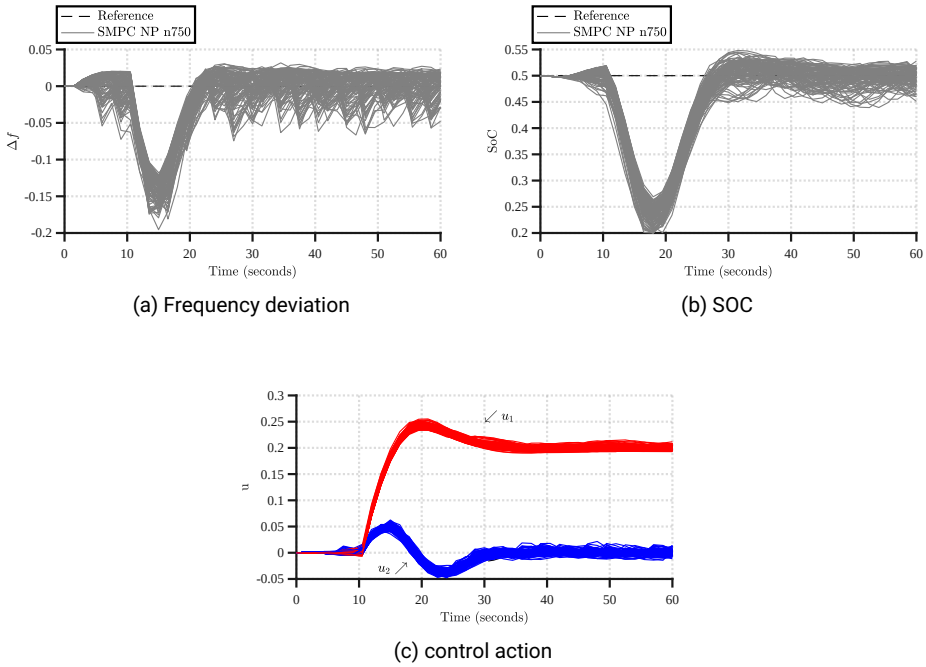

FIGURE 7.9. Response with disturbance and 10% parametric uncertainty for SMPC-NP 750 scenarios

defined in eq. (7.34), where from Figure 7.15 we can see that the SMPC-SF design is associated with the smallest total fuel usage probability compared to the other designs and the H_∞ is associated with the largest one with a big difference. The other designs (stochastic and deterministic) all have very similar behavior in terms of the total units of fuel distributions.

7.4.5 Effect of BESS related parameters on the dynamic performance

From the analysis above it is clear that different control methods and parametrizations lead to different dynamic performance of the system. However, it is not only these two factors that affect the system's behavior. Different weighting of the multiple objectives of the MPC optimization problem or different battery characteristics, such as its size, affect the resulting behaviors. Under this perspective, it is worth mentioning that the resulting behaviors shown in the previous sections where all derived for the same weightings and BESS size. The latter was set equal to unity (see Section 7.6, Table 7.1) in order to consider a general case and in accordance with a per unit representation of the power deviations associated with the system operation (see Section 7.6). Therefore, the proposed control methodology can be built upon a generic idealized system to remain as general as possible, since the target is not to provide case-specific results but a general control design framework where the control design procedure should be the

same irrespectively of the battery capacity.

In particular, when referring to the SoC trajectories observed in the previous sections, it is important to highlight their dependence on 3 main parameters: i) the SoC deviation weight ℓ, ii) the energy capacity value C_b and iii) the maximum power to energy ratio defined as $\lambda = \frac{\bar{P}_b}{C_b}$. Even though the BESS capacity and the power rating are design parameters, whose selection is beyond the scope of this study but requires detailed analyses considering techno-economical perspectives, it is useful to study the effect of those parameters under the proposed MPC framework, for the nominal conditions. For this reason, we performed three individual sensitivity analyses which are explained in detail below. For all the following analyses we follow the same color convention where red represents the SoC deviation, blue the BESS power deviation and green the system's frequency deviation.

Sensitivity analysis for the SoC weighting

First, the effect of the SoC deviation weight ℓ was studied. We performed various simulations (load step disturbance) with increasing values ℓ, giving more significance to large SoC deviations and thus better constraining the discharge/charge C-rates of the battery. The results are illustrated in Figure 7.16. From 7.16a we observe that increasing ℓ not only leads to less SoC variation but also to decreasing discharging/charging

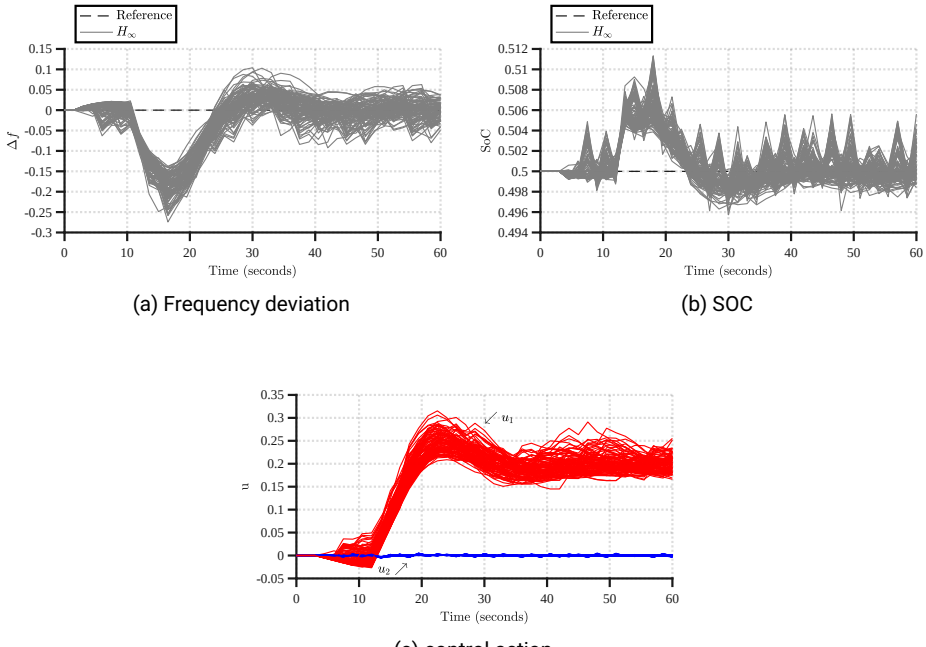

(a) Frequency deviation

(b) SOC

(c) control action

FIGURE 7.10. Response with disturbance and 10% parametric uncertainty for H_∞

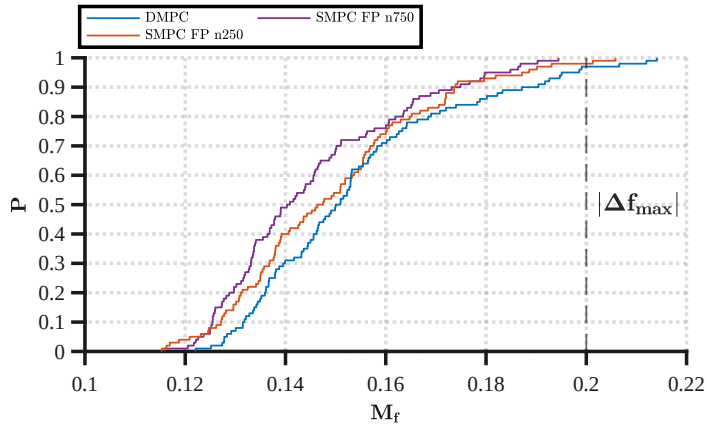

(a) Max frequency deviation

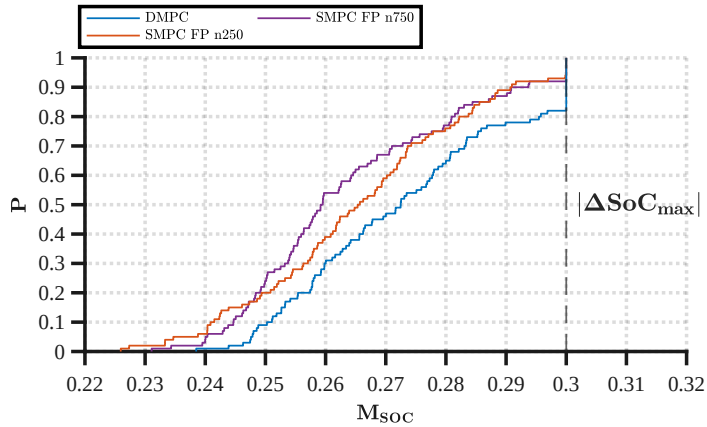

(b) Max SOC deviation

Figure 7.11. States empirical cumulative distribution functions with SMPC-FP controller

rates, which can be of great importance when specific limits for the C-rates of the battery have to be respected. For example, selecting the maximum value of $\ell = 80$ and considering the battery's discharging at the load step (approximately 2% in 5 seconds, red curve in fig. 7.16a) we can estimate a C-rate of around 0.1440, which is much lower than the one for $\ell = 2$. However, putting a lot of weight to the SoC deviation comes at the cost of a higher overshoot at the systems frequency response, as can be observed from fig. 7.16b (bold green line). From this analysis, we can conclude that a value of $\ell = 20$ would give a fair trade-off between the SoC deviation penalization and a realistic C-rate for the battery charging/discharging process. For this reason, we kept this value for the next analyses.

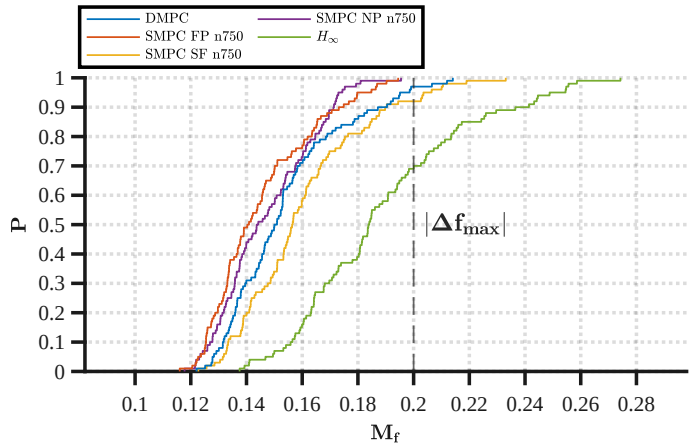

(a) Max frequency deviation

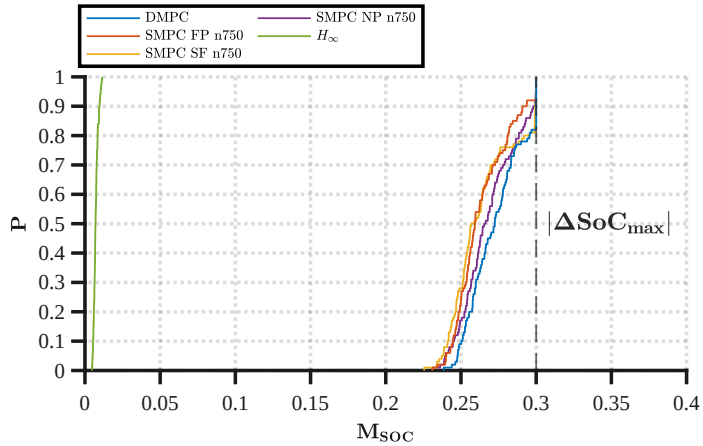

(b) Max SOC deviation

FIGURE 7.12. States empirical cumulative distribution functions SMPC-FP vs SMPC-SF vs SMPC-NP vs DMPC vs H_∞

Sensitivity analysis for the BESS capacity

Another very important factor affecting the resulting charge/discharge rates is the total available energy capacity of the battery system. It is expected that for larger capacities and same discharge levels, the C-rates will be decreasing. Again we performed various simulations (load step disturbance) where the BESS per unit scaled capacity C_b is changing in multiples of the nominal one ($C_b = 1$). In fig. 7.17a and fig. 7.17b we observe the resulting trajectories of the SoC, the BESS power and the system's frequency response. We see that increasing the battery size, the minimum value of SoC is increasing, leading to lower peak C-rate and higher minimum frequency deviation,

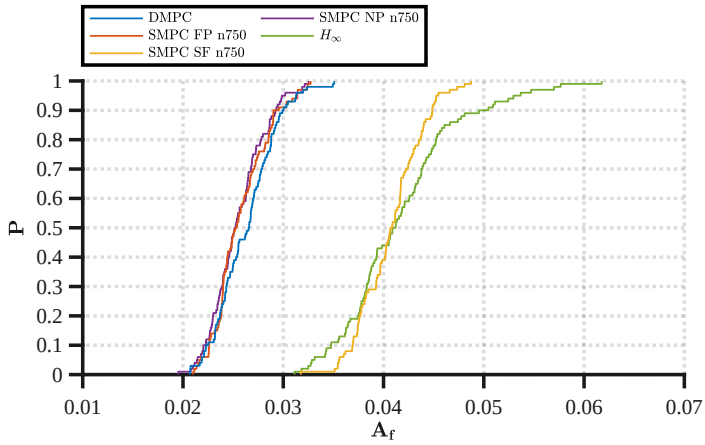

(a) Average frequency deviation

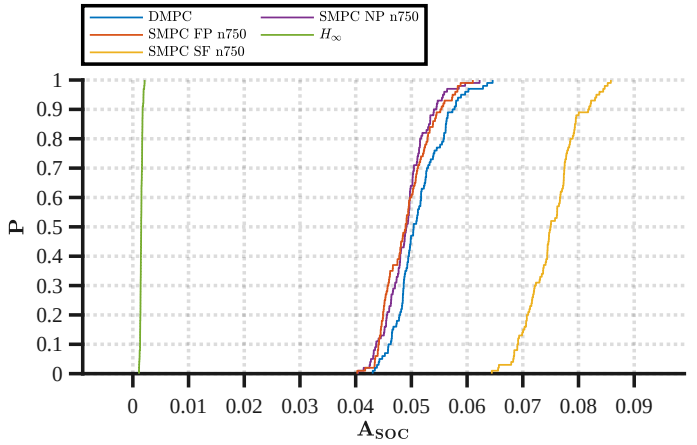

(b) Average SoC deviation

FIGURE 7.13. Average frequency and SoC deviation SMPC-FP vs SMPC-SF vs SMPC-NP vs DMPC vs H_∞

even though the frequency response is a less dumped. In other words, increasing the battery size, the system can tolerate higher discharge power rates, resulting in lower C-rates for the battery and improved frequency nadir.

Sensitivity analysis for the BESS power to energy ratio

Finally, the effect of the maximum power to energy ratio was studied by varying the λ parameter from 1 to 0.1. This means that a BESS with $\lambda = 1$ has 10 times higher power provision capability than the one for $\lambda = 0.1$, for the given (same) energy capacity. In other words, λ reflects the effect of further restricting the battery charge/discharge power $\bar{P}_b$, resembling different technologies with different C-rate limits which are

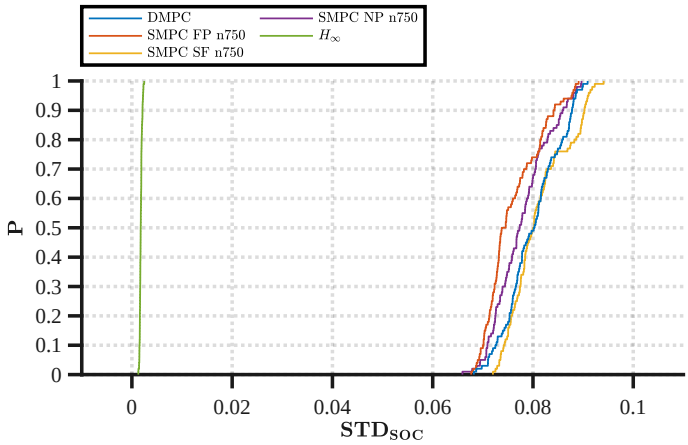

FIGURE 7.14. SoC standard deviation (BESS cycling indicator) SMPC-FP vs SMPC-SF vs SMPC-NP vs DMPC vs H_∞

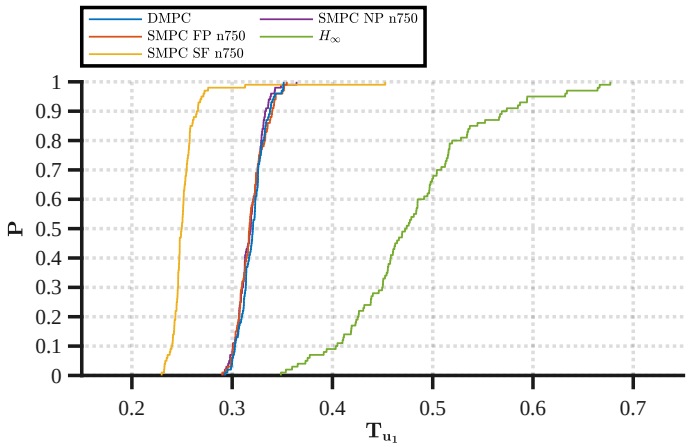

FIGURE 7.15. Total units of fuel SMPC-FP vs SMPC-SF vs SMPC-NP vs DMPC vs H_∞

effectively power constraints. Then, from fig. 7.18a we observe that by increasing λ we can effectively reduce the C-rate of the BESS not only by reducing its minimum SoC deviation but also by slowing down the BESS response, meaning that to reach its minimum SoC deviation value, more time is required. It is remarkable in that case, since the goalsẃeights were kept to the same values, that the controller requested more power from the BESS for lower λ values, resulting in almost identical system frequency response (fig. 7.18b). However, this is only available when the power rating of the BESS is large enough (as in our case) not to saturate the requested power.

7.5 Discussion and Conclusions

This study proposed, analysed and compared a set of multi-objective MIMO supervisory controllers for isolated power systems composed of a GT, a wind turbine and a BESS. The proposed controllers are all based on the concept of integrating optimal frequency regulation for the isolated grid (isochronous operation) while at the same time tracking scheduling commands for the energy storage system. This was achieved though different model predictive controllers accounting for different types of uncertainty and different controller parametrizations. Overall, the goal has been of comparing deterministic MPC approaches against stochastic MPC ones and robust

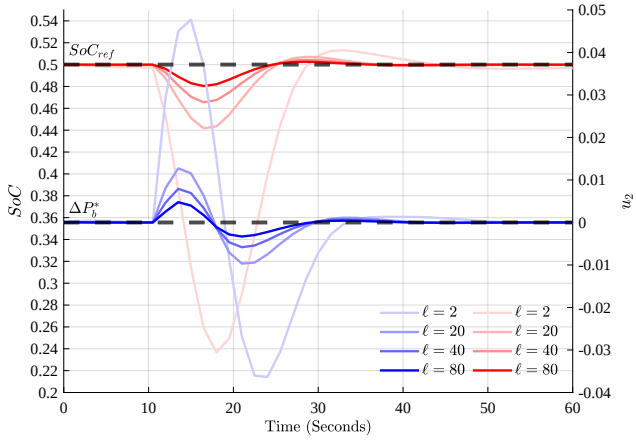

(a) SoC and battery power deviations

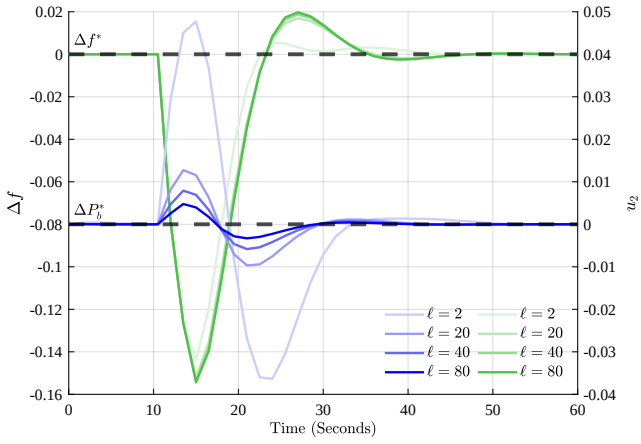

(b) System frequency and battery power deviations

Figure 7.16. Sensitivity analysis results for varying ℓ

control.

The results showed that stochastic control is *not* always associated with smaller constraint violation probability compared to the deterministic case. The occurrence of this event was, though, strongly correlated on the controller parametrization. In particular, we found that an affine disturbance parametrization is almost always associated with lower violations probabilities and very close to the open loop optimal policy (i.e., no parametrization of the controller). In addition, state feedback was found to be worse not only in terms of nominal performance but also in terms of constraint violation even when compared to the DMPC. However a state feedback approach resulted in

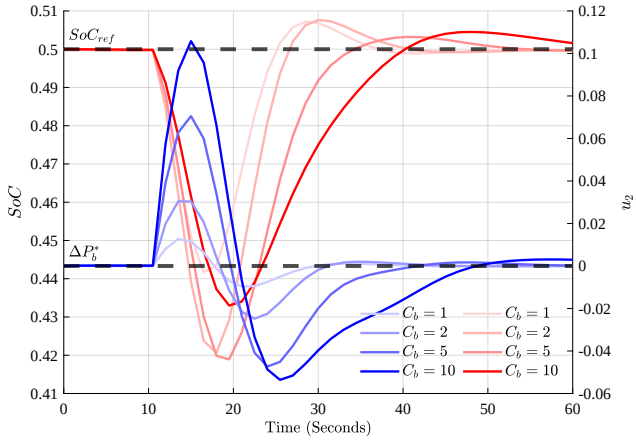

(a) SoC and battery power deviations

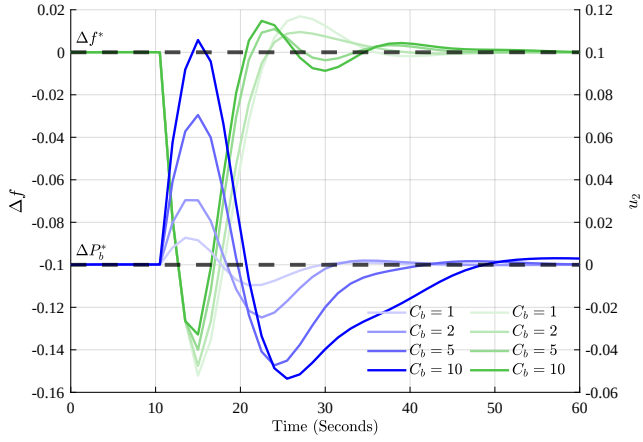

(b) System frequency and battery power deviations

FIGURE 7.17. Sensitivity analysis results for varying C_b

the smallest fuel consumption – at the cost though of slower regulation. Last but not least, the analysed H_∞ robust controller was found resulting in higher constraint violations and sub-optimal coordination of the different subsystems, revealing the need for specialized tuning.

As for possible future work, higher parametric uncertainty could be considered for the comparison of the various proposed controllers and check to what extend the comparison results match the one presented in this study. In addition, higher fidelity simulation models could be used to further validate the results of the comparative analysis, while different specific battery technologies could also be examined for ap-

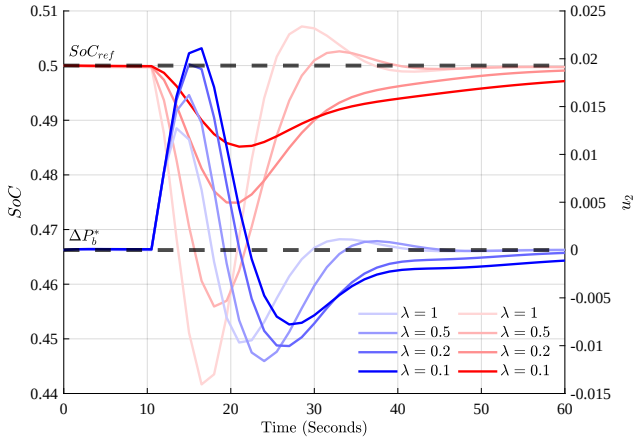

(a) SoC and battery power deviations

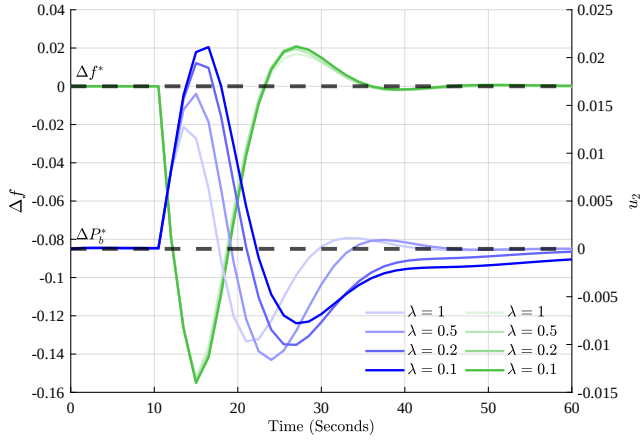

(b) System frequency and battery power deviations

FIGURE 7.18. Sensitivity analysis results for varying λ

plication suitability, given actual C-rate restrictions. Finally, a controller with risk aversion capabilities (i.e. by reducing the number of scenarios in the scenario approach) could be designed and be included in the comparison study.

7.6 APPENDIX A

$$\boldsymbol{X}^T = [\boldsymbol{x}_{\tau+1}^T, \ldots, \boldsymbol{x}_{\tau+N_p}^T]$$

$$\boldsymbol{U}^T = [\boldsymbol{u}_{\tau+0}^T, \ldots, \boldsymbol{u}_{\tau+N_c}^T]$$

$$\boldsymbol{\Delta U}^T = [\boldsymbol{\Delta u}_{\tau+0}^T, \ldots, \boldsymbol{\Delta u}_{\tau+N_c}^T]$$

$$\boldsymbol{W}^T = [\boldsymbol{w}_{\tau+0}^T, \ldots, \boldsymbol{w}_{\tau+N_c}^T]$$

$$A_e = \begin{bmatrix} A \\ A^2 \\ \vdots \\ A^{N_p} \end{bmatrix}, \quad B_0 = \begin{bmatrix} B \\ AB + B \\ \vdots \\ \sum_{i=1}^{N_p} A^{N_p - i} B \end{bmatrix},$$

$$B_e = \begin{bmatrix} B & 0 & \cdots & 0 \\ AB + B & B & \cdots & 0 \\ \vdots & \vdots & \ddots & \vdots \\ \sum_{i=1}^{N_p} A^{N_p - i} B & \sum_{i=2}^{N_p} A^{N_p - i} B & \cdots & \sum_{i=1+N_c}^{N_p} A^{N_p - i} B \end{bmatrix},$$

$$H_e = \begin{bmatrix} H & 0 & \cdots & 0 \\ AH & H & \cdots & 0 \\ \vdots & \vdots & \ddots & \vdots \\ A^{N_p - 1} H & A^{N_p - 2} H & \cdots & A^{N_p - N_p} H \end{bmatrix}$$

$$\boldsymbol{Q} = \begin{bmatrix} Q_{\tau+1} & 0 & 0 \\ 0 & \ddots & 0 \\ 0 & 0 & Q_{\tau+N_p} \end{bmatrix}$$

$$\boldsymbol{R} = \begin{bmatrix} R_{\tau+1} & 0 & 0 \\ 0 & \ddots & 0 \\ 0 & 0 & R_{\tau+N_c} \end{bmatrix}$$

$$\boldsymbol{s}^T = [0, 0, 0, 0, 1, 1]$$

$$\boldsymbol{S} = \begin{bmatrix} \mathbf{0}_{(1-1)\cdot 6+4} & 1 & 1 & \mathbf{0}_{(N_p-1)\cdot 6} \\ \mathbf{0}_{(2-1)\cdot 6+4} & 1 & 1 & \mathbf{0}_{(N_p-2)\cdot 6} \\ \vdots & \vdots & \vdots & \vdots \\ \mathbf{0}_{(N_p-1)\cdot 6+4} & 1 & 1 & \mathbf{0}_{(N_p-N_p)\cdot 6} \end{bmatrix}$$

$$P = \begin{bmatrix} 0 & 0 & 0 & 1 & 0 & 0 \\ 0 & 0 & 0 & -1 & 0 & 0 \\ 0 & 0 & 0 & 0 & 1 & 1 \\ 0 & 0 & 0 & 0 & -1 & -1 \end{bmatrix}$$

$$\boldsymbol{P} = \begin{bmatrix} P_{\tau+1} & 0 & 0 \\ 0 & \ddots & 0 \\ 0 & 0 & P_{\tau+N_p} \end{bmatrix}$$

$$\boldsymbol{L} = \begin{bmatrix} \ell_{\tau+1} & 0 & 0 \\ 0 & \ddots & 0 \\ 0 & 0 & \ell_{\tau+N_p} \end{bmatrix}$$

$$c = \begin{bmatrix} -\Delta f_{max} \\ \Delta f_{max} \\ -SoC^{ref} - \Delta SoC_{max} \\ SoC^{ref} - \Delta SoC_{max} \end{bmatrix}$$

$$\boldsymbol{c}^T = [c_{\tau+0}^T, \ldots, c_{\tau+N_p}^T]$$

$$\boldsymbol{X}_{soc}^{ref\,T} = [SoC_{\tau+0}^{ref}, \ldots, SoC_{\tau+N_p}^{ref}]$$

$$\Gamma^T = [\boldsymbol{\gamma_1}, \ldots, \boldsymbol{\gamma_{N_c}}]$$

$$\Theta = \begin{bmatrix} \mathbf{0} & \mathbf{0} & \ldots & \mathbf{0} \\ \boldsymbol{\theta_{1,0}} & \mathbf{0} & \ddots & \mathbf{0} \\ \vdots & \ddots & \ddots & \mathbf{0} \\ \boldsymbol{\theta_{N_c-1,0}} & \ldots & \boldsymbol{\theta_{N_c-1,N_p-2}} & \mathbf{0} \end{bmatrix}$$

$$\boldsymbol{\gamma_i}^T = [\gamma_{i,1}, \gamma_{i,2}]$$

$$\boldsymbol{\theta_{i,j}}^T = [\theta_{i,j,1}, \theta_{i,j,2}]$$

$$N_{sim} = \frac{T_{sim}}{\Delta t}$$

TABLE 7.1. Table of constants

Parameter	Symbol	Value	Units
Nominal Plant			
governor time constant	$T_{g,0}$	0.05 [8]	[s]
turbine time constant	$T_{t,0}$	0.5 [8]	[s]
wind turbine time constant	$T_{WTG,0}$	0.04 [8]	[s]
BESS time constant	$T_{B,0}$	0.1 [8]	[s]
battery capacity	$C_{b,0}$	1	[p.u.]
charging well width	$c_{W,0}$	0.93 [36]	[-]
charging well conductance	$c_{r,0}$	$2.24 \cdot 10^{-5}$ [36]	[-]
load damping	D_0	1 [8]	$\left[\frac{p.u.}{Hz}\right]$
inertia constant	M_0	3 [8]	$\left[\frac{p.u.s}{Hz}\right]$
Wind Turbine Power Curve			
cut in speed	V_{ci}	13	$\left[\frac{m}{s}\right]$
cut off speed	V_{co}	17	$\left[\frac{m}{s}\right]$
rated wind speed	V_r	15.5	$\left[\frac{m}{s}\right]$
rated power	P_r	0.2	[p.u.]
MPC constrains			
max power deviation	$\mathbf{u_{min}}$	-1	[p.u.]
min power deviation	$\mathbf{u_{max}}$	1	[p.u.]
max power increment	$\mathbf{\Delta u_{max}}$	0.5	[p.u.]
min power increment	$\mathbf{\Delta u_{min}}$	-0.5	[p.u.]
max frequency deviation	Δf_{max}	0.2	[p.u.]
max SoC deviation	ΔSoC_{max}	0.3	[p.u.]
Simulation parameters			
control horizon	N_c	4	[-]
prediction horizon	N_p	10	[-]
discrete time step	Δt	1.5	[s]
simulation length	T_{sim}	60	[s]

7.7 APPENDIX B

This paper presents a design methodology (proposed multi-objective controller) and a preliminary comparative analysis of various designs either with respect to the way uncertainty is considered (deterministic vs. robust vs. stochastic) or for different control parametrizations for the scenario-based MPC (SMPC). The scenario approach [40, 41, 43, 48] gives the designer the unique capability to leverage risk of violating unseen constraints (from the randomly sampled scenarios). That means that we can reduce the number of scenarios considered by accepting higher risk for the sake of decreasing the controller's computational complexity and therefore the required calculation time. Under this perspective, we performed an analysis investigating the required time for the optimization problem to be solved, for different number of scenarios. The results are given in Table 7.2. Such times are recorded when using our available computational resources, a 2010 MacBook Pro with 2,4 GHz Intel Core 2 Duo processor, where just a single core was used (not parallel computing). We also not that the recorded execution times include several internal processes of the Matlab-based modeling system for convex optimization (CVX) and interactions with the selected simulation environment

Matlab-Simulink. CVX is loaded with numerous additional tasks other than solving the problem itself, such as interpreting the high-level modelling language into numerical matrices, loading searching and accessing those and many other staff that are not open to the user.

In practice, increasing the number of scenarios we include more constraints to the optimization problem, making its solution harder. As we see from the table above, even for relatively low number of scenarios, the required solution time can be significant, giving rise to potential real-time implementation issues. The computational time to solve the optimization problem highly depends on the availability of computational resources which, from a system operator point of view, won't probably be a deadlock, since advanced computing may already be there as it is necessary for other tasks, too. While in the simulation environment there is always sufficient time for the optimization problem to be solved before the next simulation iteration, in a real time implementation non-sufficient time for the problem solution would result in a significant delay which is ignored in the simulations. Therefore, the results presented in this study can be thought of as an upper bound of the controller's performance and further studies are required to investigate what the required computational resources are and what parallelization techniques should be considered before the real-time implementation of the controllers proposed in this theoretical/numerical study.

7.8 References

[1] K. S. El-Bidairi, H. D. Nguyen, T. S. Mahmoud, S. D. G. Jayasinghe, and J. M. Guerrero, "Optimal sizing of Battery Energy Storage Systems for dynamic frequency control in an islanded microgrid: A case study of Flinders Island, Australia," *Energy*, vol. 195, p. 117059, Mar. 2020. [Online]. Available: http://www.sciencedirect.com/science/article/pii/S0360544220301663 Cited on page/s 154, 155.

[2] R. Itiki, S. G. Di Santo, C. Itiki, M. Manjrekar, and B. H. Chowdhury, "A comprehensive review and proposed architecture for offshore power system," *International Journal of Electrical Power & Energy Systems*, vol. 111, pp. 79–92, Oct. 2019. [Online]. Available: http://www.sciencedirect.com/science/article/pii/S014206151930095X Cited on page/s 154.

[3] (2021) Electrification of oil and gas operations. Equinor ASA. [Online]. Available: https://www.equinor.com/en/what-we-do/electrification.html Cited on page/s 154.

Table 7.2. MPC optimization solution time

	SMPC-FP	*SMPC-SF*	*SMPC-NP*
variables #	32	8	8
N	Optimization solution time [s]		
200	4.97	2.03	2.21
400	9.14	3.16	2.74
600	14.95	4.95	3.78
800	22.19	6.63	5.17
1000	29.12	8.58	6.80

[4] T. Yang, Y. Zhang, Z. Wang, and H. Pen, "Secondary frequency stochastic optimal control in independent microgrids with virtual synchronous generator-controlled energy storage systems," *Energies*, vol. 11, no. 9, 2018. [Online]. Available: https://www.mdpi.com/1996-1073/11/9/2388 Cited on page/s 154.

[5] H. Bevrani, B. Francois, and T. Ise, *Microgrid Dynamics and Control*, 07 2017. Cited on page/s 154.

[6] T. Kerdphol, F. Rahman, Y. Mitani, and M. Watanabe, "Robust virtual inertia control of an islanded microgrid considering high penetration of renewable energy," *IEEE Access*, vol. 6, pp. 625–636, 02 2018. Cited on page/s 154.

[7] S. Oh, S. Chae, J. Neely, J. Baek, and M. Cook, "Efficient model predictive control strategies for resource management in an islanded microgrid," *Energies*, vol. 10, p. 1008, 07 2017. Cited on page/s 154, 156.

[8] Z. Rostami, S. N. Ravadanegh, N. T. Kalantari, J. M. Guerrero, and J. C. Vasquez, "Dynamic modeling of multiple microgrid clusters using regional demand response programs," *Energies*, vol. 13, no. 16, 2020. [Online]. Available: https://www.mdpi.com/1996-1073/13/16/4050 Cited on page/s 154, 161, 185.

[9] K. Sabah, H. Nguyen, T. Mahmoud, S. Jayasinghe, and J. Guerrero, "Optimal sizing of battery energy storage systems for dynamic frequency control in an islanded microgrid: A case study of flinders island, australia," *Energy*, p. 117059, 03 2020. Cited on page/s 154.

[10] Y. Zhang, N. Gatsis, and G. B. Giannakis, "Robust energy management for microgrids with high-penetration renewables," *IEEE transactions on sustainable energy*, vol. 4, no. 4, pp. 944–953, 2013. Cited on page/s 154, 156.

[11] P. Fortenbacher, J. L. Mathieu, and G. Andersson, "Modeling and Optimal Operation of Distributed Battery Storage in Low Voltage Grids," *IEEE Transactions on Power Systems*, vol. 32, no. 6, pp. 4340–4350, Nov. 2017. Cited on page/s 154.

[12] T. Dragičević, H. Pandžić, D. Škrlec, I. Kuzle, J. M. Guerrero, and D. S. Kirschen, "Capacity optimization of renewable energy sources and battery storage in an autonomous telecommunication facility," *IEEE Transactions on Sustainable Energy*, vol. 5, no. 4, pp. 1367–1378, 2014. Cited on page/s 154.

[13] R. Machlev, N. Zargari, N. R. Chowdhury, J. Belikov, and Y. Levron, "A review of optimal control methods for energy storage systems - energy trading, energy balancing and electric vehicles," *Journal of Energy Storage*, vol. 32, p. 101787, Dec. 2020. [Online]. Available: http://www.sciencedirect.com/science/article/pii/S2352152X20316248 Cited on page/s 154.

[14] H. Bevrani, *Robust Power System Frequency Control*, ser. Power Electronics and Power Systems. Cham: Springer International Publishing, 2014. [Online]. Available: http://link.springer.com/10.1007/978-3-319-07278-4 Cited on page/s 154, 158.

[15] H. Bevrani, B. Francois, and T. Ise, *Microgrid Dynamics and Control*. Hoboken, NJ, USA: John Wiley & Sons, Inc., Jul. 2017. [Online]. Available: http://doi.wiley.com/10.1002/9781119263739 Cited on page/s 154, 158.

[16] L. Meegahapola, "Characterisation of gas turbine dynamics during frequency excursions in power networks," *IET Generation, Transmission & Distribution*, vol. 8, no. 10, pp. 1733–1743, Oct. 2014. [Online]. Available: https://digital-library.theiet.org/content/journals/10.1049/iet-gtd.2013.0824 Cited on page/s 155.

[17] K. Gubba Ravikumar, B. Bosley, T. Clark, and J. Garcia, "Generation Control System: Using Isochronous Load-Sharing Principles With Gas and Steam Turbine Generators," *IEEE Industry Applications Magazine*, vol. 25, no. 2, pp. 36–44, Mar. 2019, conference Name: IEEE Industry Applications Magazine. Cited on page/s 155.

[18] Z. Rostami, S. N. Ravadanegh, N. T. Kalantari, J. M. Guerrero, and J. C. Vasquez, "Dynamic Modeling of Multiple Microgrid Clusters Using Regional Demand Response Programs," *Energies*, vol. 13, no. 16, p. 4050, Jan. 2020, number: 16 Publisher: Multidisciplinary Digital Publishing Institute. [Online]. Available: https://www.mdpi.com/1996-1073/13/16/4050 Cited on page/s 155.

[19] P. C. Sahu, S. Mishra, R. C. Prusty, and S. Panda, "Improved-salp swarm optimized

type-II fuzzy controller in load frequency control of multi area islanded AC microgrid," *Sustainable Energy, Grids and Networks*, vol. 16, pp. 380–392, Dec. 2018. [Online]. Available: https://linkinghub.elsevier.com/retrieve/pii/S2352467718303369 Cited on page/s 155.

[20] V. P. Singh, S. R. Mohanty, N. Kishor, and P. K. Ray, "Robust H-infinity load frequency control in hybrid distributed generation system," *International Journal of Electrical Power & Energy Systems*, vol. 46, pp. 294–305, Mar. 2013. [Online]. Available: https://linkinghub.elsevier.com/retrieve/pii/S0142061512005789 Cited on page/s 155, 157.

[21] H. Bevrani, M. R. Feizi, and S. Ataee, "Robust Frequency Control in an Islanded Microgrid: $H _ınfty $ and $\mu $ -Synthesis Approaches," *IEEE Transactions on Smart Grid*, vol. 7, no. 2, pp. 706–717, Mar. 2016, conference Name: IEEE Transactions on Smart Grid. Cited on page/s 155.

[22] T. Kerdphol, F. S. Rahman, Y. Mitani, M. Watanabe, and S. K. Küfeoğlu, "Robust Virtual Inertia Control of an Islanded Microgrid Considering High Penetration of Renewable Energy," *IEEE Access*, vol. 6, pp. 625–636, 2018, conference Name: IEEE Access. Cited on page/s 155.

[23] A. M. Ersdal, L. Imsland, and K. Uhlen, "Model Predictive Load-Frequency Control," *IEEE Transactions on Power Systems*, vol. 31, no. 1, pp. 777–785, Jan. 2016, conference Name: IEEE Transactions on Power Systems. Cited on page/s 155, 171.

[24] T. Yang, Y. Zhang, Z. Wang, and H. Pen, "Secondary Frequency Stochastic Optimal Control in Independent Microgrids with Virtual Synchronous Generator-Controlled Energy Storage Systems," *Energies*, vol. 11, no. 9, p. 2388, Sep. 2018. [Online]. Available: http://www.mdpi.com/1996-1073/11/9/2388 Cited on page/s 155.

[25] M.-R. Chen, G.-Q. Zeng, Y.-X. Dai, K.-D. Lu, and D.-Q. Bi, "Fractional-Order Model Predictive Frequency Control of an Islanded Microgrid," *Energies*, vol. 12, no. 1, p. 84, Dec. 2018. [Online]. Available: http://www.mdpi.com/1996-1073/12/1/84 Cited on page/s 155.

[26] S. Jain and Y. V. Hote, "Design of fractional PID for Load frequency control via Internal model control and Big bang Big crunch optimization," *IFAC-PapersOnLine*, vol. 51, no. 4, pp. 610–615, 2018. [Online]. Available: https://linkinghub.elsevier.com/retrieve/pii/S2405896318304609 Cited on page/s 155.

[27] J. Singh, K. Chattterjee, and C. Vishwakarma, "Two degree of freedom internal model control-PID design for LFC of power systems via logarithmic approximations," *ISA Transactions*, vol. 72, pp. 185–196, Jan. 2018. [Online]. Available: https://linkinghub.elsevier.com/retrieve/pii/S0019057817306213 Cited on page/s 155.

[28] P. Patrinos, S. Trimboli, and A. Bemporad, "Stochastic mpc for real-time market-based optimal power dispatch," in *2011 50th IEEE Conference on Decision and Control and European Control Conference*. IEEE, 2011, pp. 7111–7116. Cited on page/s 156, 157, 164.

[29] E. González Querubín, J. Sanchis, S. Garcia-Nieto Rodriguez, and J. Salcedo, "A comparative study of stochastic model predictive controllers," *Electronics*, vol. 9, p. 2078, 12 2020. Cited on page/s 156, 164.

[30] S. Di Cairano, D. Bernardini, A. Bemporad, and I. V. Kolmanovsky, "Stochastic mpc with learning for driver-predictive vehicle control and its application to hev energy management," *IEEE transactions on control systems technology*, vol. 22, no. 3, pp. 1018–1031, 2014. Cited on page/s 157, 164.

[31] H. Bevrani, M. R. Feizi, and S. Ataee, "Robust frequency control in an islanded microgrid: H_∞ and μ -synthesis approaches," *IEEE Transactions on Smart Grid*, vol. 7, no. 2, pp. 706–717, 2016. Cited on page/s 157.

[32] Kundur, *[prabha kundur] power system stability and control.pdf*. Cited on page/s 158.

[33] C. Gavriluta, S. Spataru, I. Mosincat, C. Citro, I. Candela, and P. Rodriguez, "Complete methodology on generating realistic wind speed profiles based on measurements," *REPQJ*, pp. 1757–1762, Apr. 2012. [Online]. Available: http://www.icrepq.com/icrepq'12/828-gavriluta.pdf Cited on page/s 159.

[34] "INTERNATIONAL STANDARD IEC 61400-1," Tech. Rep. [Online]. Available: http://dlbargh.ir/mbayat/46.pdf Cited on page/s 159.

[35] J. F. Manwell and J. G. McGowan, "Lead acid battery storage model for hybrid energy systems," *Solar energy*, vol. 50, no. 5, pp. 399–405, 1993. Cited on page/s 159.

[36] P. Fortenbacher, J. L. Mathieu, and G. Andersson, "Modeling, identification, and optimal control of batteries for power system applications," in *2014 Power Systems Computation Conference*, 2014, pp. 1–7. Cited on page/s 159, 160, 185.

[37] ——, "Modeling and Optimal Operation of Distributed Battery Storage in Low Voltage Grids," *IEEE Trans. Power Syst.*, vol. 32, no. 6, pp. 4340–4350, Nov. 2017. [Online]. Available: http://ieeexplore.ieee.org/document/7879188/ Cited on page/s 159, 160.

[38] W. Tan, "Unified tuning of pid load frequency controller for power systems via imc," *IEEE Transactions on Power Systems*, vol. 25, no. 1, pp. 341–350, 2010. Cited on page/s 161.

[39] Y. Shi, B. Xu, Y. Tan, and B. Zhang, "A convex cycle-based degradation model for battery energy storage planning and operation," 2017. Cited on page/s 162.

[40] G. Calafiore and M. Campi, "Robust convex programs: randomized solutions and applications in control," in *42nd IEEE International Conference on Decision and Control (IEEE Cat. No.03CH37475)*, vol. 3, 2003, pp. 2423–2428 Vol.3. Cited on page/s 164, 185.

[41] M. C. Campi, S. Garatti, and M. Prandini, "Scenario Optimization for MPC," in *Handbook of Model Predictive Control*, S. V. Raković and W. S. Levine, Eds. Cham: Springer International Publishing, 2019, pp. 445–463, series Title: Control Engineering. [Online]. Available: http://link.springer.com/10.1007/978-3-319-77489-3_19 Cited on page/s 164, 166, 185.

[42] A. Shapiro, D. Dentcheva, and A. Ruszczyński, *Lectures on Stochastic Programming: Modeling and Theory*. Society for Industrial and Applied Mathematics, Jan. 2009. [Online]. Available: http://epubs.siam.org/doi/book/10.1137/1.9780898718751 Cited on page/s 164.

[43] M. C. Campi, S. Garatti, and M. Prandini, "The scenario approach for systems and control design," *Annual Reviews in Control*, vol. 33, no. 2, pp. 149–157, Dec. 2009. [Online]. Available: https://linkinghub.elsevier.com/retrieve/pii/S1367578809000479 Cited on page/s 164, 185.

[44] E. F. Camacho and C. Bordons, *Model Predictive control*, ser. Advanced Textbooks in Control and Signal Processing, M. J. Grimble and M. A. Johnson, Eds. London: Springer London, 2007. [Online]. Available: http://link.springer.com/10.1007/978-0-85729-398-5 Cited on page/s 165.

[45] *Model Predictive Control System Design and Implementation Using MATLAB®*, ser. Advances in Industrial Control. London: Springer London, 2009, iSSN: 1430-9491. [Online]. Available: http://link.springer.com/10.1007/978-1-84882-331-0 Cited on page/s 165.

[46] S. Skogestad, "Multivariable feedback control : analysis and design," Chichester, 2005. Cited on page/s 166.

[47] A. M. Ersdal, L. Imsland, K. Uhlen, D. Fabozzi, and N. F. Thornhill, "Model predictive load–frequency control taking into account imbalance uncertainty," *Control Engineering Practice*, vol. 53, pp. 139–150, May 2016. [Online]. Available: https://www.sciencedirect.com/science/article/pii/S0967066115300496 Cited on page/s 171.

[48] S. Garatti and M. C. Campi, "Modulating robustness in control design: Principles and algorithms," *IEEE Control Systems Magazine*, vol. 33, no. 2, pp. 36–51, Apr. 2013, conference Name: IEEE Control Systems Magazine. Cited on page/s 185.

Chapter 8

Optimal Energy Management in Autonomous Power Systems with Probabilistic Security Constraints and Adaptive Frequency Control

Spyridon Chapaloglou[1,*], Erick Alves[1], Vincenzo Trovato[2,3] and Elisabetta Tedeschi[1,4]

Published in: *IEEE Transactions on Power Systems (2023)*.
DOI: 10.1109/TPWRS.2023.3236378

Abstract

The decarbonization of many heavy power-consuming industries is dependent on the integration of renewable energy sources and energy storage systems in isolated autonomous power systems. The optimal energy management in such schemes becomes harder due to the increased complexity and stability requirements, the rapidly varying operating conditions and uncertainty of renewable sources, the conflicting objectives across different timescales, and the limited amount of reliable power sources and energy storage. The state of charge management when energy storage is used for multiple services, such as optimal scheduling and frequency support, is one of the most notorious problems in this context. To address this issue, an optimal energy management system is proposed in this paper. It co-optimizes the primary frequency control layer and the dispatch schedule of conventional generators and energy storage by taking advantage of an algorithm that provides adaptive active power demand uncertainty quantification, theoretical guarantees for frequency stability, and bounds for the reserves for frequency support assigned to the energy storage system. A pattern-based reformulation of the frequency stability constraints is derived enabling the efficient solution of the involved optimization problem, being a test case of an isolated offshore oil and gas platform presented for validation.

[1]Department of Electric Power Engineering, Norwegian University of Science and Technology (NTNU), Trondheim, Norway. [2]Department of Civil, Environmental and Mechanical Engineering, University of Trento, Italy. [3]Department of Electrical and Electronic Engineering, Imperial College London, England. [4]Department of Industrial Engineering, University of Trento, Italy. *e-mail: spyridon.chapaloglou@ntnu.no, erick.f.alves@ntnu.no, vincenzo.trovato@unitn.it and elisabetta.tedeschi@ntnu.no

8.1 Introduction

Taking optimal decisions to reduce *i)* fuel consumption, *ii)* GHG emissions, *iii)* equipment degradation, and *iv)* system insecurity in power systems with a high share of RESs is an intricate task. This endeavor requires the solution of problems such as the UC [1], ED [2], and allocation of reserves for frequency control [3], resulting in complex non-convex optimization formulations. Those have typically conflicting objectives, continuous and binary decision variables, and high uncertainty from particular nodes, such as loads and RESs. Reliability can, for instance, be increased where more dispatchable units, such as GTs, are kept online for longer periods, as they respond well to fast variations of loads and RESs. This action may, however, increase fuel consumption, emissions, and equipment degradation, affecting negatively operational expenditure (OPEX).

When compared to traditional bulk power systems (BPSs), this type of optimization can have different characteristics in autonomous power systems (APSs), such as isolated industrial plants, oil and gas (O&G) platforms, ships, islands, and community microgrids. Due to the size and complexity of the problem, several challenges exist in BPSs to implement real-time, advanced algorithms for optimal dispatch and real-time allocation of frequency reserves [4]. Such problems can, however, be addressed in many APSs due to the limited number of dispatchable power sources, which typically provide several ancillary services simultaneously. The methods for allocation of frequency reserves and tuning of the system damping may also differ considerably between BPSs and APSs. The system damping is, in the former, adapted using binary decision variables that switch on and off units having a fixed active power-frequency droop, as usually the individual contribution of each unit to the total damping is small. In the latter, the droop of individual units may represent a large portion of the system damping, therefore making it necessary to readjust them in real-time using integer variables to obtain optimal results.

Optimization objectives and decisions in APSs may also be coupled and affected by constraints in different time scales, with ESSs remarkable examples of equipment that enhances such dependencies. ESSs can, for instance, provide increased flexibility toward the optimal scheduling of fossil-based energy sources and avoid prolonged operation in partial loads, where emissions are much higher. They can also be assigned as spinning reserves for frequency control, which would require fewer GTs on for the same system security requirements and increase environmental gains even further. Where these two grid services are provided simultaneously, the scheduled trajectory of the ESS's SoE may be disturbed, affecting the optimality or even the feasibility of the original schedule. To decide in BPSs the effect that the provision of frequency reserves has on the ESS's optimal schedule, scenarios such as the worst-case APD or the N-1 criterion are often used [3, 5]. These criteria can, however, be over-conservative in APSs [6] and the capital expenditure necessary for a fully-fledged ESS may not justify its benefits, with some probability of load shedding and generation curtailment frequently

acceptable [7]. Regarding energy management in APSs with high penetration of RES, there is therefore a need and potential for better assessment of frequency stability requirements as well as coordination and scheduling of reserves.

8.1.1 Literature review

The integration of frequency stability constraints in the scheduling phase of BPSs with high penetration of RES has been an active area of research in recent years and is well described in the literature [8]. The use of linear constraints had been a typical approach to increase the fidelity of the frequency response in the UC and ED problems, which are obtained by linearizations and/or analytical solutions of the swing equation model [9–16]. These procedures provide good approximations in BPSs, where the largest APD is a small fraction of the installed capacity and transient and steady-state frequency deviations are usually required to be below 2% of its rated value [5]. Frequency deviations may, on the other hand, be much higher in APSs due to low inertia and limited amount of frequency reserves when compared to the worst-case APDs, causing the effects of non-linear dynamics to be sizeable during large disturbances [17]. Where these non-linear effects are considered, bilinear terms are introduced in the frequency stability constraints, those requiring specialized reformulation-linearization techniques [18–20]. This increase of the optimization model complexity can play an important role in APSs, while it may bring only negligible frequency stability improvements in BPSs.

The challenge of leveraging optimal system operation and security in APSs was also addressed recently, with alternatives presented to the deterministic evaluation of the worst-case APD or the N-1 criterion. References [13, 21–24], for instance, considered the effect of anticipated net load variations and applied dynamic constraints for sizing frequency containment reserves and required inertia. These works did not evaluate, however, the impact that re-adjusting the droop of online units, instead of switching on and off units with fixed droops, would have on frequency stability and OPEX. References [9, 15, 20, 25] tried moreover to tackle the problem by applying simplified and static uncertainty models, such as non adaptive and arbitrary uncertainty intervals, distributions, and scenario selection, which have the limitation of not providing probabilistic guarantees.

8.1.2 Paper contributions

The main contribution of this paper is an algorithm for the EMS of a generalized APS equipped with an ESS that is capable of simultaneously achieving optimal scheduling and securing system operation under dynamic uncertainty considerations and bounded impact on its optimal scheduling. The proposed algorithm introduces a particular set of frequency constraints with general applicability, those not being limited to small-scale power variations. Compared to the formulation based on the linearized swing equation traditionally adopted in frequency-constrained UC (e.g.,[10, 18]), our formulation is

robust to large frequency deviations around the system equilibrium point. This is an important feature for APSs, which are often subject to larger frequency deviations than BPSs. Likewise, this feature might be key in future BPSs dominated by power electronic converters. Such constraints are combined with a probabilistic security framework based on a novel adaptive APD uncertainty quantification scheme. Additional novel energy constraints to frequency reserves (inertial and primary) provided by an ESS are derived, bounding the impact of the uncertain grid service provision on the optimal schedule. This new method allows an EMS to allocate time-varying optimal frequency control reserves with bounded divergence from its optimal SoE. A simple strong MILP reformulation is derived to efficiently implement the proposed algorithm, whose effectiveness is verified by simulations using the case study of a wind-powered offshore O&G platform. In summary, we propose an EMS for APSs with the following novel features:

- adaptive APD uncertainty quantification with probabilistic guarantees for frequency-constrained energy management
- integration of frequency stability constraints into the optimal scheduling that consider non-linear frequency dynamics and are valid for large frequency deviations
- energy constraints bounding the impact of uncertain frequency support provision (inertial and primary) by an ESS, on its optimal SoE schedule

The rest of the paper is organized as follows. The proposed EMS algorithm and its numerical implementation are presented in Section 8.2, while simulations in Matlab/Simulink are performed to validate and discuss the various features of the proposed algorithm using the case study of a wind-powered offshore O&G platform in Section 8.3. The main conclusions are finally presented in Section 8.4.

8.2 METHOD

The concept and the methodology proposed in this paper is presented in detail in this section. It assumes the existence of a centralized EMS in an APS that is capable not only to dispatch a set of g generators and a single ESS b, but also to decide, for the primary frequency controllers, the proportional gain (droop) D_g of each generator, the proportional gain (droop) D_b and derivative gain (virtual inertia) M_b of the ESS. Figure 8.1 shows a conceptual illustration of the proposed scheme for the hierarchical EMS. The set v_0 represents the control inputs to the low-level primary frequency controllers, which include droop and virtual inertia coefficients, and is embedded into the set of commands u_0 from the EMS. The latter also includes the decisions to startup (green circles) or to shutdown (red circles) the GTs. The techno-economic optimal schedule included in u_0 not only shall be feasible for the actual net load disturbance ξ_0 at $t = t_0$, but also will define the inertial support $\sum_g M_g$ of conventional generators during $[t_0, t_0 + T]$, where T is the time step of the scheduling, further complicating the frequency control problem. Note that the commands u_0 are given for discrete points of the time interval (i.e., $k = 0 \Rightarrow t = t_0$ and $k = 1 \Rightarrow t = t_0 + T$) based on the discrete net load forecasts $(\xi_{t+0|t}, \xi_{t+1|t})$. The transition from $\xi_{t+0|t}$ to $\xi_{t+1|t}$, however, can happen at any time in the continuous time interval $[t_0, t_0 + T]$. In the proposed EMS algorithm, the power reserves ΔP_g^{gt} and ΔP^b are decided in an adaptive way respecting the ESS SoE bounds. The forecast net load values $\xi_{t+k|t}$ at time t, along with their corresponding uncertainties, are used to characterize the potential APDs $P_b^{nl}(\delta_i \mid \xi)$ that can occur in the interval $[t_0, t_0 + T]$. This is illustrated in Figure 8.2, where the APD came off at a time $t_0 \leq t_0' \leq t_0 + T$. As the forecasts are

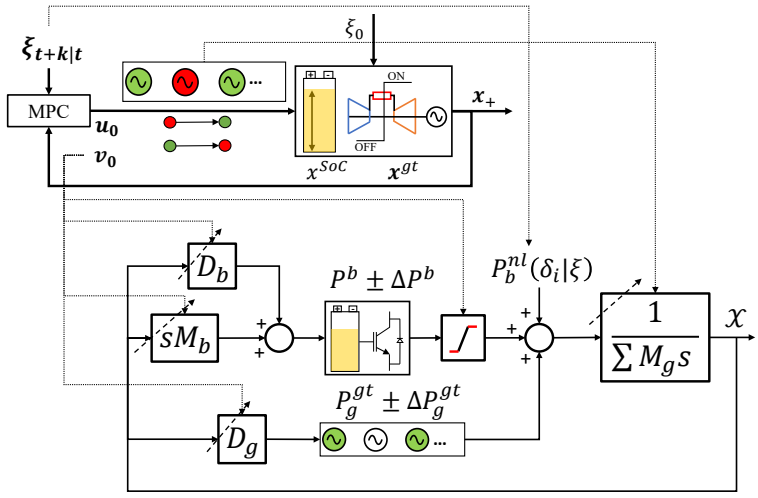

FIGURE 8.1. Hierarchical control system schematic where the upper layer optimal discrete time control is integrated with the lower time scale continuous adaptive primary frequency control

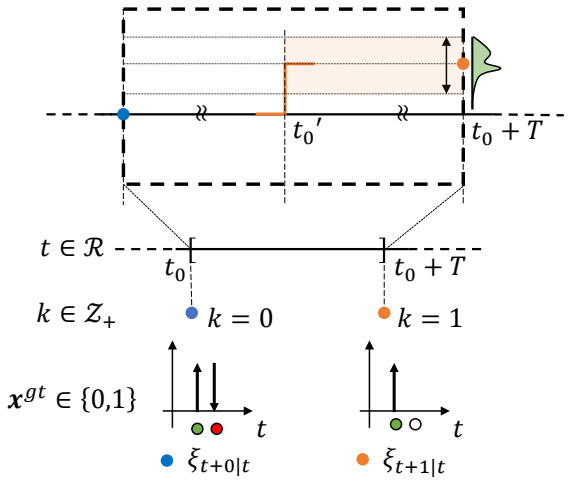

FIGURE 8.2. Visualization of the proposed adaptive and probabilistic step-like net Active Power Disturbance quantification at a time instant in the continuous range between the discrete points in time where decisions are taken

uncertain, the APD amplitude belongs to a value range (orange region), being, therefore, a function of the underlying probability density (green area) at the next scheduling instance $k = 1 \Rightarrow t = t_0 + T$. Where this probabilistic quantification algorithm is applied, the frequency control parameters D_g, D_b, M_b to be implemented in the current time instance $t = t_0$ through the command v_0 are decided in an adaptive way. This algorithm is further detailed in sections 8.2.3 and 8.2.4.

8.2.1 *Frequency control and reserves allocation*

The non-linear dynamics of the frequency deviation for the center of inertia (COI) in an ac power system are given in eq. (8.1), where $\mathcal{X} = \frac{\omega}{\omega_s}$, and ω, ω_s are the COI frequency and its rated value, respectively.

$$\dot{\mathcal{X}} = \frac{\mathcal{D}}{\mathcal{M}}(\mathcal{X} - 1) + \frac{P_b^{nl}}{\mathcal{X}\mathcal{M}} \tag{8.1}$$

$$\mathcal{D} \geq \frac{P_b^{nl}}{r_{ss}(1 - r_{tr})} \tag{8.2}$$

$$\mathcal{M} \geq \frac{P_b^{nl}}{\bar{\gamma}} \tag{8.3}$$

It is shown in [17] that if the total system damping $\mathcal{D}$ is selected as in eq. (8.2), then $\mathcal{X}$ will be bounded post-disturbance by r_{ss} for an instantaneous net active power imbalance P_b^{nl}, where r_{tr} is a pre-defined constant bound for the nadir/zenith of $\mathcal{X}$ during the transient period. Note that the step-response of frequency for active power disturbances is, in most ac power systems, underdamped due to delays of actuators

and their non-linearities [26]. Those effects are not modelled in eq. (8.1) because they influence only the frequency nadir or zenith after the disturbance P_b^{nl} occurs, being the post-disturbance steady-state value of $\mathcal{X}$ unaffected [17]. The variables r_{ss} and r_{tr} in eq. (8.2) represent, in other words, the allowed steady-state and transient frequency deviations in per unit of $\mathcal{X}$, usually defined in grid codes or by the system operator.

It is typical to assume $r_{tr} > r_{ss}$ to provide a safety margin that avoids triggering protection schemes such as under frequency load shedding or over frequency generation curtailment during large disturbances. When $r_{ss} = r_{tr}$, there exists no safety margin between steady-state and transient values. Note that eq. (8.2) is valid for any value of $\mathcal{X}$, and not only for small deviations around the operating point.

The minimum required inertia $\mathcal{M}$ is retrieved from eq. (8.1), assuming that a) the disturbance P_b^{nl} occurs at $t = t_0'$, b) the system was previously in balance ($\mathcal{X}|_{t=t_0'} = 1$), and c) the maximum Rate of Change of Frequency ($RoCoF$) is $\dot{\mathcal{X}}|_{t=t_0'} = \bar{\gamma}$, which results in eq. (8.3).

Ensuring that enough power reserves are available in an APS is a necessary condition to satisfy the constraints for frequency control imposed by eqs. (8.2) and (8.3). The values of $\mathcal{D}$ and $\mathcal{M}$ depend on the number of online units and their individual parameters, expressed by eqs. (8.4) and (8.5), where D_g and M_g denote the droop setting and the inertia of each online generator, and D_b and M_b are the virtual damping and inertia emulated by the ESS, respectively. The EMS must guarantee that each individual piece of equipment has enough available power capacity to provide the frequency reserves assigned to it, which leads to the constraints in eqs. (8.6) and (8.7).

$$\mathcal{D} = \sum_{g}^{N_g} x_g^{gt} D_g + D_b \tag{8.4}$$

$$\mathcal{M} = \sum_{g}^{N_g} x_g^{gt} M_g + M_b \tag{8.5}$$

$$|\Delta P_b(t)| \leq M_b \bar{\gamma} + D_b r_{tr} \tag{8.6}$$

$$|\Delta P_g(t)| \leq x_g^{gt} D_g r_{tr}, \ \forall \ g \in \mathcal{N}_g \tag{8.7}$$

8.2.2 *Frequency and energy bounded optimal energy management under uncertainty*

Allocation of frequency reserves with bounded energy storage

The EMS must also ensure that enough energy capacity is available in the ESS. This is required not to violate the storage limits when providing frequency control in the current scheduling step t_0 while charge or discharge events have already been scheduled for the next step $t_0 + T$, where T is the time step of the EMS. To deal with this situation, the constraint in eq. (8.8) is proposed, where $\Delta E^b(t)$ is a deviation around

the optimal scheduled *SoE* $E^b(t)$, and λ is a user-defined (absolute) percentage value. The proposed constraint allows, in other words, an allocation of frequency reserves to the ESS that is proportional to its current energy level.

$$\Delta E^b(t) \leq \overline{\Delta E^b}(t) = \lambda E^b(t) \tag{8.8}$$

For energy calculations of frequency containment reserves in EMS algorithms, one can assume that $\mathcal{X} \leq r_{ss},\ \forall\ t\ \in\ [t_0, t_0+T]$ when the system is frequency stable [17]. This simplification results in eq. (8.9). Note that, on one hand, $r_{ss} \leq \mathcal{X} \leq r_{tr}$ during the arrest and rebound periods of frequency containment. On the other hand, those periods combined last only a couple of seconds, while T may vary from 5 minutes to 15 minutes in typical EMSs. The integration error would therefore be minimal when adopting this simplification. The latter, however, allows $\widehat{\Delta E^b} \leq \overline{\Delta E^b}(t)$ to be enforced in the optimization problem, as described later in Subsection 8.2.3, and to satisfy eq. (8.8), which avoids excessive deviations of the *SoE* from its optimal dispatch.

$$\begin{aligned} \Delta E^b(t) = \Delta E^b(\mathcal{X}) = \int_{t_0}^{t_0+T} \left(M_b\dot{\mathcal{X}} + D_b\mathcal{X}\right) \mathrm{d}t = \\ M_b\mathcal{X}\Big|_{t_0}^{t_0+T} + D_b \int_{t_0}^{t_0+T} \mathcal{X}\mathrm{d}t \leq M_b r_{tr} + D_b r_{ss} T = \widehat{\Delta E^b} \end{aligned} \tag{8.9}$$

Adaptive Uncertainty Quantification

Load uncertainty is, in the proposed method, evaluated not only in rapidly varying loads but also in the intermittency of non-dispatchable power sources, being the net load variation defined as the combination of two random variables P^p, where $p = \{\ell, w\}$ corresponds to load and non-dispatchable sources respectively. To achieve adaptive quantification of the uncertainty for a given prediction horizon $\mathcal{K}$, it is sufficient to estimate a time-dependent (conditional) multivariate CDF $\hat{F}^p_{K|t}$ [27]. Ensembles of RF models [28] can, therefore, be assembled together to perform multi-step ahead predictions given available datasets $\mathcal{D}^p_k = \{X^p_{d,k}, P^p_{d,k}\}_{d=1:N_\mathcal{D}}, \forall\ k \in \mathcal{K}$, where $X^p_{d,k}$ are the input features and $P^p_{d,k}$ the available observations for regression representing realizations of each random variable P^p at the k^{th} step ahead. For that, individual RF models are trained for each variable P^p and lead time $k \in \mathcal{K}$. Each RF is composed of $|\mathcal{T}|$ auto-regressive trees $f^p_{n,k}(\cdot),\ n \in \mathcal{T}$. The inputs to the trees (regressors) $\boldsymbol{x}_r(t)$ are composed only by the current ($k = 0$) and L lagged values of the corresponding variable, that is $\boldsymbol{x}_r(t) = [P^p_t, P^p_{t-1}, \ldots, P^p_{t-L}]^T\ \forall\ p = \{\ell, w\}$. Following the procedure described in [27], a point forecast can be calculated for the corresponding prediction horizon $\mathcal{K}$ using eq. (8.10), where $\mathbb{1}\{\cdot\}$ is the indicator function operator, $N_\mathcal{D}$ the

number of observations $P^p_{d,k}$ in the corresponding training datasets, and $\mathcal{S}_{n,k}(\boldsymbol{x}_r)$ is the leaf node of the corresponding tree n and RF model k in which the new input $\boldsymbol{x}_r(t)$ falls in.

$$\begin{aligned}
\hat{P}^p_{t+k}(\boldsymbol{x}_r(t)) &= \frac{1}{|\mathcal{T}|}\sum_{n\in\mathcal{T}} f^p_{n,k}(\boldsymbol{x}_r(t)) \;\; \forall\, k \;\in\; \mathcal{K},\; p=\{\ell,w\} \\
f^p_{n,k}(\boldsymbol{x}_r(t)) &= \sum_{d=1}^{N_{\mathcal{D}}} \frac{\mathbb{1}\{X^p_{d,k}\in\mathcal{S}_{n,k}(\boldsymbol{x}_r(t))\}}{\sum_{m=1}^{N_{\mathcal{D}}}\mathbb{1}\{X^p_{m,k}\in\mathcal{S}_{n,k}(\boldsymbol{x}_r(t))\}} P^p_{d,k} \Rightarrow \\
f^p_n(\boldsymbol{x}_r(t)) &= \sum_{d=1}^{N_{\mathcal{D}}} \tau_{d,k}(\boldsymbol{x}_r(t)) P^p_{d,k} \;\; \forall\, k \;\in\; \mathcal{K},\; p=\{\ell,w\}
\end{aligned} \tag{8.10}$$

From eq. (8.10), the conditional expected value $\hat{\mathbb{E}}[P^p_{t+k}|\boldsymbol{x}_r(t)]$ of each random variable and lead time can be expressed by the corresponding estimates $\hat{P}^p_{t+k}$ as a function of time [29]. Time-varying CDFs $\hat{F^p}_{t+k|t}$ can also be inferred [29] for each random variable and lead time as in eq. (8.11), besides the time-varying estimates of the expectations which can be considered a "mean" multi-step ahead prediction. It is shown in [27] that, using eq. (8.11), the multi-variate $\hat{F^p}_{K|t}$ can be approximated by sampling of the marginals $\hat{F}^p_{t+k|t}$. By combining the random variables P^p_{t+k} for $p=\{\ell,w\}$, the net load can be also represented as a time-dependent random variable as $\xi_{t+k}(t)=P^\ell_{t+k}(t)-P^w_{t+k}(t)$ which encapsulates the system disturbance uncertainty for the EMS.

$$\begin{aligned}
\hat{F^p}_{t+k|t} &= \frac{1}{|\mathcal{T}|}\sum_{n\in\mathcal{T}}\sum_{d=1}^{N_{\mathcal{D}}} \tau_{d,k}(\boldsymbol{x}_r(t))\mathbb{1}\{P^p_{d,k}\le P^p_{t+k}\} \Rightarrow \\
P^p_{t+k} &\sim \hat{F^p}_{t+k|t}\left(P^p_{t+k}\mid \boldsymbol{x}_r(t)\right),\; \forall\, k \;\in\; \mathcal{K},\;\; p=\{\ell,w\}
\end{aligned} \tag{8.11}$$

Any decision taken by a predictive EMS algorithm relying on that forecast will however be sub-optimal, as the net load ξ_0 that actually hits the system at $t=t_0$ (see Figure 8.2) is a realization of the random $\xi_{t+k}(t)$. The latter is, in principle, different from the forecasted value due to inevitable forecasting errors, a fact that not only degrades the optimality of the decision in terms of economic value but most importantly is critical to evaluate the APDs which may threaten the system's frequency stability due to insufficient inertia or damping. It is therefore important to quantify the uncertainty of the random net load $\xi(t)$ and subsequently, of the APD that can occur in the interval $[t_0, t_0+T]$. For the sake of brevity, this paper will not detail further the uncertainty quantification method, its validation, and how net load scenarios can be generated. The interested reader can however refer to [27] for a full description. Where the procedure

described in [27] is applied, the uncertainty of the net load affecting an isolated APS can be quantified through the adaptive probabilistic forecasting framework described in this section. This procedure will be exploited in the construction of the security-constrained energy management algorithm described in section 8.2.3.

8.2.3 Probabilistically Constrained EMS

This section presents how the proposed EMS algorithm integrates into a single optimization problem including the various objectives and multiple time-scale requirements described in sections 8.2.1 and 8.2.2. The system dynamics are first expressed in a hybrid state space system to achieve this integration as shown in eq. (8.12), where $\mathbf{x}_+$ is the state at the next discrete time, $\mathbf{u}$ the corresponding control inputs, and $\boldsymbol{A}, \boldsymbol{B}$ the corresponding system matrices. Note that $x^{SoC} = E^b/\bar{E}^b \in [\underline{x}^{SoC}, \bar{x}^{SoC}]$ and $\mathbf{x}^{gt}_{1:N_g} = \{x^{gt}_g\}_{1:N_g} \in \{0,1\}$.

$$\mathbf{x}_+ = \boldsymbol{A}\mathbf{x} + \boldsymbol{B}\mathbf{u} \tag{8.12}$$

The optimization problem presented in eq. (8.13) is then formulated and solved in each discrete time step t, where $\boldsymbol{\delta} = \{\delta^i_k\}_{1:K}$ is a random multi-sample, $\boldsymbol{\xi} = \{\xi_k\}_{0:K-1}$ is the deterministic mean net load forecast including the measured value ξ_0 at $t = t_0$, and $\boldsymbol{P}^{nl}_b = \{P^{nl}_b(\delta_{k+1}|\xi_k)\}_{0:K-1}$ is the net load perturbation for the whole prediction horizon $\mathcal{K}$ as a function of the sample and the mean forecast. The control horizon was set to be equal to the prediction horizon $\mathcal{K}$, which is a common practice in MPC schemes [30]. $|\mathcal{K}| = 6$ is used by the adaptive uncertainty quantification module explained in section 8.2.2, being this value long enough to provide reliable forecasts to some quarters ahead but short enough to limit the additional computational burden and processing time for the EMS

$$\begin{aligned}
\mathcal{P}: \quad & \min_{\mathbf{u},\mathbf{v},\mathbf{z}} \{\mathcal{F}(\mathbf{x}_+, \mathbf{z}, \mathbf{u}, \mathbf{v}; \boldsymbol{\xi})\} \\
\text{where,} \quad & \mathcal{F} := \underbrace{\mathcal{J}(\mathbf{x}_+)}_{\text{states cost}} + \underbrace{\mathcal{J}(\mathbf{z})}_{\text{operation cost}} + \underbrace{\mathcal{J}(\mathbf{u})}_{\text{control cost}} + \underbrace{\mathbf{w}^T\mathbf{v}}_{\text{reserves cost}} \\
\text{s.t.} \quad & \mathcal{C}(\mathbf{x}_+, \mathbf{z}, \mathbf{u}, \mathbf{v}, \xi) \preceq \mathbf{0}, \\
& \mathbb{P}(\boldsymbol{\delta} \in \Delta \mid |\boldsymbol{\xi} - \boldsymbol{\delta}| = \boldsymbol{P}^b_{nl} \preceq \min\{\mathcal{D} r_{ss}(1 - r_{tr}), \mathcal{M}\bar{\gamma}\}\mathbb{1}_{\{1:K\}}) \geq 1 - \epsilon.
\end{aligned} \tag{8.13}$$

In the cost function $\mathcal{F}$, $\mathcal{J}(\mathbf{x}_+)$ represents the cost of having generators online, $\mathcal{J}(\mathbf{z})$ penalizes the deviation from optimal operating conditions of online generators and the ESS, $\mathcal{J}(\mathbf{u})$ captures the startup cost of generators, and finally, $\mathbf{w}^T\mathbf{v}$ accounts for costs of activating reserves for frequency control. The decision variables $\mathbf{v} = [\boldsymbol{D}_g, D_b, M_b]^T$ used for frequency reserves are weighted by $\mathbf{w}$ so that different contributions can be assigned to online generators and the ESS to ensure the system frequency stability. In that aspect, the higher the numerical value of the corresponding $\mathbf{w}$ element, the closer a generator will remain to its optimal operating point, as its

contribution to frequency control is penalized. Each term of $\mathcal{F}$ is described in detail in [27] and expresses the corresponding economical cost defined by coefficients such as GT startup cost, fuel consumption, battery cycling, and so on.

The term $\mathcal{C}(\cdot)$ encapsulates all the constraints related to the operation of the energy system, as described in [27]. The last expression in eq. (8.13) is a chance constraint that, given the estimated distributions from eq. (8.11), relates potential instantaneous perturbations for a net load value ξ_k and the next step sampled net load δ^i_{k+1}. Equations (8.2) and (8.3) are, in other words, risk-constrained by ϵ, which acts as a mechanism to leverage cases with rather pessimistic prediction intervals resulting from poor uncertainty range estimation.

The chance constraint complicates, however, the optimization problem. Note that $\mathcal{P}$ is a stochastic mixed integer nonlinear problem and therefore non-convex, so a standard *sa* cannot be applied. Following [31, 32], a probabilistic set composed of a finite number of samples $\boldsymbol{\delta^i} \in \Delta^N$ is computed as in eq. (8.14), being β and e user-defined parameters that tighten the non-violation of the original chance constraint. Note that the number of random variables is $2|\mathcal{K}|$ because two sources of uncertainty exist (load and renewable power injection) for the whole prediction horizon. The chance constraint can, however, be replaced by the deterministic set of linear inequalities presented in eq. (8.15), which transforms the SP $\mathcal{P}$ into a robust one, where the set Δ^N encapsulates the same risk-volume ϵ as the original chance constraint. When solving the corresponding *ro* program, solutions are not only feasible for the initial $\mathcal{P}$ but also satisfy the same probabilistic guarantees [33].

$$N \geq \frac{1}{\epsilon}\frac{e}{e-1}\left(\ln\frac{1}{\beta} + 4|\mathcal{K}| - 1\right) \tag{8.14}$$

$$|\boldsymbol{\xi} - \boldsymbol{\delta^i}| = \boldsymbol{P}^b_{nl} \preceq \min\{\mathcal{D}r_{ss}(1 - r_{tr}), \mathcal{M}\bar{\gamma}\}\mathbb{1}_{\{1:K\}},\ \forall\ \boldsymbol{\delta^i} \in \Delta^N$$

8.2.4 *MILP reformulation of frequency stability and bounded energy storage constraints*

It is not feasible, on the one hand, to implement the constraints expressed in eqs. (8.2), (8.4) and (8.7) directly into a MILP formulation because of the bi-linear terms $x^{gt}_g D_g$. It is possible, on the other hand, to take advantage of the following observation: with N_g generators, there are exactly 2^{N_g} different possible system configurations depending on the values of $\mathbf{x}^{gt}_{1:N_g} \in \{0, 1\}$. The status variable $x^{gt}_{g,t}$ takes a particular value (0 or 1) for each generator and configuration, making it feasible, therefore, to represent it by binary strings of length N_g. The feasible system configurations are then enumerated by taking all the possible permutations, which can be gathered in a data table $\boldsymbol{A}_{cf}$ $[2^{N_g} \times N_g]$. The variables $x^{gt}_{g,k},\ \forall\ k \in \mathcal{K}$ can, in this way, be treated as constants given a selected system configuration, being indicator variables b_j introduced to identify the configuration selected, and associate it with the status of the generators by the set of constraints in eqs. (8.15) and (8.16). Equation (8.4) can, as consequence, be linearized using $\boldsymbol{A}_{cf}$ as in eq. (8.17).

$$x^{gt}_{g,k} \geq b_j,\ \{(j,g) \in \mathcal{J} \times \mathcal{N}_g \mid [A_{cf}]_{j,g} = 1\} \tag{8.15}$$

$$x^{gt}_{g,k} \leq 1 - b_j,\ \{(j,g) \in \mathcal{J} \times \mathcal{N}_g \mid [A_{cf}]_{j,g} = 0\} \tag{8.16}$$

$$\boldsymbol{\mathcal{D}} = \boldsymbol{A}_{cf}\boldsymbol{D}_g + D_b \mathbb{1}_{\{1:J\}} \tag{8.17}$$

With Equations (8.15) to (8.17) the initial *non-linear* formulation in Equations (8.1) to (8.7), which includes *bi-linear* terms, is translated into a set of equations appropriate for a MILP framework, and more precisely, one that has a good LP relaxation (strong formulation). Equations (8.2) and (8.3) can also be reformulated using the sampled net APD terms from eq. (8.15). This is presented in eq. (8.18), where M_B is a big-M value, $\boldsymbol{b}_k, \boldsymbol{\mathcal{D}}_k$ correspond to each lead time of the prediction horizon ($k \in \mathcal{K}$) assuming that M_g are constant values. The different possible configurations are restricted by a type 1 special ordered set constraint as in eq. (8.19).

$$\begin{gathered} \boldsymbol{P}^{nl}_b\left(\delta^i_{k+1}|\xi_k\right) + M_B \boldsymbol{b}_k \preceq \boldsymbol{\mathcal{D}}_k r_{ss}\left(1 - r_{tr}\right) + M_B \mathbb{1}_{\{1:J\}} \\ \frac{1}{\bar{\gamma}} \boldsymbol{P}^{nl}_b\left(\delta^i_{k+1}|\xi_k\right) \leq M_g \mathbb{1}^T_{\{1:N_g\}} \boldsymbol{x}^{gt}_k + M_{b,k},\ \ \forall\, \delta^i_k\ \in \Delta^N,\ \ \forall\, k \in \mathcal{K} \end{gathered} \tag{8.18}$$

$$\mathbb{1}^T_{\{1:J\}} \cdot \boldsymbol{b}_k = 1,\ \ \forall\, k \in \mathcal{K} \tag{8.19}$$

Equation (8.7) is similarly linearized using $\boldsymbol{A}_{cf}$ and M_B as in eqs. (8.20) and (8.21) where S_b is the system's base power.

$$\begin{gathered} \boldsymbol{P}^{gt}_k + M_B \boldsymbol{b}_k \preceq \left(\bar{P}^{gt} - D_{g,k} \cdot r_{tr} \cdot S_b\right) + M_B \mathbb{1}_{\{1:J\}}, \\ \left(\underline{P}^{gt} + D_{g,k} \cdot r_{tr} \cdot S_b\right) + M_B \boldsymbol{b}_k \preceq \boldsymbol{P}^{gt}_k + M_B \mathbb{1}_{\{1:J\}} \\ \forall\, k \in \mathcal{K},\ \{(j,g) \in \mathcal{J} \times \mathcal{N}_g \mid [A_{cf}]_{j,g} = 1\} \end{gathered} \tag{8.20}$$

$$\begin{gathered} \boldsymbol{P}^{gt}_k + M_B \boldsymbol{b}_k \preceq M_B \mathbb{1}_{\{1:J\}}, \\ M_B \boldsymbol{b}_k \preceq \boldsymbol{P}^{gt}_k + M_B \mathbb{1}_{\{1:J\}}, \\ \forall\, k \in \mathcal{K},\ \{(j,g) \in \mathcal{J} \times \mathcal{N}_g \mid [A_{cf}]_{j,g} = 0\} \end{gathered} \tag{8.21}$$

The ESS reserves from eq. (8.6) are reformulated in terms of discharging and charging power, as in eq. (8.22), where s_k is the discharging binary indicator variable.

$$\begin{gathered} P^{dis}_k \leq s_k \bar{P}^b, \\ P^{dis}_k \leq \bar{P}^b - \left(D_{b,k} \cdot r_{tr} + M_{b,k} \cdot \bar{\gamma}\right) \cdot S_b, \\ P^{ch}_k \leq (1 - s_k)\bar{P}^b, \\ P^{ch}_k \leq \bar{P}^b - \left(D_{b,k} \cdot r_{tr} + M_{b,k} \cdot \bar{\gamma}\right) \cdot S_b,\ \forall\, k \in \mathcal{K} \end{gathered} \tag{8.22}$$

The bound derived in eq. (8.9) can be easily integrated to $\mathcal{P}$ through the linear constraints in eq. (8.23), where $\nu = \frac{r_{ss} S_b}{3600 \bar{E}^b}$.

$$\nu\left(M_{b,k} + D_{b,k}T\right) \leq \min\{\bar{x}^{SoC} - x_{k-1}^{SoC}, x_{k-1}^{SoC} - \underline{x}^{SoC}, \lambda x_k^{SoC}\}, \quad \forall\, k \in \mathcal{K} \tag{8.23}$$

Equation (8.13) may therefore be expressed as a deterministic MILP *ro* program and solved efficiently by the EMS at each time iteration, as $\mathcal{F}(\cdot)$ and $\mathcal{C}(\cdot)$ can be expressed as linear combinations of the optimization variables when including the reformulations proposed in eqs. (8.15) to (8.23).

8.3 SIMULATIONS

The various components of the proposed methodology are demonstrated in this section, namely the adaptive uncertainty quantification and the integration of frequency stability constraints with bounded use of the ESS stored energy in the optimal scheduling. To achieve this goal, the case study of a wind-powered offshore O&G platform is presented, where a reference operation time period is considered involving both regions of smooth, low magnitude, and sudden, large net load variations. The effectiveness of the proposed methodology is then demonstrated with time domain simulations on the scheduling time scale. The optimization problem is solved with *Gurobi 9.1.0* in a 28 physical core multi-node cluster with Intel(R) Xeon(R) CPU E5-2690 v4 @ 2.60 Hz and 25 GB RAM. The solution time of eq. (8.13) using the proposed formulation is well below 15 minutes, which is assumed here as the minimum threshold for real-time power system scheduling.

8.3.1 *Capabilities of adaptive uncertainty quantification*

A representative example of how the adaptive uncertainty quantification framework works is illustrated in Figure 8.3, where a case of a sudden APD was selected since these are the most interesting from a power imbalance perspective. The actual load values p^{ℓ} are presented with the solid black line and the blue cross ($p_{t|t}^{\ell}$) indicates the time instant at which a probabilistic forecast is issued. As described in section 8.2.2, the probabilistic forecasts are composed of the expected values $\hat{\mathbb{E}}[P_{t+k}^{\ell}|\boldsymbol{x}_r(t)]$ of the random variable P^{ℓ}, plotted with solid red line, and the prediction intervals $\hat{\alpha}(x)$ plotted around them in different shades of green, depending the quantile level $\tau = \{20\%, 40\%, 60\%, 80\%, 90\%\}$, for the whole prediction horizon ($k \in \mathcal{K}$). Two extreme quantile values $Q_{\tau}^{\ell}(\boldsymbol{x}_r(t))$ (for $\tau = \{5\%, 95\%\}$) are plotted with solid green lines, to illustrate that, as expected, most of the randomly generated sample values of load δ^i fall inside those. The random load samples δ^i are plotted in pink dots and represent one out of two components used for the net load scenarios. These scenarios are fed into the optimization problem $\mathcal{P}$ through eq. (8.15), being only 100 of them plotted in figs. 8.3a to 8.3g for the sake of visualization clarity.

The proposed adaptive uncertainty quantification algorithm generates samples that better describe the size of an APD as a function of time. Observe that the prediction

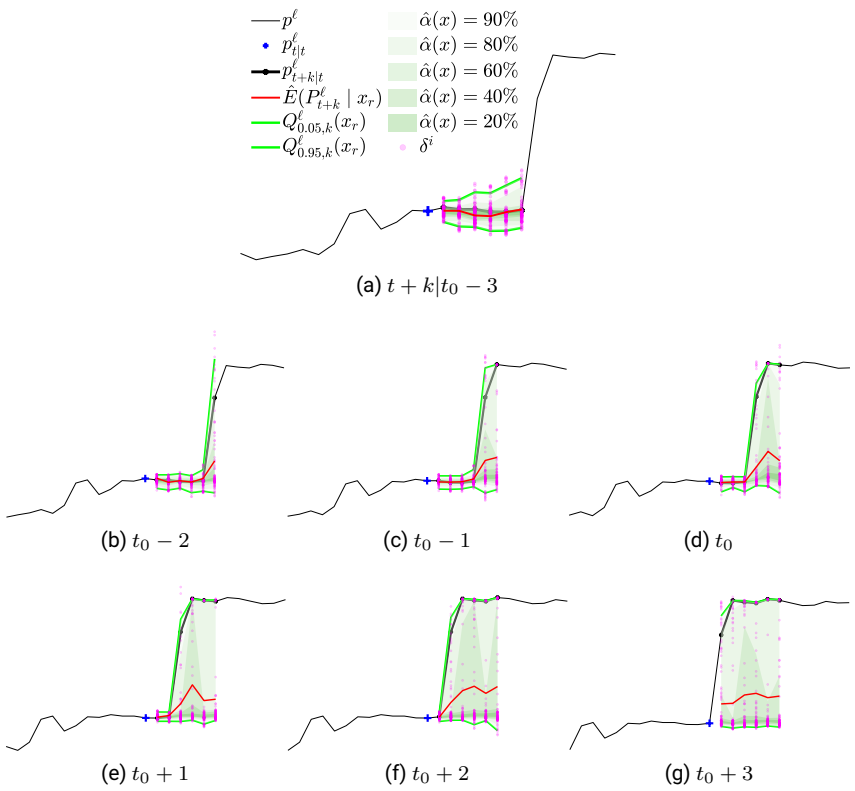

FIGURE 8.3. Demonstration of adaptive uncertainty quantification by using auto-regressive probabilistic forecasting for the load time-series. A case for a sudden step-like variation is presented for consecutive lead times (figs. 8.3a to 8.3g). By updating the estimated prediction intervals it is possible to capture the sudden load variation and draw samples (purple dots) that span an appropriate range of values

intervals $\hat{\alpha}$ and quantiles Q^ℓ_τ adapt to capture the irregular event of the sudden load increase as the blue cross moves forward in time (i.e., time t is updated from $t_0 - 3$ towards $t_0 + 3$), and a new forecast is issued from $p^\ell_{t|t}$ for the prediction horizon $t + k|t$. Note also that, at the initial time $t = t_0 - 3$ (8.3a), the prediction intervals are narrow and all the sampled values δ^i (pink dots) fall close and around the actual load values. For the following intervals (i.e., $t = t_0 - 2, \ldots, t_0 + 3$, figs. 8.3b to 8.3g), however, the uncertainty increases and the prediction intervals $\hat{\alpha}$ and quantiles Q^ℓ_τ expand to capture the possibility of an irregular sudden load increase. Observe that at the intervals prior to the APD, random load samples δ^i (pink dots) were generated at higher load values in the prediction horizon and close to the actual step (solid black line). The deterministic forecast (solid red line) which expresses the expected predictions ($\hat{\mathbb{E}}[P^\ell_{t+k}|\boldsymbol{x}_r]$), in contrast, fails to capture the variation adequately, because it is dominated by the inertia of past values (lagged load values in $\boldsymbol{x}_r(t)$), a common drawback of auto-regressive models.

8.3.2 Effect of optimal and bounded frequency support from ESS

To demonstrate the effect of optimally controlling the ESS to provide frequency support for an isolated APS, a step APD is considered at time $t'_0 = 2s$ representing a 0.4 pu load increase from a sudden motor startup, where a single GT is on in the platform of the case study. Simulations were run in Matlab/Simulink 2022a using the model given in eq. (8.1), which do not include delay of actuators. This simplification facilitate the interpretation of results, not implying, however, any loss of generality.

The results are illustrated in Figure 8.4, where the frequency deviation (solid lines) and the $RoCoF$ (dashed lines) for two cases are represented. In the first case (grey lines), the single online GT is the only source of primary frequency control, while, in the second case (black lines), the ESS supports in this task the GT, which has the same droop setting as in the previous case. Observe that the system's response in the first case violates not only the steady-state frequency bound r_{ss}, but also the maximum allowable $RoCoF$ ($\bar{\gamma}$), whereas in the second case, both limits are respected. To respect the defined bound in the first case, the GT droop setting must be increased, leading to a larger deviation from the optimal GT operating point, decreased efficiency and increased fuel consumption and emissions. The same droop setting for the GT, on the other hand, can be maintained and the r_{ss} threshold observed where an optimal participation of the ESS in the primary frequency control (PFC) has been decided beforehand by the algorithm using an adaptive droop setting. Note also the compliance with the $RoCoF$ limit where the ESS provides virtual inertia. To respect this limit without the ESS support would require an additional GT to be on, affecting significantly the overall efficiency of the system. The proposed algorithm, in other words, employs an adaptive droop and virtual inertia scheme, enabling not only the optimal scheduling of the power system by avoiding having an additional GT on, but also guaranteeing that the services provided by the ESS to the grid will not cause it to deviate significantly from its optimal schedule, as the use of stored energy is bounded by eq. (8.23). As a matter of fact, the calculated energy for frequency support provision by the ESS to the described disturbance for T (15 minutes) is 0.9179 MWh while the bound for $\lambda = 3\%$ is 0.9369 MWh.

8.3.3 Comparative analysis and effect of bounds

To further demonstrate the capabilities of the proposed EMS, a reference operation period is simulated considering: *I)* the default EMS that does not integrate any bounds; *II)* the version that includes frequency variation bounds but not the energy bounds on the ESS; and *III)* the proposed version that includes all of them.

System inertia and damping evolution

The results for all EMS versions are aggregated in Figure 8.5, being the system inertia and damping evolution depicted in 8.5a and 8.5b along with the net load signal $P_b^{nl}(t)$

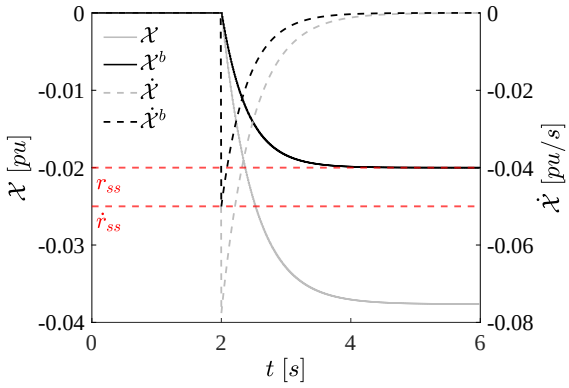

FIGURE 8.4. Effect of the optimally calculated participation of the ESS in providing frequency support for a step load change when only one GT is on. In contrast with the case of non participation of the ESS to frequency regulation (solid and dashed grey lines), the optimally designed virtual inertia and damping results in a frequency response (solid black) and Rate of Change of Frequency (dashed black) that are bounded by their defined limit values

(solid black line), during a reference period of eight hours. No frequency and $RoCoF$ containment reserves are considered in case *I*, the droop settings not being optimization variables and the ESS not contributing with virtual inertia. The system inertia $\mathcal{M}(t)$ (red line in fig. 8.5a) is therefore just the result of the online GTs based on the optimal techno-economic scheduling, not having any virtual component $M_b(t)$. Following the same color notation in both fig. 8.5a and fig. 8.5b, the evolution of the system inertia and damping is observed, being the contribution of the ESS in case *II* denoted by the superscript f (frequency bound) and in case *III* by f, e (frequency and energy bound).

Two main patterns are evident when observing fig. 8.5a and fig. 8.5b. Firstly, more inertia and damping are assigned for both cases *II* and *III* close to the time instants of the sudden net load variations (around 14:00 and 18:00 correspondingly). Secondly, the same inertia and damping are noticed during the relatively constant net load conditions (between 14:00 and 18:00). This effect demonstrates the adaptive capabilities of the proposed EMS algorithm to assign more or less inertia and damping in correspondence with the anticipated net load variations. The larger the variations expected, the more secure the system will be by properly deciding its power and energy reserves. Whether the ESS is not assigned to frequency control, securing the system for possible net load variations would require additional GTs to be on. This is confirmed in fig. 8.5a during both sudden net load variations, where $\mathcal{M}(t) \leq \mathcal{M}^f(t)$ (green line) and $\mathcal{M}(t) \leq \mathcal{M}^{f,e}(t)$ (magenta line). Note also that around those instants, $M_b^f(t) \geq 0$ (cyan line) and $M_b^{f,e}(t) \geq 0$ (blue line), meaning that the additional GT can be avoided by properly assigning virtual inertia to the ESS. Similar observations are drawn from fig. 8.5b where $D_b^f(t) \geq 0$ (cyan line) and $D_b^{f,e}(t) \geq 0$ (blue line) around the sudden variation instants and $D_b^f(t) = 0$ and $D_b^{f,e}(t) = 0$ for the rest period.

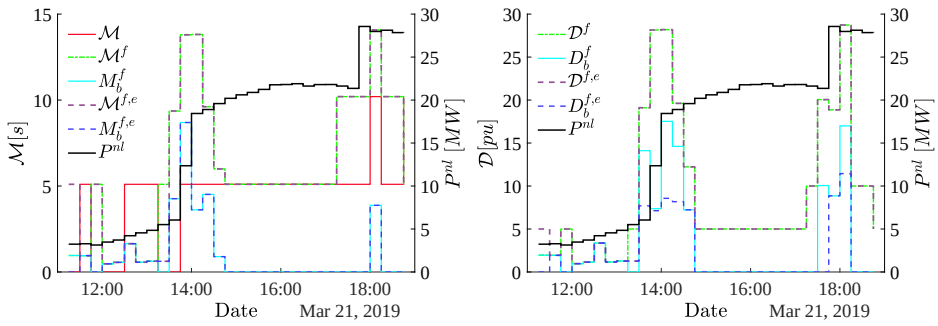

(a) Total system inertia.

(b) Total system damping.

FIGURE 8.5. Trajectories of the optimally designed system inertia (top) and damping (bottom) and optimal split between primary control provision by the GTs and the ESS for different bounds considerations. The simulated results are plotted against the net load signal (solid black) for a case where sudden step-like variations occur

Note that the effect of the energy bounds on the ESS are stronger in the damping terms than in the inertia. Figure 8.5a shows that the signals $M_b^f(t)$ and $M_b^{f,e}(t)$ are almost identical for the whole time period, whereas fig. 8.5b depicts that $\sup D_b^{f,e}(t) \leq \sup D_b^f(t)$. This means that the peak contribution of the ESS for case *III* is smaller than the one for case *II*. It is indeed possible to observe that $D_b^{f,e}(t)$ is almost always less than $D_b^f(t)$, further demonstrating that version *III* is more cautious not to overuse the PFC of the ESS.

The comparison of the different methods (*I*, *II*, *III*) is also quantified through the cumulative results of the specified key performance indicators in Table 8.1. Including bounds on the EMS results in slightly higher fuel consumption and operating costs, which is primarily attributed to higher cumulative operational hours of the GTs. This is in agreement with the results presented in Figure 8.5, as securing the system against possible disturbances may be associated with increased inertia requirements. It is also noteworthy in Table 8.1 that the incremental cost for including bounds on the use of ESS stored energy (*III*) compared to case *II* is negligible, meaning that the optimal GT scheduling is almost unaffected by the inclusion of energy bounds in the ESS. The main difference is that the resulting optimal GT trajectory for *II* is associated with one fewer GT startup compared to *III* and slightly lower ESS cycling, reflected in the lower degradation, which is, however, almost equal in cases *I* and *III*.

State of charge evolution and energy bounds effect

An additional comparison demonstrating the additional benefits coming from method *III* over method *II* is illustrated in Figure 8.6. The resulting $x^{SoC}(t)$ signals from the application of *II* and *III* are depicted in fig. 8.6a and fig. 8.6b correspondingly. Notice

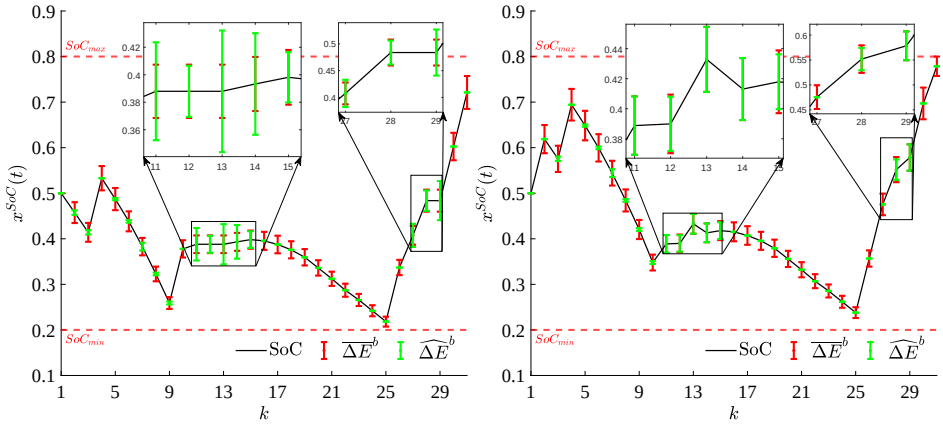

(a) Without bounds on the energy deviation. (b) With bounds on the energy deviation.

FIGURE 8.6. State of charge trajectories from the optimal scheduling and primary control design of the ESS, during the simulation period, for the cases of not including bounds on the resulting energy deviation from the participation in PFC (top) and the one when including the bounds (bottom)

that both methods respect the upper and lower SoC limits, as originally designed in the default method *I*. Both trajectories seem to follow similar patterns, i.e., initial discharge until $k = 9$, smooth re-bouncing and discharge until $k = 25$, and charging until the end. There are, however, small but important differences, those being clearly depicted in the two zoomed in areas ($k = 11 - 15$ and $k = 27 - 29$), where the maximum allowed energy deviation $\overline{\Delta E^b}(t)$ from the frequency support offered by the ESS is illustrated with red error bars and the calculated upper bound $\widehat{\Delta E^b}$ is illustrated with green error bars. It is evident that, for case *II*, there would be requirements for the ESS that could cause it to violate the upper bound $\widehat{\Delta E^b} > \overline{\Delta E^b}(t)$ at $k = 11, 14, 27, 29$, while the method in *III* controlled the ESS in a way that $\widehat{\Delta E^b} \leq \overline{\Delta E^b}(t)$ is guaranteed for the whole period.

TABLE 8.1. Performance comparison for the whole simulation period

Performance indicator	Method		
	I	*II*	*III*
fuel consumption (ON GTs) [kg]	29,695	29,929	30,131
fuel costs (ON GTs) [€]	8,846	8,916	8,976
GTs ON time [$N_g \times T$]	27	31	31
GTs startup times [-]	5	4	5
ESS degradation [%]	0.164	0.148	0.165

8.4 Conclusions

Achieving optimal energy management in isolated power systems with energy storage and sudden load variations cannot be decoupled from ensuring their secure and robust operation, especially under the presence of intermittent renewable power sources. Even though decisions related to techno-economical operation are conventionally taken in a discrete-time, those will inevitably affect the system's stability in its continuous operation and vice versa. To address this problem, this article proposed an energy management algorithm capable of integrating both higher time scale economic objectives and lower time scale stability constraints under adaptive uncertainty considerations. Additional constraints regarding the optimal use of the energy storage for providing flexibility and frequency support with bounded interaction between both services were proposed. A MILP formulation was derived and validated through time-domain simulations for an isolated offshore O&G platform integrating wind power. The results indicated that, under the proposed adaptive uncertainty framework, optimal decisions with dynamic frequency stability guarantees could be achieved and secured the system under an adaptive assessment of possible active power perturbations. This also reduced the conservatism from setting fixed damping and inertia requirements based on the expected worst-case and allowed better scheduling and operation of the GTs for longer periods. At the same time, the optimal sharing of primary frequency control contribution from conventional generators and the energy storage was found, while ensuring a tolerable impact on the storage optimal state of charge schedule and a negligible impact on the rest of energy management objectives.

The presented method targeted a small scale APSs (an isolated offshore O&G platform), but the formulation is based on general principles and can potentially be applied to BPSs, where enough computational resources and proper assumptions (e.g., aggregation of regions/generator groups) are applied to solve the optimization problem within the scheduling period (i.e., 15 min.). Remark that, while possible configurations grow exponentially with the number of generators, a strong MILP structure is preserved in the proposed method, allowing an efficient solution to the resulting optimization problem. A topic for future research therefore may be verifying the applicability of the suggested algorithm to regional dispatch centers that can operate autonomously. From this perspective, practical implementation in BPS also demands a standard framework for real-time command and telemetry of frequency reserves from the dispatch center to local primary controllers, which not only is a topic for future research but also should be addressed by regulatory and standardization bodies.

8.5 References

[1] Y.-Y. Hong and G. F. D. Apolinario, "Uncertainty in Unit Commitment in Power Systems: A Review of Models, Methods, and Applications," *Energies*, vol. 14, no. 20, p. 6658, Jan. 2021. Cited on page/s 192.

[2] X. Xia and A. M. Elaiw, "Optimal dynamic economic dispatch of generation: A review," *Electr. Power. Syst. Res.*, vol. 80, no. 8, pp. 975–986, Aug. 2010. Cited on page/s 192.

[3] B. Mohandes, M. S. E. Moursi, N. Hatziargyriou, and S. E. Khatib, "A Review of Power System

Flexibility With High Penetration of Renewables," *IEEE Trans. Power Syst.*, vol. 34, no. 4, pp. 3140–3155, Jul. 2019. Cited on page/s 192.

[4] F. Dorfler, S. Bolognani, J. W. Simpson-Porco, and S. Grammatico, "Distributed Control and Optimization for Autonomous Power Grids," in *2019 18th European Control Conference (ECC)*. Naples, Italy: IEEE, Jun. 2019, pp. 2436–2453. Cited on page/s 192.

[5] Comission Regulation (EU) 2017/1485, "Guideline on electricity transmission system operation," Aug. 2017. [Online]. Available: http://data.europa.eu/eli/reg/2017/1485/oj Cited on page/s 192, 193.

[6] L. Polleux, E. F. Alves, M. Korpås, E. Tedeschi, and G. Guerassimoff, "Allocation of spinning reserves for autonomous grids subject to frequency stability constraints and short-term renewable power variations," *arXiv:2203.07233 [cs, eess]*, Mar. 2022. [Online]. Available: http://arxiv.org/abs/2203.07233 Cited on page/s 192.

[7] L. Sigrist, L. Rouco, and F. M. Echavarren, "A review of the state of the art of UFLS schemes for isolated power systems," *Intl. J. Electr. Power Energy Syst.*, vol. 99, pp. 525–539, Jul. 2018. Cited on page/s 193.

[8] J. Luo, F. Teng, and S. Bu, "Stability-Constrained Power System Scheduling: A Review," *IEEE Access*, vol. 8, pp. 219 331–219 343, 2020, conference Name: IEEE Access. Cited on page/s 193.

[9] V. Prakash, K. C. Sharma, R. Bhakar, H. P. Tiwari, and F. Li, "Frequency Response Constrained Modified Interval Scheduling Under Wind Uncertainty," *IEEE Trans. Sust. Energy*, vol. 9, no. 1, pp. 302–310, Jan. 2018, conference Name: IEEE Trans. Sust. Energy. Cited on page/s 193.

[10] Q. Shi, F. Li, and H. Cui, "Analytical Method to Aggregate Multi-Machine SFR Model With Applications in Power System Dynamic Studies," *IEEE Trans. Power Syst.*, vol. 33, no. 6, pp. 6355–6367, Aug. 2018, conference Name: IEEE Trans. Power Syst. Cited on page/s 193.

[11] L. Badesa, F. Teng, and G. Strbac, "Simultaneous Scheduling of Multiple Frequency Services in Stochastic Unit Commitment," *IEEE Trans. Power Syst.*, vol. 34, no. 5, pp. 3858–3868, Sep. 2019, conference Name: IEEE Trans. Power Syst. Cited on page/s 193.

[12] V. Trovato, A. Bialecki, and A. Dallagi, "Unit Commitment With Inertia-Dependent and Multispeed Allocation of Frequency Response Services," *IEEE Trans. Power Syst.*, vol. 34, no. 2, p. 12, 2019. Cited on page/s 193.

[13] Z. Zhang, E. Du, F. Teng, N. Zhang, and C. Kang, "Modeling Frequency Dynamics in Unit Commitment With a High Share of Renewable Energy," *IEEE Trans. Power Syst.*, vol. 35, no. 6, pp. 4383–4395, Aug. 2020, conference Name: IEEE Trans. Power Syst. Cited on page/s 193.

[14] S. S. Oskouee, S. Kamali, and T. Amraee, "Primary Frequency Support in Unit Commitment Using a Multi-Area Frequency Model With Flywheel Energy Storage," *IEEE Trans. Power Syst.*, vol. 36, no. 6, pp. 5105–5119, Aug. 2021, conference Name: IEEE Trans. Power Syst. Cited on page/s 193.

[15] T. Ding, Z. Zeng, M. Qu, J. P. S. Catalão, and M. Shahidehpour, "Two-Stage Chance-Constrained Stochastic Thermal Unit Commitment for Optimal Provision of Virtual Inertia in Wind-Storage Systems," *IEEE Trans. Power Syst.*, vol. 36, no. 4, pp. 3520–3530, Jul. 2021, conference Name: IEEE Trans. Power Syst. Cited on page/s 193.

[16] V. Trovato, "System Scheduling with Optimal Time-varying Delivery Intervals for Frequency Response," *IEEE Trans. Power Syst. (Early Access)*, Feb. 2022. Cited on page/s 193.

[17] E. Alves, G. Bergna-Diaz, D. Brandao, and E. Tedeschi, "Sufficient Conditions for Robust Frequency Stability of AC Power Systems," *IEEE Trans. Power Syst.*, vol. 36, no. 3, pp. 2684–2692, May 2021, conference Name: IEEE Trans. Power Syst. Cited on page/s 193, 196, 197, 198.

[18] H. Ahmadi and H. Ghasemi, "Security-Constrained Unit Commitment With Linearized System Frequency Limit Constraints," *IEEE Trans. Power Syst.*, vol. 29, no. 4, pp. 1536–1545, Jul. 2014, conference Name: IEEE Trans. Power Syst. Cited on page/s 193.

[19] Y. Wen, W. Li, G. Huang, and X. Liu, "Frequency Dynamics Constrained Unit Commitment With Battery Energy Storage," *IEEE Trans. Power Syst.*, vol. 31, no. 6, pp. 5115–5125, Aug. 2016, conference Name: IEEE Trans. Power Syst. Cited on page/s 193.

[20] C. Zhang, L. Liu, H. Cheng, D. Liu, J. Zhang, and G. Li, "Frequency-constrained Co-planning of Generation and Energy Storage with High-penetration Renewable Energy," *J. Mod. Power Syst. Clean*, vol. 9, no. 4, pp. 760–775, Jul. 2021, conference Name: J. Mod. Power Syst. Clean. Cited on page/s 193.

[21] C. Cardozo, L. Capely, and P. Dessante, "Frequency constrained unit commitment," *Energy Syst*, vol. 8, no. 1, pp. 31–56, Feb. 2017. [Online]. Available: http://link.springer.com/10.1007/s12667-015-0166-4 Cited on page/s 193.

[22] M. Javadi, T. Amraee, and F. Capitanescu, "Look ahead dynamic security-constrained economic dispatch considering frequency stability and smart loads," *Intl. J. Electr. Power Energy Syst.*, vol. 108, pp. 240–251, Mar. 2019. [Online]. Available: https://www.sciencedirect.com/science/article/pii/S0142061518325122 Cited on page/s 193.

[23] Y. Yin, T. Liu, L. Wu, C. He, and Y. Liu, "Frequency-constrained multi-source power system scheduling against N-1 contingency and renewable uncertainty," *Energy*, vol. 216, p. 119296, Oct. 2021. [Online]. Available: https://www.sciencedirect.com/science/article/pii/S0360544220324038 Cited on page/s 193.

[24] A. Safari, M. Farrokhifar, H. Shahsavari, and V. Hosseinnezhad, "Stochastic planning of integrated power and natural gas networks with simplified system frequency constraints," *Intl. J. Electr. Power Energy Syst.*, vol. 132, p. 107144, Aug. 2021. [Online]. Available: https://www.sciencedirect.com/science/article/pii/S0142061521003835 Cited on page/s 193.

[25] M. Carrión, R. Zárate-Miñano, and F. Milano, "Impact of off-nominal frequency values on the generation scheduling of small-size power systems," *Intl. J. Electr. Power Energy Syst.*, vol. 122, p. 106174, Aug. 2020. [Online]. Available: https://www.sciencedirect.com/science/article/pii/S0142061519343431 Cited on page/s 193.

[26] IEEE Task Force on Turbine-Governor Modeling, "Dynamic Models for Turbine-Governors in Power System Studies," IEEE, New York, NY, Technical Report PES-TR1, Aug. 2013. Cited on page/s 197.

[27] S. Chapaloglou, D. Varagnolo, F. Marra, and E. Tedeschi, "Data-driven energy management of isolated power systems under rapidly varying operating conditions," *Appl. Energy*, vol. 314, p. 118906, May 2022. [Online]. Available: https://linkinghub.elsevier.com/retrieve/pii/S0306261922003294 Cited on page/s 198, 199, 200, 201.

[28] L. Breiman, "Random Forests," *Machine Learning*, vol. 45, pp. 5–32, Oct. 2001. Cited on page/s 198.

[29] N. Meinshausen, "Quantile Regression Forests," *J. Mach. Learn. Res.*, vol. 7, pp. 983–999, Dec. 2006. Cited on page/s 199.

[30] E. F. Camacho and C. Bordons, *Model Predictive control*, ser. Advanced Textbooks in Control and Signal Processing, M. J. Grimble and M. A. Johnson, Eds. London: Springer London, 2007. [Online]. Available: http://link.springer.com/10.1007/978-0-85729-398-5 Cited on page/s 200.

[31] M. Vrakopoulou, K. Margellos, J. Lygeros, and G. Andersson, "A Probabilistic Framework for Reserve Scheduling and ${\rm N}-1$ Security Assessment of Systems With High Wind Power Penetration," *IEEE Trans. Power Syst.*, vol. 28, no. 4, pp. 3885–3896, Nov. 2013. [Online]. Available: http://ieeexplore.ieee.org/document/6570751/ Cited on page/s 201.

[32] K. Hreinsson, M. Vrakopoulou, and G. Andersson, "Stochastic security constrained unit commitment and non-spinning reserve allocation with performance guarantees," *Intl. J. Electr. Power Energy Syst.*, vol. 72, pp. 109–115, Aug. 2015. [Online]. Available: https://www.sciencedirect.com/science/article/pii/S0142061515001003 Cited on page/s 201.

[33] K. Margellos, P. Goulart, and J. Lygeros, "On the Road Between Robust Optimization and the Scenario Approach for Chance Constrained Optimization Problems," *IEEE Trans. Automat. Contr.*, vol. 59, no. 8, pp. 2258–2263, Aug. 2014. [Online]. Available: http://ieeexplore.ieee.org/document/6727399/ Cited on page/s 201.

Part III

EPILOGUE

Chapter 9

Conclusion

The following chapter summarizes the conclusions drawn from the work in this thesis and proposes directions for future research.

9.1 Concluding remarks

The effort toward dealing with climate change, one of the major open challenges of our times, is arguably associated with re-designing the future power systems that will serve the needs of our constantly expanding societies, aiming for sustainable development. Such an effort cannot neglect the particular case of isolated systems, whether those are formed by natural geographical isolation (e.g., distant island or mountain communities) or arise from specialized requirements of industrial applications (i.e., offshore activities). Additional challenges emerge from the latter cases, when trying to meet a demand that can be highly variable and intermittent, and as much as possible, exploiting clean energy resources. Throughout this thesis, the focus was shed on identifying such challenges and exploring relevant potential technological solutions, considering the particular case example of wind-powered offshore O&G platforms. Despite this case being considered the main example, the scientific concepts investigated and the proposed methods can easily be transferred to other types of isolated power systems sharing common features.

From the results presented in the previous chapters, it is deduced that O&G platforms that integrate renewable energy can benefit from further integration of properly designed energy storage in multiple ways and time scales. In fact, from Chapter 3 it can be deduced that a proper combination of wind power penetration (according to the platform's peak demand) and properly sized BESS could replace the use of a GT, leading in turn to economic and environmental benefits compared to a case without energy storage. However, there might be cases where the incremental benefits of storage do not justify its investment cost. In addition, properly/accurately quantifying the potential benefits from such an investment decision means that an accurate and adequate uncertainty description is considered. Chapter 4 demonstrates that not only the BESS sizing decision highly depends on how uncertainties from various sources are combined, when the operational stage is included in the decision-making process, but also that data-driven methods are necessary to generalize and better capture such combined uncertainties (compared to the use of pure historical data). If such a sizing

methodology is followed (as proposed), it reveals that despite the "expected" benefits associated with the integration of energy store, there might be cases where the limited available resources of the isolated system do not favor storing energy, and therefore, the risk of worst-cases combinations cannot be mitigated through the storage sizing decision. Notably, the latter highly depends on the time frame of the sizing and the operational horizon specified in the relevant optimization problems, factors that remain open for further investigation.

The environmental and economical benefits resulting from the introduction of a BESS in an O&G platform's power generation equipment vary depending on the energy management algorithm implemented. In particular, greater benefits are to be expected during the system's operation when uncertainty is integrated into the control decisions for the various assets (i.e., power generators, dumping loads, and the ESS itself) implementing the preferred management strategy. The proposed algorithm described in Chapter 5 is therefore capable of improving the anticipated benefits in terms of operational cost savings with respect to a state-of-the-art EMS. When properly using past information from the system's power demand and RES power generation, a better description of the very short-term future uncertainties can be obtained, making it possible to anticipate sudden variations and irregular events without any prior knowledge of the future. This can eventually result in improving fuel consumption and the switching of the GTs (on/off), which is directly translated to reduced emissions and GT wear and tear during system operation.

Besides the expected techno-economical benefits eventuating from the integration of a BESS, the electric system of isolated wind-powered O&G platforms can be benefited in terms of real-time power balancing and grid support functionalities. As demonstrated in Chapter 6, using available historical data (system level aggregation), appropriate combinations of energy storage requirements and control actions can be found to support the regulation of the local grid's frequency. Risk-dependent guidelines can be created/instructed as a decision support tool providing energy storage power specifications and control laws with embedded anti-saturation characteristics, that will improve the dynamic characteristics of the O&G power system. In fact, such ancillary services can be provided by the BESS on top of its optimal reference tracking capabilities, even with partial system information. Chapter 7 shows that the optimal reference trajectory (as instructed from the EMS of Chapter 5) can be followed along with the provision of frequency support under uncertain disturbances and system dynamics (following the uncertainty description from Chapter 6), making the BESS multifunctional and further exploiting it in multiple time scales. This can be achieved by using the MPC framework. Interestingly, the performance of such controllers highly depends on the control law parametrization and the user-defined objective prioritization. It is also remarkable that considering uncertainty in the control design (i.e., stochastic MPC) will not always lead to smaller constraint violation probability when compared to a deterministic MPC. Again, this highly depends on the control law parametrization, with the open loop optimal policy and the affine disturbance feedback

being the ones associated with the best performance and constraint satisfaction, in the probabilistic sense.

From a different perspective, even though evident that techno-economical benefits are to be expected if there is the possibility of switching the operation of GTs (on/off), from the systems security point of view, such decisions may not only threaten the system but even be infeasible in practice. In addition, using the ESS to provide virtual inertia and damping characteristics in cooperation with the operating GTs units may affect its ability to track the optimal reference (i.e., as instructed by the EMS). Such challenges are addressed under the algorithm proposed in Chapter 8, taking advantage of the data-driven adaptive uncertainty quantification module and the EMS from Chapter 5. Therefore, it becomes possible to coordinate the frequency response of the GTs and ESS units in real time by using adaptive control, and ensuring that the frequency will be contained inside the allowable range, under almost all possible very short-term future net load variations, within a predefined risk acceptance level. This capability has the potential to overcome problems related to the applicability of techno-economically optimal scheduling decisions, which most of the time are overwritten from sub-optimal solutions that only guarantee system stability. In addition, it is demonstrated that besides combining the optimal scheduling with the system's stability requirements, it will be guaranteed that the ESS will follow its predefined optimal trajectory with only a bounded and preselected deviation from it.

9.2 FUTURE RESEARCH DIRECTIONS

Some potential directions for future research, stemming from the work presented in this thesis, are summarized in the following:

9.2.1 Related to Chapter 4

As discussed above, one of the main challenges for ESS sizing in isolated power systems is due to the fact that there exist several individual sources of uncertainty (i.e., various types of RES and load patterns) with particular characteristics that, however, affect the system in a combined way.

Appending the uncertainty space dimensionality with more types of RES and initial conditions parameters

Thus, a potential extension of the work presented in Chapter 4 could involve further investigation of the developed methodology but with the introduction of additional uncertainty sources (i.e., different RES types) and the inclusion of the SoC initial condition as an uncertain parameter (additional dimension in the uncertainty space). This would be an important step toward the generalization of the methodology, and a potential approach to deal with the open problem of the time-frame dependency of the storage sizing problem.

Data-driven scenario generation methods for so with implicit statistical stability characteristics

In addition, new *sg* methods for solving the ESS sizing problem incorporating the uncertainty of the operational stage are needed. The main criterion for such methods should be their potential to achieve solutions that are as independent as possible to the particular scenario realizations that are considered when solving the problem. In other words, they should provide efficient methods that reduce the dispersion of the optimal solutions obtained when solving the optimization problem under uncertainty. For that, modern machine learning algorithms (i.e., GANs) could be employed for the task of directly learning the "important" scenarios of combined uncertainty that result in statistically stable solutions of the sizing problem, thus eliminating the need for iterative procedures and repetitive *sg* until statistical stability is achieved.

9.2.2 Related to Chapter 5

Optimal EMS for isolated power systems with learning-based system stability constraints

Many issues in the optimal management of isolated power systems arise from the lower time scale dynamic security requirements of such grids, with the most important being the ones of frequency and voltage stability. Therefore, even though the cost-optimal high-level (higher time scale) operation of the energy system can be instructed by properly designed EMSs (see Chapter 5), the resiliency of the power system in the smaller time scale is not always guaranteed. For that to be achieved, the optimization problem defined and solved at the EMS level should also include low-level operational constraints. However, one of the main challenges related to that is the lack of general and accurate closed form expressions ensuring the system's security and stability. Those are typically case specific, depend on the type and modelling detail of the power system, and are hard to be integrated into linear programming/integer linear programming routines, due to the non-linearities associated with the power system operation. An alternative to that is the adoption of statistical and machine learning methods to infer such constraints from high fidelity models. Basically, those could be used as tunable data generation mechanisms, providing the training samples to be used not only for the learning of the main system dynamics but also for the development of data-driven security criteria, which will be eventually translated into constraints for the optimal EMS problem.

9.2.3 Related to Chapter 7

Distributionally Robust Model Predictive Control of isolated power systems integrating energy storage

A recent development in the field of optimization has brought to light the Distributionally Robust Optimization (DRO) method, which combines principles from both

so and *ro* but has not been extensively studied for control applications (i.e., MPC). A potential direction could therefore be the development of a Distributionally Robust Model Predictive Controller (DRMPC) for an isolated industrial power system application and its comparison to alternatives approaches such as the SMPC versions presented in Chapter 7. The DRMPC ambiguity sets can be constructed by inferring the distributions of the *RV*s, implementing *sg* methodologies that can effectively and systematically generalize the uncertainty of the problem, without using parametric/arbitrary probability functions. Then, efficient solution methods should be investigated for the computationally efficient implementation of such controllers.

9.2.4 Related to Chapter 8

Tight constraints for the SoC management in frequency-constrained EMS and nonlinear system dynamics

A natural extension of the algorithm presented in Chapter 8 is related to finding tighter and less conservative constraints for incorporating the SoC trajectory evolution into the optimal EMS problem when the latter provides a frequency response (both inertial and primary). This problem is directly connected with the approximation of the non-linear dynamics of isolated systems under large active power variations where finding an analytical solution can be extremely tedious. An alternative would be to use suitable statistical/machine learning methods that can predict the dynamic response of such non-linear systems but are also simple enough to be easily included in MILP formulations of the EMS problem.

Appendix A

Supplementary information for Chapter 4

A.1 Explanation and visualization of scenario generation methods

The purpose of this section is to explain the various *sg* methodologies/techniques and how they compare to the one proposed in Chapter 4. Each technique is presented separately and explained from the perspective of the technical optimization problem under consideration, that is, the techno-economic sizing of ESS for an isolated power system under uncertain load consumption and power generation.

A.1.1 Datasets

First the available historical datasets $\mathcal{D}^{\ell}$, $\mathcal{D}^{w}$ ($|\mathcal{D}^{\ell}| = |\mathcal{D}^{w}|$) of the two random variables (load consumption) ξ^{ℓ} and ξ^{w} (wind power), respectively, are presented in Figure A.1. In fig. A.1a, we observe the load profiles (patterns) and in fig. A.1b, the wind power profiles. We refer to the dataset containing both the load and wind profiles as $\mathcal{D}$. The task is to create a reduced dataset Ω_s with specified cardinality ($|\Omega_s^*|$), containing both load and wind power profiles, to solve the stochastic optimization problem and monitor the statistical stability of the objective value statistic. In other words, datasets $\mathcal{D}_s$ will serve as the reduced scenario sets Ω_s that are required to estimate $\hat{F}^*(\boldsymbol{x}; \Omega_s)$ and corresponding confidence intervals to examine the consistency of the estimated value. For that, the summary statistics including *Range*, *IQR*, *standard deviation* defined as

$$Rg(\hat{F}^*) = \sup\{\hat{F}^*(\boldsymbol{x}; \Omega_s^m)\} - \inf\{\hat{F}^*(\boldsymbol{x}; \Omega_s^m)\},\ m = 1, \ldots, M \tag{1}$$

$$IQR = CDF^{-1}_{\hat{F}^*}(0.75) - CDF^{-1}_{\hat{F}^*}(0.25) \tag{2}$$

$$s(\hat{F}^*) = \sqrt{Var\left(\hat{F}^*\right)} \tag{3}$$

respectively, are calculated using bootstrap resampling based on each of the following methods. In the above, each sample of scenarios set Ω_s^m leads to the estimator $\hat{F}^*$ and with the resampling method, we estimate its cumulative distribution as $CDF_{\hat{F}^*}$.

A.1.2 "Data"

The first approach (named *Data*) consists of the naive random selection from $\mathcal{D}$ where each sample is an exact element of that set. This means that each sample consists of load and wind profiles observed on the same day. This simple approach has often

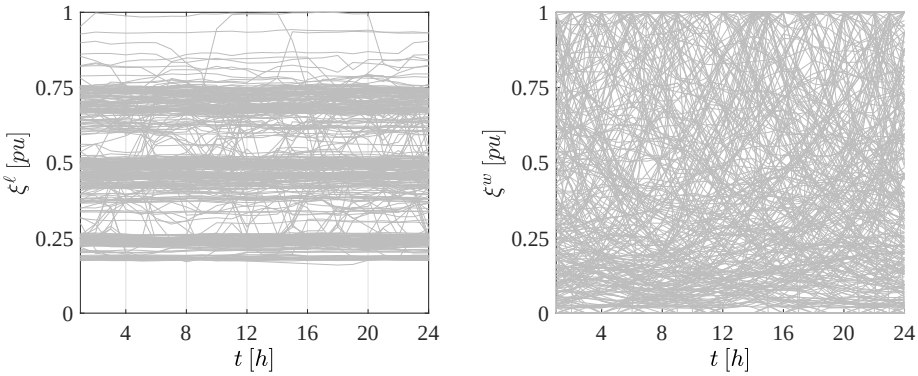

(a) load (b) wind power

FIGURE A.1. Historical datasets

been adopted in creating reduced subsets $\mathcal{D}_r$. Such an approach suffers from the generalization issue since the observed dataset $\mathcal{D}$ is just a marginalization of the true underlying probability of combinations of load and wind power profiles. This sampling process is described as

$$\begin{aligned} \mathcal{D}_{r,m} = \{\hat{\boldsymbol{\xi}}_s \ \forall \ \ s = 1, \ldots, |\Omega_s^*| : \omega_s \sim \mathcal{U}\{1, |\mathcal{D}^{\ell}|\}, \\ \boldsymbol{\xi}^{\ell}(\omega_s) \in \mathcal{D}^{\ell}, \ \boldsymbol{\xi}^{w}(\omega_s) \in \mathcal{D}^{w}\}, \ \forall \ \ m = 1, \ldots, M \end{aligned} \tag{4}$$

That means that at each sampling instant s, a scenario $\hat{\boldsymbol{\xi}}_s$ will be created to populate the reduced subset $\mathcal{D}_{r,m}$ such that if a particular load profile $\boldsymbol{\xi}^{\ell}(\omega_s)$ is selected from the initial load profiles dataset $\mathcal{D}^{\ell}$, then the corresponding wind power profile with the same index $\boldsymbol{\xi}^{w}(\omega_s)$ should be selected from its original dataset $\mathcal{D}^{w}$. This whole procedure is repeated M times to create the required statistics. This process is also illustrated in Figure A.2 where there is a one-to-one correspondence between the colors in fig. A.2a and fig. A.2b, meaning that the red profiles share the same index ω_1, the green profiles the same index ω_2, the blue profiles the same index ω_3, and so on. Each profile is considered to be equiprobable in its set and profiles are mutually independent among them, meaning that the probability of each scenario is

$$\pi_s(\hat{\boldsymbol{\xi}}_s) = \frac{\frac{1}{|\mathcal{D}^{\ell}|}\frac{1}{|\mathcal{D}^{w}|}}{\sum_s \frac{1}{|\mathcal{D}^{\ell}|}\frac{1}{|\mathcal{D}^{w}|}} = \frac{1}{|\Omega_s^*|} \tag{5}$$

since $|\mathcal{D}^{\ell}| = |\mathcal{D}^{w}|$.

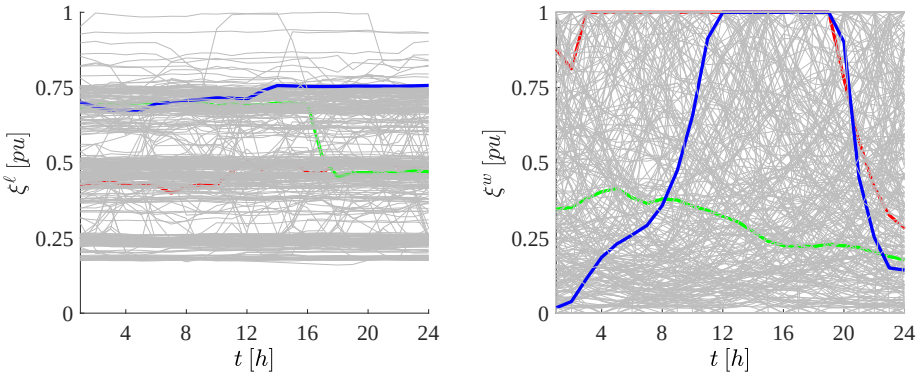

(a) load (b) wind power

FIGURE A.2. Profiles selection with sg method: *Data*

A.1.3 "Random"

A similar approach, but without restricting that a particular combination of load and wind power profiles should happen only as was observed, is replicated through method *Random*. This is described similarly with eq. (4) as

$$\mathcal{D}_{r,m} = \{\hat{\boldsymbol{\xi}}_s \;\forall\; s = 1,\dots,|\Omega_s^*| : \omega_s^{\ell} \sim \mathcal{U}\{1,|\mathcal{D}^{\ell}|\},\; \omega_s^{w} \sim \mathcal{U}\{1,|\mathcal{D}^{w}|\}, \\ \boldsymbol{\xi}^{\ell}(\omega_s^{\ell}) \in \mathcal{D}^{\ell},\; \boldsymbol{\xi}^{w}(\omega_s^{w}) \in \mathcal{D}^{w}\},\; \forall\; m = 1,\dots,M \tag{6}$$

As evident from eq. (6), now indices ω_s^{ℓ} and ω_s^{w} are different in general, meaning that the wind power profiles can be combined with load profiles of different days than the ones observed. This is replicated in Figure A.3 where the color convention follows Figure A.2. Thus, now during the sampling procedure, red, green, and blue profiles do not share the same index among the two datasets $\mathcal{D}^{\ell}$ and $\mathcal{D}^{w}$. The probabilities of the equiprobable scenarios are given again as eq. (5). Both *Data* and *Random* methods rely on random resampling of the original datasets, and therefore, there are no guarantees that with the specified $|\Omega_s^*|$ the true variance of the datasets is replicated into the SP problem. This is also the reason for the increased variance noticed in Figure 4.5, where its sample m results in different values for the objective function.

S

A.1.4 Fast Forward Selection (FFS)

A more structured way to create reduced subsets instead of just randomly picking some of them is to use a scenario reduction technique. One of the most popular and commonly used methods to optimally reduce scenarios is the heuristic *FFS* technique, explained in Chapter 2. The third sampling methodology, *FFS*, makes use of this process

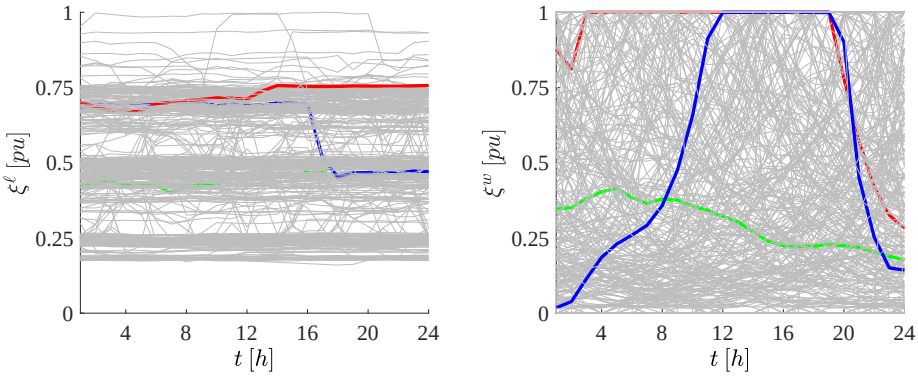

(a) load (b) wind power

FIGURE A.3. Profiles selection with sg method: *Random*

to reduce the original datasets $\mathcal{D}^{\ell}$ and $\mathcal{D}^{w}$ to the specified cardinality $|\Omega_s^*|$ and then randomly combine profiles to generate scenarios. This is described as

$$\begin{gathered}\mathcal{D}_r^{\ell} = FFS(\mathcal{D}^{\ell}),\ \mathcal{D}_r^{w} = FFS(\mathcal{D}^{w}) \\ \mathcal{D}_{r,m} = \{\hat{\boldsymbol{\xi}}_s\ \forall\ \ s = 1,\dots,|\Omega_s^*| : \omega_s^{\ell} \sim \mathcal{U}\{1,|\mathcal{D}_r^{\ell}|\},\ \omega_s^{w} \sim \mathcal{U}\{1,|\mathcal{D}_r^{w}|\}, \\ \boldsymbol{\xi}^{\ell}(\omega_s^{\ell}) \in \mathcal{D}_r^{\ell},\ \boldsymbol{\xi}^{w}(\omega_s^{w}) \in \mathcal{D}_r^{w}\},\ \forall\ \ m = 1,\dots,M\end{gathered} \tag{7}$$

where $FFS(\cdot)$ is the operation of applying the *FFS* algorithm. This means that, after each set of profiles has been optimally reduced and the probabilities of the discarded scenarios have been reassigned to the ones of the preserved, then the sets $\mathcal{D}^{\ell}$ and $\mathcal{D}^{w}$ are bootstrapped to generate the estimator (objective value) statistics. This process is illustrated in Figure A.4. First $\mathcal{D}^{\ell}$ and $\mathcal{D}^{w}$ are populated (blue profiles are the preserved ones from the scenario reduction for load in fig. A.4a and wind power in fig. A.4b) and then those are randomly sampled (figs. A.4c and A.4d), where red, green, and blue profiles correspond to different indices. The probability of each scenario is then given as

$$\pi_s(\hat{\boldsymbol{\xi}}_s) = \frac{\pi_s^{ffs}(\boldsymbol{\xi}^{\ell}(\omega_s^{\ell}))\pi_s^{ffs}(\boldsymbol{\xi}^{w}(\omega_s^{w}))}{\sum_s \pi_s^{ffs}(\boldsymbol{\xi}^{\ell}(\omega_s^{\ell}))\pi_s^{ffs}(\boldsymbol{\xi}^{w}(\omega_s^{w}))} \tag{8}$$

where $\pi_s^{ffs}(\cdot)$ denotes the probability of the preserved profile s after the redistribution from *FFS*. The denominator of eq. (8) is just the normalization constant for combining probabilities of load and wind power profiles. As is observed from fig. A.4a, the *FFS* method fails to capture the variation of the whole dataset, since it tends to preserve only the "average" scenarios, therefore creating a high bias to the result. The same applies to wind (fig. A.4b) where cases of larger wind power drops are not captured by the scenario technique. This bias is also reflected in the results of Figure 4.5, where

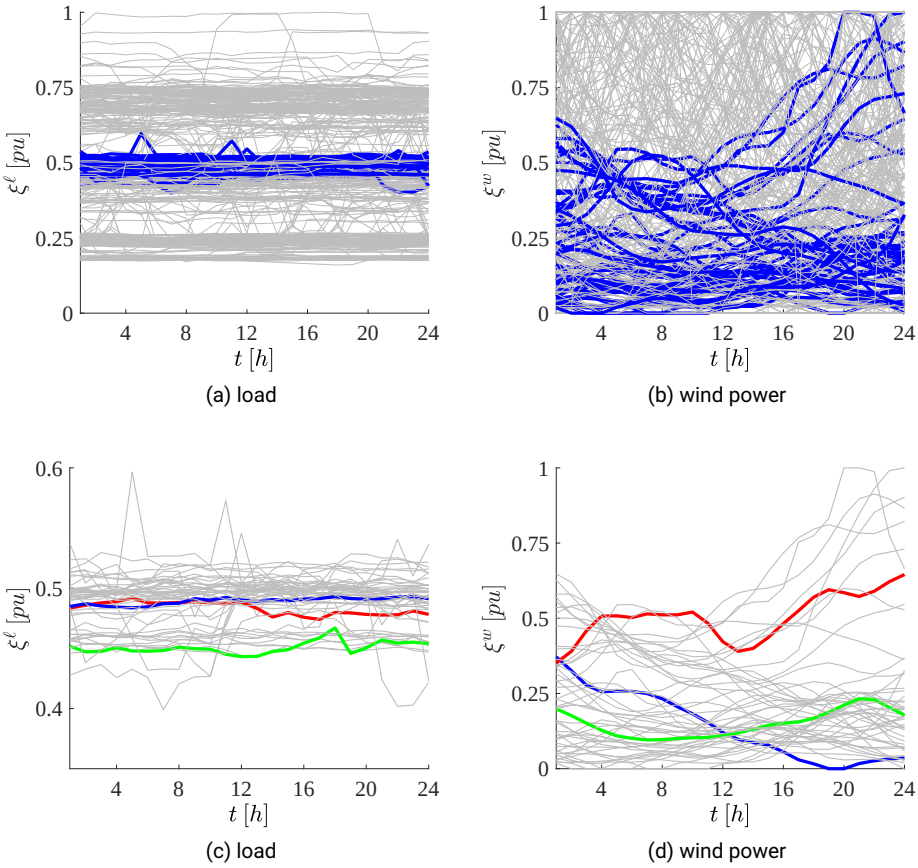

FIGURE A.4. Profiles selection with sg method: *FFS*

the median value of the objective function is relatively higher compared to the other methods.

A.1.5 H-cl

Another possibility to capture more of the variance of the original dataset is to perform scenario reduction by clustering techniques. Those are basically unsupervised learning algorithms used for pattern recognition by data partitioning around some central values. In this case, one of the most common types of clustering algorithms, the Agglomerative Hierarchical Clustering approach, was adopted to perform clustering on $\mathcal{D}^{\ell}$ and $\mathcal{D}^{w}$. The centers of the clusters defining the representative profile of each cluster were found based on Ward's minimum variance method and using the Euclidean metric by

minimizing the following linkage distance between clusters C_i and C_j

$$\Delta(C_i, C_j) = \sqrt{\frac{|C_i||C_j|}{|C_i| + |C_j|}} \left\| \mu_{C_i} - \mu_{C_j} \right\|_2 \tag{9}$$

where μ_{C_i}, μ_{C_j} are the centroids of clusters C_i, C_j, respectively defined as

$$\mu_{C_i} = \frac{1}{|C_i|} \sum_{k}^{|C_i|} \mu_{C_{ik}} \tag{10}$$

The above is a recursive bottom-up procedure where each sample starts as a single own cluster and each time the union of clusters that minimizes the variance compared to the original clusters is found. This results in a dendrogram where different layers of connectivity are achieved. Those dendrograms with the respective centroids are illustrated in figs. A.5a and A.5c for load and in figs. A.5b and A.5d for wind power, respectively, for the case of $|\Omega_s| = 10$ (for visualization). Eventually, datasets $\mathcal{D}^\ell$ and $\mathcal{D}^w$ are partitioned in $|\Omega_s^*|$ clusters each and the corresponding reduced subsets $\mathcal{D}_r^\ell$ and $\mathcal{D}_r^w$ are found as

$$\begin{gathered} \mathcal{D}_r^\ell = \{\mu_1^\ell, \ldots, \mu_{|\Omega_s^*|}^\ell\},\ \mathcal{D}_r^w = \{\mu_1^w, \ldots, \mu_{|\Omega_s^*|}^w\} \\ \mathcal{D}_{r,m} = \{\hat{\boldsymbol{\xi}}_s \ \forall\ \ s = 1, \ldots, |\Omega_s^*| : \omega_s^\ell \sim \mathcal{U}\{1, |\mathcal{D}_r^\ell|\},\ \omega_s^w \sim \mathcal{U}\{1, |\mathcal{D}_r^w|\}, \\ \boldsymbol{\xi}^\ell(\omega_s^\ell) \in \mathcal{D}_r^\ell,\ \boldsymbol{\xi}^w(\omega_s^w) \in \mathcal{D}_r^w\},\ \forall\ \ m = 1, \ldots, M \end{gathered} \tag{11}$$

where the probability of each scenario $\hat{\boldsymbol{\xi}}_s$ is calculated based on the centroid probabilities as

$$\pi_s(\hat{\boldsymbol{\xi}}_s) = \frac{\pi(\mu_s^\ell)\pi(\mu_s^w)}{\sum_s \pi(\mu_s^\ell)\pi(\mu_s^w)} = \frac{\frac{|C_s^\ell|}{|\mathcal{D}^\ell|}\frac{|C_s^w|}{|\mathcal{D}^w|}}{\sum_s \frac{|C_s^\ell|}{|\mathcal{D}^\ell|}\frac{|C_s^w|}{|\mathcal{D}^w|}} \tag{12}$$

where $\mu_s^\ell, C_s^\ell, |C_s^\ell|$ and $\mu_s^w, C_s^w, |C_s^w|$ are the centroids, their corresponding cluster and its size for load and wind power, respectively. The centroids are presented in figs. A.6a and A.6b with blue, and three random samples from them are presented with red, green, and blue profiles in figs. A.6c and A.6d.

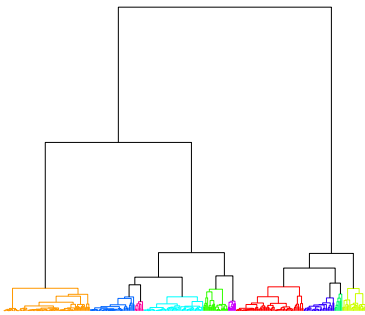

(a) load

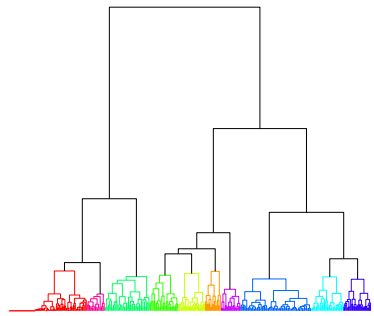

(b) wind power

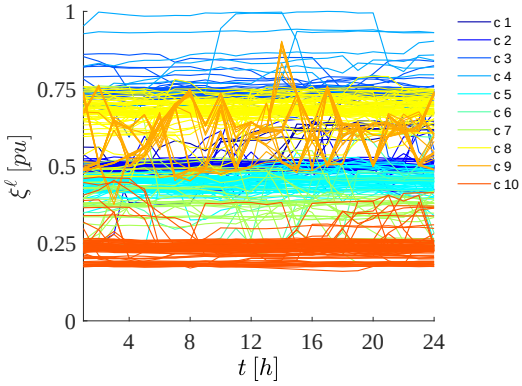

(c) load

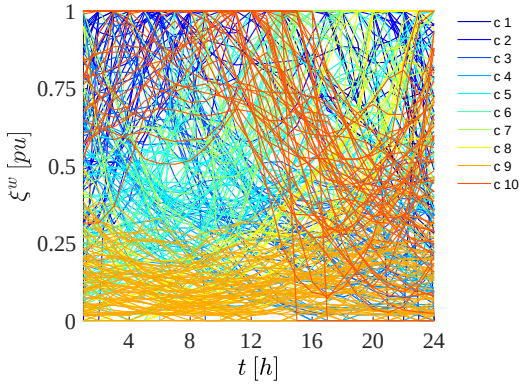

(d) wind power

FIGURE A.5. Dendrograms and clustered profiles using HAC

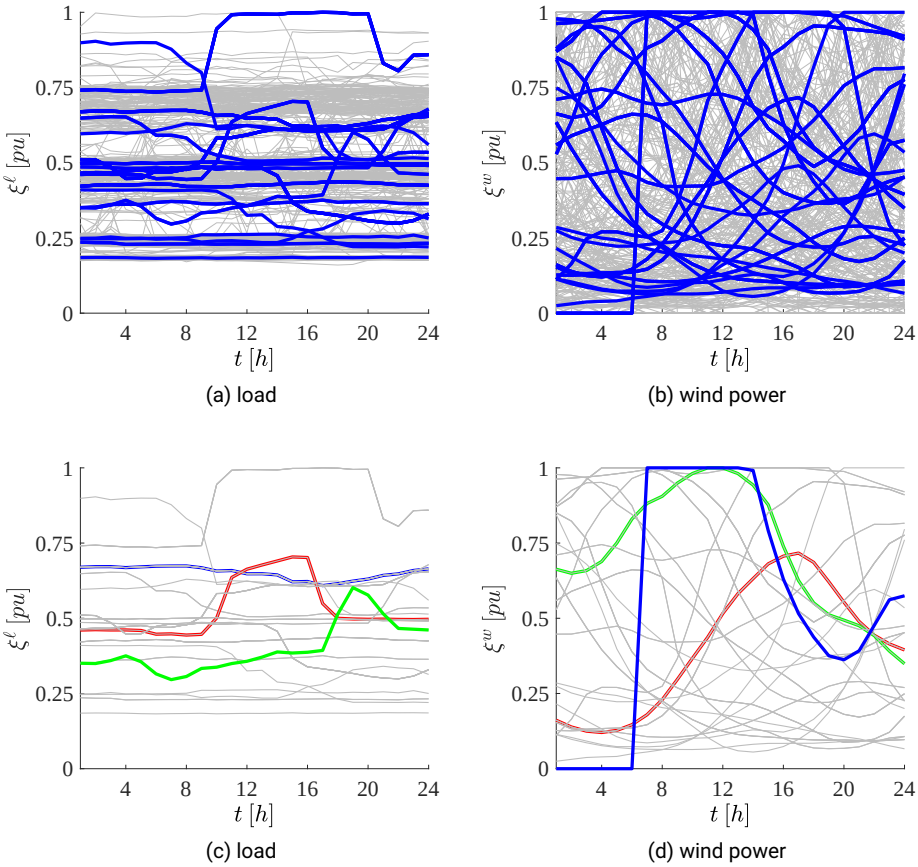

FIGURE A.6. Profiles selection with sg method: *H-cl*

As it is evident from Figure A.6, even though the variances of $\mathcal{D}^{\ell}$ and $\mathcal{D}^{w}$ are well captured by the cluster centroids, the combinations of a load and wind power profiles are still random. This means that since the centroids are weighted by the size of their own cluster, the combinations that will have the largest (and correspondingly the smallest) probabilities will depend on the random draw because of the multiplicative effect. In other words, in a first draw, a particular combination will dominate the solution of the problem (resulting in a specific objective value) and in a second draw probably a different combination will dominate, resulting in a different objective value. This fact also justifies the resulting high variance of $\hat{F}^{*}$ in Figure 4.5.

A.1.6 "SetCorr"

An alternative method comprises generating reduced subsets based on the load and wind power historical correlation. Despite the important related discussion in Chap-

ter 4, for the sake of a complete comparative analysis, we assume that this particular correlation value $\bar{\rho}$ is determined based on history for the specific case study and location, and we select it to generate scenarios that follow this correlation. For that value, we selected $\bar{\rho} = 0.28$ based on one of the most cited analyses in relevant studies. The process relies on the proposed random profile generation method described in Subsection A.1.3 with the following modifications. The linear (Pearson) correlation between the generated profiles $\tilde{\boldsymbol{\xi}}^{\ell}$, $\tilde{\boldsymbol{\xi}}^{w}$ is estimated as

$$\rho(\tilde{\boldsymbol{\xi}}^{\ell}(\omega_s), \tilde{\boldsymbol{\xi}}^{w}(\omega_s)) = \frac{\sum_{t}^{T} \left(\tilde{\xi}_t^{\ell}(\omega_s) - \frac{1}{T} \sum_{t}^{T} \tilde{\xi}_t^{\ell}(\omega_s) \right) \left(\tilde{\xi}_t^{w}(\omega_s) - \frac{1}{T} \sum_{t}^{T} \tilde{\xi}_t^{w}(\omega_s) \right)}{\sqrt{\sum_{t}^{T} \left(\tilde{\xi}_t^{\ell}(\omega_s) - \frac{1}{T} \sum_{t}^{T} \tilde{\xi}_t^{\ell}(\omega_s) \right)^2 \sum_{t}^{T} \left(\tilde{\xi}_t^{w}(\omega_s) - \frac{1}{T} \sum_{t}^{T} \tilde{\xi}_t^{w}(\omega_s) \right)^2}} \tag{13}$$

Then, the combinations are ranked based on their absolute distance with the nominal correlation $|\rho(\tilde{\boldsymbol{\xi}}^{\ell}(\omega_s), \tilde{\boldsymbol{\xi}}^{w}(\omega_s)) - \bar{\rho}|$ and the subset $\mathcal{D}_r$ is populated with the first $|\Omega_s^*|$ combinations (i.e., scenarios $\hat{\boldsymbol{\xi}}(\omega_s) = [\tilde{\boldsymbol{\xi}}^{\ell}(\omega_s), \tilde{\boldsymbol{\xi}}^{w}(\omega_s)]^T$) as

$$\begin{aligned} \mathcal{D}_r^{\rho} = \{ \hat{\boldsymbol{\xi}}_s \; \forall \;\; s = 1, \ldots, |\Omega_s^*| : \\ |\rho(\tilde{\boldsymbol{\xi}}^{\ell}(\omega_1), \tilde{\boldsymbol{\xi}}^{w}(\omega_1)) - \bar{\rho}| \leq \ldots \leq |\rho(\tilde{\boldsymbol{\xi}}^{\ell}(\omega_{|\Omega_s^*|}), \tilde{\boldsymbol{\xi}}^{w}(\omega_{|\Omega_s^*|})) - \bar{\rho}| \; \} \end{aligned} \tag{14}$$

To prioritize the combinations with correlation values close to $\bar{\rho}$ and penalize the rest, we weigh each combination by

$$w_s = \frac{1}{|\rho(\tilde{\boldsymbol{\xi}}^{\ell}(\omega_s), \tilde{\boldsymbol{\xi}}^{w}(\omega_s)) - \bar{\rho}|} \tag{15}$$

Eventually, the probability of each combination is calculated as

$$\pi_s(\hat{\boldsymbol{\xi}}_s) = \frac{w_s}{\sum_{s} w_s} \tag{16}$$

The above process is repeated for $m = 1, \ldots, M$ times (similarly to the previous methods), and corresponding sets $\mathcal{D}_{r,m}^{\rho}$ are generated to solve the optimization problem eq. (4.16) and get the objective value statistics. The sampling procedure is illustrated in Figure A.7 for two different m values. The colors correspond to each other, meaning that red is the combination of load (figs. A.7a and A.7c) and wind power (figs. A.7b and A.7d) with rank closest to the specified rank $\bar{\rho}$, green is the second best, blue the third, and so on. Note that all of these combinations have correlation values extremely close to $\bar{\rho}$. Nevertheless, evidently, we can achieve the same correlation values with completely different profile shapes (compare $m = 1, 2$), meaning that the solution

to the optimization problem would be significantly different. That also justifies the variance of method *SetCorr* in Figure 4.5 and further reinforces the fact that a correlation coefficient alone does not guarantee statistical stability to the solution of problem eq. (4.16).

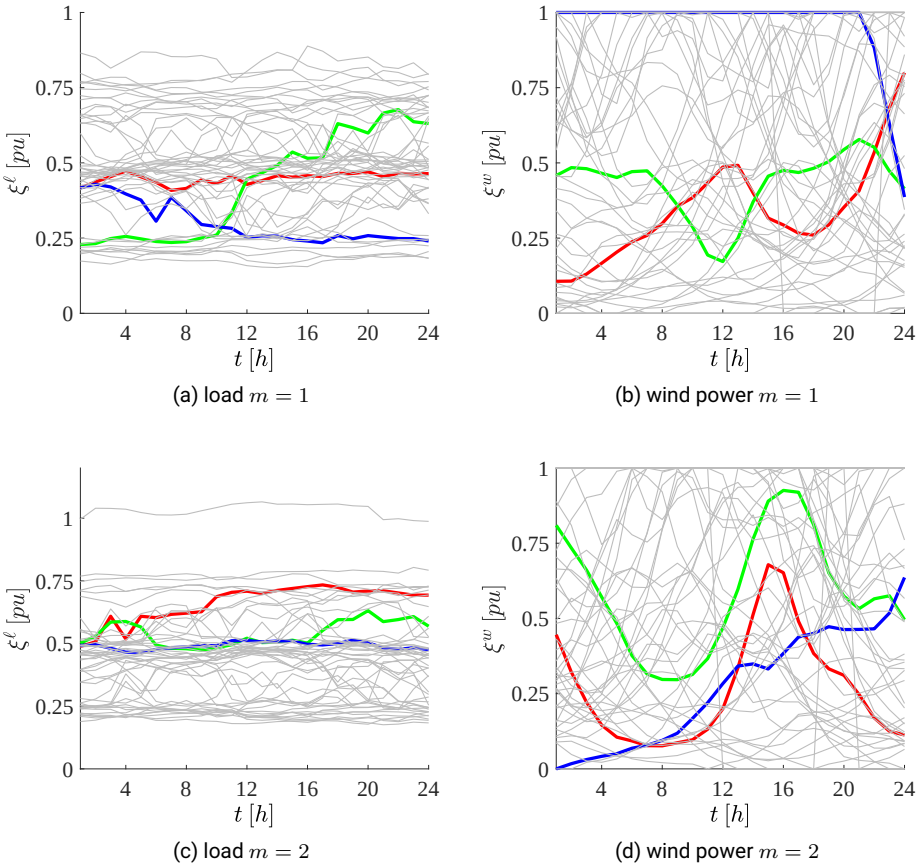

(a) load $m = 1$ (b) wind power $m = 1$

(c) load $m = 2$ (d) wind power $m = 2$

FIGURE A.7. Profiles selection with sg method: *SetCorr*

Appendix B

Supplementary information for Chapter 5

B.1 Effect of degradation weighting on the ESS cycling

It is evident from Figure 5.9 to Figure 5.14 that the BESS experiences rapid charge/discharge variations during the simulated operating period for both DMPC and SMPC methods, which may negatively effect its lifetime. We note, though, that the resulting SoC trajectories are actually sequences of optimal SoC points that come as solutions of an optimization procedure that embeds considerations about battery degradation from cycling. Thus the formulation of the optimization problem accounts for such concerns by design (and if an operator is even more worried than we are, they may just change the parameters of the cost function so to penalize rapid variations even more). In addition, the solution of the resulting MILP problems is performed with one of the best commercially available MILP solvers (Gurobi) and tight termination criteria were set for the optimality gap (difference between UB and LB of the solution, with a relative gap tolerance <=0.5%). So, the optimality of the solutions we obtain is guaranteed to the defined accuracy level.

To comment on the results presented in Chapter 5, the oscillatory behavior is a result of the controller trying to optimally coordinate the operating point of the GT, how many of them should be on, and how much the battery should be used. This behavior is present in both the deterministic version (DMPC) and the proposed stochastic one (SMPC). Under the assumption that the minimum required startup time of the GT is 15 minutes, then the optimal solution alternates between one and two GTs being on, which, in turn, results in the battery rapid charging/discharging to bring the GTs loading as close as possible to the maximum efficiency operating points.

Nevertheless, again we highlight that this behavior highly depends on what we choose to penalize more. In our basic setup, the battery degradation is penalized by the percentage lost capacity from cycling and its investment cost (as is commonly done in other studies in the literature). However, our proposed method is flexible enough to accept the user's preferences regarding on how to prioritize the multiple objectives. We demonstrate this by defining the extra weighing factor w_{dg} that scales the term related to the battery degradation (in the objective function). So, we have considered and simulated three characteristic cases:

- $w_{dg} = 0$: no battery degradation is considered among the objectives;
- $w_{dg} = 1$: normal battery degradation (standard case);

- $w_{dg} = 1000$: battery degradation is highly penalized relative to the rest of the objectives.

The results of the simulations are summarized in the following figures. As we can observe there, both methods, i.e. DMPC and the proposed SMPC, present similar behaviors for the different weight values. When $w_{dg} = 0$ the state of charge is highly volatile in both methods and this results in more cycles and rapid charges/discharges. When $w_{dg} = 1$ (the default case), again we notice oscillations, but these are mostly after the step of the net load and their amplitude is reduced compared to the no degradation case. Finally, when $w_{dg} = 1,000$, we observe that the optimal control action defines a single big cycle (discharge/charge) for both methods (DMPC and SMPC) and no significant oscillations are observed.

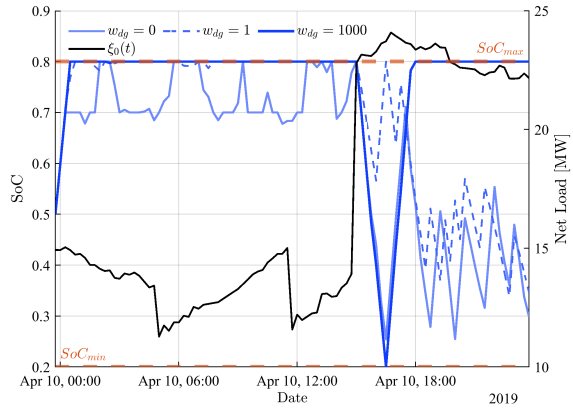

(a) DMPC

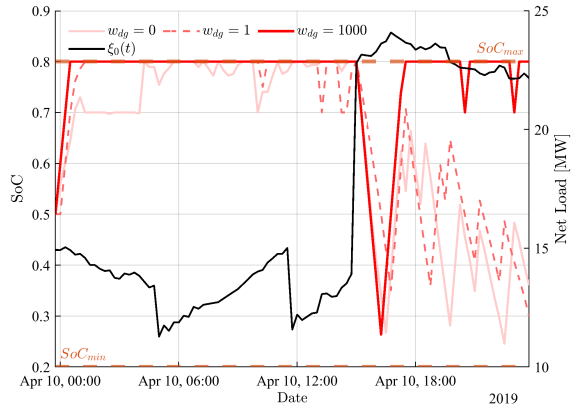

(b) SMPC

FIGURE B.1. Effect of degradation weighting on the cycling behavior of the BESS

Appendix C

Supplementary information for Chapter 6

C.1 Wind speed data generation mechanism

Besides the load deviations profiles, the second source of variability is the wind power generation mechanism. To model realistic wind power generation profiles, that will in turn result in a more realistic Δ set, we considered wind speed measurements v_m (sampling period 1 min) collected from the location of the offshore wind farm and adjusted to the wind turbines hub height. For completeness, we note that we used a Kaimal filter [1] to model the smaller time scale turbulence related phenomena. This was performed after the Normal Turbulence Model [2] as

$$\tilde{v}(t) = H_K(s)WN(0,1) = \frac{v_m}{\sqrt{2L_t\sigma_1}} \frac{0.0182\left(\frac{v_m}{L_t}\right)^2 s^2 + 1.3653\frac{v_m}{L_t}s + 0.9846}{1.3463\left(\frac{v_m}{L_t}\right)^2 s^2 + 3.7593\frac{v_m}{L_t}s + 1} WN(0,1) \tag{17}$$

where $WN(0,1)$ is a white noise signal with zero mean and unit standard deviation, $\sigma_1 = I_{ref}\,(0.75v_m + 5.6)$ with parameters tuned for the specific offshore location.

The wind power production profiles acquired in this way were then used to populate the δ_i set using the simplified power curve of the specific wind turbine model and the actual wind speed $v(t) = \tilde{v}(t) + v_m(t)$ as

$$P_W(v(t,\delta_i)) = \begin{cases} 0, & v(t,\delta_i) \le v^{in} \\ N_{wt}P^n_{wt}\left(\frac{v(t,\delta_i)}{v_n}\right)^3, & v^{in} \le v(t,\delta_i) \le v_n \\ N_{wt}P^n_{wt}, & v_n \le v(t,\delta_i) < v^{off} \\ 0, & v^{off} \le v(t,\delta_i) \end{cases} \tag{18}$$
$$\forall\ \delta_i \in \Delta \text{ and } t = 0,\ldots,t_h$$

where v^{in} is the cut-in wind speed; v_n is the nominal wind speed; v^{off} is the cut-off wind speed; P^n_{wt} is the nominal power of each wind turbine; and N_{wt} is the number of wind turbines in the considered wind farm. Considering the commonly used typical dynamics of a wind turbine [3], all the considerations above lead to electrical wind power that is injected into the power system to be equal to

$$P_{WF}(v(\delta_i)) = \frac{P_W(v(\delta_i))}{sT_w + 1} \quad \forall\ \delta_i \in \Delta\ . \tag{19}$$

C.2 FREQUENCY RESPONSE

It is interesting then to visualize the effect of choosing different $\overline{u}$ designs on the impulse/step responses of the open and closed loop systems. The results, summarized in Figure C.1, reveal that decreasing $\overline{u}$ leads to higher peak response value to the impulsive disturbance, meaning that the nadir value of frequency deviation is increased. However, for all control designs, the nadir is better compared to the open loop system $S_d(z)$. This effect is directly associated with the inertia of the system, meaning that the proposed controllers can effectively use the storage system to provide additional (virtual) inertia to the isolated system. In addition, we observe that by increasing the saturation level $\overline{u}$, we obtain lower $RoCoF$, which is also an indication of the increased damping capability of the closed loop system.

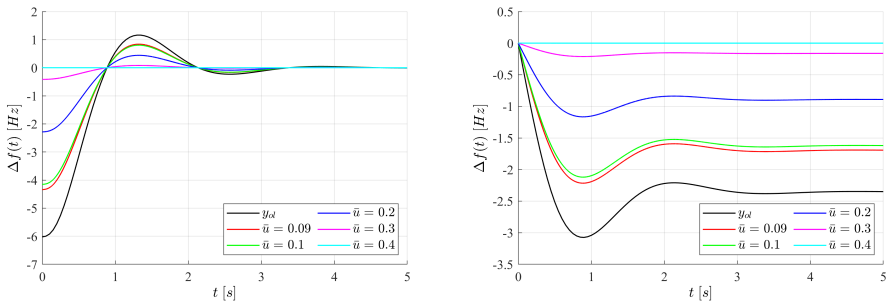

(a) impulse response (b) step response

FIGURE C.1. Frequency response improvement for various ESS sizes and control laws for an isolated O&G grid

C.3 REFERENCES

[1] C. Gavriluta, S. Spataru, I. Mosincat, C. Citro, I. Candela, and P. Rodriguez. Complete methodology on generating realistic wind speed profiles based on measurements. *REPQJ* pages 1757–1762 (April 2012). ISSN 2172038X, 2172038X. doi: 10.24084/repqj10.828. URL http://www.icrepq.com/icrepq'12/828-gavriluta.pdf. Cited on page/s A-13.

[2] INTERNATIONAL STANDARD IEC 61400-1. Technical report (). URL http://dlbargh.ir/mbayat/46.pdf. Cited on page/s A-13.

[3] D. Lee and L. Wang. Small-Signal Stability Analysis of an Autonomous Hybrid Renewable Energy Power Generation/Energy Storage System Part I: Time-Domain Simulations. *IEEE Transactions on Energy Conversion* **23** (1), 311–320 (March 2008). ISSN 1558-0059. doi: 10.1109/TEC.2007.914309. Conference Name: IEEE Transactions on Energy Conversion. Cited on page/s A-13.

ISBN 978-82-326-5995-1 (printed ver.)
ISBN 978-82-326-5544-1 (electronic ver.)
ISSN 1503-8181 (printed ver.)
ISSN 2703-8084 (online ver.)

NTNU

Norwegian University of
Science and Technology